Nonlinear Vibration Control and Limit-Cycle Analysis of Rotor/Autobalancer Systems Equipped with Hydrodynamic and Active Magnetic Bearing Supports

A Dissertation Presented for the
Doctor of Philosophy
Degree
The University of Tennessee, Knoxville

DAEYI JUNG
August 2012

Copyright © 2012 by Jung, DaeYi.
All rights reserved.

DEDICATION

My better half
Kim, Mina

My parents
Jang HyunJa & Jung, SangGu

My brother
Jung MyungJun

My adorable son
David, Naram, Jung

ACKNOWLEDGEMENTS

I would like to thank my advisor Dr. DeSmidt, Hans August for all his support and guidance throughout my time at graduate school. Special thanks to Dr. Ekici Kivanc, Dr. Seddik M, Djouadi and Dr. Zhao, Xiaopeng for serving in my committee.

This research was supported by a grant from the National Science Foundation (Grant Number: NSF-CMMI-0856471) under the Dynamical Systems Program directed by Dr. Eduardo A. Misawa.

ABSTRACT

In recent years, there has been much interest in the use of automatic balancing devices (ABDs) in rotating machinery. Autobalancers consists of several freely moving eccentric balancing masses mounted on the rotor, which, at certain operating speeds, act to cancel rotor imbalance. This "automatic balancing" phenomena occurs as a result of nonlinear dynamic interactions between the balancer and rotor wherein the balancer masses naturally synchronize with the rotor with appropriate phase to cancel the imbalance. However, due to inherent nonlinearity of the autobalancer, the potential for other undesirable non-synchronous limit-cycle behavior exists. In such situations, the balancer masses do not reach their desired synchronous balanced positions resulting in increased rotor vibration. By recognizing this issues, this research explores this non-synchronous behavior for rotor-shaft system in the augmented with auto-balancer device(ABD) supported by various types of bearing and suggests methods to prevent this undesirable condition by searching for either desirable operating condition to avoid it or suppress it using active actuation. Specifically, an approximated harmonic solution for the limit-cycle is obtained and the limit-cycle stability is assessed via a perturbation and Floquet analysis and the coexistence of the stable balanced synchronous condition and undesired non-synchronous limit-cycle are studied. It is found that for certain combinations of bearing parameters and operating speeds, the non-synchronous limit-cycle can be made unstable thus guaranteeing global asymptotic stability of the synchronous balanced condition and the inherent nonlinear characteristic of the driving frequency induced by ball mass running on ABD track under limit cycle condition is revealed here. Finally, the analysis is validated through numerical time and frequency domain simulation. The findings in this study yield important insights for researchers wishing to utilize automatic balancing devices in shaft/eccentric rotor system with various types of bearing. Additionally, a new adaptive active control algorithm for the rotor/bearing/ABD system supported by active magnetic bearing(AMB) is derived based on the Lyapunov approach which guarantees global asymptotic stability of the synchronous balanced condition. This approach enables the controller to cope with both the system nonlinearity introduced by the passive ABD and with the rotor imbalance uncertainty. Here, the controllability of system is established through an accessible distribution Lie bracket operational analysis. The simulation results demonstrate the advantages of the hybrid ABD/AMB. In particular, it is shown that the balanced equilibrium can be made globally attractive under the action of the adaptive bearing control law, and that the steady-state power

levels are significantly reduced via the addition of the ABD. These findings are relevant to limited power applications such as in satellite reaction wheels or flywheel energy storage batteries.

TABLE OF CONTENTS

CHAPTER I Introduction and General Information 11
1.1 Auto-balancer Device 11
1.2 Operating Principle and Feature of ABD 11
1.3 Non-synchronous Limit cycle Behavior of ABD 12
1.4 Purpose and Summary of Research 13
1.5 Analysis Method 17
1.5.1 Numerical Continuation method 17
1.5.2 Stability Analysis using Floquet Transition Matrix(FTM) 17
CHAPTER II Limit-Cycle Analysis of Planar Rotor/Autobalancer System influenced by Alford's Force 19
2.1 Planar Rotor/Autobalancer system 19
2.2 Limit-cycle Solution of Symmetric Bearing with Alford's Force 21
2.3 Stability analysis 24
2.4 Numerical Simulation Results 25
2.5 Concluding Remarks 36
CHAPTER III Limit-Cycle Analysis of Planar Rotor/Autobalancer System Supported on Hydrodynamic Journal Bearing 38
3.1 Planar Rotor/Autobalancer system 38
3.2 Limit-cycle solution of generalized bearing support 40
3.3 Stability analysis 43
3.4 Numerical Simulation Results 45
3.4.1 Rotor/ABD with Fully Cavitated Short Bearing 45
3.4.2 Rotor/ABD with Tilting-Pad Bearing 53
3.5 Concluding Remarks 60
CHAPTER IV Hybrid Adaptive Rotor Imbalance Vibration Control via Passive Autobalancer and Active Bearing Actuation 61
4.1 Rotor/Autobalancer/Active bearing System 61
4.2 Controllability of System 63

4.3 Adaptive Control law Development 65
4.4 Hybrid Control strategy 72
4.5 Simulation Results 76
4.6 Concluding Remarks 82

CHAPTER V Limit-Cycle Analysis of three dimensional rigid Rotor/shaft/Autobalancer System with symmetric bearing support 83
5.1 3-Dimensional Rigid shaft/Rotor/Autobalancer system 83
5.2 Limit-cycle Response 89
5.3 Stability Analysis 93
5.4 Numerical Simulation Results 95
5.5 Concluding Remarks 103
CHAPTER VI Limit-Cycle Analysis of three dimensional flexible shaft/rigid rotor/Autobalancer System with symmetric Rigid support 104
6.1 3-Dimensional flexible shaft/rigid Rotor/Autobalancer system 104
6.2 Limit-cycle Solution 112
6.3 Stability analysis 118
6.4 Numerical Simulation Results 120
6.5 Concluding Remarks 131
LIST OF REFERENCES 132
APPENDIX 136
Vita 140

LIST OF FIGURES

Figure.1.1 The sketch of autobalancer and typical usage of ABD in CD-Drive. 11
Figure.1.2 The operating principle of autobalancer(ABD) via operating speed. 12
Figure.1.3 Simulation results for synchronous behavior and non-synchronous limit cycle behavior. 13
Figure.1.4 rotor-shaft system with ABD and AMB. 15
Figure.2.1 Rigid planar rotor-ABD system supported by a general bearing holding asymmetric damping and stiffness force including cross-coupling ones. 19
Figure.2.2 Comparison between full numerical solutions and assumed limit-cycle solutions. 29
Figure.2.3. Coexistence of limit-cycle solutions and balanced solution. 32
Figure.2.4 Stability contour plots ($\overline{\Omega}$ vs.$\overline{K}_{XY}$) under the influence of Alford's force. 33
Figure.2.5 Stability contour plots ($\overline{\Omega}$ vs.$\overline{K}_{XY}$) under the influence of Alford's force. 34
Figure.2.6 Bearing stiffness and damping domain for the critical operating speed. 36
Figure.3.1 Rigid planar rotor-ABD system supported by a general bearing holding asymmetric damping and stiffness force including cross-coupling ones. 38
Figure.3.2 Characteristic of dimensionless bearing coefficients for fully cavitated short bearing. 46
Figure.3.3. Comparison between full numerical solutions and assumed limit-cycle solutions. 49
Figure.3.4. Stability contour plots ($\overline{\Omega}$ vs.ε) for the short journal bearing. 53
Figure.3.5 Characteristic of dimensionless bearing coefficients for the tilting bearing with five pads. 54
Figure.3.6. Comparison between full numerical solutions and assumed limit-cycle solutions. 55
Figure.3.7 Stability contour plots ($\overline{\Omega}$ vs.ε)for the tilting pad bearing 59
Figure.4.1. Rigid planar imbalanced rotor system with auto-balancing device and active bearing actuators. 61
Figure.4.2 The trajectory of ABD-ball with three different control activation times. 70
Figure.4.3 The comparison of steady-state control force due to the function of ABD. 71

Figure.4.4 Supervisory hybrid control strategy map and four examples. 74
Figure. 4.5. Adaptive control for the case where the imbalance exceeds the maximum ABD balancing force. 76
Figure.4.6 Adaptive estimation of unknown parameters. 78
Figure.4.7 Comparison of control force consumed between w/o ABD and w ABD. 79
Figure.4.8 The performance of control under the limit-cycles condition. 79
Figure.4.9 The performance of control under the undesirable synchronous condition. 81
Figure.4.10 The performance of control under the limit-cycle and undesirable synchronous condition. 82
Figure.5.1 System coordinates transformation and three Dimensional Rigid shaft- rotor-ABD system supported by a passive symmetric bearing. 84
Figure.5.2. Comparison between full numerical response and analytical one. 98
Figure.5.3 whirl speed of balancer mass in ABD and damped natural frequency of system. 101
Figure.5.4. a) System stability influence of the relative mass size of ABD to entire system mass b) System stability influence of ABD ball damping coefficient. 102
Figure.5.5 The relative suggested location of ABD along with shaft to imbalance source. 103
Figure.6.1 Three dimensional flexible shaft/rigid rotor/ABD system with rigid supports.. 107
Figure.6.2. Comparison between full numerical response and analytical one. 121
Figure.6.3. whirl speed of balancer mass in ABD and damped natural frequency of system. 128
Figure.6.4 Synchronous fixed equilibrium position of ABD balls. 128
Figure.6.5 a) Stability influence of the relative mass size m_b of ABD to entire system mass b) System stability influence of ABD ball damping coefficient c_b.. 130
Figure.6.6 The relative suggested location of ABD along with shaft to imbalance source. 131

CHAPTER I
INTRODUCTION AND GENERAL INFROMATION

1.1 Auto-balancer Device

This imbalance vibration is a significant concern for all rotor dynamic systems and engineering problems associated with them. Therefore, with this concern, how to suppress the effect of imbalance vibration is also a critical issue for ensuring reliable and efficient operation of these systems. One elegant approach to deal with this issue is based on so-called auto-balancing devices(ABD). These are a special class of passive devices with freely moving eccentric masses, which naturally adjust to cancel the rotor's imbalance at certain operating condition (speed). This cancelling phenomenon or so called "automatic balancing" is a results of the interaction between balancer balls and the rotor transverse vibration. The merit of this device is the ability to compensate for imbalance changes/configuration without requiring the power, sensors, or a control system. In Figure.1.1 displays the configuration of ABD and its practical usage in CD-drive.

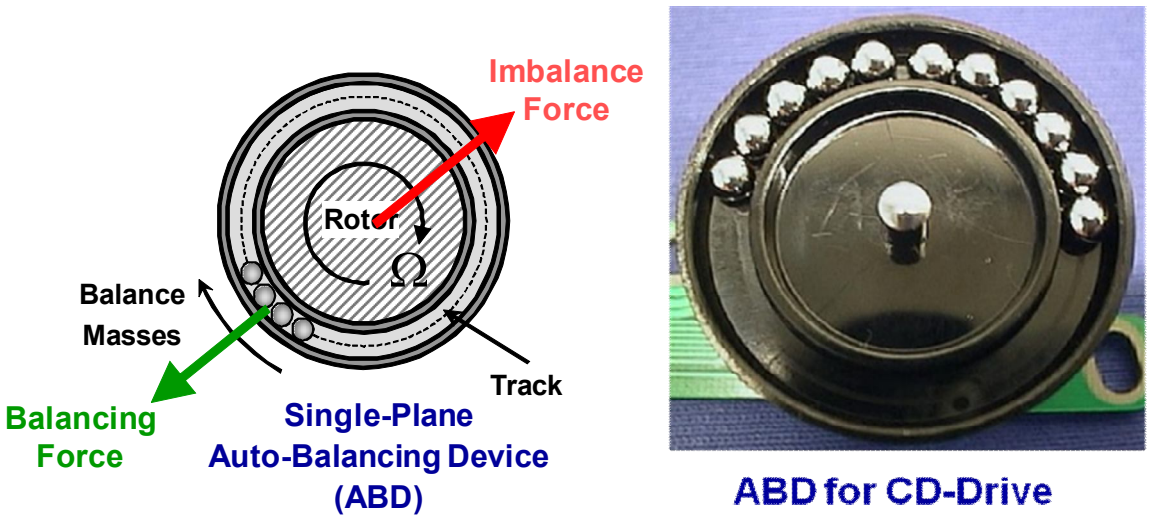


Figure.1.1 The sketch of autobalancer and typical usage of ABD in CD-Drive

1.2 Operating Principle and Feature of ABD

One early experimental study of automatic balancing was conducted by Thearle [1], who characterized the dynamics of a planar ball ABD under various imbalance levels. Further, [2] and [3] numerically explored the spinup and steady-state response of planar rotor-ABD system and showed that complete balancing can be achieved by an ABD containing a minimum two balancer masses. Majewski, [4], constructed planar equation-of-motion and examined the effects of ball-rolling resistance and runway

eccentricity on the rotor-balancer system at steady state. Jinnouchi et al. [5] showed that the planar rotor-ABD system provides excellent balancing at the supercritical speed but leads to amplified vibration at sub-critical speeds. This operating principle of ABD relative to the operating speed is summarized in Figure.1.2. Lindell, [6], installed ABD in a hand-held grinding machine to reduce the unbalance vibration. More recently, Kim et al. [7] and Rajalingham and Bhat [8] considered the three-dimensional dynamic behavior of various ABD-rotor system including in-plane twisting, out-of-plane tilting and gyroscopic effect and concluded that the balancing behavior can be accomplished at supercritical speeds. Furthermore, Chao et al[9-10] analytically and experimentally studied automatic balancing of a vertically oriented optical disk drive spindle. It was shown that, through proper choice of autobalancer initial position along the spindle axis, both lateral displacements and tilting angle vibrations could be simultaneously reduced. Also, Sohn et al[11] and Horvath et al[12] explored a dual pendulum autobalancer devices. By introducing hinge offsets between the rotor center and pendulum pivot points, it was shown the pendulum autobalancer can achieve balancing at both sub and supercritical operating speed.

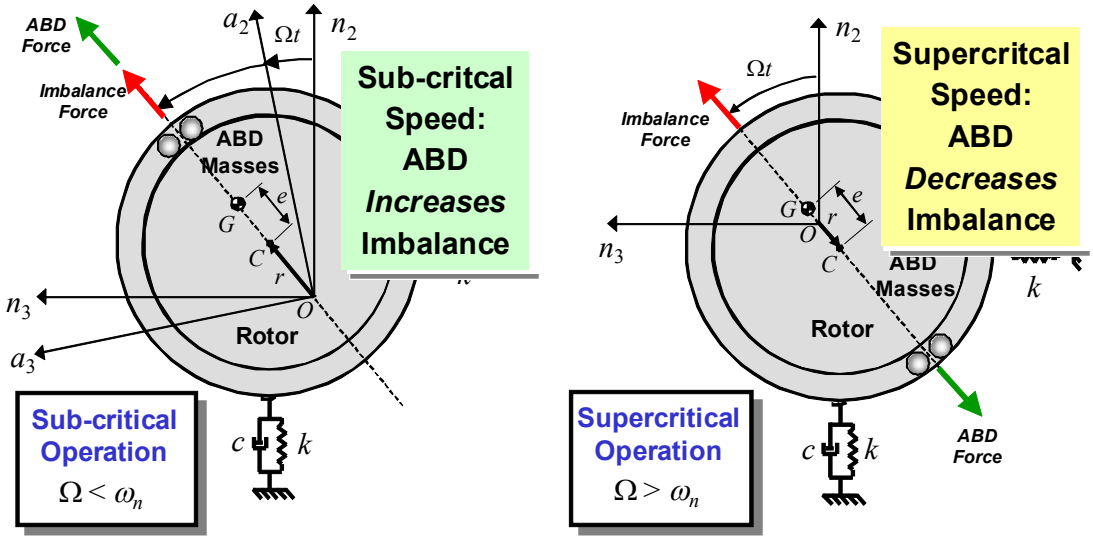


Figure.1.2 The operating principle of autobalancer(ABD) via operating speed

1.3 Non-synchronous Limit cycle Behavior of ABD

Although the ABD possesses the advantage to cope with the system vibration at certain condition, [15] and [16] investigated the behavior of a rotor-autobalancer system and noted the co-existence of stable synchronous(i.e, balanced fixed-point equiliburium) and sub-synchronous limit-cycle which is highly undesirable and causes a significant level of vibration amplitude. This limit-cycle behavior is mainly addressed as one of serious ABD's drawbacks which should be avoided. Specifically, this phenomena in

ABD-rotor system is described as the condition where the balls(balancer mass) are merged together and kept rotating in the combining multiple speeds or constant speed relative to the rotor operating speed. Thus, it is so called “non-synchronous behavior” and the existence of this behavior heavily relies on the supporting bearing characteristic, the balancer mass’ initial position as well as operating environment where the system exposure to undesired destabilizing force. Figure.1.3 shows the simulation results for synchronous behavior and non-synchronous limit cycle behavior relative to rotating rotor. In synchronous behavior, the balancer mass reaches the fixed equilibrium position and are synchronous with rotating rotor, which leads reduction of imbalance vibration. However, the balancers are kept rotating and exhibit non-synchronous behavior relative to rotating rotor, which results in large vibration level as shown in Figure.1.3.

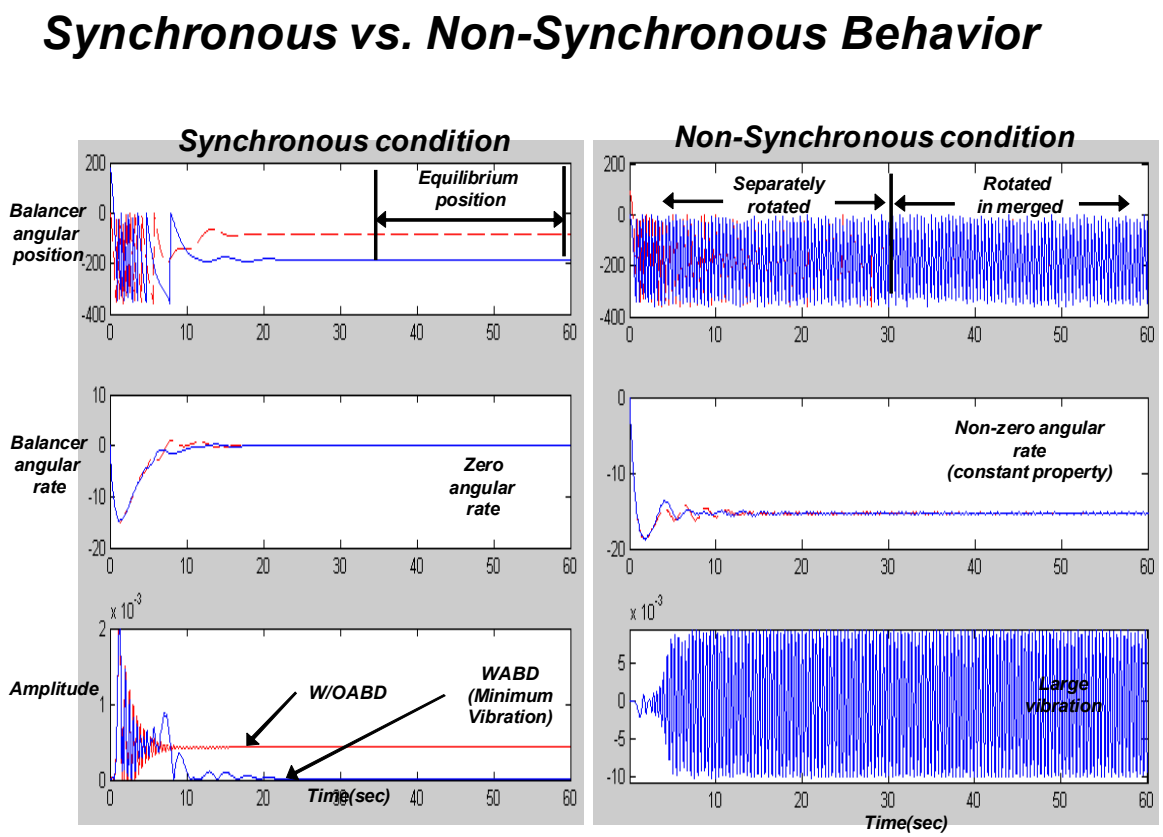


Figure.1.3 Simulation results for synchronous behavior and non-synchronous limit cycle behavior

1.4 Purpose and Summary of Research

Recognizing the issue of undesirable limit cycle behavior of ABD, this research focus on the understating of this inherent nature of limit cycle and present the methods such that searching for either desirable

operating condition to avoid it or suppress it using active actuation. Specifically, Chapter.II suggests the well approximated harmonic form of limit-cycle solution capturing the essence of this unwanted behavior and explores the stability of the system influenced by Alford's force which is the destabilizing force that often occurs in turbomachinery. This force is caused by the variation of blade-tip clearance around an shrouded axial flow stage in compressor, due to any deflection of shaft away from the center of the housing[17]. This is the cross-coupling stiffness force (appeared as off-diagonal elements in system stiffness matrix) producing a tangential force driving forward whirl resulting in undesired instability of system. Therefore, with several assumptions, the effect of this force for limit-cycle behavior is investigated as this force is varied at a given steady-state operating speed and the corresponding analytical bifurcation boundary characterizing coexistence of limit-cycle and synchronous balanced condition under the influence of this force has been assessed. Additionally, the guideline of bearing damping and stiffness design is also discussed to suppress the unwanted limit cycle behavior based upon the analytical bifurcation obtained here and the important finding of the inherent characteristic of system driving frequency induced by ABD ball under non-synchronous(limit cycle) behavior is presented in this chapter. This feature of the driving frequency enhances us to understand the nature of limit cycle condition.

Chapter.III suggests the harmonic form of limit-cycle solution capturing the essence of this unwanted behavior and explores the system stability with two commonly-used hydrodynamic bearings, a short journal bearing and a tilting pad bearing, by using the perturbed system about this limit-cycle solution. Compared to the rolling/contacting type bearing assumed to hold symmetric balancing force with some constraints, both bearings used here are the fluid-film ones inducing asymmetric damping and stiffness force. Additionally, the short journal bearing generates the cross-coupling damping and stiffness terms whereas the tilting pad bearing don't because of its geometrical benefit. These bearings are most often used due to their long life for industrial and utility applications and the performance of these bearing is primarily determined by the eccentricity and radial clearance of bearing journal. [18], [19] and [20] provides the damping and stiffness coefficients by using mathematical expression which conveniently allow us to apply the characteristic of these two bearing into the ABD-rotor system. This application enables us to achieve more precise and distinctive research for the interaction between the ABD-rotor system and the hydrodynamic/fluid film bearings, although [21] explores the response of the rotor system supported by oil film bearing without ABD. Regardless of bearing type presented here, the important finding of the inherent characteristic of system driving frequency induced by ABD ball under non-synchronous limit cycle behavior is also revealed in this chapter.

Besides of this limit-cycles, if the change of imbalance is suddenly occurred on a certain operation and then this change may produce an imbalance force which exceeds the allowable capacity of ABD. This situation lead that the system might becomes unstable or can be subjected to undesirable steady-state

vibration level. Also, as pointed out in [5], ABD increases imbalance effect due to unfavorable angular equilibrium position of balancer mass relative to imbalance at subcritical speeds and it results in unwanted vibration level. Thus, in order to compensate the drawbacks of ABD, the extra countermeasure is required to avoid the unwanted situations explained above.

Another common way to deal with the vibration issue is the active control or active balancing founded in [22] and [23] using the magnetic type of actuator/bearing(AMB) or the actively controlled journal bearing. AMB generate the electromagnetic field through the coil inside it and maintain a certain level of air gap/clearance between a shaft and the coil by controlling the magnetic force induced by the arranged coils. Although this active control can ensure the global stability of system and be adaptive for the change of operating environment, this strategy definitively requests a certain amount of control power to meet a desired vibration level. Therefore, in the Chapter.III, we investigate that the hybrid interaction between the ABD and the AMB governed by the adaptive control law can produce desired performance compared to the system equipped with only ABD as well as reduce the control power consumption of AMB relative to the case controlled actively without ABD.

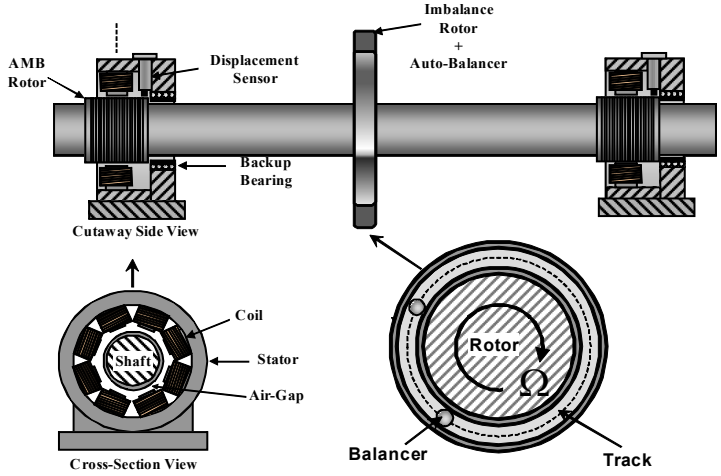


Figure.1.4 rotor-shaft system with ABD and AMB

Specifically, AMB compensate the deficiencies of ABD system s.t, the limit-cycles condition and its own limited capacity. At same time, ABD assists reducing the consumption of AMB control force by partially or entirely cancelling the imbalance effect/force. Additionally, besides of the ability to minimize the vibration amplitude, the active control derived here owns the capability to cope with unknown parameters such that the imbalance effect and the ball damping coefficient of ABD which are complicate to be assessed. By using the advantages of both devices, we can eliminate the imbalance vibration efficiently and robustly.

In the Chapter.III, additionally, through the accessible distribution spanned by Lie bracket operation, the system controllability is investigated to determine whether the control force produced by AMB can

control the state of ABD balancer masses. Finally, the effectiveness of proposed technique is validated through the MATLAB/ Simulink simulation.

Since [15], [16] and [29] use rigid planar ABD-rotor system, the in-plane transverse deflection of system is only considered under limit-cycle condition. Thus, the Chapter.IV focuses on the limit cycle analysis of three dimensional rigid rotor/shaft system including out-plane tilting motion and gyroscopic effect, which is never considered so far. In this paper, an approximated harmonic solution to capture the undesirable limit-cycle behavior is obtained for the three dimensional rigid shaft/rotor in augmented with ABD supported by the symmetric stiffness bearing. Essentially, the solutions presented here capture both in-plane transverse deflection and out-planes tilting of system under the limit cycle condition and the important property of whirl speed for ABD balancer mass is also explored. The limit-cycle stability is assessed via a perturbation and Floquet analysis with three main parameters of ABD (ABD balancer mass, viscous damping coefficient of balancer, and the location of ABD along with shaft) and the coexistence of the stable balanced synchronous condition and undesired non-synchronous limit-cycle is studied. It is found that for certain combinations of appropriate three main parameters of ABD and operating speeds, the non-synchronous limit-cycle can be made unstable thus guaranteeing global asymptotic stability of the synchronous balanced condition.

However, the rigid shaft is valid in some situations and the flexibility of shaft can be negligible in certain applications. Hence, the limit-cycle analysis of three dimensional flexible shaft/rigid rotor/ABD has been explored in the Chapter.V. Although [24] employed the flexible shaft/rigid rotor/ABD system with symmetric bearing support to explore the synchronous balancing condition of system, the non-synchronous limit-cycle condition had not been discussed in detail. Based upon the knowledge of previous studies [24] and [29], this research presents an approximate harmonic analytical solution to describe the limit-cycle behavior of system interacting with flexible shaft which is a Euler-Bernoulli beam. Thus, the shape function of the shaft is determined by using well known fixed-fixed boundary condition due to symmetric rigid support employed here. The whirl speed of the ABD balancer masses is determined via the solution of a non-linear characteristic equation. Also, based upon the limit-cycle solutions, the limit-cycle stability is assessed via a perturbation and Floquet analysis exploring three main parameters; ABD balancer mass, ABD damping, and axial location of ABD along the shaft. Again, the coexistence of the stable balanced synchronous condition and undesired non-synchronous limit-cycle is studied. It is found that for certain combinations of ABD parameters and rotor speeds, the non-synchronous limit-cycle can be made unstable thus guaranteeing global asymptotic stability of the synchronous balanced condition. Finally, the analysis is validated through numerical simulation. The findings in this research yield important insights for researchers wishing to utilize automatic balancing devices in flexible shaft/rigid rotor systems and limit-cycle mitigation.

1.5 Analysis Method

1.5.1 Numerical Continuation method

Here, we selected the Riks-Wempner method [28] using linear constraint. The cleverness of this method simultaneously traces unknowns and an interesting system parameter satisfying a set of nonlinear equations and a given constraint equation.

Specifically, let $f(x,\varepsilon)=0\in\Re^n$ be a set of nonlinear equations and $x\in\Re^n$ and $\varepsilon\in\Re$ be unknowns and an interesting parameter respectively. Riks-Wempner method utilized a linear constraint such that $\alpha x+\beta\varepsilon=\gamma$ intersecting with $f(x,\varepsilon)=0$. where, $\alpha\in\Re^n$ and $\beta\in\Re$ are a constant vector and a constant, respectively. If the linear constraint is chosen to be orthogonal to a tangential vector of any pairs (x,ε) on $f(x,\varepsilon)=0$ and then the predicting discretizing iteration process for the solution is followed,

$$\varepsilon_{i+1}=\varepsilon_i+\frac{\alpha_i f_{x.i}\, f_i}{1-\alpha_i f_{\varepsilon.i}} \tag{1-1}$$

$$x_{i+1}=x_i-f_{x.i}^{-1}\left[f_i+f_{\varepsilon.i}\frac{\alpha_i f_{x.i}\, f_i}{1-\alpha_i f_{\varepsilon.i}}\right] \tag{1-2}$$

where, $f_{x.i}=\left.\frac{\partial f(x,\varepsilon)}{\partial x}\right|_i\in\Re^{n\times n}$ and $f_{\varepsilon.i}=\left.\frac{\partial f(x,\varepsilon)}{\partial \varepsilon}\right|_i\in\Re^n$ are respectively the Jacobian matrix and a partial differential vector of $f(x,\varepsilon)$ with respect to ε at *i*-th iteration. Also, $\alpha_i=-\frac{\left[f_{x.i}^{-1}f_{\varepsilon.i}\right]^T}{\left\|f_{x.i}^{-1}f_{\varepsilon.i}\right\|_2}\in\Re^n$ and $f_i=f(x_i,\varepsilon_i)$. Both (1-1) and (1-2) search for the solution (x_i,ε_i) satisfying $\left|f(x_i,\varepsilon_i)\right|\approx 0$. It should be noted that the initial solution (x_0,ε_0) should meet $f(x_0,\varepsilon_0)=0$ to predict next solution intersecting the constraint hence the initial x_0 will be computed by using Newton's Raphson method at given ε_0 prior to that (1-1) and (1-2) find the solution based upon (x_0,ε_0). (1-1) and (1-2) are the vector version of Riks-Wempner method derived based upon the scalar version of Riks-Wempner method in [27] and [28].

1.5.2 Stability Analysis using Floquet Transition Matrix(FTM)

Let's consider the following linear time-variant differential equation such that,

$$\dot{x}(t)=A(q_L,t)x(t) \tag{1-3}$$

where, $A(q_L,t)$, q_L, and t are n by n system matrix, the equilibrium position of system, and a time, respectively.

To determine the stability of (1-3), we employ the Floquet's Transition Matrix (FTM) method. By the linear theory[26], the solution for (1-3) is expressed as

$$x(t) = \Phi(q_L,t)x_0 \tag{1-4}$$

where, $\Phi(q_L,t) \in \Re^{n\times n}$ and $x_0 \in \Re^n$ are FTM and the initial condition respectively.

Replacing the x_0 as the n by n identical matrix, $x(t)$ becomes n by n matrix solution and then, with the period T, we can obtain the periodic solution such that $x(T) = \Phi(q_L,T)$. Ultimately, the stability criterion is determined by

$$\begin{aligned} &\max_{1\le i\le n}\left|\lambda_i(x(T))\right| < 1 \quad \textit{stable} \\ &\max_{1\le i\le n}\left|\lambda_i(x(T))\right| > 1 \quad \textit{unstable} \end{aligned} \tag{1-5}$$

where λ_i is the eigenvalues of matrix solution $x(T) = \Phi(q_L,T)$.

CHAPTER II
LIMIT-CYCLE ANALYSIS OF PLANAR ROTOR/AUTOBALANCER SYSTEM INFLUENCED BY ALFORD'S FORCE

2.1 Planar Rotor/Autobalancer system

In this section, we present the mathematical model of the planar-rigid rotor/Autobalancer system mounted on a generalized linear bearing system including the cross-coupling terms. Initially, the dynamics of system are derived in the fixed frame $\{n_1, n_2, n_3\}$.

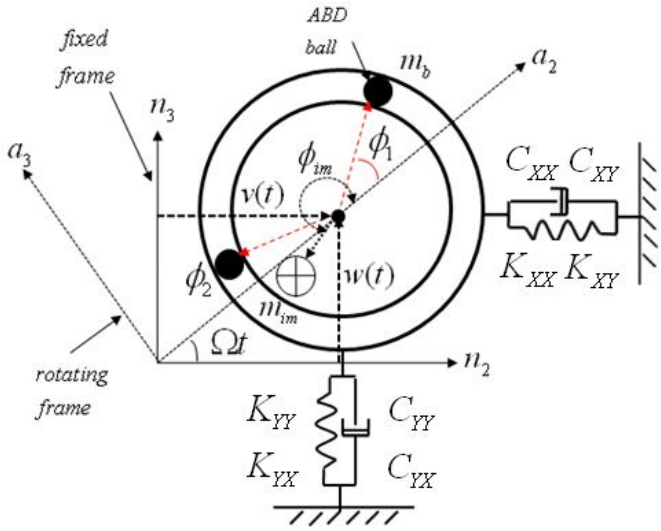


Figure.2.1 Rigid planar rotor-ABD system supported by a general bearing holding asymmetric damping and stiffness force including cross-coupling ones

Specifically, the vertical and horizontal displacements of the rotor $v(t)$ and $w(t)$ are described relative to the fixed-frame and the angular positions of the ABD balancer masses $\phi_1(t)$, $\phi_2(t)$ in the circular track of ABD together with the imbalance phase ϕ_{im} are described with respect to a set of rotating frame $\{a_1, a_2, a_3\}$, as shown in Figure.2.1. The rotor is assumed to be driven with a constant angular speed Ω. The transformation from $\{n_1, n_2, n_3\}$ to $\{a_1, a_2, a_3\}$ is

$$\begin{bmatrix} a_1 \\ a_2 \\ a_3 \end{bmatrix} = \begin{bmatrix} 1 & 0 & 0 \\ 0 & \cos(\Omega t) & \sin(\Omega t) \\ 0 & -\sin(\Omega t) & \cos(\Omega t) \end{bmatrix} \begin{bmatrix} n_1 \\ n_2 \\ n_3 \end{bmatrix} \tag{2-1}$$

The center position of the rotor is provided by,

$$R_{oc} = v(t)n_2 + w(t)n_3 \tag{2-2}$$

The position vector of imbalance mass and the balls position vector are given by,

$$R_{im} = R_{oc} + r_{im}[\cos(\phi_{im})a_2 + \sin(\phi_{im})a_3] \tag{2-3}$$

$$R_{ball.i} = R_{oc} + r_b[\cos(\phi_i(t))a_2 + \sin(\phi_i(t))a_3] \quad for\ i = 1,2 \tag{2-4}$$

where, r_{im} and r_b are the radial length of imbalance mass and ABD's balls, respectively and $r_{im} = r_b$ is assumed.

The kinetic energy of the whole system is given by,

$$T_{total} = \frac{m}{2}[\dot{v}(t)^2 + \dot{w}(t)^2] + \frac{m_{im}}{2}[\dot{R}_{im} \cdot \dot{R}_{im}] + \frac{m_b}{2}\left(\sum_{i=1}^{2}[\dot{R}_{ball.i} \cdot \dot{R}_{ball.i}]\right) \tag{2-5}$$

where, m, m_b and m_{im} are the mass of a shaft-rotor, a ball and an imbalance mass.

Next, the potential energy and dissipation energy of the bearing are

$$V_{bearing} = \frac{1}{2}[K_{XX}v(t)^2 + K_{YY}w(t)^2 + K_{XY}v(t)^2 + K_{YX}w(t)^2] \tag{2-6}$$

$$D_{bearing} = \frac{1}{2}\left[C_{XX}\dot{v}(t)^2 + C_{YY}\dot{w}(t)^2 + C_{XY}\dot{v}(t)^2 + C_{YX}\dot{w}(t)^2\right] \tag{2-7}$$

where, $K_{ij}, C_{ij}\ for\ i, j = X, Y$ are the constant bearing stiffness and damping coefficients. Note that subscripts *X* and *Y* in bearing are corresponding to the direction of *v(t)* and *w(t)*.

Providing the dissipation energy of ABD's balls,

$$D_{ball} = \frac{1}{2}c_b\left(\sum_{i=1}^{2}(\dot{\phi}_i(t)^2)\right) \tag{2-8}$$

Defining the state of system such that, $q \equiv [v(t)\ w(t)\ \phi_1(t)\ \phi_2(t)] \in R^4$ and using the Lagrange's equation with (2-5) through (2-8),

$$\frac{d}{dt}\left[\frac{\partial T_{total}}{\partial \dot{q}}\right] - \frac{\partial T_{total}}{\partial q} + \frac{\partial V_{bearing}}{\partial q} + \frac{\partial [D_{bearing} + D_{ball}]}{\partial \dot{q}} = 0 \tag{2-9}$$

We can obtain the equation of motion,

$$M(\phi_i, t)\ddot{q} + C(\phi_i, t)\dot{q} + Kq = F_{im}(t) + F_{ball}(\dot{\phi}_i, \phi_i, t) \tag{2-10}$$

where $M(\phi_i, t) \in R^{4\times4}$, $C(\phi_i, t) \in R^{4\times4}$ and $K \in R^{4\times4}$ are an inertia matrix, a damping matrix, and a stiffness matrix and, $F_{ball}(\dot{\phi}_i, \phi_i, t) \in R^4$ and $F_{im}(t) \in R^4$ are the force excitation terms induced by ABD's balls and imbalance mass, respectively. The detail of matrices is given in Appendix.

Now, we have the general dynamic equation for ABD-rotor system in (2-10) with respect to the fixed coordinate. To facilitate the analysis for one's purpose and convenience in this study, assuming the bearing used here has completely symmetrical stiffness and damping properties s.t, $K_{XX} = K_{YY}$ and $C_{XX} = C_{YY}$, and no cross-coupling damping (i.e, $C_{XY} = C_{YX} = 0$) with the skew symmetric cross coupling stiffness holding

the property of Alford's force such that, $K_{A.XY} = -K_{A.YX}$ ($K_{A.XY} > 0, K_{A.YX} < 0$) can turn (2-10) into the autonomous dynamics relative to the rotating coordinates. Thus, adding subscript *r* into *v(t)* and *w(t)* to define the state of system relative to the rotating frame $\{a_1, a_2, a_3\}$ such that, $v_r(t)$ and $w_r(t)$ and using the transformation in (2-1), the relation between *v(t)*,*w(t)* and $v_r(t)$, $w_r(t)$ is given by,

$$\begin{aligned} v(t) &= \cos(\Omega t) v_r(t) - \sin(\Omega t) w_r(t) \\ w(t) &= \sin(\Omega t) v_r(t) + \cos(\Omega t) w_r(t) \end{aligned} \tag{2-12}$$

Substituting (2-12), the first and second derivative of (2-12) with respect to time into (2-10) and manipulating it yields,

$$M_r(\phi_i)\ddot{q}_r + C_r(\phi_i)\dot{q}_r + K_r(\phi_i)q_r = F_{imr} + F_{ballr}(\dot{\phi}_i, \phi_i) \tag{2-13}$$

where $q_r = \left[v_r(t)\ w_r(t)\ \phi_1(t)\ \phi_2(t)\right]^T \in \Re^4$ is the system state relative to the rotating frame. The detail of system matrices are also given in Appendix. Now, we use (2-13) for further subsequent analysis and simulation.

2.2 Limit-cycle Solution of Symmetric Bearing with Alford's Force

In this section, the assumed limit-cycle solution of the ABD-rotor system with a symmetric supporting bearing under the effect of destabilizing cross-coupling stiffness force/Alford's force is presented to reveal the inherent characteristic of the non synchronous limit cycle behavior. The solution is assumed as the harmonic type one. Thus, using the harmonic balancing technique, we generate the set of nonlinear equations to solve the unknown parameters of the solution. For further derivation, we make the following assumptions.

i) For the limit-cycle condition, two balls are merged and rotated together so that one ball motion is absorbed into another. Consequently, the coordinate of system in (2-13) is reduced into $q_r = \left[v_r(t)\ w_r(t)\ \phi(t)\right]^T \in \Re^3$ and the mass of merged two balls is simply defined as $m_{b.m}$ equivalent to the mass of two balls(i.e, $m_{b.m} = 2m_b$). It should be noted that the contact mechanism of two balls is out of our research scope. Based upon [16] also characterized the balanced equilibrium attraction basin as a function of ball initial position, the non-synchronous behavior/limit cycle is mostly created by setting that the initial angular position of two ABD-balls is located near for each other or identical. Reversely, if one ball is stayed away from another, the system is highly subject to the stable synchronous behavior due to the different angular phase between two balls according to [16]. Thus, the merging situation of two balls is highly probable under limit cycle condition. *ii)* The ball speed denoted as ω is assumed to be constant under the limit-cycle condition. Hence, we have, $\dot{\phi} = \omega \Rightarrow \phi = \omega t$ and $\ddot{\phi} = 0$. Due to the circular track of ABD

and the symmetrical property of supporting bearings and the feature of forces acting on the system, the actual ball speed is well approximated as constant under allowable assumptions and this point of view will be discussed with simulation results. Applying the assumptions above into (2-13) yields,

$$M_r(\phi)\ddot{q}_r + C_r(\phi)\dot{q}_r + K_r(\phi)q_r = F_{imr} + F_{ballr}(\dot{\phi},\phi) \tag{2-14}$$

The detail of system matrices is given in Appendix. The detail of (2-13) should not be confused with (14)'s.

Next, the harmonic solution of the limit-cycle relative to the rotating frame is assumed to be

$$v_r(t) = a\cos[\omega t + \gamma] + v_{r0} \quad w_r(t) = a\sin[\omega t + \gamma] + w_{r0} \tag{2-15}$$

where, a , ω , γ , v_{r0} and w_{r0} are unknown amplitudes, the ball speed, the phase and constant offsets to be solved.

Substituting (2-15) into (2-14) and rearranging it in terms of each harmonic yields,

$$\begin{aligned}&[-m_{b.m}r_b(\Omega+\omega)^2 - a(C_{XX}(\Omega+\omega) - K_{A.XY})\sin(\gamma) + a(K_{XX} - m_t(\Omega+\omega)^2)\cos(\gamma)]\cos(\omega t)\\ &\cdots + [-a(C_{XX}(\Omega+\omega) - K_{A.XY})\cos(\gamma) - a(K_{XX} - m_t(\Omega+\omega)^2)\sin(\gamma)]\sin(\omega t)\\ &\cdots + [K_{XX} - m_t\Omega^2]v_{r0} + [K_{A.XY.} - C_{XX}\Omega]w_{r0} - m_{im}r_{im}\Omega^2\cos(\phi_{im}) = 0\end{aligned} \tag{2-16}$$

$$\begin{aligned}&[-m_{b.m}r_b(\Omega+\omega)^2 - a(C_{XX}(\Omega+\omega) - K_{A.XY})\sin(\gamma) + a(K_{XX} - m_t(\Omega+\omega)^2)\cos(\gamma)]\sin(\omega t)\\ &\cdots + [-a(C_{XX}(\Omega+\omega) - K_{A.XY})\cos(\gamma) - a(K_{XX} - m_t(\Omega+\omega)^2)\sin(\gamma)]\cos(\omega t)\\ &\cdots + [K_{XX} - m_t\Omega^2]w_{r0} + [K_{A.YX.} + C_{XX}\Omega]v_{r0} - m_{im}r_{im}\Omega^2\sin(\phi_{im}) = 0\end{aligned} \tag{2-17}$$

$$\frac{c_b r_b \omega}{m_{b.m}\Omega^2} - \frac{a(\Omega+\omega)^2}{\Omega^2}\sin(\gamma) + [v_{r0}\sin(\omega t) - w_{r0}\cos(\omega t)] = 0 \tag{2-18}$$

where, $m_t = m + m_{b.m}$. Again, it should be noted that $m_{b.m} = 2m_b$.

Then, from (2-16) and (2-17), we have four nonlinear equations s.t,

$$-m_{b.m}r_b(\Omega+\omega)^2 - a(C_{XX}(\Omega+\omega) - K_{A.XY})\sin(\gamma) + a(K_{XX} - m_t(\Omega+\omega)^2)\cos(\gamma) = 0 \tag{2-19}$$

$$-a(C_{XX}(\Omega+\omega) - K_{A.XY})\cos(\gamma) - a(K_{XX} - m_t(\Omega+\omega)^2)\sin(\gamma) = 0 \tag{2-20}$$

$$[K_{XX} - m_t\Omega^2]v_{r0} + [K_{A.XY.} - C_{XX}\Omega]w_{r0} - m_{im}r_{im}\Omega^2\cos(\phi_{im}) = 0 \tag{2-21}$$

$$[K_{XX} - m_t\Omega^2]w_{r0} + [K_{A.YX.} + C_{XX}\Omega]v_{r0} - m_{im}r_{im}\Omega^2\sin(\phi_{im}) = 0 \tag{2-22}$$

From (2-21) and (2-22), we have,

$$\begin{bmatrix} v_{r0} \\ w_{r0} \end{bmatrix} = \begin{bmatrix} K_{XX} - m_t\Omega^2 & K_{A.XY} - C_{XX}\Omega \\ K_{A.YX} + C_{XX}\Omega & K_{XX} - m_t\Omega^2 \end{bmatrix}^{-1} \begin{bmatrix} m_{im}r_{im}\Omega^2\cos(\phi_{im}) \\ m_{im}r_{im}\Omega^2\sin(\phi_{im}) \end{bmatrix} \tag{2-23}$$

As shown in (2-23), the constant offsets v_{r0} and w_{r0} of (2-15) are determined by the size of imbalance mass, inherent characteristic of bearing, rotor system as well as operating speed and those are independent of any properties of ABD. Both (2-19) and (2-20) don't hold any time-varying terms. However, the time-

varying terms violating the assumption $\ddot{\phi} = \dot{\omega} = 0$ are observed in (2-18) and the influence of these terms is strongly dependent on the offsets v_{r0} and w_{r0}. Since the unknowns a and γ are the function of the ball speed ω which is influenced by imbalance effect as seen in (2-18) and (2-23), this effect should be insignificant not to heavily deteriorate the accuracy of suggested solution. Fortunately, the effect of time-varying terms can be insignificant in the two following reasons. *i*) The offsets v_{r0} and w_{r0} which are directly proportional to the size of imbalance mass. The best performance of ABD can be usually achieved under the condition $m_{im} < 2m_b = m_{b.m}$ if $r_{im} = r_b$. The complete synchronous balancing condition of ABD-rotor system is founded with this condition for the co-located case where the location of imbalance mass coincides with ABD-ball's relative to the axial direction of rotor-shaft. Under this condition $m_{im} < 2m_b$, the effect of time-varying terms can be insignificant. In other words, there exists allowable imbalance size not to heavily deteriorate the accuracy of the limit cycle solution. *ii*) The inherent nature of limit cycle related with the running frequency of ABD-ball dominates the imbalance effect so that the time-varying terms in (2-18) directly associated with imbalance can be less important contribution to the solution. These two conditions above enhance us to achieve the well approximated solution and these aspects will be explained with and validated through the numerical simulation results.

By assuming that the effect of time-varying terms in (2-18) is insignificant and truncating those terms yields,

$$\sin(\gamma) = \frac{c_b r_b \omega}{a m_{b.m} (\Omega + \omega)^2} \tag{2-24}$$

Using the trigonometry identity, (2-24) yields $\cos(\gamma) = \frac{\sqrt{(a\, m_{b.m}(\Omega+\omega)^2)^2 - (c_b r_b \omega)^2}}{a\, m_{b.m}(\Omega+\omega)^2}$.

Substituting (2-24) and $\cos(\gamma)$ expression into (2-19) and (2-20) and rearranging them yields,

$$m_{b.m}{}^2 r_b (\Omega+\omega)^4 + c_b r_b \omega (C_{XX}(\Omega+\omega) - K_{A.XY}) = (K_{XX} - m_t(\Omega+\omega)^2)\sqrt{-c_b{}^2 r_b{}^2 \omega^2 + a^2 m_{b.m}{}^2 (\Omega+\omega)^4} \tag{2-25}$$

$$c_b r_b \omega (m_t(\Omega+\omega)^2 - K_{XX}) = (C_{XX}(\Omega+\omega) - K_{A.XY})\sqrt{-c_b{}^2 r_b{}^2 \omega^2 + a^2 m_{b.m}{}^2 (\Omega+\omega)^4} \tag{2-26}$$

From (2-25) and (2-26), by eliminating amplitude *a*, we have the fifth-order characteristic polynomials about ω such that,

$$p_1 \omega^5 + p_2 \omega^4 + p_3 \omega^3 + p_4 \omega^2 + p_5 \omega + p_6 = 0 \tag{2-27}$$

The detail of coefficients $p_i \; for \; i = 1,2,\cdots,6$ is given in Appendix. From (2-23) to (2-27), we can solve for all unknowns a, ω , γ, v_{r0} and w_{r0}. The suggested solution (2-15) is used for subsequent analysis.

2.3 Stability analysis

To investigate the local stability of the system in the neighborhood of the limit-cycle solution founded in previous sections, (2-14) is linearized using the perturbation approach. By considering the small perturbations $\Delta v_L(t)$, $\Delta w_L(t)$, and $\Delta\phi_L(t)$, the perturbed system configuration is $v_r(t)=v_L(t)+\Delta v_L(t)$, $w_r(t)=w_L(t)+\Delta w_L(t)$, and $\phi(t)=\phi_L(t)+\Delta\phi_L(t)$, where $v_L(t)$, $w_L(t)$, and $\phi_L(t)$ are the limit-cycle harmonic solutions in (2-15) and the ball's angular speed computed by (2-27). Substituting this perturbed configuration into the dynamics (2-14), and truncating the higher order terms results in a set of linearized equation about the set of limit-cycle solution $v_L(t)$, $w_L(t)$,and $\phi_L(t)$. Denoting a set of perturbed coordinate as $\Delta q_L=[\Delta v_L(t)\ \Delta w_L(t)\ \Delta\phi_L(t)]^T\in\Re^3$ and a set of limit-cycle solution as $q_L=[v_L(t)\ w_L(t)\ \phi_L(t)]^T\in\Re^3$, we have from (2-14),

$$\Delta M(q_L,t)\Delta\ddot{q}_L+\Delta C(q_L,t)\Delta\dot{q}_L+\Delta K(q_L,t)\Delta q_L=0 \tag{2-28}$$

Defining the state vector $x(t)=[\Delta q_L^{\ T}\ \Delta\dot{q}_L^{\ T}]^T\in\Re^6$, we can transform (2-28) into,

$$\dot{x}(t)=A(q_L,t)x(t) \tag{2-29}$$

with a system matrix $A(q_L,t)=\begin{bmatrix}0 & I\\ -\Delta M^{-1}(q_L,t)\Delta K(q_L,t) & -\Delta M^{-1}(q_L,t)\Delta C(q_L,t)\end{bmatrix}$.

To determine the stability of (2-29) which is the linear time-varying equation, we employ the Floquet's Transition Matrix (FTM) method. By the linear theory, the solution for (2-29) is expressed as

$$x(t)=\Phi(q_L,t)x_0 \tag{2-30}$$

where, $\Phi(q_L,t)\in\Re^{6\times6}$ and $x_0\in\Re^6$ are FTM and the initial condition respectively.

Replacing the x_0 as the 6 by 6 identical matrix, $x(t)$ becomes 6 by 6 matrix solution and then, with the period $T=\dfrac{2\pi}{\omega}$, we can obtain the periodic solution such that $x(T)=\Phi(q_L,T)$. Ultimately, the stability criterion is determined by

$$\begin{aligned}&\max_{1\le i\le6}\left|\lambda_i(x(T))\right|<1 \quad stable\\ &\max_{1\le i\le6}\left|\lambda_i(x(T))\right|>1 \quad unstable\end{aligned} \tag{2-31}$$

where λ_i is the eigenvalues of matrix solution $x(T)=\Phi(q_L,T)$.

To investigate the local stability of system about a fixed balanced equilibrium solution, (2-13) is linearized using perturbation method with perturbed system coordinates $v_r(t)=v_{eq}(t)+\Delta v_{eq}(t)$, $w_r(t)=w_{eq}(t)+\Delta w_{eq}(t)$, and $\phi_{eq.i}(t)=\phi_{eq.i}(t)+\Delta\phi_{eq.i}(t)$ *for* $i=1,2$ and, by substituting the perturbed coordinates into (2-13) and truncating the higher order terms, we have a linear time-

invariant equation describing the perturbed coordinate $\Delta q = [\Delta v_{eq}(t)\ \Delta w_{eq}(t)\ \Delta\phi_{eq.1}(t)\ \Delta\phi_{eq2}(t)]^T \in \Re^4$. Based upon this equation, the simple eigenvalue analysis can be applied to determine the local stability about the fixed equilibrium point $q_{eq} = [v_{eq}(t)\ \ w_{eq}(t)\ \ \phi_{eq1}(t)\ \phi_{eq2}(t)]^T$. The fixed equilibrium point of complete balancing condition for the co-located case is simply computed as $q_{eq} = [v_{eq}(t)\ \ w_{eq}(t)\ \ \phi_{eq1}(t)\ \phi_{eq2}(t)]^T = [0\ \ 0\ \ \phi_{bal1}{}^*\ \phi_{bal2}{}^*]^T \in \Re^4$ where, $\phi_{bal.i}{}^* = \phi_{im} \pm \arccos[-\delta]$ *for* $i = 1,2$, where, $\delta = \frac{m_{im} r_{im}}{2 m_b r_b}$ and this balanced solution exists under the condition of $\delta \le 1$. It is also noted that the assumption of reasonable imbalance size(i.e, $m_{im} \le 2m_b = m_{b.m}$) in the previous section is originated from this condition. The subsequent stability analysis of the balanced solution is conducted in the neighborhood of $[0\ \ 0\ \ \phi_{bal.1}{}^*\ \phi_{bal.2}{}^*]^T$. Additionally, the merged equilibrium solution where two balls are merged and synchronous with the operating speed of system is also considered on the subsequent stability analysis. This equilibrium solution is specified as $\phi_{meg.i} = \phi_{im} \pm \pi\ or\ \phi_{im}\ \ for\ i = 1,2$ with the corresponding steady-state amplitude v_{meg} and w_{meg} assessed by.

$$\begin{bmatrix} v_{meg} \\ w_{meg} \end{bmatrix} = \begin{bmatrix} K_{XX} - (m + 2m_b)\Omega^2 & -C_{XX}\Omega + K_{A.XY} \\ C_{XX}\Omega + K_{A.YX} & K_{XX} - (m + 2m_b)\Omega^2 \end{bmatrix}^{-1} \begin{bmatrix} m_{im} r_{im} \Omega^2 \cos[\phi_{im}] + m_b r_b \sum_{i=1}^{2} \Omega^2 \cos[\phi_{meg.i}] \\ m_{im} r_{im} \Omega^2 \sin[\phi_{im}] + m_b r_b \sum_{i=1}^{2} \Omega^2 \sin[\phi_{meg.i}] \end{bmatrix}$$

2.4 Numerical Simulation Results

In this section, the limit-cycle behavior of system under the influence of assumed Alford's force is investigated by using full-nonlinear numerical simulation of (2-13) and solving the set of nonlinear equations obtained in (2-23) through (2-27). Also, at given operating speeds and Alford's force, the analytical bifurcation boundary characterizing the unwanted coexistence of both stable synchronous behavior and limit cycle appeared on the stability distribution plot is provided here. First, the procedure to assess the bifurcation boundary will be given before presenting the numerical results and the corresponding discussions.

To obtain the physically feasible solution(i.e avoiding the imaginary part) of (2-25) and (2-26), the following condition should be imposed such that,

$$-c_b{}^2 r_b{}^2 \omega^2 + a^2 m_{b.m}{}^2 (\Omega + \omega)^4 > 0 \qquad (2\text{-}32)$$

(2-32) can be commonly founded inside a square root in the right side of (2-25) and (2-26). Consequently, the critical condition would be obtained to set the right side of (2-32) as zero such that, $-c_b^2 r_b^2 \omega^2 + a^2 m_{b.m}^2 (\Omega+\omega)^4 = 0$.

Thus, with this critical condition above, adding the subscripts *cr* (i.e, critical) such that (Ω_{cr}, ω_{cr}, and $K_{A.XY.cr}$) into both (2-25) and (2-26) yields,

$$m_{b.m}^2 r_b (\Omega_{cr} + \omega_{cr})^4 + c_b r_b \omega_{cr} (C_{XX} (\Omega_{cr} + \omega_{cr}) - K_{A.XY.cr}) = 0 \tag{2-33}$$

$$c_b r_b \omega_{cr} (m_t (\Omega_{cr} + \omega_{cr})^2 - K_{XX}) = 0 \tag{2-34}$$

From (2-34), for limit cycle condition, we have $\omega_{cr} \neq 0$ and,

$$\Omega_{cr} + \omega_{cr} = \sqrt{\frac{K_{XX}}{m_t}} \tag{2-35}$$

Substituting (2-35) into (2-33) yields,

$$K_{A.XY.cr} = -\frac{m_{b.m}^2 \left[\frac{K_{XX}}{m_t}\right]^2}{c_b \left[\Omega_{cr} - \sqrt{\frac{K_{XX}}{m_t}}\right]} + C_{XX} \sqrt{\frac{K_{XX}}{m_t}} \tag{2-36}$$

(2-36) represents the critical condition where the property of solutions/roots for (2-25) and (2-26) is changed from a set of physical solutions to the one associated with an imaginary. We can see this point of view by examining (2-27). Since (2-27) is the fifth-order polynomials, it owns five roots. The possible cases of the roots' combination are followed. *i*) three physical roots and two imaginary ones and *ii*) one physical root and four imaginary ones. The case *i*) refers the coexistence of two limit-cycle solutions and a balanced one, whereas the case *ii*) implies there exists no limit-cycle but only balanced condition(We will see this points from Figure.3). Specifically, (2-36) is the critical condition to discern the case *i*) from *ii*). Thus, (2-36) is the bifurcation boundary where the characteristic of system stability is altered. In other words, the trajectory of (2-36) at given Ω and $K_{A.XY.}$ is the critical line to distinguish the unwanted coexistence zone from the desired one in the stability contour plot such that Ω vs. $K_{A.XY.}$. This stand point of view will be explained and validated through the simulation results presented in Figure.2.4 and Figure.2.5.

Now, it is necessary for us to validate the suggested assumptions, approximated solution, as well as approaches presented so far. In Figure.2.2, we compare the limit-cycle solution in (2-15) with the numerical simulation of full nonlinear system in (2-13) which is constructed in MATLAB/Simulink environment. In Simulink simulation, the limit-cycle condition can be also generated by setting the initial condition leading to the outside of the provided attraction basin described in [16]. Thus, the initial position of two balls is presumed to be merged on the full nonlinear simulation s.t, $\phi_1(0) = \phi_2(0)$. In (*a*) of

Figure.2.2, the star-dotted line represents the time domain response obtained via Simulink while the circle dotted line do the assumed limit-cycle one. In (*b*), the maximum amplitude of $w_r(t)$ is illustrated at given each operating speed. The straight lines represent the maximum of amplitude $w_r(t)$ of limit-cycle solution computed s.t, $a + w_{r0}$ while both the star($m_{im} = m_b = 0.5m_{b.m}$) and circle($m_{im} = 3m_b = 1.5m_{b.m}$) dots describe numerical simulation results obtained through $\max_{T-t_a<t<T} w_{r.S}(t)$ where $w_{r.S}(t)$ is belong to outcomes from simulation and, T and t_a are the end of simulation time and the sampling period respectively. The results in (*b*) are accurately matched for each other in the range of supercritical operating speed. In (*c*) and (*d*), the whirl orbits are exhibited with two different cases of imbalance effect such that, $m_{im} = 6m_b = 3m_{b.m}$ for (*c*) and $m_{im} = m_b = 0.5m_{b.m}$ for (*d*). Both limit-cycle solutions(circle-dotted line) and numerical outcomes(star-dotted line) are synchronous for each other. The whirl orbits displayed are perfectly circular ones due to the symmetric property of bearing and the feature of assumed cross coupling stiffness of Alford's force. The offset of orbit in (*c*) is different from one in (*d*) due to the imbalance mass size as expected from (2-15) and (2-23). As the imbalance mass is increased, the center of whirl orbit is located away from the origin of plot. In (*a*), (*c*), and (*d*), the transient part of time domain response and whirl orbits in the numerical(Simulink) simulation is discarded for clarity. Here, the transient part implies the chaotic behavior before the motion of system reach the level where one can interpret as the form of steady-state harmonic type response.

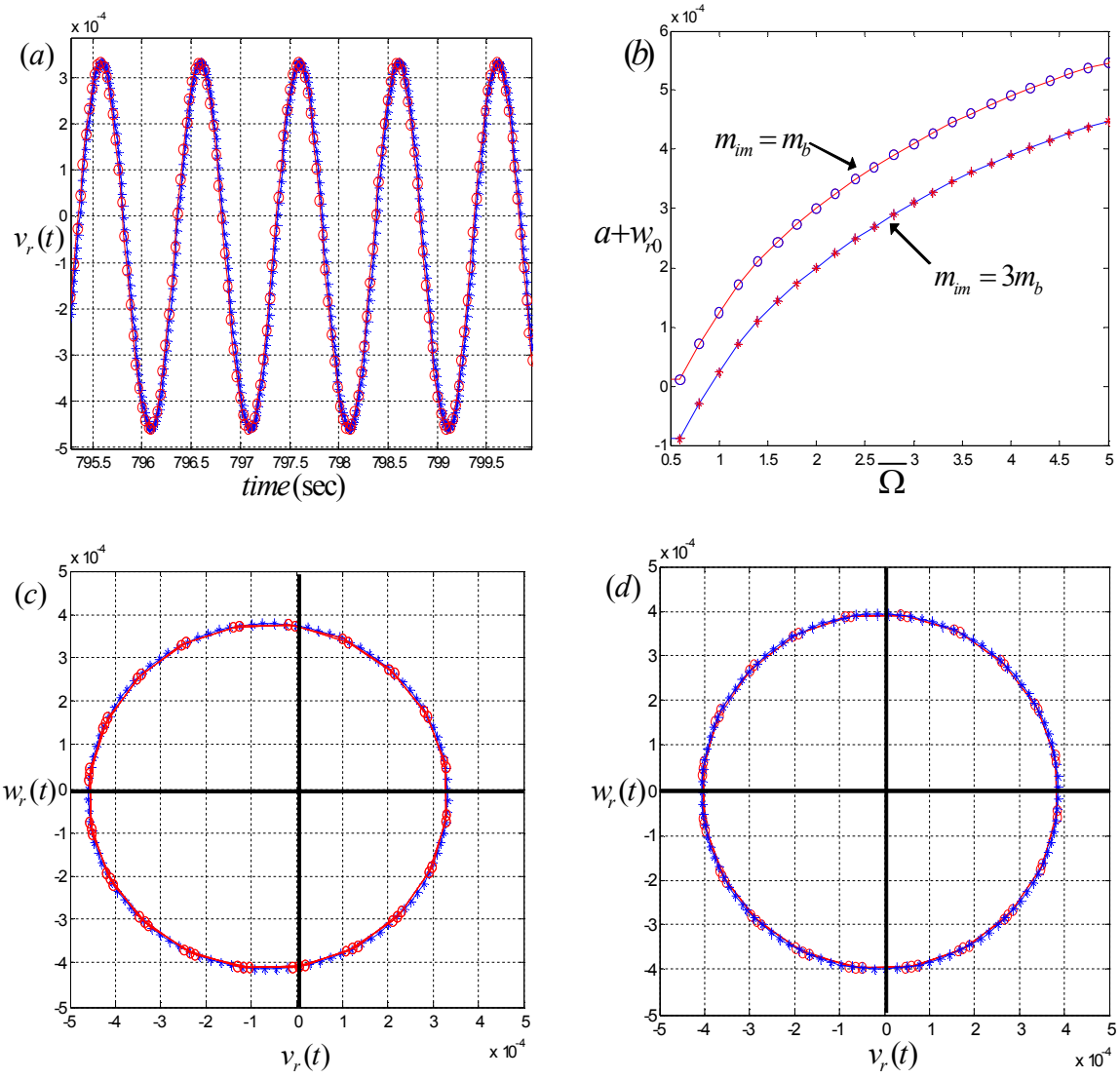
In (*e*) and (*f*), the power spectrums of the proposed harmonic limit-cycle solutions (shown as the circle-dotted line) and the numerically simulated ones (shown as the star-dotted line) are presented. The significant frequencies of both are matched for each other and approximately 1.1 *Hz*. Due to non-zero constant offset of solution, there exists a peak near zero frequency in each plot. In (*g*), the straight line is the merged ABD's ball speed computed by (2-25) and (2-26) and the fluctuating lines belong to the numerical outcomes. As expected from (2-18), the amplitude of numerical results becomes grown with larger imbalance effect. In (*h*), the power spectrum of numerically simulated ball speed is shown and the peak of magnitude appears as the frequency approaches zero, which implies that its property is almost identical to constant signal's one. However, it should be noted the significant of frequency appears near 1 *Hz* as imbalance mass increases. Although the performance of approximate solution is deteriorated with large imbalance effect, the actual ball speed is well behaved as a constant one under condition $m_{im} < 5m_b = 2.5m_{m.b}$. Furthermore, in (*i*), one can see that the ball speed(straight line) computed via (2-25) and (2-26) at each operating speed can capture the average of the numerically simulated ball speed(circle-dotted line) collected for a certain sampling period at a given operating speed(i.e, $0.5\left[\max_{T-t_a<t<T} \omega_s(t) + \min_{T-t_a<t<T} \omega_s(t)\right]$). Along with the average speed at each operating speed, the

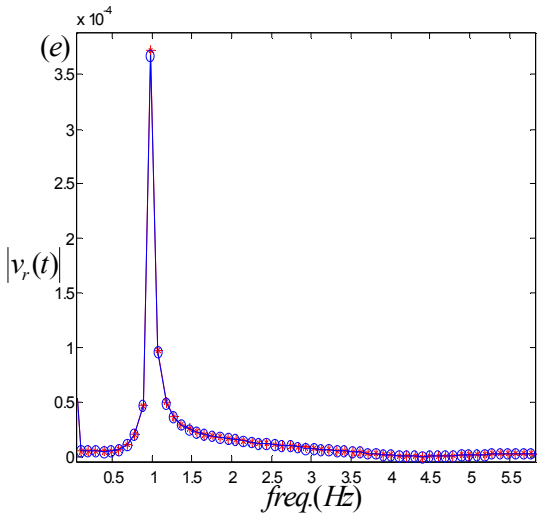
minimum($\min_{T-t_a<t<T}\omega_s(t)$) and maximum($\max_{T-t_a<t<T}\omega_s(t)$) of ball speed are specified as star and triangular dots respectively. It is founded that the difference between the minimum and maximum of ball speed obtained through Simulink simulation is very small. Also, (*j*) in Figure.2.2 displays the difference between the maximum and minimum of ball speed (i.e, the fluctuating magnitude) relative to the average ball speed and *d* in (*j*) can be computed in the following manner s.t,

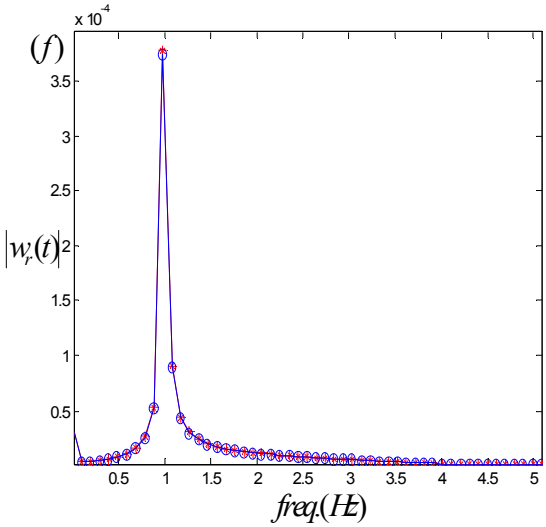
$$d = 2\frac{\max_{T-t_a<t<T}\omega(t) - \min_{T-t_a<t<T}\omega(t)}{\max_{T-t_a<t<T}\omega(t) + \min_{T-t_a<t<T}\omega(t)}$$

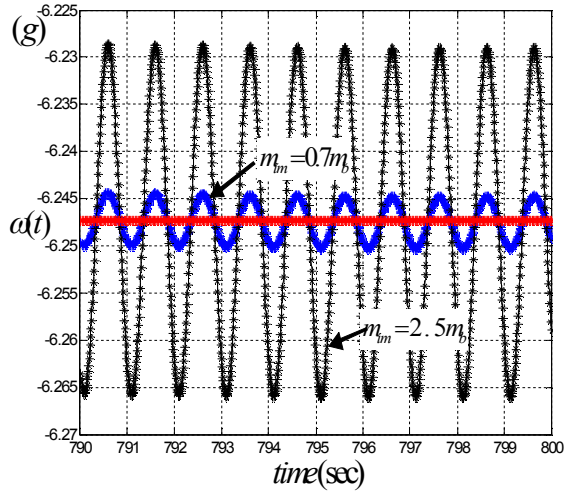
Except few cases below critical speed, *d* is below 4% for all cases of imbalance mass in (*j*) although *d* is up to 20% near critical speed. However, the limit-cycle appeared in the supercritical speed is more critical issue than one below or near critical speed. The solution provided here well approximate the actual ball speed in the supercritical operating speed. Physically explaining the balancing between imbalance effect and running ABD-ball under limit cycle condition, (*k*) present the ball speed relative to the fixed coordinate at each operating speed. It is close to the resonance frequency of the system. The straight line and dots in (*k*) are respectively computed using the ball speed obtained by (2-25) and (2-26) and the average of ball speed via $0.5\left[\max_{T-t_a<t<T}\omega_s(t) + \min_{T-t_a<t<T}\omega_s(t)\right]$ at given operating speed. Investigating the force excitation term $F_{ball}(\dot{\phi}_i, \phi_i, t)$ in (2-10), the driving frequency of $F_{ball}(\dot{\phi}_i, \phi_i, t)$ is founded as $\dot{\phi}_i + \Omega$ and we have $\dot{\phi}_i + \Omega = \omega + \Omega \approx \sqrt{\frac{K_{XX}}{m}}$ according to the results in (*k*), which can be hinted from (2-35). Thus, regardless of system operating speed, this driving frequency is approximately the resonance frequency of system so that the effect of this frequency property generates the large vibration amplitude of system, which implies that another force excitation term $F_{im}(t)$ in (2-10) less significantly influences to the system under the limit-cycle condition because the driving frequency of $F_{im}(t)$ is a given operating speed Ω. In other words, the force excited by ABD-ball become far more dominant than one transmitted by imbalance effect deteriorating the accuracy of limit cycle solution presented here. Consequently, the amplitude $\sqrt{v_{r0}^2 + w_{r0}^2}$ of the time-varying terms $[v_{r0}\sin(\omega t) - w_{r0}\cos(\omega t)]$ (results from $F_{im.r}$ in (2-14) produced by $F_{im}(t)$ in (2-10)) appeared in (2-18) is heavily unable to contribute to the limit cycle solution. Also, one can see this point of view in (*l*) and we compare the amplitude $|a|$ of limit cycle solution with the amplitude($\sqrt{v_{r0}^2 + w_{r0}^2}$) induced by imbalance effect with condition $m_{im} = 6m_b = 3m_{b.m}$. Even though the imbalance size is far larger than ABD ball's, the huge amplitude difference between $|a|$ and $\sqrt{v_{r0}^2 + w_{r0}^2}$ is exhibited as the operating speed increases. This result explains us the functions of two different driving

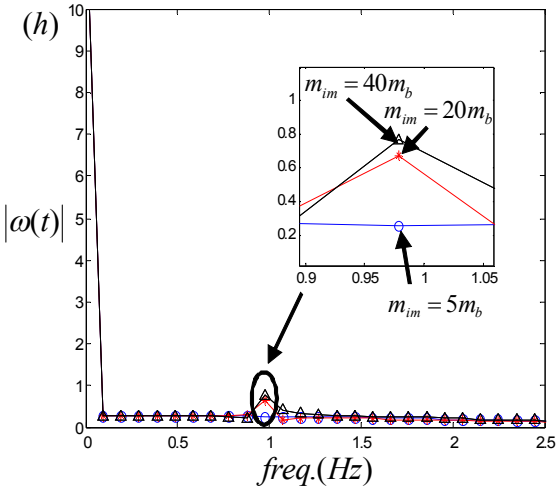
frequencies(One is $\omega+\Omega\approx\sqrt{\frac{K_{XX}}{m}}$ and another is Ω). The results (*g*),(*h*), (*i*), as well as (*j*) can be understood by the simulation results presented in both (*k*) and (*l*). Since the effect of imbalance is far less dominant than one associated with ABD, the influence of imbalance is very small in system response with even large imbalance size s.t $m_{im}>2m_b$ as shown in other simulation results of Figure.2.2. Thus, the accuracy of solution can be guaranteed with allowable size of imbalance s.t, $m_{im}<2m_b$ which is discussed earlier. Under the reasonable assumption of imbalance effect and with the inherent characteristic of limit cycle behavior, all results presented in Figure.2.2 indicate us that the proposed harmonic solution is accurate enough to capture the essence of limit-cycle behavior in terms of both time and frequency domains. Note that dimensionless operating speed $\overline{\Omega}$ presented here is defined by $\frac{\Omega}{\omega_n}$ where, $\omega_n=\sqrt{\frac{K_{XX}}{m}}$.

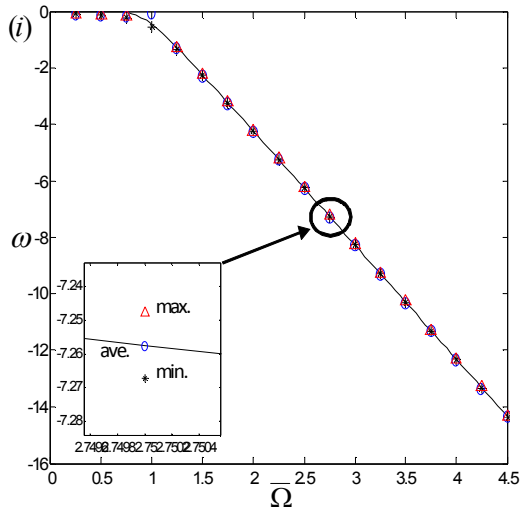


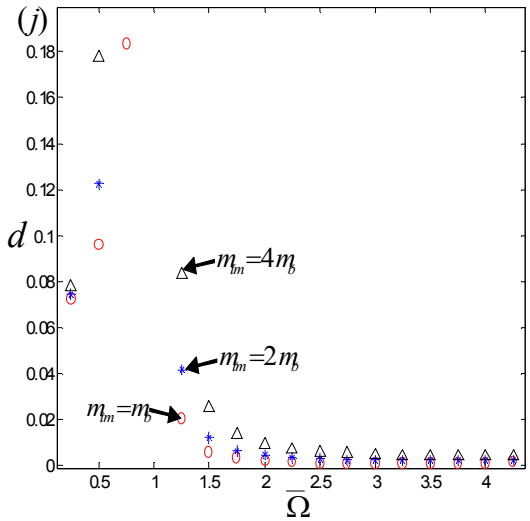

(e)
x 10^-4
|v_r(t)|
freq.(Hz)


(f)
x 10^-4
|w_r(t)|2
freq.(Hz)


(g)
ω(t)
m_m=0.7m_b
m_m=2.5m_b
time(sec)


(h)
|ω(t)|
m_im = 40m_b
m_im = 20m_b
m_im = 5m_b
freq.(Hz)


(i)
ω
max.
ave.
min.
Ω


(j)
d
m_m=4m_b
m_m=2m_b
m_m=m_b
Ω

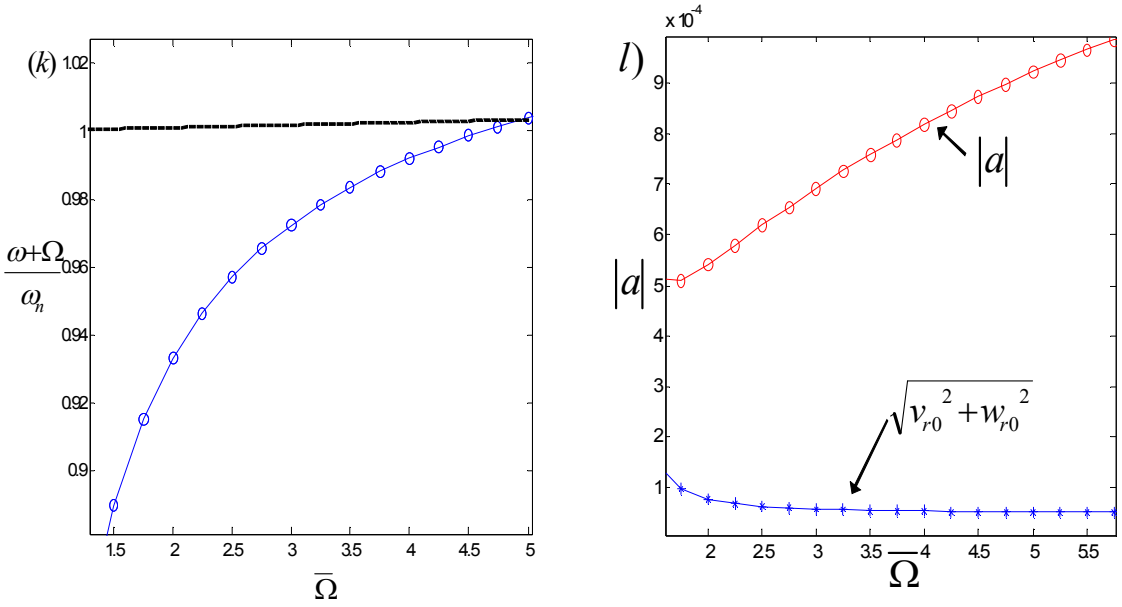


Figure.2.2 Comparison between full numerical solutions and assumed limit-cycle solutions((*a*) $K_{A.XY}=0.007K_{XX}$, $\overline{\Omega}=2.5$ /(*b*) $K_{A.XY}=0.035K_{XX}$ / (*c*) and (*d*) $K_{A.XY}=0.025K_{XX}$, $\overline{\Omega}=2.0$ with $m_{im}=6m_b$, $m_{im}=m_b, \phi_{im}=15^\circ$ / (*e*) and(*f*) $K_{A.XY}=0.01K_{XX}$, $\overline{\Omega}=1.5$ / (*g*) $K_{A.XY}=0.03K_{XX}$, $\overline{\Omega}=2$ /(*h*) $K_{A.XY}=0.03K_{XX}$, $\overline{\Omega}=4$ / (*i*) and (*j*) $K_{A.XY}=0.035K_{XX}$/(*k*) and (*l*) $m_{im}=6m_b$ with $K_{A.XY}=0.037K_{XX}$))

The results presented in Figure.2.2 are associated with one of limit cycle solutions of (2-24) through (2-26). As discussed in the early stage of this section, there exist other solutions. To illustrate other solutions including one shown in Figure.2.2, in Figure.2.3, all solutions of ball speed ω (*rad/sec*), the amplitude a (*m*), and the phase γ (*rad*) relative to $\overline{\Omega}$ are presented by solving (2-24) through (2-26). Each plot in Figure.2.3 contains three separate solutions/curves obtained through three numerical continuation processes. The first two are the limit-cycle solutions (denoted as **L1** and **L2** / $\omega \neq 0$) and the last is the fixed equilibrium balanced solution(denoted as **B** / $\omega = 0$). The first curve (**L1**) is computed such that $\overline{\Omega}$ is increased by taking the previously solved solution as the initial condition in the numerically continuation solving process. With same manner, the second and third ones are obtained in the way that $\overline{\Omega}$ is decreased from the high to low operating speed. At the supercritical operating speeds, these three solutions are coexisted and this coexistence is terminated at a certain stage of supercritical operating speed and, this result is synchronous with the outcome from [15] and earlier discussion about (2-27). Also, the terminated point of undesired coexistence of three solutions satisfies the condition (2-36). By comparing the case $K_{A.XY}=0.015K_{XX}$ to $K_{A.XY}=0.025K_{XX}$, one can observe that the limit-cycle solution exists and remained up to the high operating speed at the larger $K_{A.XY}$. Essentially, this Alford's force affects the limit-cycle behavior.

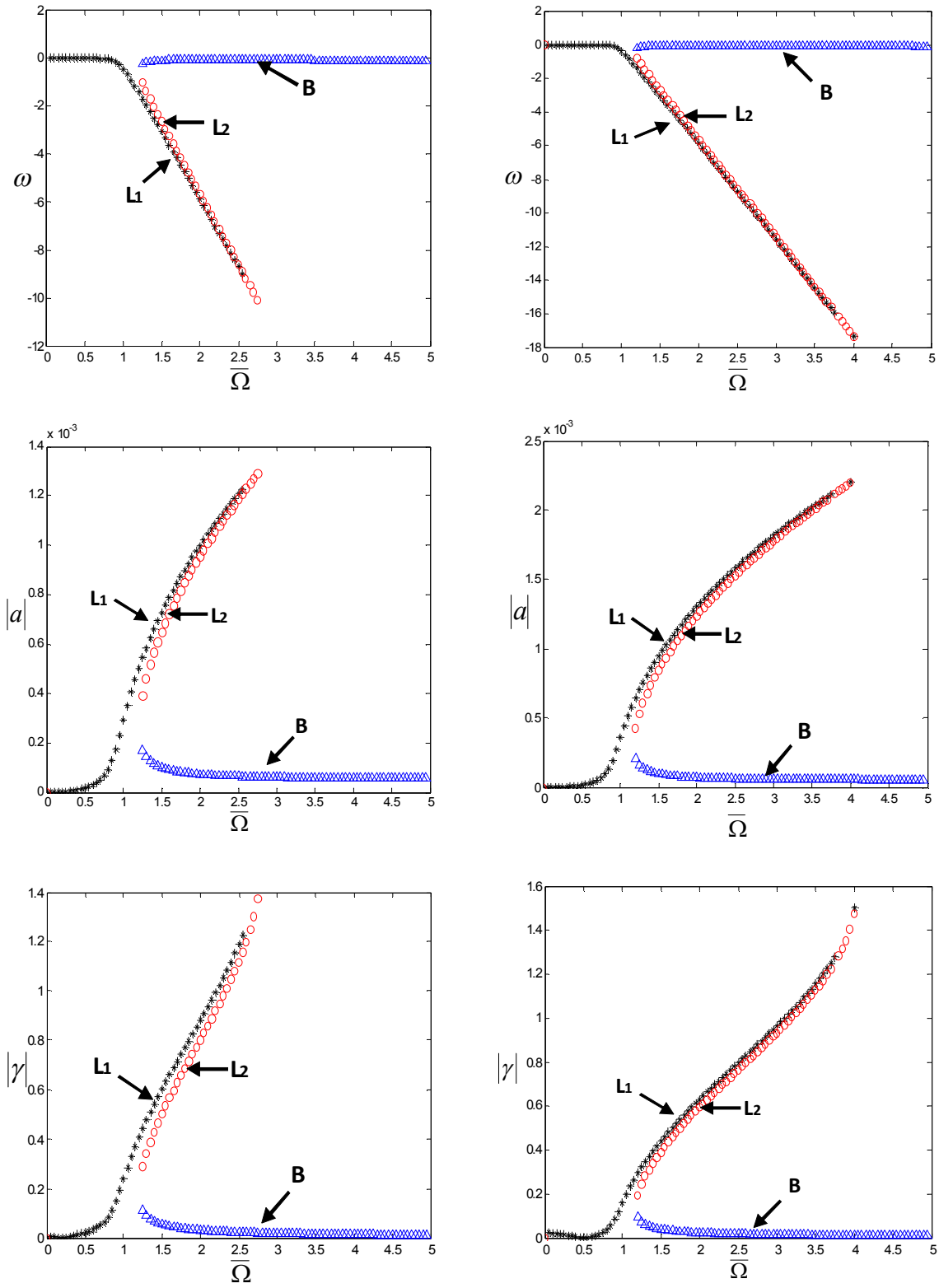


Figure.2.3. Coexistence of limit-cycle solutions and balanced solution (three plots in the first column for $K_{A.XY} = 0.015K_{XX}$ and three plots in the second column for $K_{A.XY} = 0.025K_{XX}$)

In Figure.2.4, using this FTM stability criterion with the **L1** type limit-cycle solution in Figure.3, the two stability contour plots ($\overline{\Omega}$ *vs.*$\overline{K}_{XY}$, note that $\overline{K}_{XY}=\frac{K_{A.XY}}{K_{XX}}$ is dimensionless Alford's force stiffness) are presented with two different bearing damping coefficients C_{XX}. Commonly, there exist upper **U** region in both $C_{XX}=0.01K_{XX}$ and $C_{XX}=0.015K_{XX}$ cases and the case with $C_{XX}=0.015K_{XX}$ (right side on Figure.2.4) suppresses the upper **U** region compared to the case $C_{XX}=0.01K_{XX}$ and the straight line(**S1**) in each plot represents the limited boundary where the system stability of both limit-cycle and balanced condition is ensured and given by the mathematical relation s.t, $\overline{K}_{XY}<\frac{C_{XX}\omega_n}{K_{XX}}$ which is shown in [11]. In each plot, the curve line(**S2**) between **B+L** (coexistence of balanced condition and limit cycle)and **B** (balanced condition) is the bifurcation boundary which is exactly congruent with (2-36). The dimensionless version with the short notations $\omega_t=\sqrt{\frac{K_{XX}}{m_t}}$, $\omega_n=\sqrt{\frac{K_{XX}}{m}}$ and $\overline{\Omega}_{cr}=\frac{\Omega_{cr}}{\omega_n}$ is,

$$\overline{K}_{XY.cr}=-\frac{1}{K_{XX}}\left[\frac{m_b{}^2\omega_t{}^4}{c_b\left[\overline{\Omega}_{cr}\omega_n-\omega_t\right]}-C_{XX}\omega_t\right] \tag{2-37}$$

This bifurcation boundary (2-37) is shifted to the left side of plot at larger C_{XX}, which implies the region **B** is expanded and **B+L** is diminished. Additionally, the fixed merged equilibrium(**M**) behavior appears in the low operating speed below the resonance.

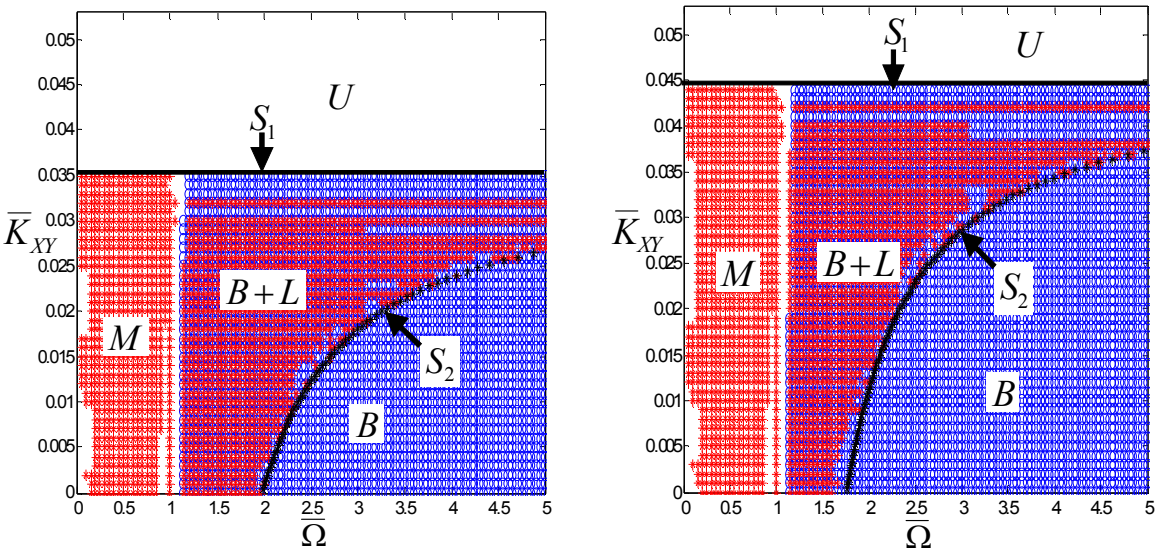


Figure.2.4 Stability contour plots ($\overline{\Omega}$ vs.$\overline{K}_{XY}$) under the influence of Alford's force($C_{XX}=0.01K_{XX}$ (left) and $C_{XX}=0.015K_{XX}$ (right)/ with $m_{im}=m_b$).

In Figure.2.5, there are two stability contour plots with two respective ball damping coefficients $c_b = 1e-4$ and $c_b = 1e-3$. As seen in (2-37), c_b is located in the denominator of the equation. Thus, as c_b is increased, the bifurcation boundary (**S2**) is moved to the left side of plot so that the region **B** is increased and **B+L** is decreased. The limit-cycle region can be suppressed by augmenting the ball damping coefficients.

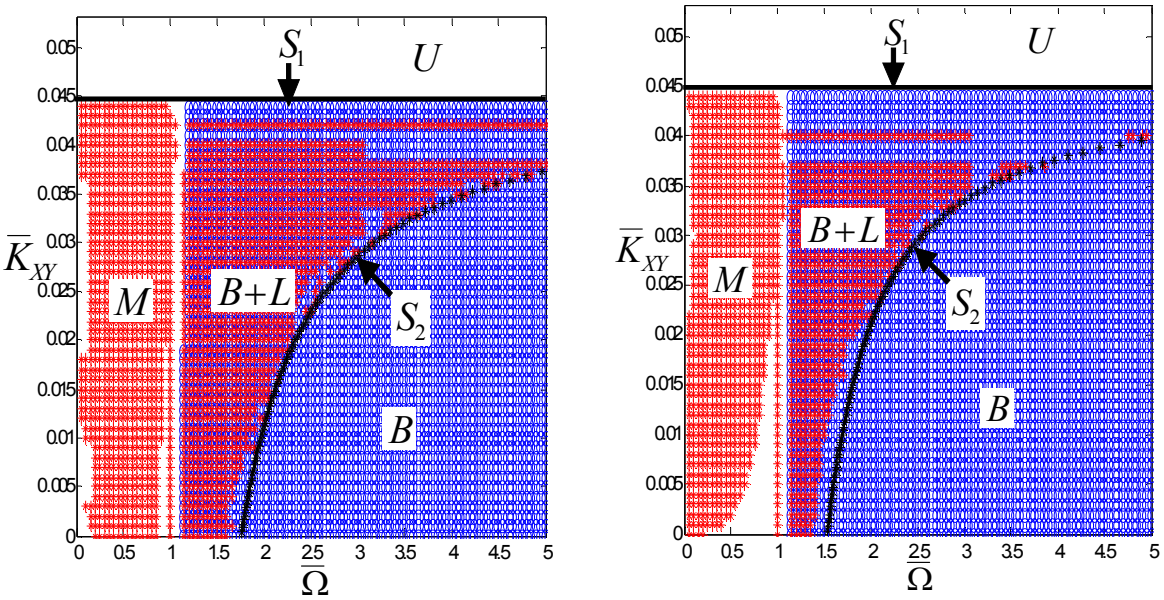


Figure.2.5 Stability contour plots ($\overline{\Omega}$ vs.$\overline{K}_{XY}$) under the influence of Alford's force ($c_b = 1e-4$ (left) and $c_b = 1e-3$ (right)/ with $m_{im} = m_b$).

Based upon (2-37), for given domain of damping and stiffness of bearing, we can determine the corresponding critical operating speed where the coexistence zone of both the limit-cycle and the balanced condition is terminated. Another form of (2-37) is given by

$$\overline{\Omega}_{cr} = \frac{1}{\omega_n}\left[\left[\frac{m_b^{\,2}\omega_t^{\,4}}{c_b\left[\frac{C_{XX}}{m_t\omega_t}m_t\omega_t^{\,2} - K_{A.XY.cr}\right]}\right] + \omega_t\right] \tag{2-38}$$

Since $\omega_n \approx \omega_t$ due to $m_t \approx m$ (i.e, $m_b << m$), (2-38) becomes with assumption $K_{A.XY.cr} = \alpha K_{XX}$ where a constant $\alpha < 1$,

$$\overline{\Omega}_{cr} = \left[\frac{\frac{m_b^{\,2}}{c_b m_t}\omega_t}{\left[\frac{C_{XX}}{m_t\omega_t} - \alpha\right]} \right] + 1 \tag{2-39}$$

(2-39) indicates that $\overline{\Omega}_{cr}$ depend on $\frac{C_{XX}}{m_t\omega_t}$ and ω_t representing the damping and stiffness property of supporting bearing and $\frac{m_b^{\,2}}{c_b m_t}$ and α are the information about ABD property relative to the rotor-shaft and the magnitude of Alford force respectively.

Now, we can set the domain of bearing satisfying the desired terminating critical operating speed s.t, $\overline{\Omega}_{tr.\min} \le \overline{\Omega}_{tr} \le \overline{\Omega}_{tr.\max}$. Thus, (2-39) can be transformed s.t,

$$\ln\left[\overline{\Omega}_{cr.\min} - 1\right] \le \ln\left[\frac{m_b^{\,2}\omega_t}{c_b m_t}\right] - \ln\left[\frac{C_{XX}}{m_t\omega_t} - \alpha\right] \le \ln\left[\overline{\Omega}_{cr.\max} - 1\right] \tag{2-39}$$

with conditions $1 < \overline{\Omega}_{cr.\min} < \overline{\Omega}_{cr.\min}$ and $\frac{C_{XX}}{m_t\omega_t} > \alpha$ for the physical solution.

In Figure.2.6, U_1 , U_2 , U_3 and U_4 represent the domains categorized by the conditions $1 < \overline{\Omega}_{cr} \le 2$, $2 < \overline{\Omega}_{cr} \le 3$, $3 < \overline{\Omega}_{cr} \le 4$, and $4 < \overline{\Omega}_{cr} \le 5$ respectively. We can compute the domain $U_i \quad for\ i = 1,2,3,4$ from (2-39) s.t,

$$U_i = \left\{ \left\{ \ln\left[\frac{m_b^{\,2}\omega_t}{c_b m_t}\right], \ln\left[\frac{C_{XX}}{m_t\omega_t} - \alpha\right] \right\} \in \Re^2 \mid \ln[i-1] < \ln\left[\frac{m_b^{\,2}\omega_t}{c_b m_t}\right] - \ln\left[\frac{C_{XX}}{m_t\omega_t} - \alpha\right] \le \ln[i] \right\} \cap U_{con}$$

U_{con} is the constraint domain for the bearing property which is arbitrarily allowable stiffness and damping property of bearing and this constraint is given by,

$$U_{con} = \left\{ \left\{ \ln\left[\frac{m_b^{\,2}\omega_t}{c_b m_t}\right], \ln\left[\frac{C_{XX}}{m_t\omega_t} - \alpha\right] \right\} \in \Re^2 \mid -0.4 < \ln\left[\frac{m_b^{\,2}\omega_t}{c_b m_t}\right] \le 0.3, \ -1.4 \le \ln\left[\frac{C_{XX}}{m_t\omega_t} - \alpha\right] \le 0.2 \right\}$$

We can terminate unwanted coexistence zone in the classified operating speed zone by selecting damping and stiffness of bearing satisfying each domain. One can observe that U_4 are expanded at larger $K_{A.XY}$ in Figure.2.6. Based upon the results in Figure.2.6, the design guideline of the supporting bearing can be suggested in the early stage of design to possibly avoid the unwanted behavior of system at a given operating environment.

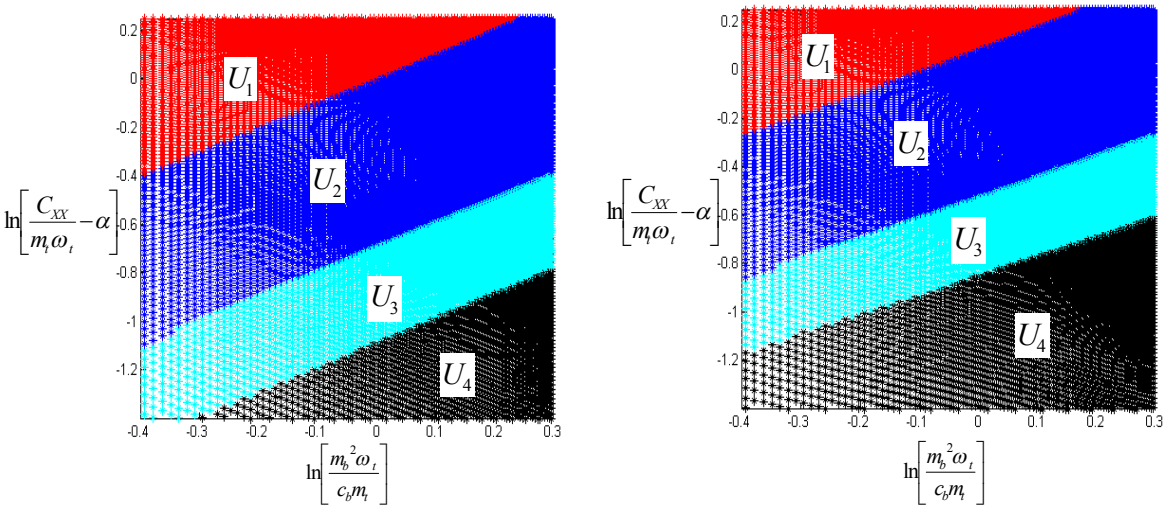


Figure.2.6 Bearing stiffness and damping domain for the critical operating speed ($K_{A.XY}=0.01K_{XX}/\alpha=0.01$ (left) $K_{A.XY}=0.1K_{XX}/\alpha=0.1$ (right)/ $m_b^{\ 2}=0.1305c_b m_t$ is used.)

2.5 Concluding Remarks

With several reasonable assumptions, this chpater provides the harmonic limit-cycle solutions of automatic balancing device for imbalanced rotor system operating with symmetric property bearing under the influence of Alford's force. The solutions are validated through the time and frequency domain numerical simulation and then, using the perturbed system about the solutions, the system stability is assessed by FTM method. Specifically, applying the Alford's force holding constant cross-coupling stiffness into the system, this research explores the limit-cycle behavior of system with the rolling element bearing and also conducted the corresponding stability analysis by varying the magnitude of the cross coupling stiffness in Alford's force. The coexistence of limit-cycle with a balancing fixed equilibrium point is also verified as specified in several published literatures and the bifurcation boundary characterizing the connectivity between Alford's force and limit-cycle at given operating speed is also analytically derived based upon the suggested limit cycles solution. This analytical bifurcation boundary provides us that increasing the damping of the supporting bearing and ABD-ball is one method to suppress the effect of limit-cycle of system under the situation where Alford's force can't be eliminated completely. Additionally, the selection of bearing damping and stiffness is also discussed for destabilizing the limit-cycle. Upon one's necessity, this work can be valuable proto-type guideline to avoid the limit cycles behavior under the influence of Alford's force in the first stage of practical design. In this chapter, the suggested approach also addresses the characteristic of system driving frequency induced by ABD-

ball under limit cycle condition. This driving frequency is approximated as the resonance excitation frequency of system thus the force excited by ABD-ball become far more dominant than one transmitted by imbalance effect deteriorating the accuracy of limit cycle solution presented here. Consequently, the accuracy of solution is guaranteed with allowable size of imbalance due to the property of this excitation frequency. These findings yield the valuable information about limit cycle phenomena in this special case.

CHAPTER III
LIMIT-CYCLE ANALYSIS OF PLANAR ROTOR/AUTOBALANCER SYSTEM SUPPORTED ON HYDRODYNAMIC JOURNAL BEARING

3.1 Planar Rotor/Autobalancer system

In this section, we present the mathematical model of the planar-rigid rotor/Autobalancer system mounted on a generalized linear bearing system including the cross-coupling terms. The dynamics of system are derived in the fixed frame $\{n_1, n_2, n_3\}$.

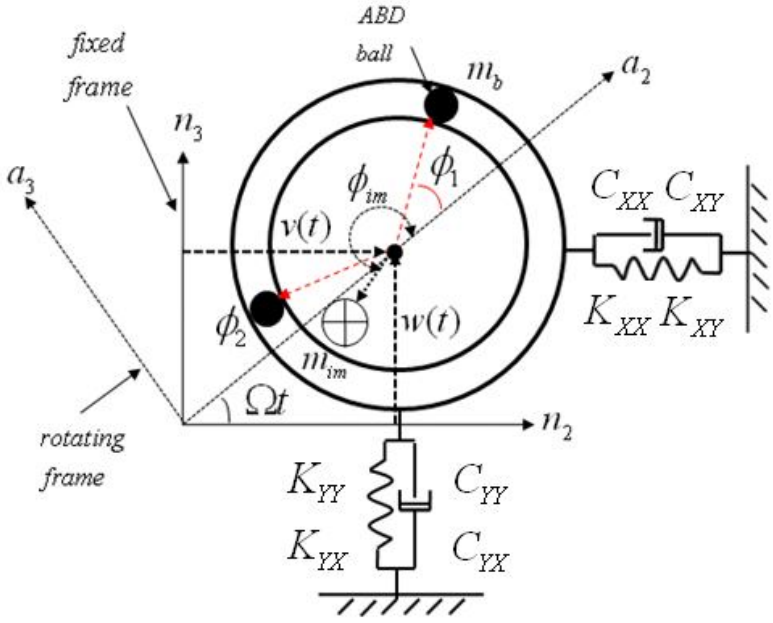


Figure.3.1 Rigid planar rotor-ABD system supported by a general bearing holding asymmetric damping and stiffness force including cross-coupling ones

Specifically, the vertical and horizontal displacements of the rotor $v(t)$ and $w(t)$ are described relative to the fixed-frame and the angular positions of the ABD balancer masses $\phi_1(t)$, $\phi_2(t)$ in the circular track of ABD together with the imbalance phase ϕ_{im} are described with respect to a set of rotating frame $\{a_1, a_2, a_3\}$, as shown in Figure.1. The rotor is assumed to be driven with constant angular speed Ω.

The transformation from $\{n_1, n_2, n_3\}$ to $\{a_1, a_2, a_3\}$ is given by,

$$\begin{bmatrix} a_1 \\ a_2 \\ a_3 \end{bmatrix} = \begin{bmatrix} 1 & 0 & 0 \\ 0 & \cos(\Omega t) & \sin(\Omega t) \\ 0 & -\sin(\Omega t) & \cos(\Omega t) \end{bmatrix} \begin{bmatrix} n_1 \\ n_2 \\ n_3 \end{bmatrix} \tag{3-1}$$

The center position of the rotor is provided by,

$$R_{oc} = v(t)n_2 + w(t)n_3 \tag{3-2}$$

The position vector of imbalance mass and the balls position vector are given by,

$$R_{im} = R_{oc} + r_{im}[\cos(\phi_{im})a_2 + \sin(\phi_{im})a_3] \tag{3-3}$$

$$R_{ball.i} = R_{oc} + r_b[\cos(\phi_i(t))a_2 + \sin(\phi_i(t))a_3] \quad for\ i = 1,2 \tag{3-4}$$

where, r_{im} and r_b are the radial length of imbalance mass and ABD's balls, respectively and $r_{im} = r_b$ is assumed.

The kinetic energy of the whole system is given by,

$$T_{total} = \frac{m}{2}[\dot{v}(t)^2 + \dot{w}(t)^2] + \frac{m_{im}}{2}[\dot{R}_{im} \cdot \dot{R}_{im}] + \frac{m_b}{2}\left(\sum_{i=1}^{2}[\dot{R}_{ball.i} \cdot \dot{R}_{ball.i}]\right) \tag{3-5}$$

where, m, m_b and m_{im} are the mass of the rotors-shaft, ABD-ball and imbalance mass.

Next, the potential energy and dissipation energy of the bearing are

$$V_{bearing} = \frac{1}{2}[K_{XX}v(t)^2 + K_{YY}w(t)^2 + K_{XY}v(t)^2 + K_{YX}w(t)^2] \tag{3-6}$$

$$D_{bearing} = \frac{1}{2}\left[C_{XX}\dot{v}(t)^2 + C_{YY}\dot{w}(t)^2 + C_{XY}\dot{v}(t)^2 + C_{YX}\dot{w}(t)^2\right] \tag{3-7}$$

where, $K_{ij}, C_{ij}\ for\ i, j = X, Y$ are the bearing stiffness and damping coefficients. Note that subscripts X and Y in bearing are corresponding to the direction of v and w.

Providing the dissipation energy of ABD's balls,

$$D_{ball} = \frac{1}{2}c_b\left(\sum_{i=1}^{2}(\dot{\phi}_i(t)^2)\right) \tag{3-8}$$

Defining the state of system such that, $q \equiv [v(t)\ w(t)\ \phi_1(t)\ \phi_2(t)] \in R^4$ and using the Lagrange's equation with (3-5) through (3-8),

$$\frac{d}{dt}\left[\frac{\partial T_{total}}{\partial \dot{q}}\right]-\frac{\partial T_{total}}{\partial q}+\frac{\partial V_{bearing}}{\partial q}+\frac{\partial[D_{bearing}+D_{ball}]}{\partial \dot{q}}=0 \tag{3-9}$$

We can obtain the equation of motion,

$$M(\phi_i,t)\ddot{q}+C(\phi_i,t)\dot{q}+Kq=F_{im}(t)+F_{ball}(\dot{\phi}_i,\phi_i,t) \tag{3-10}$$

where $M(\phi_i,t)\in R^{4\times4}$, $C(\phi_i,t)\in R^{4\times4}$ and $K\in R^{4\times4}$ is an inertia matrix, a damping matrix, and a stiffness matrix and, $F_{ball}(\dot{\phi}_i,\phi_i,t)\in R^4$ and $F_{im}(t)\in R^4$ are the force excitation terms induced by ABD's balls and imbalance mass, respectively. The detail of matrices is given in Appendix.

3.2 Limit-cycle solution of generalized bearing support

In this section, we proposed the assumed limit-cycle solution of ABD-rotor system supported by bearing producing all directional forces which are expressed as diagonal and off-diagonal components in damping and stiffness matrices. Before proceeding, the following assumptions were made to facilitate the analysis. *i)* For the limit-cycle condition, two balls are merged and rotated together so that one ball motion is synchronous with another. Consequently, the coordinate of system in (10) is reduced into $q=[v(t)\ w(t)\ \phi(t)]^T\in\Re^3$ and the mass of merged two balls is simply defined as $m_{b.m}$ equivalent to the mass of two balls (i.e, $m_{b.m}=2m_b$). It should be noted that the contact mechanism of two balls is out of our research scope. Based upon [16] also characterized the balanced equilibrium attraction basin as a function of ball initial position, the non-synchronous behavior/limit cycle is mostly created by setting that the initial angular position of two ABD-balls is located near for each other or identically. Reversely, if one ball is initially stayed away from another, the system is highly subject to the stable synchronous behavior due to the different angular phase between two balls according to [16]. Thus, the merging situation of two balls is highly probable under limit cycle condition. *ii)* The ball speed denoted as ω is assumed to be constant under the limit-cycle condition. Hence, $\dot{\phi}=\omega\Rightarrow\phi=\omega t$ and $\ddot{\phi}=0$. It should be noted that this assumption is not valid for every case but there exists allowable condition for this assumption so that the running speed of ball mass in ABD track can be approximated as constant one and this point of view will be discussed with the simulation results. *iii)* the limit-cycle solution is assumed to be a harmonic solution and given by,

$$
\begin{aligned}
v(t) &= a_1\cos[(\omega+\Omega)t] + a_2\sin[(\omega+\Omega)t] + a_3\cos(\Omega t) + a_4\sin(\Omega t) + v_0 \\
w(t) &= b_1\cos[(\omega+\Omega)t] + b_2\sin[(\omega+\Omega)t] + b_3\cos(\Omega t) + b_4\sin(\Omega t) + w_0
\end{aligned}
\tag{3-11}
$$

where, $a_i, b_i, v_0, w_0 \;\; for\; i = 1,2,3,4$ and ω are the unknown amplitudes and merged ball whirl speed to be solved.

Applying assumption *i)* and *ii)*, the system dynamics (10) is reduced into,

$$
M(\phi,t)\ddot{q} + C(\phi,t)\dot{q} + Kq = F_{im}(t) + F_{ball}(\dot{\phi},\phi,t) \tag{3-12}
$$

with the reduced coordinates $q = [v\ w\ \phi]^T \in \Re^3$. Basically, (3-12) is the version of dynamic excluding one of dynamic equations about a ball motion. The detail of matrices is given in Appendix.

Substituting (3-11) into (3-12) and rearranging it yields,

$$
\begin{aligned}
&[(K_{XX} - m_t(\omega+\Omega)^2)a_1 + C_{XX}(\omega+\Omega)a_2 + K_{XY}b_1 + C_{XY}(\omega+\Omega)b_2 - m_{b.m}r_b(\omega+\Omega)^2]\cos[(\omega+\Omega)t] + \\
&[-C_{XX}(\omega+\Omega)a_1 + (K_{XX} - m_t(\omega+\Omega)^2)a_2 - C_{XY}(\omega+\Omega)b_1 + K_{XY}b_2]\sin[(\omega+\Omega)t] + \\
&[a_3(K_{XX} - m_t\Omega^2) + a_4C_{XX}\Omega + b_3K_{XY} + b_4C_{XY}\Omega - m_{im}r_{im}\Omega^2\cos(\phi_{im})]\cos(\Omega t) + \\
&[a_4(K_{XX} - m_t\Omega^2) - a_3C_{XX}\Omega + b_4K_{XY} - b_3C_{XY}\Omega + m_{im}r_{im}\Omega^2\sin(\phi_{im})]\sin(\Omega t) + \\
&K_{XX}v_0 + K_{XY}w_0 = 0
\end{aligned}
\tag{3-13}
$$

$$
\begin{aligned}
&[K_{YX}a_1 + C_{YX}(\omega+\Omega)a_2 + (K_{YY} - m_t(\omega+\Omega)^2)b_1 + C_{YY}(\omega+\Omega)b_2]\cos[(\omega+\Omega)t] + \\
&[-C_{YX}(\omega+\Omega)a_1 + K_{YX}a_2 - C_{YY}(\omega+\Omega)b_1 + (K_{YY} - m_t(\omega+\Omega)^2)b_2 - m_{b.m}r_b(\omega+\Omega)^2]\sin[(\omega+\Omega)t] \\
&[a_3K_{YX} + a_4C_{YX}\Omega + b_3(K_{YY} - m_t\Omega^2) + b_4C_{YY}\Omega - m_{im}r_{im}\Omega^2\sin(\phi_{im})]\cos(\Omega t) + \\
&[a_4K_{YX} - a_3C_{YX}\Omega + a_4(K_{YY} - m_t\Omega^2) - b_3C_{YY}\Omega - m_{im}r_{im}\Omega^2\cos(\phi_{im})]\sin(\Omega t) \\
&K_{YX}v_0 + K_{YY}w_0 = 0
\end{aligned}
\tag{3-14}
$$

$$
\frac{2c_br_b\omega}{m_{b.m}} + (a_2 - b_1)(\omega+\Omega)^2 + (a_4 - b_3)\Omega^2\cos(\omega t) + (a_3 + b_4)\Omega^2\sin(\omega t) + H.O.T(t) = 0 \tag{3-15}
$$

where $m_t = m + m_{b.m}$. If the coefficients of each harmonic in (3-13) and (3-14) can be set to zero, the eight nonlinear equations and two linear ones are generated for solving unknowns and placing them into matrix form yields,

$$\begin{bmatrix} K_{XX}-m_t(\omega+\Omega)^2 & C_{XX}(\omega+\Omega) & K_{XY} & C_{XY}(\omega+\Omega) \\ -C_{XX}(\omega+\Omega) & K_{XX}-m_t(\omega+\Omega)^2 & -C_{XY}(\omega+\Omega) & K_{XY} \\ K_{YX} & C_{YX}(\omega+\Omega) & K_{YY}-m_t(\omega+\Omega)^2 & C_{YY}(\omega+\Omega) \\ -C_{YX}(\omega+\Omega) & K_{YX} & -C_{YY}(\omega+\Omega) & K_{YY}-m_t(\omega+\Omega)^2 \end{bmatrix} \begin{bmatrix} a_1 \\ a_2 \\ b_1 \\ b_2 \end{bmatrix} = \begin{bmatrix} m_{b.m}r_b(\omega+\Omega)^2 \\ 0 \\ 0 \\ m_{b.m}r_b(\omega+\Omega)^2 \end{bmatrix} \tag{3-16}$$

$$\begin{bmatrix} K_{XX}-m_t\Omega^2 & C_{XX}\Omega & K_{XY} & C_{XY}\Omega \\ -C_{XX}\Omega & K_{XX}-m_t\Omega^2 & -C_{XY}\Omega & K_{XY} \\ K_{YX} & C_{YX}\Omega & K_{YY}-m_t\Omega^2 & C_{YY}\Omega \\ -C_{YX}\Omega & K_{YX} & -C_{YY}\Omega & K_{YY}-m_t\Omega^2 \end{bmatrix} \begin{bmatrix} a_3 \\ a_4 \\ b_3 \\ b_4 \end{bmatrix} = \begin{bmatrix} m_{im}r_{im}\Omega^2\cos(\phi_{im}) \\ -m_{im}r_{im}\Omega^2\sin(\phi_{im}) \\ m_{im}r_{im}\Omega^2\sin(\phi_{im}) \\ m_{im}r_{im}\Omega^2\cos(\phi_{im}) \end{bmatrix} \tag{3-17}$$

Additionally, we have two linear equations $K_{XX}v_0 + K_{XY}w_0 = 0$ and $K_{YX}v_0 + K_{YX}w_0 = 0$. Both v_0 and w_0 are zeros if $K_{XX} \neq K_{XY} \neq K_{YX} \neq K_{YY} \neq 0$.

As seen in (3-15), although neglecting high order time-varying terms (*H.O.T(t)*) for approximation, the first order time-varying terms(i.e, $(a_4 - b_3)\Omega^2\cos(\omega t) + (a_3 + b_4)\Omega^2\sin(\omega t)$) are still observed, which consequently violates the assumption *ii)* $\ddot{\phi} = 0$. The influence of these terms are strongly dependent on the amplitude of a_3, a_4, b_3, b_4 which are determined by the magnitude of imbalance mass, bearing characteristics as well as operating speed as seen in (3-17) and those are independent of any properties of ABD. Since the unknowns a_1, a_2, b_1, b_2 are the function of the ball speed ω which is influenced by imbalance effect as seen in (3-15) and (3-16). To truncate the time-varying terms for an approximate analytical solution, the effect of time-varying terms in (3-15) should be insignificant not to heavily deteriorate the accuracy of suggested solution. Fortunately, the effect of time-varying terms can be less important for the limit cycle solution in the two following reasons. *1*) As seen in (3-17), the unknowns a_3, a_4, b_3, b_4 which are directly proportional to the size of imbalance mass. The best performance of ABD can be usually achieved under the condition $m_{im} < 2m_b = m_{b.m}$ if $r_{im} = r_b$. The complete synchronous balancing condition of ABD-rotor system is founded with this condition for the co-located case where the location of imbalance mass coincides with ABD-ball's relative to the axial direction of rotor-shaft. Under this condition $m_{im} < 2m_b$, the effect of time-varying terms can be insignificant. In other words, there exists allowable imbalance size not to heavily deteriorate the accuracy of the limit cycle solution. *2*) The inherent nature of limit cycle associated with the running frequency of ABD-ball dominates the imbalance effect so that the time-varying terms in (3-15) directly associated with imbalance can be less important contribution to the solution. As seen in (3-12), there are two exciting force terms

$F_{im}(t)$ and $F_{ball}(\dot{\phi},\phi,t)$. The driving frequencies of $F_{im}(t)$ and $F_{ball}(\dot{\phi},\phi,t)$ are respectively Ω and $\omega+\Omega$. If $\omega+\Omega$ is near the system resonance frequency in the range of supercritical operating speed, the vibration amplitude of system caused by $F_{ball}(\dot{\phi},\phi,t)$ dominant one induced by $F_{im}(t)$. Under the limit cycle condition, it is founded that the driving frequency of ABD ball movement is close to the system natural frequency. These two conditions *1)* and *2)* above enhance us to achieve the well approximated solution and these aspects will be explained with and validated through the numerical simulation results.

Thus, with *1*) and *2*) above, truncating the time-varying terms of (3-15) results in,

$$\frac{c_b r_b \omega}{m_b} + \frac{(a_2 - b_1)(\omega+\Omega)^2}{2} = 0 . \tag{3-18}$$

Now, the unknowns can be solved through (3-16), (3-17) and (3-18). This paper does not provide the analytical expression for unknown parameters. However, upon one's intention, the complete expression of approximated analytical solution can be achieved via (3-16), (3-17) and (3-18).

3.3 Stability analysis

To investigate the local stability of the system in the neighborhood of the limit-cycle solution founded in previous sections, (3-12) is linearized using the perturbation approach. By considering the small perturbations $\Delta v_L(t)$, $\Delta w_L(t)$, and $\Delta\phi_L(t)$, the perturbed system configuration is $v(t)=v_L(t)+\Delta v_L(t)$, $w(t)=w_L(t)+\Delta w_L(t)$, and $\phi(t)=\phi_L(t)+\Delta\phi_L(t)$ where $v_L(t)$, $w_L(t)$, and $\phi_L(t)$ are the limit-cycle solutions in (3-11) and the ball's angular position computed by (3-16) through (3-18). Substituting this perturbed configuration into the original nonlinear dynamics (3-12), and truncating the higher order terms results in a set of linearized equation about each limit-cycle solution $v_L(t)$, $w_L(t)$,and $\phi_L(t)$. Denoting a set of perturbed coordinate as $\Delta q_L=[\Delta v_L(t)\ \Delta w_L(t)\ \Delta\phi_L(t)]^T\in\Re^3$ and a set of limit-cycle solution as $q_L=[v_L(t)\ w_L(t)\ \phi_L(t)]^T\in\Re^3$, we finally have,

$$\Delta M(q_L,t)\Delta\ddot{q}_L + \Delta C(q_L,t)\Delta\dot{q}_L + \Delta K(q_L,t)\Delta q_L = 0 \tag{3-19}$$

Defining the state vector $x(t)=[\Delta q_L{}^T\ \Delta\dot{q}_L{}^T]^T\in\Re^6$, we can transform (3-19) into,

$$\dot{x}(t) = A(q_L,t)x(t) \tag{3-20}$$

with a system matrix $A(q_L,t)=\begin{bmatrix} 0 & I \\ -\Delta M^{-1}(q_L,t)\Delta K(q_L,t) & -\Delta M^{-1}(q_L,t)\Delta C(q_L,t) \end{bmatrix}$.

To determine the stability of (3-20) which is the linear time-varying equation, we employ the Floquet's Transition Matrix (FTM) method. By the linear theory, the solution for (3-20) is expressed as

$$x(t) = \Phi(q_L,t)x_0 \tag{3-21}$$

where, $\Phi(q_L,t) \in \Re^{6\times 6}$ and $x_0 \in \Re^6$ are FTM and the initial condition respectively.

Replacing the x_0 as the 6 by 6 identity matrix, $x(t)$ becomes 6 by 6 matrix solution and then, with the period $T=\frac{2\pi}{\Omega+\omega}$, we can obtain the periodic solution s.t $x(T)=\Phi(q_L,T)$. Ultimately, the stability criterion is determined by

$$\begin{aligned} &\max_{1\le i\le 6}\left|\lambda_i(x(T))\right| < 1 \quad stable \\ &\max_{1\le i\le 6}\left|\lambda_i(x(T))\right| > 1 \quad unstable \end{aligned} \tag{3-22}$$

where λ_i is the eigenvalues of matrix solution $x(T)=\Phi(q_L,T)$.

Among the limit cycle solutions q_L, we also have the solution satisfying $\omega = 0$. This is the merged equilibrium solution where two balls are merged together and synchronously rotated in an identical rotor operating speed Ω. This is a synchronous behavior usually exhibited before the critical speed, which is not belonging to the non-synchronous condition($\omega \neq 0$). The stability of merged equilibrium condition is also considered in the subsequent simulation results.

In the same manner, we also determine the stability of balanced equilibrium solution using this FTM approach. To do this, (3-10) is linearized by using perturbation approach as done in (3-19) but with $v(t)=v_{bal}(t)+\Delta v_{bal}(t)$, $w(t)=w_{bal}(t)+\Delta w_{bal}(t)$, and $\phi_{bal.i}(t)=\phi_{bal.i}(t)+\Delta\phi_{bal.i}(t)$ $for\ i=1,2$. The fixed equilibrium point of balancing condition for the co-located case is simply computed as $q_{bal}=[v_{bal}\quad w_{bal}\quad \phi_{bal1}\ \phi_{bal2}]^T=[0\quad 0\quad \phi_{bal1}\ \phi_{bal2}]^T\in\Re^4$ where, $\phi_{bal.i}=\phi_{im}\pm\arccos[-\delta]$ $for\ i=1,2$, note, $\delta=\frac{m_{im}r_{im}}{2m_br_b}$ and this balanced solution exist under the condition of $\delta\le 1$. The subsequent stability analysis of the balanced solution is conducted in the neighborhood of q_{bal}.

3.4 Numerical simulation results

In this section, two typical hydrodynamic bearings widely used in the industrial applications s.t turbo-machinery and rotary machines due to their long life are engaged to explore the limit-cycle and balanced condition of ABD-rotor system mounted on these bearings with numerical simulation outcomes. These two bearings are classified as the typical sliding-element bearings or fluid film bearings where fluid supply pressure need to high enough to maintain a copious supply of lubricant in the load supporting clearance around bearing journal[11]. In extreme operating condition, there might be a contact between the shaft surface and bearing journal if the pressure of supplying lubricant can't hold the rotor-shaft system orbiting relative to the geometrical center of system. Thus, the performance of bearing damping and stiffness heavily depends on the dimensionless ratio between the eccentricity and the radial clearance of the bearing, which are determined by the static loading, the bearing structure and fluid characteristic inside bearing journal. In other words, the starting position of rotor-shaft/loading relative to the inner surface of a bearing plays a central role of bearing capacity. The first bearing used here is a short journal bearing so called pi-film bearing and another is a tilting pad bearing. The short journal bearing holds asymmetric damping and stiffness and generate full cross-coupling terms. The tilting pad bearing has the similar property like the short journal bearing but no cross-coupling force created due to its geometric benefit. From[18] through [20], we simply acquired the mathematically parameterized models for these two bearings and used these for the subsequent analysis. Before proceeding, it should be noted that dimensionless operating speed $\overline{\Omega}$ introduced here is defined by $\frac{\Omega}{\omega_n}$ where, $\omega_n = \sqrt{\frac{average(K_{XX})}{m}}$ and $c_b = 1e-4$, $m_b = 0.005m$, $r_b = r_{im} = 0.01$,and $\phi_{im} = 45^{\circ}$ are commonly used for the all simulations presented in next two subsections.

3.4.1 Rotor/ABD with Fully Cavitated Short Bearing

To replace the damping and stiffness coefficients generally expressed in (3-16) and (3-17) by ones associated with Pi-film short journal bearing parameters, the detail of bearing damping and stiffness coefficients are provided in (3-23). These are the function of the non-dimensional parameter $\varepsilon = \frac{e}{c}$ which is the ratio of the journal eccentricity(e) and the radial clearance(c). The mathematical expression of the dimensionless stiffness and damping coefficients for fully cavitated short bearing are given by[18],

$$
\begin{aligned}
\overline{K}_{XX} &= 4(2\pi^2 + (16-\pi^2)\varepsilon^2)Q(\varepsilon) \\
\overline{K}_{XY} &= \frac{\pi(-\pi^2 + 2\pi^2\varepsilon^2 + (16-\pi^2)\varepsilon^4)Q(\varepsilon)}{\varepsilon\sqrt{(1-\varepsilon^2)}} \\
\overline{K}_{YX} &= \frac{\pi(\pi^2 + (32+\pi^2)\varepsilon^2 + 2(16-\pi^2)\varepsilon^4)Q(\varepsilon)}{\varepsilon\sqrt{(1-\varepsilon^2)}} \\
\overline{K}_{YY} &= \frac{4(\pi^2 + (32+\pi^2)\varepsilon^2 + 2(16-\pi^2)\varepsilon^4)Q(\varepsilon)}{\sqrt{(1-\varepsilon^2)}} \\
\overline{C}_{XX} &= \frac{2\pi\sqrt{1-\varepsilon^2}(\pi^2 + 2(\pi^2-8)\varepsilon^2)Q(\varepsilon)}{\varepsilon} \\
\overline{C}_{YY} &= \frac{2\pi(\pi^2 + 2(24-\pi^2)\varepsilon^2 + \pi^2\varepsilon^4)Q(\varepsilon)}{\varepsilon\sqrt{(1-\varepsilon^2)}} \\
\overline{C}_{XY} &= 8(\pi^2 + 2(\pi^2-8)\varepsilon^2)Q(\varepsilon) \qquad \overline{C}_{XY} = \overline{C}_{YX}
\end{aligned}
\tag{3-23}
$$

where, $Q(\varepsilon) = \dfrac{1}{(\pi^2 + (16-\pi^2)\varepsilon^2)^{\frac{3}{2}}}$ and the conversion to the physical coefficients are recovered by the relations s.t $K_{ij} = \dfrac{F}{c}\overline{K}_{ij}$ and $C_{ij} = \dfrac{F}{c\Omega}\overline{C}_{ij}$ (note that this relation is used for another bearing in the next subsection), where, F is the static load supported by the bearing. Cautiously, some components of (3-23) reach to the infinity for both $\varepsilon \to 0$ and $\varepsilon \to 1$ so that these two cases are excluded in subsequent computation. The physical damping coefficients are function of operating speed(Ω) and is inversely proportional to Ω. The curves for each dimensionless coefficient are plotted in Figure.2.

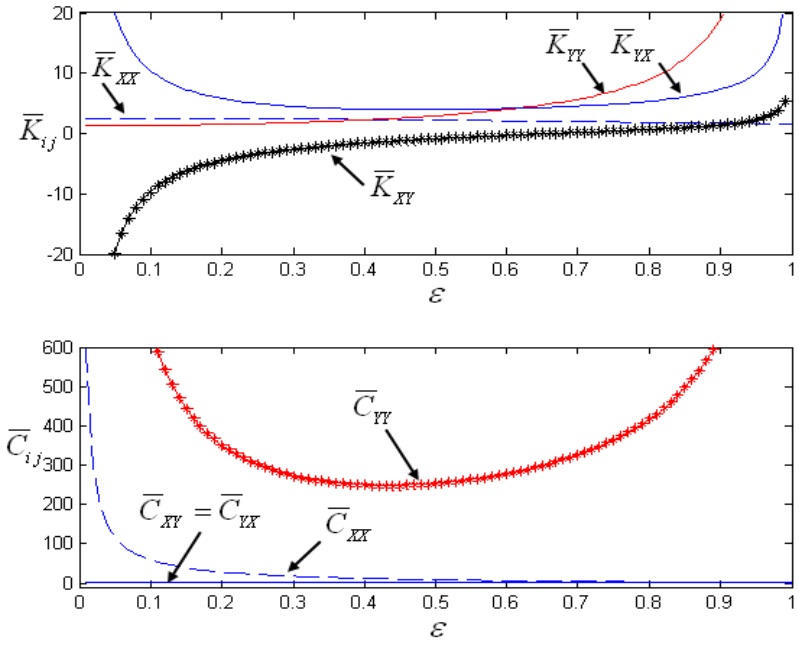


Figure.3.2 Characteristic of dimensionless bearing coefficients for fully cavitated short bearing

Now, applying the characteristic of physical bearing coefficients into (3-16) and (3-17), we solve for unknowns $a_i, b_i, \omega \ for\ i = 1,2,3,4$ (i.e, limit-cycle solution in (3-11)) via "fminsearch" provided by MATLAB for a given operating speed $\overline{\Omega}$. To validate the proposed limit-cycle solution in (3-11), we compared it with the results obtained via the full nonlinear dynamics (3-10) simulated in Simulink/MATLAB environment. For the simplicity, we use the short notations **LC** and **FS** for limit cycle solution in (3-11) and the results obtained through the full nonlinear simulation (3-10) throughout this paper. In **FS**, the limit-cycle condition can be also generated by setting the initial condition leading to the outside of the provided attraction basin based upon [16]. Thus, the initial position of two balls is presumed to be merged on the full nonlinear simulation s.t, $\phi_1(t_0) = \phi_2(t_0)$ where t_0 is the initial time. In (a) and (b) of Figure.3.3, the star-dotted lines on both plots represent the time domain response and whirl orbit obtained via **FS**, while the circle-dotted lines do the assumed **LC**. The transient part of time domain response and whirl orbits in **FS** is discarded for clarity. Here, the transient part implies the chaotic behavior before the motion of system reach the level where one can interpret as the form of steady-state harmonic type response. The whirl orbits in (b) are the elliptical form due to the asymmetric property of the bearing with the effect of cross-coupling terms. In (c) and (d), the local extremums of system appeared in a certain sampling time period of **FS** are illustrated at each $\overline{\Omega}$ with $\varepsilon = 0.82$ and $\varepsilon = 0.05$. As seen in (c) and (d), the several local extremums are founded at a given $\overline{\Omega}$ and this fact can be understood by examining the results in (a) where the multiple local extremums are observed. The star dots and circle dots in (c) and (d) represent **FS** and **LC** respectively and they are coincided for the most of cases. In (e) and (f), the power spectrums of the proposed **LC**(shown as the circle-dotted line) and **FS**(shown as the star-dotted line) are presented. As expected from (3-11), two significant frequencies are commonly observed. One is the operating frequency($\Omega = 3\ Hz$) of system excited by an imbalance effect while another is the running frequency of merged ball ($\Omega + \omega = 2.5\ Hz$) on ABD-track. In (g), the straight lines are the merged ABD's ball speeds ω of **LC** relative to the rotating frame and the three star-dotted fluctuating lines are the outcomes from **FS** at given three imbalance mass magnitudes. As the imbalance masses increase, the fluctuating amplitudes become larger. Since the third and fourth time-varying terms of (3-15) with the truncated *H.O.T(t)* are truncated for **LC**, the fluctuating amplitudes of **FS** can't be captured by ω which is assumed to be constant for **LC**. However, the fluctuation magnitudes are very small under $m_{im} \le 2m_b$ and the constant ball speed of **LC** represents the average of actual ball speed of **FS**. In (h), the three power spectrums of simulated ball speed via **FS** are shown and, with conditions $m_{im} = 5m_b$ and $m_{im} = 10m_b$, there are no significant frequencies but ones near zero, which implies that the property of actual ball speed of **FS** is very similar to constant signal's one. However, we can observe that

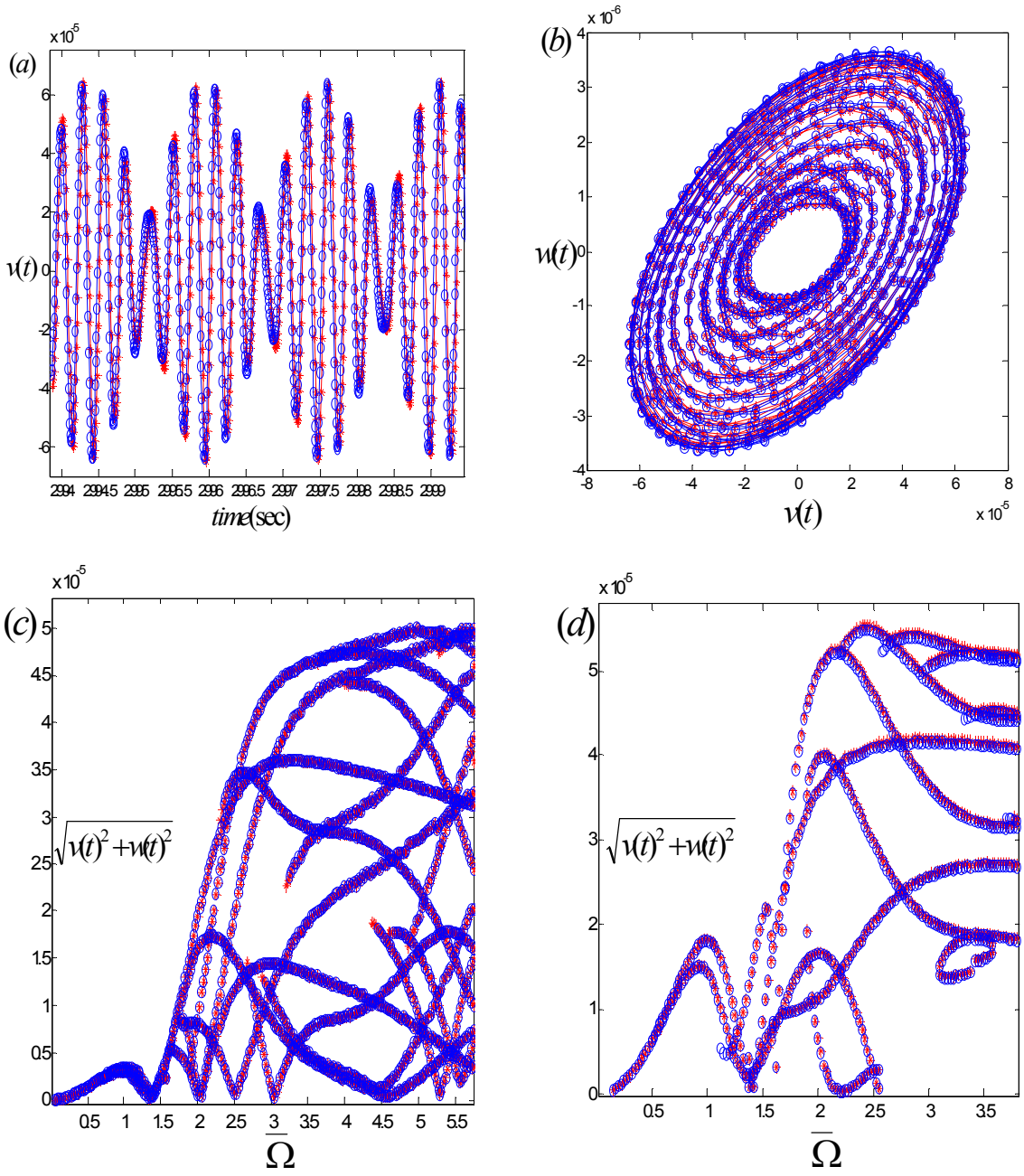
there exists a significant frequency near 0.5 *Hz* with $m_{im} = 20m_b$. This result also supports that the limit-cycle ball speed can be assumed to be constant under the reasonable size of imbalance mass. Additionally, from (i), one can see that the constant ball speed(displayed as straight line) of **LC** can capture the average of ball speed via **FS**(depicted as star-dotted line) collected for a certain sampling period at a given $\overline{\Omega}$ s.t $0.5[\max_{T-t_a<t<T} \omega(t) + \min_{T-t_a<t<T} \omega(t)]$, where where T and t_a are the end of simulation time and the sampling period respectively. Three pairs of triangular and circle dots in (i) represent the minimum($\min_{T-t_a<t<T} \omega(t)$) and maximum($\max_{T-t_a<t<T} \omega(t)$) ball speed obtained through **FS** for each $\overline{\Omega}$. One can see that the difference between minimum and maximum amplitude of ball speed becomes increased with larger imbalance effect but this difference is so small under the condition $m_{im} \le 2m_b$. The results in (j) display the quantity computed based upon (i) s.t,

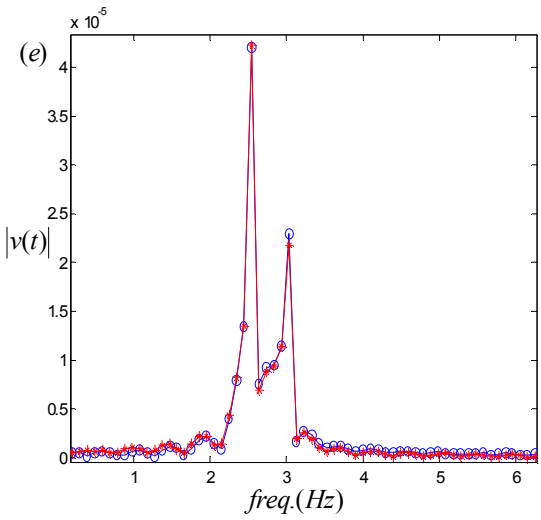
$$d = \left| 2\frac{\max_{T-t_a<t<T} \omega(t) - \min_{T-t_a<t<T} \omega(t)}{\max_{T-t_a<t<T} \omega(t) + \min_{T-t_a<t<T} \omega(t)} \right|$$

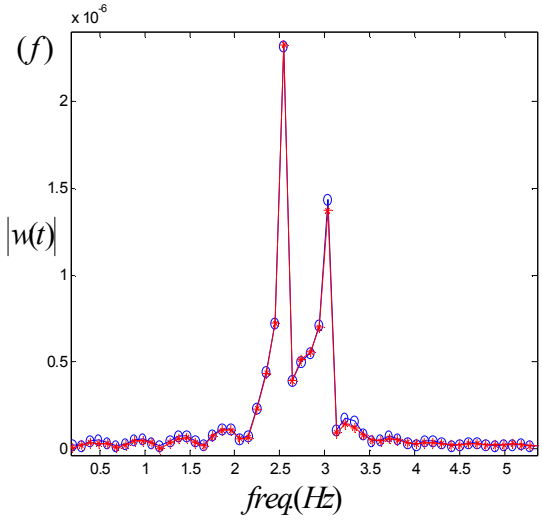
d is the relative fluctuating amplitude to the average ball speed. In (j), both $m_{im} = m_b$ and $m_{im} = 2m_b$ cases, d is below 6% in the most of $\overline{\Omega}$, which implies that the fluctuation effect is mostly negligible under the condition $m_{im} \le 2m_b$. With $m_{im} = 4m_b$, d is even below 6% in the supercritical operating speed. Using the average ball speed of **FS** for each $\overline{\Omega}$, (k),(l),(m) and (n) display the driving frequency $\omega + \Omega$ of $F_{ball}(\dot{\phi}, \phi, t)$ with $\varepsilon = 0.05,\ 0.3,\ 0.6,\ 0.82$. The results indicate that the driving frequencies are close to the system resonance which are described as dotted lines in (k),(l),(m) as well as (n) and obtained by computing the eigenvalues of $\begin{bmatrix} m & 0 \\ 0 & m \end{bmatrix}^{-1} \begin{bmatrix} K_{XX}(\varepsilon) & K_{XY}(\varepsilon) \\ K_{YX}(\varepsilon) & K_{YY}(\varepsilon) \end{bmatrix}$. Due to this property, the vibration amplitude driven by $\omega + \Omega$ in $F_{ball}(\dot{\phi}, \phi, t)$ far exceeds to one caused by $F_{im}(t)$ under the limit cycle. In other words, this inherent nature of driving frequency under limit cycle condition dominates the imbalance effect driven by Ω (i.e, $F_{im}(t)$) so that all results in Figure.3 are not heavily affected by imbalance size. However, as the operating speed is increased, the driving frequency is deviated from each dotted critical line. When the trajectory $\omega + \Omega$ stays away from the system resonance, the limit cycle condition can be destabilized because the simulation results in (k),(l), (m), and (n) represent the solution satisfying limit cycle condition $\omega \neq 0$ and the limit cycle condition becomes destabilized out of specified axis scope in (k),(l),(m) and (n). For an instance, in (k), the limit cycle condition exists until $\overline{\Omega} = 4.1$ and it is

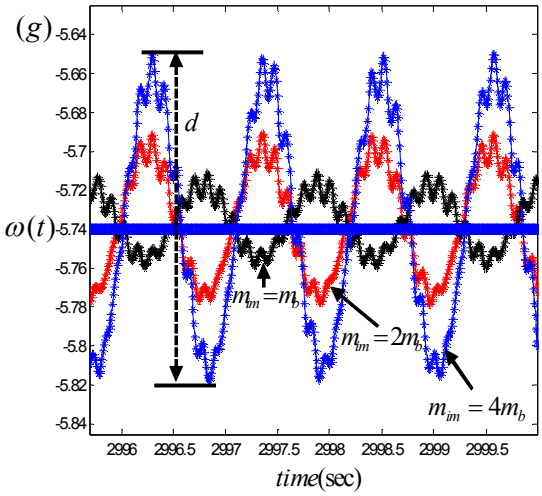
terminated under $\overline{\Omega} > 4.1$. This implies that the characteristic of limit cycle is changed when $\omega + \Omega$ escapes from the certain range of system resonance.

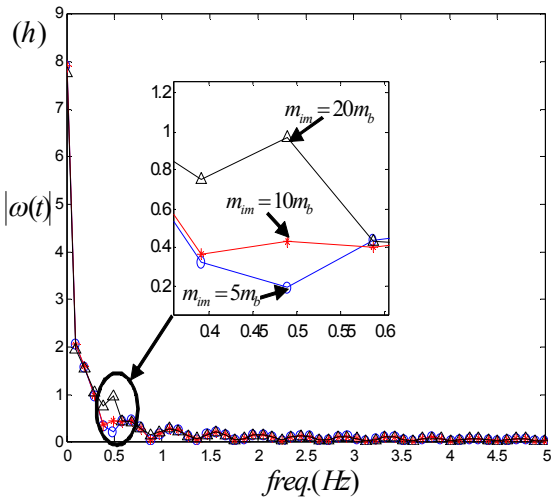
Under reasonable size of imbalance and the nature of limit cycle, all results presented in Figure.3 indicate us that the proposed harmonic solution is well approximated for capturing the essence of limit-cycle behavior in terms of both time and frequency domain.

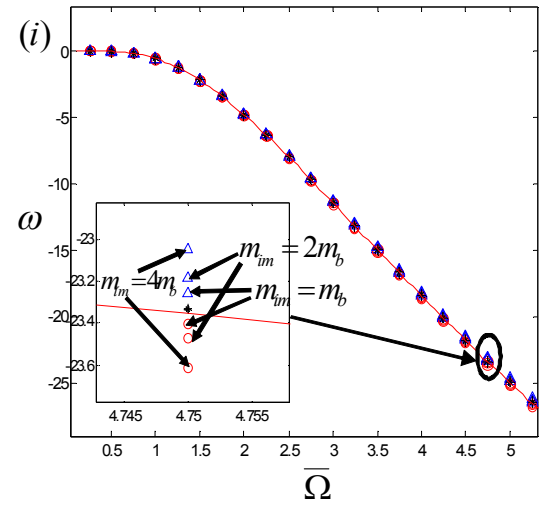


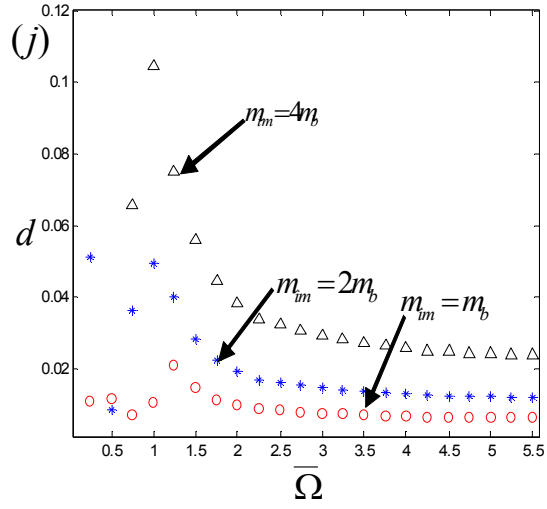

(e)
x 10^-5
|v(t)|
freq.(Hz)


(f)
x 10^-6
|w(t)|
freq.(Hz)


(g)
ω(t)
d
m_im = m_b
m_im = 2m_b
m_im = 4m_b
time(sec)


(h)
|ω(t)|
m_im = 20m_b
m_im = 10m_b
m_im = 5m_b
freq.(Hz)


(i)
ω
m_im = 2m_b
m_im = m_b
m_im = 4m_b
Ω̄


(j)
d
m_im = 4m_b
m_im = 2m_b
m_im = m_b
Ω̄

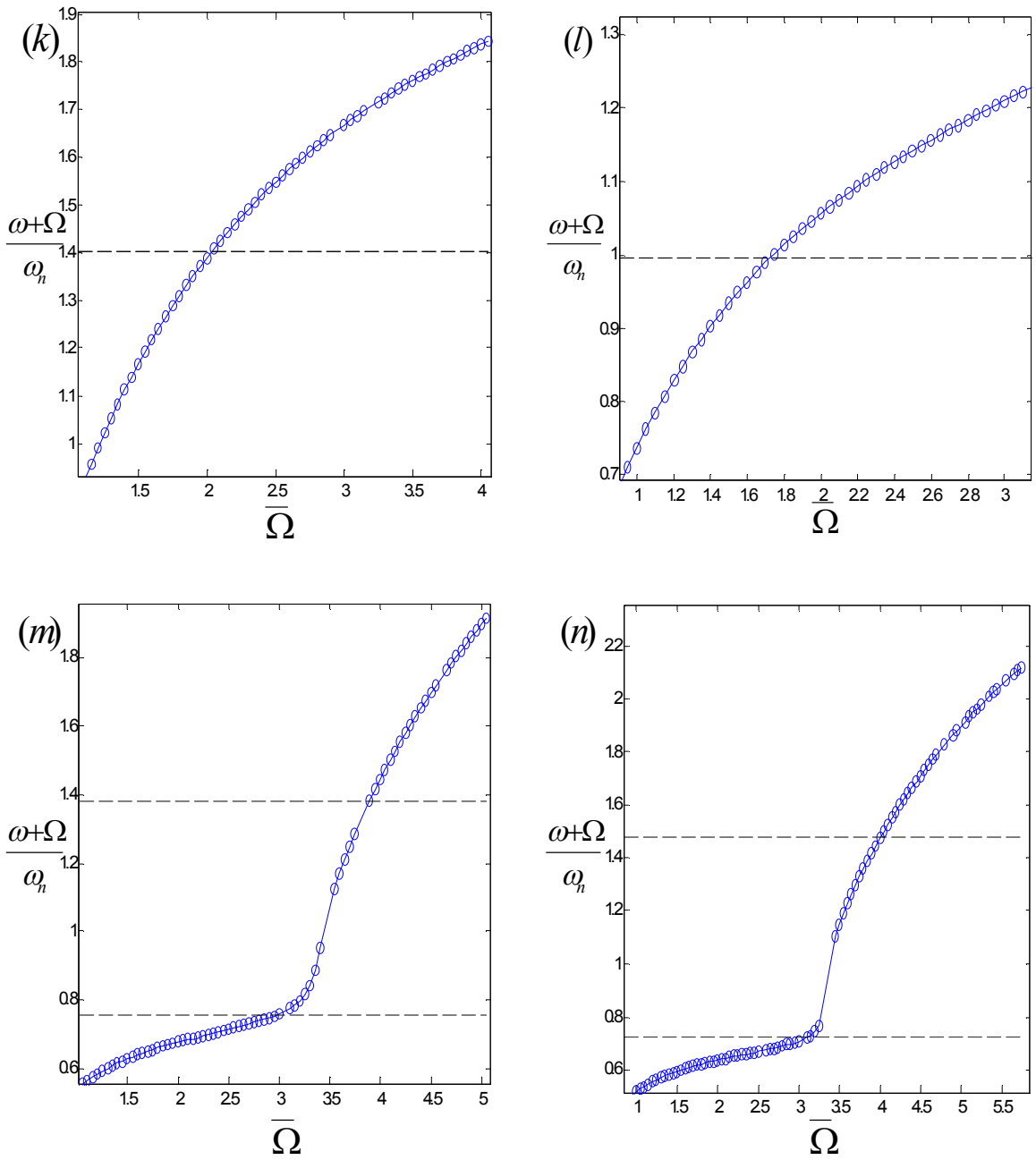


Figure.3.3. Comparison between full numerical solutions and assumed limit-cycle solutions((a)and (b) with $\overline{\Omega} = 2.5$ and $\varepsilon = 0.6$/ (c) with $\varepsilon = 0.82$/ (d) with $\varepsilon = 0.05$/ (e) and(f) with $\varepsilon = 0.3$/(g) with $\overline{\Omega} = 1.7$ and $\varepsilon = 0.7$ /(h) with $\overline{\Omega} = 2.2$ and $\varepsilon = 0.45$ /(i) and(j) with $\varepsilon = 0.75$ /(k) $\varepsilon = 0.05$ /(l) $\varepsilon = 0.3$ /(m) $\varepsilon = 0.6$ /(n) $\varepsilon = 0.82$)

Using the validated limit-cycle solution and FTM stability criterion, in Figure.3.4, the four stability contour plots($\overline{\Omega}$ *vs.*ε) are displayed with four different radial clearance of the bearing denoted as *c*

(*c=0.005*,*c=0.0025*,*c=0.00125*, and *c=0.000625*). The short notations **U**, **M**, **B**, **L**, and **B+L** in plots are followed and used throughout this paper, i) **U**: **M**, **B**, **L**, and **B+L** are unstable. ii) **M**: the only synchronous merged solution exists and is stable. iii) **B**: the only balanced solution exists and is stable. iv) **L**: the pure limit-cycle solution exists and is stable. v) **B+L**: both the balanced and limit cycle solution coexist and are stable, which is the unwanted coexistence zone.

As *c* is decreased, **B+L** area also become reduced and **B** region dominates the stability plot. Commonly, we can observe **M** at the low $\overline{\Omega}$ on each plot. The unwanted coexistence zones **B+L** is captured in the range of supercritical $\overline{\Omega}$ at the high ε in both cases *c=0.005* and *c=0.0025* while **B+L** is mostly eliminated in both cases *c=0.00125* and *c=0.000625*.

In $\varepsilon \le 0.1$, regardless of *c*, traveling on the contour plot in the manner that $\overline{\Omega}$ is increased(i.e, from the left to the right on each plot) enable us to undergo the bifurcation with two boundaries (i.e, **M** $\rightarrow$ **L** $\rightarrow$ **B**). In $0.1 < \varepsilon \le 0.7$, the bifurcation holding three boundaries is commonly shown s.t, **M** $\rightarrow$ **L** $\rightarrow$ **B+L** $\rightarrow$ **B**.

According to Figure.3.2, in $\varepsilon \le 0.5$, the stuffiness $\overline{K}_{XX}$ and $\overline{K}_{YY}$ are well balanced and the directions of $\overline{K}_{XY}$ and $\overline{K}_{YX}$ respectively hold the negative and positive ones which are the exactly opposite directions of destabilizing cross-coupling stiffness inducing forward whirl[11](In other words, the directions of $\overline{K}_{XY}$ and $\overline{K}_{YX}$ of this bearing assist the system stable). Thus, these two combinations suppress the unwanted behavior on the domain $\left\{(\overline{\Omega}, \varepsilon) \in \Re^2 \mid 2.5 < \overline{\Omega},\ \varepsilon \le 0.5\right\}$ as shown in the results(cases *c=0.005* and *c=0.0025*) of Figure.3.4. However, in $\varepsilon > 0.5$, the balance between $\overline{K}_{XX}$ and $\overline{K}_{YY}$ is deteriorated and the direction of $\overline{K}_{XY}$ becomes the positive which may cause instability of system hence the unwanted zones are illustrated in the range of supercritical $\overline{\Omega}$ at high ε.

Interestingly, in both cases *c=0.00125* and *c=0.000625*, unwanted coexistence zone is not exhibited in the supercritical operating speed under $\varepsilon > 0.5$. This implies that the damping of bearing reach sufficient level to destabilize the limit cycle with smaller *c* since the damping is inversely proportional to *c*. As seen in Figure.3.4, the unwanted coexistence zone **B+L** exists regardless of *c* and the characteristic of bearing and the range of system operating speed play the central role to control this unwanted condition.

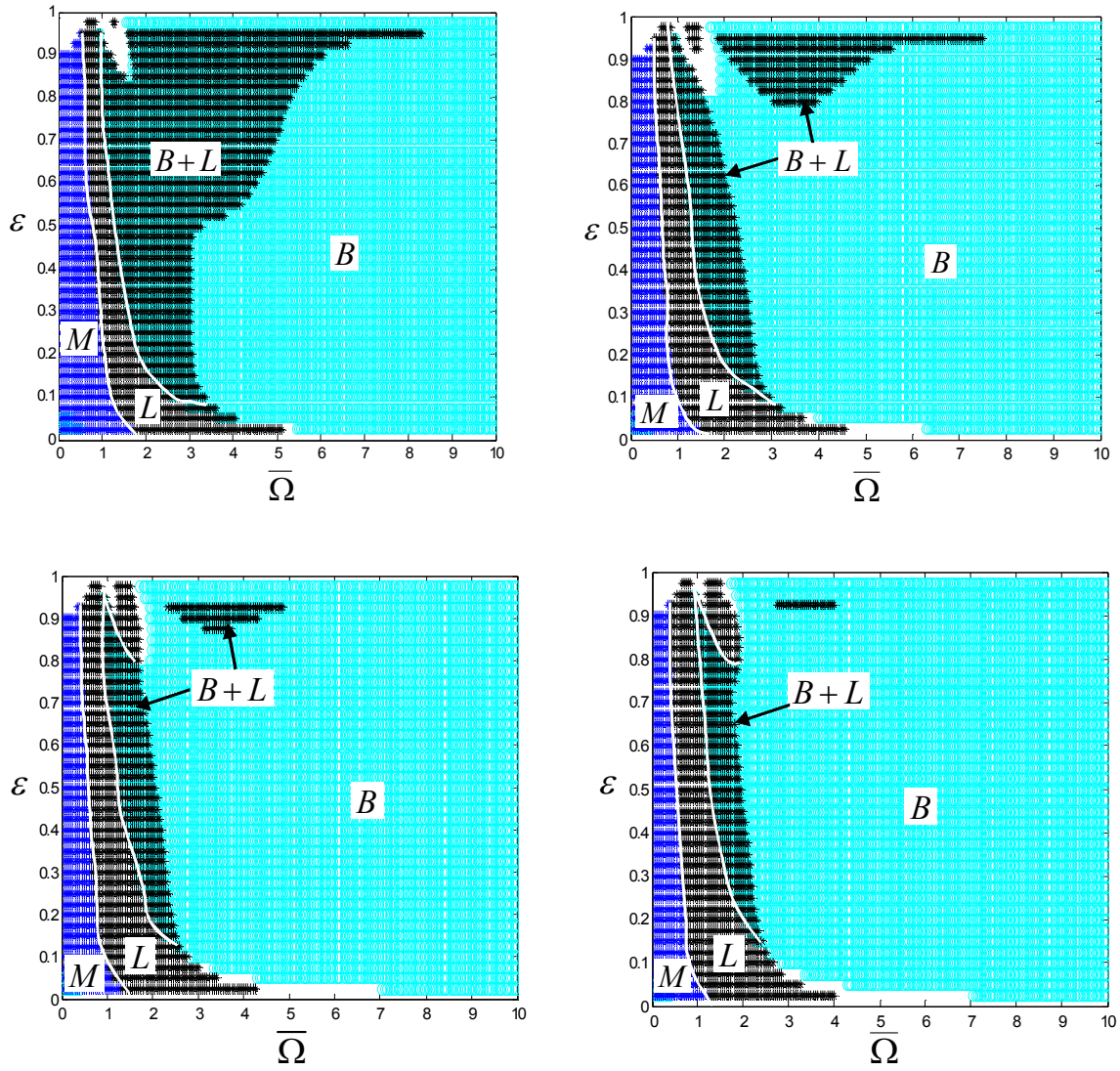


Figure.3.4. Stability contour plots ($\overline{\Omega}$ *vs.*ε) for the short journal bearing (two plots in the first row(left to right) for *c=0.005* and *c=0.0025*and two plots in the second row(left to right) for *c=0.00125* and *c=0.000625*/$2m_b = m_{im}$ is used).

3.4.2 Rotor/ABD with Tilting-Pad Bearing

The approximate expression for the dimensionless stiffness and damping coefficients for the tilt-pad bearing with five pads(60 arc)[20] are given by

$$
\begin{aligned}
\overline{K}_{XX} &= \begin{cases} 4.01e^{-3.84\varepsilon} & \varepsilon > 0.3 \\ 2.01 - 2.24\varepsilon & \varepsilon \le 0.3 \end{cases} \\
\overline{K}_{YY} &= 1.67e^{2.47\varepsilon} \\
\overline{C}_{XX} &= \begin{cases} 13.5(1-\varepsilon)^{2.11} & \varepsilon > 0.3 \\ 35.0e^{-6.34\varepsilon} & \varepsilon \le 0.3 \end{cases} \\
\overline{C}_{YY} &= 30 - 83.2\varepsilon + 76.4\varepsilon^2 \\
\overline{C}_{XY} &= \overline{C}_{YX} = \overline{K}_{XY} = \overline{K}_{YX} = 0
\end{aligned}
\tag{3-24}
$$

As mentioned earlier and shown in (3-24), this type of bearing has no cross-coupling force to be produced via the fluid force inside bearing journal. Technically, there exist cross-coupling forces but they are almost negligible in practice. Enhancing us to understand of the traits of this bearing, the curves for dimensionless coefficients are plotted in Figure.3.5. The conversion of physical coefficients is recovered by the relations used in the previous section.

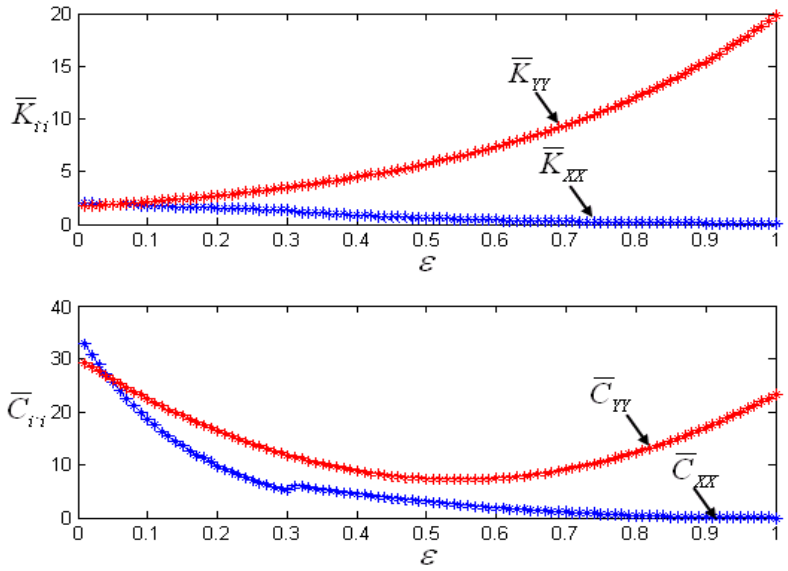
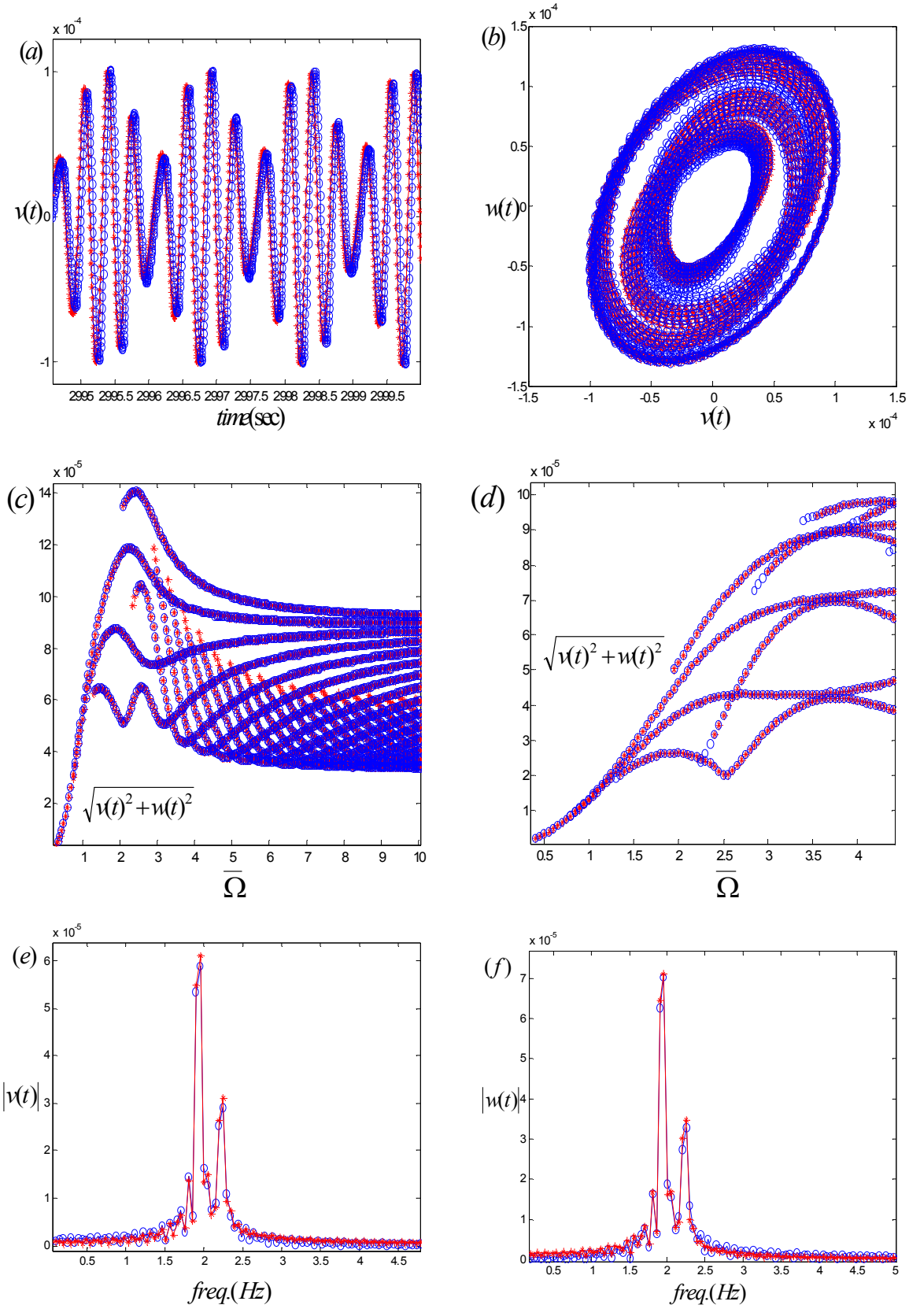
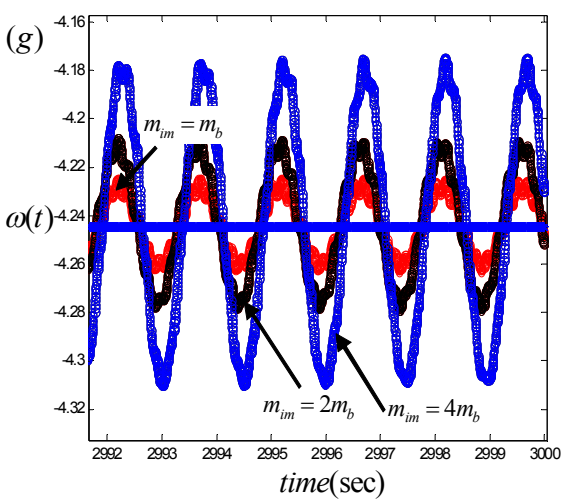


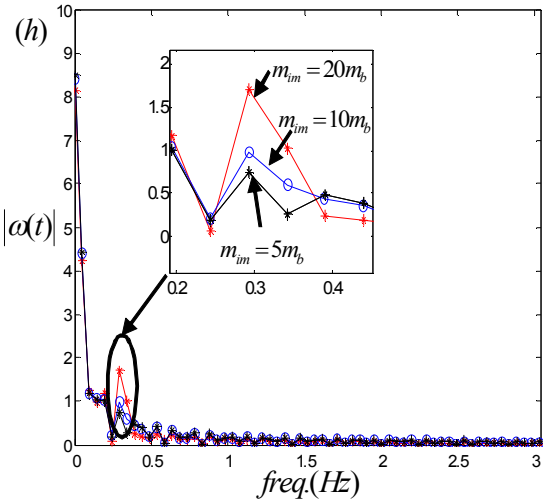
Figure.3.5 Characteristic of dimensionless bearing coefficients for the tilting bearing with five pads

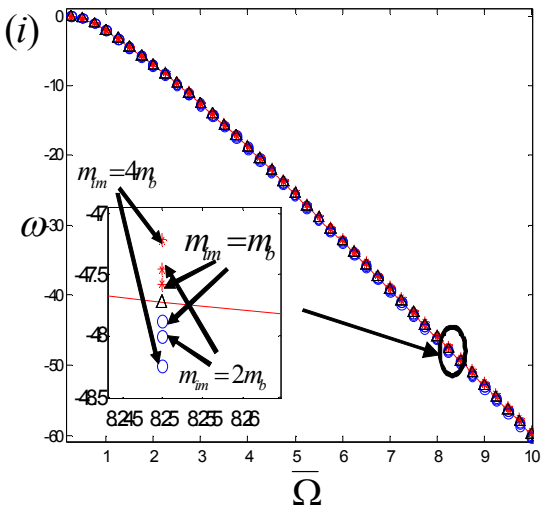
Similarly, by substituting (3-24) into (3-16) and (3-17), we also validate the limit-cycle solution(**LC**) with numerical results(**FS**). In (a) and (b) of Figure.6, the star-dotted lines represent the time domain response and whirl orbit simulated via **FS**, while the circle-dotted lines do the assumed **LC** in (3-11). The whirl orbit in (b) is also the elliptical form due to the asymmetric property. In (c) and (d), the local extremums of system are illustrated at each operating speed with $\varepsilon = 0.45$ and $\varepsilon = 0.1$. The star dots and circle dots

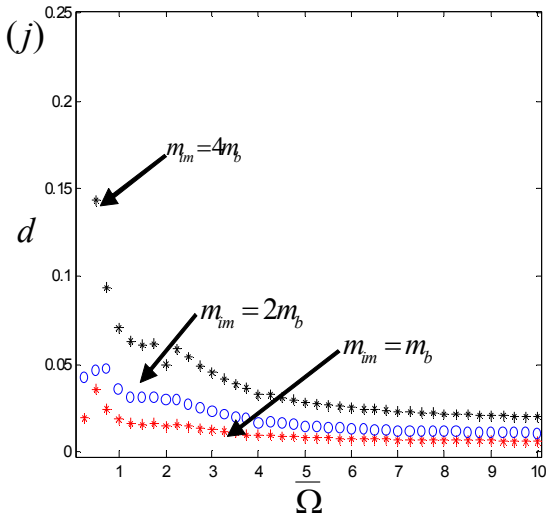
represent **FS** and **LC** respectively. In (e) and (f) of Figure.3.6, the power spectrums of **LC**(shown as the circle-dotted line) and **FS**(shown as the star-dotted line) are presented. The exciting frequency via an imbalance effect is 2.3 *Hz* while the merged ball running frequency is 1.9 *Hz*. In (g), the straight lines are the merged ABD's ball speeds of **LC** relative to the rotating frame and the three star-dotted fluctuating lines are the outcomes from **FS** at given three imbalance mass magnitudes. As the imbalance masses increase, the amplitudes become larger as seen in the results in the previous subsection. In (h), the power spectrums of ball speed simulated via **FS** are shown with different imbalance sizes and, with conditions $m_{im} = 5m_b$, there are no significant frequencies but ones near zero, which implies that its property is very similar to constant signal's one. However, we can observe that there exists a significant frequency near 0.3 *Hz* for both $m_{im} = 10m_b$ and $m_{im} = 20m_b$. Again, this result also supports that the limit-cycle ball speed can be assumed to be constant under allowable size of imbalance mass. Additionally, from (i), one can see that the constant ball speed(displayed as straight line) of **LC** can capture the average of the numerical one in **FS**(depicted as triangular-dotted line) collected for a certain simulation period at each operating speed. Three pairs of triangular and circle dots in (i) represent the minimum and maximum ball speed obtained through **FS**. Again, the difference between minimum and maximum amplitude of ball speed becomes increased with larger imbalance effect and high operating speed. In (j), with $m_{im} = m_b$ and $m_{im} = 2m_b$ case, d is below 5 % in the most of operating speed, which implies that the fluctuation effect appeared on the actual ball speed of **FS** is not great under the condition $m_{im} < 2m_b$. However, the result is also showing that the fluctuation effect can be increased with large imbalance effect. Using the average ball speed of **FS** for each operating speed, (k),(l),(m) and (n) display the driving frequency $\omega + \Omega$ of $F_{ball}(\dot{\phi}, \phi, t)$ with $\varepsilon = 0.15,\ 0.35,\ 0.5,\ 0.6$. The results indicate that the driving frequency $\omega + \Omega$ is near the system resonances which are depicted as the dotted lines in (k),(l),(m) as well as (n) and obtained by using the eigenvalues of $\begin{bmatrix} m & 0 \\ 0 & m \end{bmatrix}^{-1} \begin{bmatrix} K_{XX}(\varepsilon) & 0 \\ 0 & K_{YY}(\varepsilon) \end{bmatrix}$. Again, the running ball frequency is approximated by the system resonances at given supercritical operating speeds so that all results in Figure.6 are not heavily affected by imbalance size. Except the result in (k), the trajectories of $\omega + \Omega$ in (l),(m) and (n) approach to the system resonance as the operating speed increases. Although the limit cycle solution exist after $\overline{\Omega} = 10$ in (l),(m) and (n), the plots display only the results up to $\overline{\Omega} = 10$ by limiting the focused operating speed range. However, the limit cycle solution does not exist after $\overline{\Omega} = 5.9$ in (k). This also shows us that the limit cycle become destabilized when $\omega + \Omega$ stays away from the system resonance. With reasonable assumption, all results presented in Figure.6 still indicate us that the proposed harmonic solution is accurate enough to capture the limit-cycle behavior of system with this tilting pad bearing.

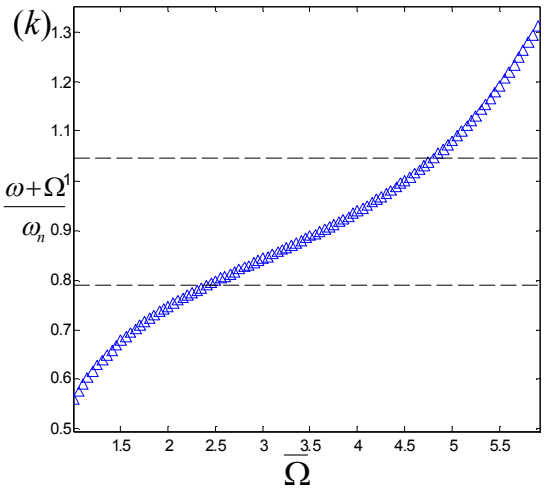

(a)
x 10^-4
v(t)
time(sec)
(b)
x 10^-4
w(t)
v(t)
x 10^-4
(c)
x 10^-5
√(v(t)^2+w(t)^2)
Ω̄
(d)
x 10^-5
√(v(t)^2+w(t)^2)
Ω̄
(e)
x 10^-5
|v(t)|
freq.(Hz)
(f)
x 10^-5
|w(t)|
freq.(Hz)

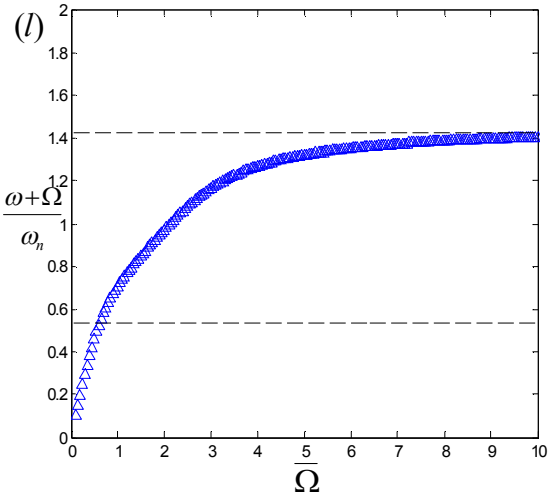

(g)
$m_{im}=m_b$
$\omega(t)$
$m_{im}=2m_b$
$m_{im}=4m_b$
time(sec)


(h)
$m_{im}=20m_b$
$m_{im}=10m_b$
$m_{im}=5m_b$
$|\omega(t)|$
freq.(Hz)


(i)
$m_{im}=4m_b$
$m_{im}=m_b$
$m_{im}=2m_b$
ω
Ω


(j)
$m_{im}=4m_b$
$m_{im}=2m_b$
$m_{im}=m_b$
d
Ω


(k)
$\frac{\omega+\Omega}{\omega_n}$
Ω


(l)
$\frac{\omega+\Omega}{\omega_n}$
Ω

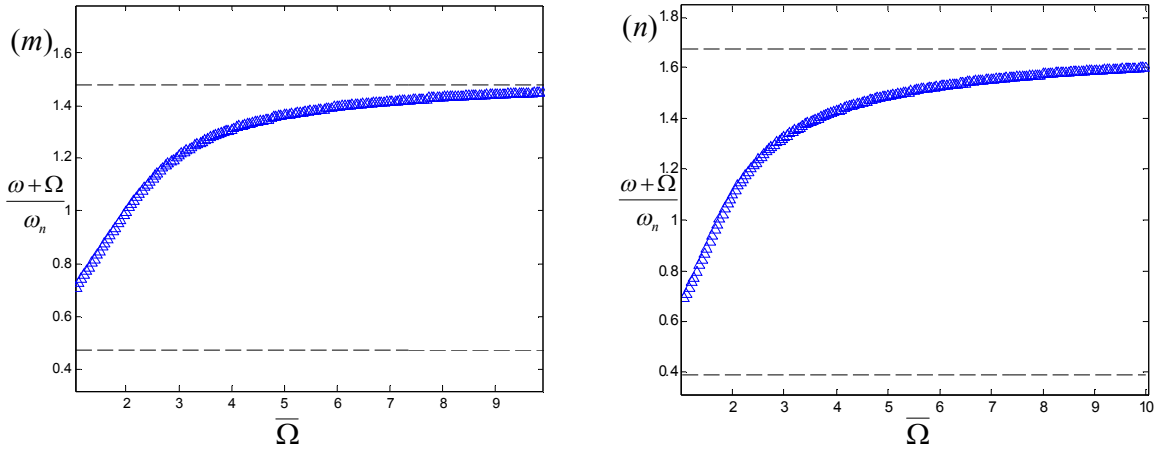


Figure.3.6. Comparison between full numerical solutions and assumed limit-cycle solutions((a) and (b) with $\overline{\Omega}=2.5$ and $\varepsilon=0.4$ / (c) with $\varepsilon=0.45$ / (d) with $\varepsilon=0.1$ / (e) and (f) with $\varepsilon=0.3$ /(g) with $\overline{\Omega}=1.5$ and $\varepsilon=0.75$ /(h) with $\overline{\Omega}=2.2$and $\varepsilon=0.85$ /(i) and(j) with $\varepsilon=0.4$ /(k) $\varepsilon=0.15$ /(l) $\varepsilon=0.35$ /(m) $\varepsilon=0.5$ /(n) $\varepsilon=0.6$))

Similarly, in Figure.3.7, the four stability contour plots($\overline{\Omega}$ *vs.*ε) are illustrated according to four different c. Also, as c is decreased, **B+L** area also become less dominant and **B** region is throughout expanded. Interestingly, the unstable region **U** exists in the middle of each plot and this region tend to be enlarged as c become smaller. This phenomenon is caused by the strong asymmetric property of bearing in high ε as seen in Figure.3.5. Also, **M** zone is decreased and **L** is increased as c is reduced.

In the low ε, marching on the contour plot in the manner that $\overline{\Omega}$ is increased (i.e, from the left to the right on each plot) enable us to recognize the bifurcation holding three boundaries(i.e, **M**$\rightarrow$**L**$\rightarrow$**B+L**$\rightarrow$**B**) on every plot. In the high ε, the bifurcation of four boundaries is commonly observed s.t, **M**$\rightarrow$**B+L** $\rightarrow$**B**$\rightarrow$**U**$\rightarrow$**B** for every c. For both *c=0.005* and *c=0.0025* cases, two bifurcations are displayed **M**$\rightarrow$**L**$\rightarrow$**B+L** (two boundaries) and **M**$\rightarrow$**B+L**$\rightarrow$**L**$\rightarrow$**U**$\rightarrow$**L**$\rightarrow$**B+L** (five boundaries) in the middle range of ε. For *c=0.00125*, the bifurcation of four boundaries is shown **M**$\rightarrow$**L**$\rightarrow$**B+L**$\rightarrow$**U**$\rightarrow$**B+L** in the middle range of ε while **M**$\rightarrow$**L**$\rightarrow$**B+L**$\rightarrow$**U**$\rightarrow$**B** (four boundaries) is shown for *c=0.000625*.

According to Figure.3.5, the both *v(t)* and *w(t)* direction of stiffness and damping force are well balanced in the low ε so that the unwanted **B+L** in the supercritical speed becomes less dominant in each plot of Figure.3.7, regardless of clearance magnitude. In the contrast, in $\varepsilon>0.3$, both direction forces are strongly asymmetric as seen in Figure.3.5. Thus, the unwanted zone becomes dominant at supercritical operating speeds. Although the performance of the bearing is varied by the clearance(c), the allowable capacity of bearing to avoid both unstable zone and limit-cycle including coexistence region in the supercritical

operating speed is commonly limited approximately in $\varepsilon < 0.15$ for high c and $\varepsilon = 0.4$ for low c, respectively.

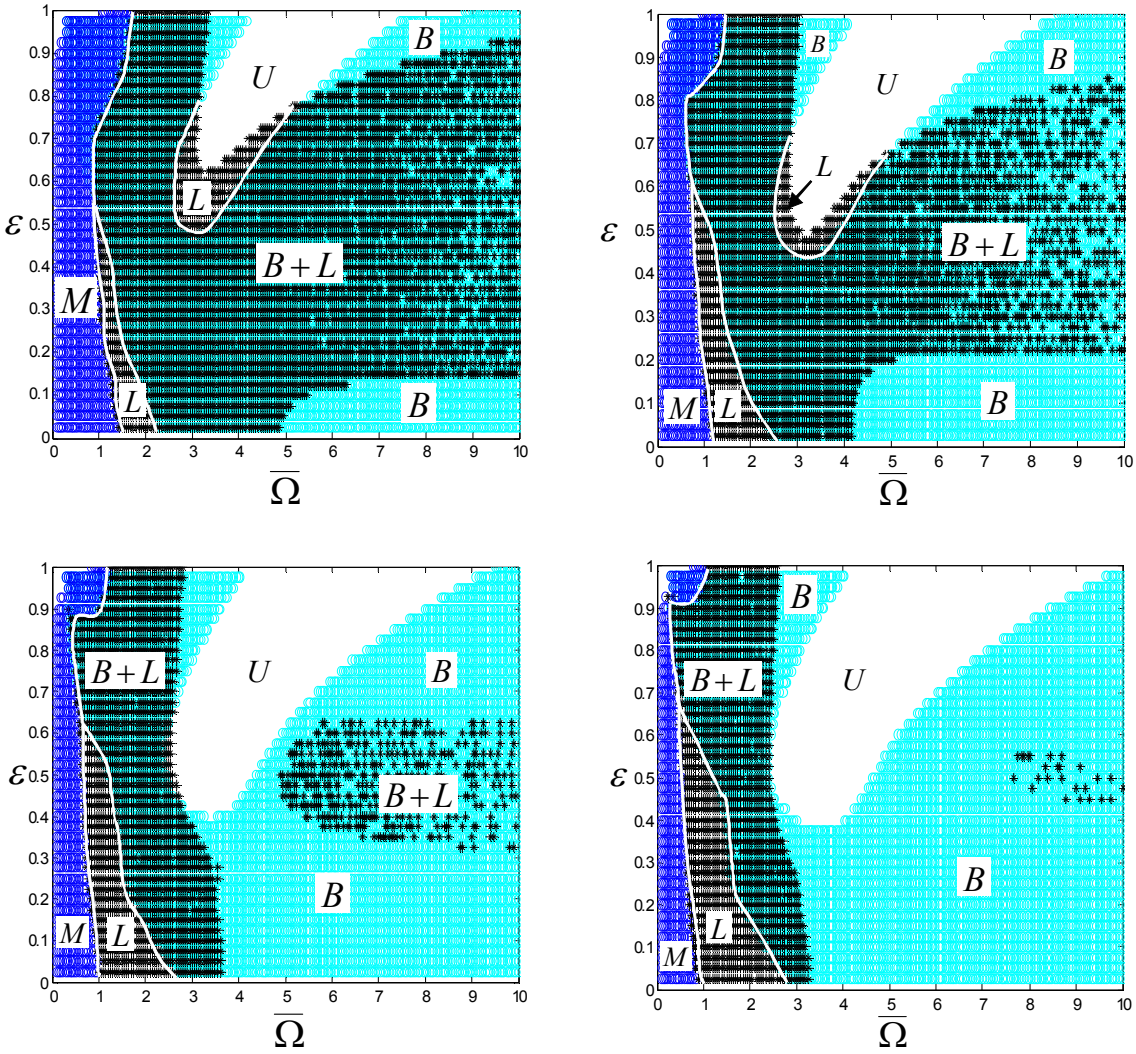


Figure.3.7 Stability contour plots ($\overline{\Omega}$ *vs.*ε)for the tilting pad bearing(two plots in the first row(left to right) for *c=0.005* and *c=0.0025*and two plots in the second row(left to right) for *c=0.00125* and *c=0.000625*/$2m_b = m_{im}$ is used).

3.5 Concluding Remarks

With several reasonable assumptions, this chapter provides the harmonic limit-cycle solution of automatic balancing device for imbalanced rotor system interacting with two widely-used hydrodynamic bearings. The solution is validated with the time and frequency domain numerical simulation and then, using the perturbed system about the solutions, the system stability is assessed by FTM method.

Noticeably, this study utilizes the characteristic curves of two actual hydrodynamic bearings obtained from [18] through [20]. Thus, the use of actual bearing property enables us to achieve more realistic and precise study for the limit-cycle as well as the balanced behavior occurred in the rotor system equipped with ABD compared to the existing studies with ideal symmetric bearing. According to the results of two hydrodynamic bearings, one can see that the several bifurcation boundaries can be founded and are determined by the variation of bearing parameters. In the case of the short journal bearing, as the radial clearance is decreased, the region of limit-cycle on the stability contour plot has been substantially reduced and the best performance of the bearing was achieved in the low scale of eccentricity. For the tilting pad bearing, although the limit-cycle behavior can be prevented at the supercritical operating speeds by decreasing the radial clearance, the unstable zone is also extended in the middle and high scale of bearing eccentricity. Also, regardless of the radial clearance, the capacity of this bearing is well defined in low eccentricity. Through the results computed in this paper, approximately, we will be able to predict and assess this unwanted limit-cycle behavior which might be generated from the system operating with similar type of hydrodynamic bearings presented here and provide the insight and direction of future research associated with the related topics. Additionally, this paper reveals that the inherent nature of limit cycle induces the condition of system resonance. The limitation of solution has been also addressed. The accuracy of solution can’t be ensured under large imbalance effect. However, the analysis and solution presented here are still enough accurate to capture the essence of limit cycle behavior under allowable size of imbalance.

CHAPTER IV
HYBRID ADAPTIVE ROTOR IMBALANCE VIBRATION CONTROL VIA PASSIVE AUTOBALANCER AND ACTIVE BEARING ACTUATION

4.1 Rotor/Autobalancer/Active bearing System

In this chapter, we present the mathematical model of the rigid planar rotor system in conjunction with auto-balancing device (ABD) supported by an active magnetic bearing (AMB). Here, expressing the equations-of-motion with respect to the fixed frame $\{X\ Y\ Z\}$ provides us the nonlinear time-varying equation which may be dealt with in some extents of complexity for further analysis.

Therefore, in order to avoid time-varying terms at least, the equations-of-motion are derived in the rotating-frame $\{x\ y\ z\}$ synchronous with the rotor rotating in a constant speed Ω by assuming that AMB serves as a symmetric bearing support. The ABD containing two balancer balls is utilized for this study. The system and the forces induced by AMB are detailed in Figure.1. Two different forces of AMB are specified. One is the offset damping (induced by damping gain C_f) and stiffness (induced by stiffness gain K_f) forces to maintain the clearance between a shaft and coils, which are symmetrically provided in both horizontal and vertical direction. These damping and stiffness force act as the passive bearing. Another is an active force(f_{con}) switched on and off in necessity during operation, which ensures the system stability under the action of ABD for various operating conditions.

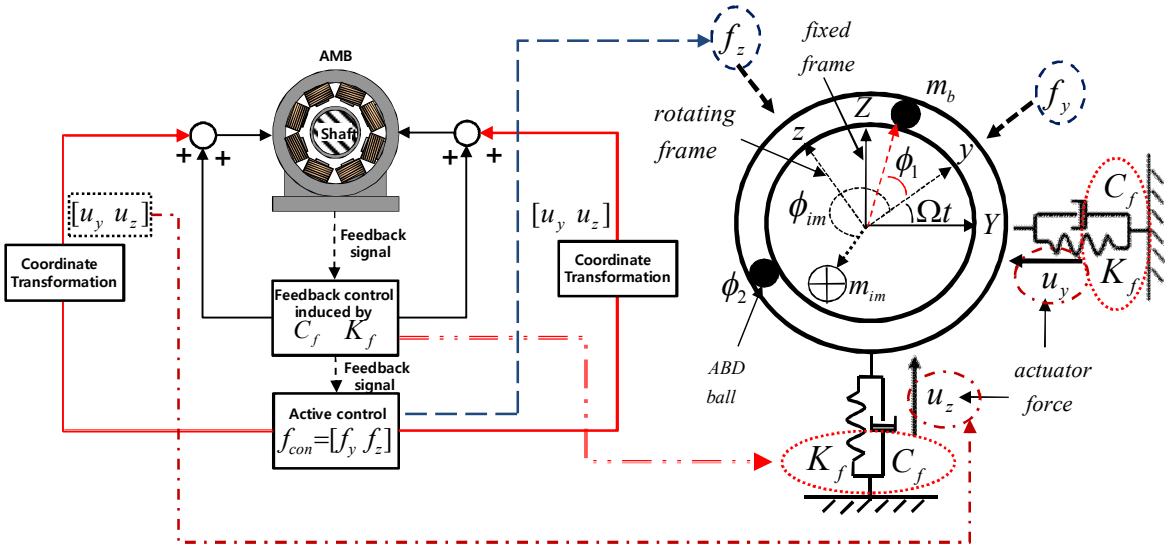


Figure.4.1. Rigid planar imbalanced rotor system with auto-balancing device and active bearing actuators.

Defining the states of system as the horizontal displacement, vertical displacement, and the angular position of two balls on ABD s.t, $q=[y\ z\ \phi_1\ \phi_2]^T \in \Re^4$ relative to the rotating frame, the equation of motion is given by,

$$M(\phi_i)\ddot{q} + C(\dot{\phi}_i,\phi_i)\dot{q} + K(\phi_i)q = f_{im} + f_{ball}(\dot{\phi}_i,\phi_i) + Bf_{con}. \tag{4-1}$$

where, $M(\phi_i)\in\Re^{4\times4}$, $C(\dot{\phi}_i,\phi_i)\in\Re^{4\times4}$,and $K(\phi_i)\in\Re^{4\times4}$ are the mass, damping, and stiffness matrices of whole system. Also, $f_{im}\in\Re^4$, $f_{ball}(\dot{\phi}_i,\phi_i)\in\Re^4$,and $f_{con}\in\Re^2$ are the imbalance force, the force transmitted by balls on ABD, and the active control force, respectively.

The mass, damping, and stiffness matrices of the system are provided by,

$$M(\phi_i)=\begin{bmatrix} m+2m_b & 0 & -m_b r_b\sin(\phi_1) & -m_b r_b\sin(\phi_2) \\ 0 & m+2m_b & m_b r_b\cos(\phi_1) & m_b r_b\cos(\phi_2) \\ -m_b r_b\sin(\phi_1) & m_b r_b\cos(\phi_1) & m_b {r_b}^2 & 0 \\ -m_b r_b\sin(\phi_2) & m_b r_b\cos(\phi_2) & 0 & m_b {r_b}^2 \end{bmatrix} \tag{4-2}$$

$$C(\dot{\phi}_i,\phi_i)=\begin{bmatrix} C_f & -2(m+2m_b)\Omega & -2m_b r_b\Omega\cos(\phi_1) & -2m_b r_b\Omega\cos(\phi_2) \\ 2(m+2m_b)\Omega & C_f & -2m_b r_b\Omega\sin(\phi_1) & -2m_b r_b\Omega\sin(\phi_2) \\ 2m_b r_b\Omega\cos(\phi_1) & 2m_b r_b\Omega\sin(\phi_1) & c_b {r_b}^2 & 0 \\ 2m_b r_b\Omega\cos(\phi_2) & 2m_b r_b\Omega\sin(\phi_2) & 0 & c_b {r_b}^2 \end{bmatrix} \tag{4-3}$$

$$K(\phi_i)=\begin{bmatrix} K_f-(m+2m_b)\Omega^2 & -C_f\Omega & 0 & 0 \\ C_f\Omega & K_f-(m+2m_b)\Omega^2 & 0 & 0 \\ m_b r_b\Omega^2\sin(\phi_1) & -m_b r_b\Omega^2\cos(\phi_1) & 0 & 0 \\ m_b r_b\Omega^2\sin(\phi_2) & -m_b r_b\Omega^2\cos(\phi_2) & 0 & 0 \end{bmatrix} \tag{4-4}$$

where, m and m_b are the mass of the rotor system and an ABD-ball, respectively. As mention earlier, C_f and K_f are the offset damping and stiffness gains of the feedback in AMB, which are embedded into matrices (4-3) and (4-4). c_b and r_b are the ball damping coefficient and the radius of ABD ball race track. Also, the detail of imbalance static force and the force caused by ABD are given by,

$$f_{im}=\begin{bmatrix} m_{im}r_{im}\Omega^2\cos(\phi_{im}) \\ m_{im}r_{im}\Omega^2\sin(\phi_{im}) \\ 0 \\ 0 \end{bmatrix} \qquad f_{ball}=\begin{bmatrix} m_b r_b\sum_{i=1}^{2}\cos(\phi_i)(\Omega^2+\dot{\phi}_i^2) \\ m_b r_b\sum_{i=1}^{2}\sin(\phi_i)(\Omega^2+\dot{\phi}_i^2) \\ 0 \\ 0 \end{bmatrix} \tag{4-5}$$

where, m_{im}, r_{im} and ϕ_{im} are the imbalance mass, the radial location of the mass, and its phase. The active control force with respect to the rotating frame becomes,

$$f_{con}=[f_y \quad f_z]^T \qquad B=\begin{bmatrix} 1 & 0 & 0 & 0 \\ 0 & 1 & 0 & 0 \end{bmatrix}^T \tag{4-6}$$

It should be noted that an active control force f_{con} excludes the force generated by C_f and K_f as shown

in Figure.4.1. In the implementation stage of the control law, the control force captured with respect to the rotating frame should be transformed s.t,

$$\begin{bmatrix} u_y \\ u_z \end{bmatrix} = \begin{bmatrix} \cos(\Omega t) & -\sin(\Omega t) \\ \sin(\Omega t) & \cos(\Omega t) \end{bmatrix} \begin{bmatrix} f_y \\ f_z \end{bmatrix} \tag{4-7}$$

where, $[u_y \;\; u_z]^T$ represents the actuator (control) force relative to the fixed frame. In this study, we focus on the design of the control force f_{con} relative to the rotating coordinates. The subsequent computations and results are specified in terms of the rotating frame.

4.2 Controllability of System

In this section, we investigate the controllability of system. According to the existing researches [9, 10], they demonstrated that an active magnetic bearing successfully achieved to cancel the high vibration of imbalance rotary machinery. The system presented here is equipped with an augmented ABD system which generates the change of mass distribution on the system. Therefore, it is meaningful for us to examine that the AMB force is capable of controlling the balls running on ABD race track. Since the limit-cycles condition(i.e, non-synchronous behavior) is the critical issue of ABD, the study of system controllability is an essential process for further analysis of control design. Since the system is nonlinear one due to ABD, to investigate the controllability of nonlinear system, Lie bracket operation is used. Thus, before proceeding, the definition of Lie bracket operation is introduced.

Definition of Lie bracket operation[12]: consider two smooth vector fields s.t $f(x)$ and $g(x)$ in $\Re^n$ and then, the Lie bracket operation generates a new vector field.

$$[f(x), g(x)] \equiv \frac{\partial g(x)}{\partial x} f(x) - \frac{\partial f(x)}{\partial x} g(x) \tag{4-8}$$

Additionally, we can define higher order Lie bracket. For simplicity, we drop the term (x).

$$(ad_f^{\,1}, g) = [f, g],\ (ad_f^{\,2}, g) = [f, [f, g]], \cdots,\ (ad_f^{\,k}, g) = [f, (ad^{k-1}, g)] \tag{4-9}$$

where *ad* stands for "adjoint".

Theorem [25] states that the given nonlinear system s.t $\dot{x} = f(x) + \sum_{i=1}^{m} g_i(x) u_i$ is locally accessible (controllable) about $x_0 \in \Re^n$ if the accessibility distribution C spans n space, where n is the rank of x and C is defined by,

$$C = [g_1, g_2, \cdots, g_m, [g_i, g_j], \cdots (ad_{g_i}^{\,k}, g_j), [f, g], (ad_f^{\,2}, g), \cdots, (ad_f^{\,k}, g)] \tag{4-10}$$

From the original nonlinear dynamics of the system in (4-1),

$$\ddot{q} = -M^{-1}(\phi_i)[C(\dot{\phi}_i, \phi_i)\dot{q} + K(\phi_i)q] + M^{-1}(\phi_i)[f_{im} + f_{ball}(\phi_i)] + M^{-1}(\phi_i) B f_{con} \tag{4-11}$$

Dropping term (ϕ_i) for simplicity, we can place (4-11) into the following format,

$$\begin{bmatrix}\dot{q}\\ \ddot{q}\end{bmatrix}=\begin{bmatrix}0 & I_4\\ -M^{-1}K & -M^{-1}C\end{bmatrix}\begin{bmatrix}q\\ \dot{q}\end{bmatrix}+\begin{bmatrix}0\\ M^{-1}[f_{im}+f_{ball}]\end{bmatrix}+\begin{bmatrix}0\\ M^{-1}B\end{bmatrix}f_{con} \tag{4-12}$$

where, M^{-1} are an inverse matrix of $M(\phi_i)$ and I_n is n by n identity matrix. Next, let $x=[q \quad \dot{q}]^T \in \Re^8$ and then the general expression of the nonlinear equation of (4-12) is given by,

$$\dot{x}=f(x)+g(x)u \tag{4-13-a}$$

where,

$$f(x)=\begin{bmatrix}0 & I_4\\ -M^{-1}K & -M^{-1}C\end{bmatrix}\begin{bmatrix}q\\ \dot{q}\end{bmatrix}+\begin{bmatrix}0\\ M^{-1}[f_{im}+f_{ball}]\end{bmatrix} \tag{4-13-b}$$

and,

$$g(x)u=\begin{bmatrix}0 & M^{-1}B\end{bmatrix}^T f_{con}=\begin{bmatrix}0 & M^{-1}B\end{bmatrix}^T\begin{bmatrix}f_y & f_z\end{bmatrix}^T \tag{4-13-c}$$

In (4-13-c), the independent vector fields $M^{-1}B \in \Re^{2\times4}$ can generate new four independent forces s.t,

$$\begin{bmatrix}M^{-1}B\end{bmatrix}^T\begin{bmatrix}f_y\\ f_z\end{bmatrix}=[\,f_{new.y} \;\; f_{new.z} \;\; f_{new.\phi_1} \;\; f_{new.\phi_2}\,]^T \tag{4-14}$$

Thus, we have (4-15) which is another form of (4-13-c) ,

$$[0 \quad M^{-1}B]^T\begin{bmatrix}f_y\\ f_z\end{bmatrix}=[0\ I_4]^T\begin{bmatrix}f_{new.y}\\ f_{new.z}\\ f_{new.\phi_1}\\ f_{new.\phi_2}\end{bmatrix} \tag{4-15}$$

With (4-15), we can reformulate (4-13) s.t,

$$\dot{x}=f(x)+g_{new1}f_{newy}+g_{new2}f_{newz}+g_{new3}f_{new\phi1}+g_{new4}f_{new\phi2} \tag{4-16-a}$$

where,

$$g_{new.1}=[0\,0\,0\,0\,1\,0\,0\,0]^T, \qquad g_{new.2}=[0\,0\,0\,0\,0\,1\,0\,0]^T \tag{4-16-b}$$

$$g_{new.3}=[0\,0\,0\,0\,0\,0\,1\,0]^T, \qquad g_{new.4}=[0\,0\,0\,0\,0\,0\,0\,1]^T \tag{4-16-c}$$

By performing the Lie bracket operation with (4-16), we can generate eight vector fields s.t,

$$C=[g_{new1},[f,g_{new1}],g_{new2},[f,g_{new2}],g_{new3},[f,g_{new3}],g_{new4},[f,g_{new4}]] \tag{4-17}$$

The rank of distribution C is 8 which is equal to the number of system state x because the determination of C is 1 regardless of x. Thus, the system is locally accessible (controllable) everywhere according to the Theorem. This result supports that the actuator force is able to manipulate the state of two balls on ABD

including the motion of imbalance rotor. The detail of (4-17) is provided in Appendix.

4.3 Adaptive Control law Development

In this section, the Lyapunov-based adaptive control law to minimize the system vibration level and ensure the system stability is introduced in the presence of unknown parameters for two cases a) without ABD and b) with the action of ABD. The case a) is presented to compare the performance of case b) in terms of the control power consumption and the control law associated with case a) might useful for one who wishes to suppress the imbalance vibration through a pure active control strategy.

First, we consider the design of control law for case a) and, with the coordinates $q_r = [y \quad z]^T$, the dynamic of system without ABD is simply given by,

$$M_r \ddot{q}_r + C_r \dot{q}_r + K_r q_r = f_{im.r} + f_{con} \tag{4-18}$$

where, $M_r = \begin{bmatrix} m+2m_b & 0 \\ 0 & m+2m_b \end{bmatrix} \in \Re^{2\times 2}, C_r = \begin{bmatrix} C_f & -2(m+2m_b)\Omega \\ 2(m+2m_b)\Omega & C_f \end{bmatrix} \in \Re^{2\times 2}$, and

$K_r = \begin{bmatrix} K_f - (m+2m_b)\Omega^2 & -C_f\Omega \\ C_f\Omega & K_f - (m+2m_b)\Omega^2 \end{bmatrix} \in \Re^{2\times 2}$ are the mass, damping, and stiffness matrices of system which can be obtained from the components of $M(\phi_i)$, $C(\dot{\phi}_i, \phi_i)$, and $K(\phi_i)$ in (4-1) mapping with the coordinates q_r. Also, $f_{im.r} = \left[m_{im} r_{im} \Omega^2 \cos(\phi_{im}) \quad m_{im} r_{im} \Omega^2 \cos(\phi_{im})\right]^T \in \Re^2$ and $f_{con} \in \Re^2$ are the imbalance force and the control(actuator) force, respectively. Before proceeding, the following assumptions are made.

i) The full state of system is supposed to be available via a sensor.

ii) Usually, assessing the imbalance mass information (m_{im}, r_{im} and ϕ_{im}) is so cumbersome that the vector $\vartheta = \left[m_{im} r_{im} \cos(\phi_{im}) \quad m_{im} r_{im} \cos(\phi_{im})\right]^T$ is assumed as the unknown parameter vector to be estimated by the adaptive control law. By the assumption ii) above, we can rearrange (4-18) into,

$$M_r \ddot{q}_r + C_r \dot{q}_r + K_r q_r = H^T \vartheta + f_{con} \tag{4-19}$$

where, $H^T = \begin{bmatrix} \Omega^2 & 0 \\ 0 & \Omega^2 \end{bmatrix}$ is a regressor matrix due to $f_{im.r} = H^T \vartheta$.

Defining the desired position, velocity, and acceleration as $q_{r.d}$, $\dot{q}_{r.d}$, and $\ddot{q}_{r.d}$, (which, for the zero vibration case we select, $\ddot{q}_{r.d} = 0$, $\dot{q}_{r.d} = 0$, and $q_{rd} = 0$). The error states are $e_r = q_r - q_{r.d}$, $\dot{e}_r = \dot{q}_r - \dot{q}_{r.d}$, and $\ddot{e}_r = \ddot{q}_r - \ddot{q}_{r.d}$.

The control law is suggested s.t,

$$f_{con} = M_r(\ddot{q}_{r.d} - \psi\, \dot{e}_r) + C_r(\dot{q}_{r.d} - \psi\, e_r) + K_r q_r - H^T \hat{\vartheta} \tag{4-20-a}$$

with a adaptive update law

$$\dot{\hat{\vartheta}} = \chi^{-1} H v \tag{4-20-b}$$

and new coordinate

$$v \equiv (\dot{e}_r + \psi e_r) \in \Re^2 \tag{4-20-c}$$

and the gain $\psi \in \Re^{2\times 2}$, and $\chi \in \Re^{2\times 2}$ are constant positive definitive gain matrices which can be chosen arbitrary. Also, $\hat{\vartheta}$ is the estimated parameter vector for the true unknown vector ϑ.

This control law (4-20) provided guarantees that the system is globally asymptotically stable.

proof: Substituting (4-20) into (4-19) yields the closed loop dynamics with $v \equiv (\dot{e}_r + \psi e_r)$ and $\dot{v} \equiv (\ddot{e}_r + \psi \dot{e}_r)$ s.t,

$$M_r \dot{v} + C_r v = H^T \overline{\vartheta}$$

where, $\overline{\vartheta} = \vartheta - \hat{\vartheta}$ is the estimation error vector and its derivatives is $\dot{\overline{\vartheta}} = -\dot{\hat{\vartheta}}$ because ϑ is a constant vector.

Let the candidate Lyapunov function s.t,

$$V = \frac{1}{2} v^T M_r v + \frac{1}{2} \overline{\vartheta}^T \chi \overline{\vartheta} + {e_r}^T \psi C_r e_r$$

The function derivative with respect to time is given by,

$$\dot{V} = v^T M_r \dot{v} + \overline{\vartheta}^T \chi \dot{\overline{\vartheta}} + {\dot{e}_r}^T \psi C_r e_r + {e_r}^T \psi C_r \dot{e}_r$$

Furthermore, substituting the closed loop dynamics into $\dot{V}$,

$$\begin{aligned}
\dot{V} &= v^T [-C_r v + H^T \overline{\vartheta}] - \overline{\vartheta}^T \chi \dot{\hat{\vartheta}} + {\dot{e}_r}^T \psi C_r e_r + {e_r}^T \psi C_r \dot{e}_r \\
&= -{\dot{e}_r}^T C_r \dot{e}_r - {e_r}^T \psi C_r \psi e_r + \overline{\vartheta}^T H v - \overline{\vartheta}^T \chi \dot{\hat{\vartheta}} \\
&= -\begin{bmatrix} \dot{e}_r \\ e_r \end{bmatrix}^T \begin{bmatrix} C_r & 0 \\ 0 & \psi C_r \psi \end{bmatrix} \begin{bmatrix} \dot{e}_r \\ e_r \end{bmatrix} + \overline{\vartheta}^T [H v - \chi \dot{\hat{\vartheta}}]
\end{aligned}$$

By the adaptive update law $\dot{\hat{\vartheta}} = \chi^{-1} H v$, we have,

$$\dot{V} = -\begin{bmatrix} \dot{e}_r \\ e_r \end{bmatrix}^T \begin{bmatrix} C_r & 0 \\ 0 & \psi C_r \psi \end{bmatrix} \begin{bmatrix} \dot{e}_r \\ e_r \end{bmatrix} \le 0, \quad \begin{bmatrix} C_r & 0 \\ 0 & \psi C_r \psi \end{bmatrix} > 0$$

Thus, $\dot{V} = 0 \Rightarrow \dot{e}_r = 0, e_r = 0 \Rightarrow \ddot{e}_r = 0$, consequently, $v = 0, \dot{v} = 0$.

From the closed-loop dynamics, we have,

$$H^T \overline{\vartheta} = 0 \Rightarrow \overline{\vartheta} = 0$$

By the invariant(LaSalle's) theorem and noting the function V is radially unbounded, the closed-loop system is globally asymptotically stable at the origin ($\dot{e}_r = 0, e_r = 0$). Since $\ddot{q}_{r.d} = 0, \dot{q}_{r.d} = 0$,and $q_{r.d}$ =0, we can verify $\ddot{q}_r = 0, \dot{q}_r = 0$,and q_r =0. The proof is completed.

Next, let's consider the design of control law for case b) which is under the action of ABD. The several assumptions are also specified before proceeding.

i) The imbalance mass information (m_{im}, r_{im} and ϕ_{im}) and the ABD ball's damping coefficient ($c_b > 0$) are unknown parameters.

ii) The full state of system is available to be measured via sensor devices. This assumption demands an additional special sensor device to measure the ABD ball position. The specification of this special sensor isn't offered in this paper.

Since the number of control force is less than the number of state, this problem is defined as so called "under actuated case" i.e, $Dim(q) > rank(B)$.

Defining the actuated state as $q_1 = [y \quad z]^T$ and the unactuated one as $q_2 = [\phi_1 \quad \phi_2]^T$, we can partition the original dynamics (4-1) s.t,

$$\begin{bmatrix} M_{11} & M_{12} \\ M_{21} & M_{22} \end{bmatrix} \begin{bmatrix} \ddot{q}_1 \\ \ddot{q}_2 \end{bmatrix} + \begin{bmatrix} C_{11} & C_{12} \\ C_{21} & C_{22} \end{bmatrix} \begin{bmatrix} \dot{q}_1 \\ \dot{q}_2 \end{bmatrix} + \begin{bmatrix} K_{11} & 0 \\ K_{21} & 0 \end{bmatrix} \begin{bmatrix} q_1 \\ q_2 \end{bmatrix} = \begin{bmatrix} F_{im.} \\ 0 \end{bmatrix} + \begin{bmatrix} F_{ball} \\ 0 \end{bmatrix} + \begin{bmatrix} U_{con} \\ 0 \end{bmatrix} \tag{4-21-a}$$

where,

$$f_{im} = [F_{im.} \; 0]^T, f_{ball} = [F_{ball.} \; 0]^T \text{ and, } Bf_{con} = [U_{con} \; 0]^T. \tag{4-21-b}$$

From(4-21), two decomposed equation are given by,

$$M_{11}\ddot{q}_1 + M_{12}\ddot{q}_2 + C_{11}\dot{q}_1 + C_{12}\dot{q}_2 + K_{11}q_1 = F_{im.} + F_{ball} + U_{con} \tag{4-22}$$

$$M_{21}\ddot{q}_1 + M_{22}\ddot{q}_2 + C_{21}\dot{q}_1 + C_{22}\dot{q}_2 + K_{21}q_1 = 0 \tag{4-23}$$

Since the inverse of M_{22} exist, (4-23) can be rearranged s.t,

$$\ddot{q}_2 = -M_{22}^{-1}[M_{21}\ddot{q}_1 + C_{21}\dot{q}_1 + C_{22}\dot{q}_2 + K_{21}q_1] \tag{4-24}$$

Substituting (4-24) into (4-22) yields,

$$\overline{M}\ddot{q}_1 + \overline{C}_1\dot{q}_1 + \overline{K}q_1 + \overline{C}_2\dot{q}_2 = F_{im.} + F_{ball} + U_{con} \tag{4-25-a}$$

where,

$$\overline{M} = [M_{11} - M_{12}M_{22}^{-1}M_{21}] \tag{4-25-b}$$

$$\overline{C}_1 = [C_{11} - M_{12}M_{22}^{-1}C_{21}], \; \overline{C}_2 = [C_{12} - M_{12}M_{22}^{-1}C_{22}] \tag{4-25-c}$$

$$\overline{K} = [K_{11} - M_{12}M_{22}^{-1}K_{21}] \tag{4-25-d}$$

Due to the assumptions i), in order to derive the adaptive control law, (4-25) needs to be rearranged to

create the regressor matrix and the unknown parameter vector.

$$\ddot{q}_1 = -\overline{M}^{-1}[\overline{C}_1\dot{q}_1 + \overline{K}q_1 + C_{12}\dot{q}_2] + \overline{M}^{-1}S^T\theta + \overline{M}^{-1}F_{ball} + \overline{M}^{-1}U_{con} \tag{4-26-a}$$

where, $S^T\theta = F_{im.} + M_{12}M_{22}^{-1}C_{22}\dot{q}_2$ and, the detail of S and θ are given by,

$$S^T = \begin{bmatrix} \Omega^2 & 0 & h_1 \\ 0 & \Omega^2 & h_2 \end{bmatrix} \quad \text{and} \quad \theta = \begin{bmatrix} m_{im}r_{im}\cos(\phi_{im}) \\ m_{im}r_{im}\sin(\phi_{im}) \\ c_b \end{bmatrix} \tag{4-26-b}$$

where, S is the regressor matrix and θ is the unknown parameters vector to be estimated by an adaptive law and,

$$\begin{bmatrix} h_1 \\ h_2 \end{bmatrix} = \begin{bmatrix} -r_b[\sin(\phi_1)\dot{\phi}_1 + \sin(\phi_2)\dot{\phi}_2] \\ r_b[\cos(\phi_1)\dot{\phi}_1 + \cos(\phi_2)\dot{\phi}_2] \end{bmatrix} \tag{4-26-c}$$

Defining the desired position, velocity, and acceleration as $q_{1.d}$, $\dot{q}_{1.d}$, and $\ddot{q}_{1.d}$, (which, for the zero vibration case we select, $\ddot{q}_{1.d} = 0$, $\dot{q}_{1.d} = 0$, and $q_{1.d} = 0$). The error states are $e_1 = q_1 - q_{1.d}$, $\dot{e}_1 = \dot{q}_1 - \dot{q}_{1.d}$, and $\ddot{e}_1 = \ddot{q}_1 - \ddot{q}_{1.d}$. Next we suggest the following adaptive control law,

$$U_{con} = [\overline{C}\dot{q}_1 + \overline{K}q_1 + C_{12}\dot{q}_2 - S^T\hat{\theta} - F_{ball} - \overline{M}K_1 r + \overline{M}(\ddot{q}_{1.d} - \xi\dot{e}_1)] \tag{4-27-a}$$

with a adaptive update law

$$\dot{\hat{\theta}} = \eta^{-T}S\overline{M}^{-T}r \tag{4-27-b}$$

where new coordinate

$$r \equiv (\dot{e}_1 + \xi e_1) \in \Re^2 \tag{4-27-c}$$

and the gain $K_1 \in \Re^{2\times 2}$, $\xi \in \Re^{2\times 2}$, and $\eta \in \Re^{3\times 3}$ are constant positive definitive gain matrices which can be chosen arbitrary. Also, $\hat{\theta}$ is the estimated parameter vector for the true unknown vector θ. This control law (4-26) provided guarantees that the system is globally asymptotically stable.

Proof: Substituting U_{con} in (4-27) into (4-26) yields the closed-loop dynamics with $r \equiv (\dot{e}_1 + \xi e_1)$ and $\dot{r} \equiv (\ddot{e}_1 + \xi\dot{e}_1)$ s.t,

$$\dot{r} = -K_1 r + \overline{M}^{-1}S^T\overline{\theta}$$

where, $\overline{\theta} = \theta - \hat{\theta}$ is the estimation error vector and its derivatives is $\dot{\overline{\theta}} = -\dot{\hat{\theta}}$ because θ is a constant vector. Let the candidate Lyapunov function s.t,

$$V = \frac{1}{2}r^T r + \frac{1}{2}\overline{\theta}^T\eta\overline{\theta} + e^T\xi K_1 e$$

The function derivative with respect to time is given by,

$$\dot{V} = r^T\dot{r} + \dot{\overline{\theta}}^T\eta\overline{\theta} + \dot{e}^T\xi K_1 e + e^T\xi K_1\dot{e}$$

Furthermore, substituting the closed dynamics into $\dot{V}$,

$$\begin{aligned}\dot{V} &= r^T[-K_1 r + \overline{M}^{-1}S^T\overline{\theta}] - \dot{\hat{\theta}}^T\eta\overline{\theta} + \dot{e}^T\xi K_1 e + e^T\xi K_1\dot{e} \\ &= -\dot{e}^T K_1\dot{e} - e^T\xi K_1\xi e + r^T\overline{M}^{-1}S^T\overline{\theta} - \dot{\hat{\theta}}^T\eta\overline{\theta} \\ &= -\begin{bmatrix}\dot{e}\\ e\end{bmatrix}^T\begin{bmatrix}K_1 & 0\\ 0 & \xi K_1\xi\end{bmatrix}\begin{bmatrix}\dot{e}\\ e\end{bmatrix} + [r^T\overline{M}^{-1}S^T - \dot{\hat{\theta}}^T\eta]\overline{\theta}\end{aligned}$$

By the adaptive update law $\dot{\hat{\theta}} = \eta^{-T}S\overline{M}^{-T}r$, we have,

$$\dot{V} = -\begin{bmatrix}\dot{e}\\ e\end{bmatrix}^T\begin{bmatrix}K_1 & 0\\ 0 & \xi K_1\xi\end{bmatrix}\begin{bmatrix}\dot{e}\\ e\end{bmatrix} \le 0,\ \begin{bmatrix}K_1 & 0\\ 0 & \xi K_1\xi\end{bmatrix} > 0$$

Thus, $\dot{V} = 0 \Rightarrow \dot{e} = 0, e = 0 \Rightarrow \ddot{e} = 0$, consequently, $r = 0 \Rightarrow \dot{r} = 0$.

From the closed-loop dynamics(i.e, $\dot{r} = -K_1 r + \overline{M}^{-1}S^T\overline{\theta}$), we have,

$$\overline{M}^{-1}S^T\overline{\theta} = 0 \Rightarrow \overline{\theta} = 0$$

By the invariant(LaSalle's) theorem and noting the function V is radially unbounded, the closed-loop system is globally asymptotically stable at the origin ($\dot{e} = 0, e = 0$). Since $\ddot{q}_{1.d} = 0, \dot{q}_{1.d} = 0$,and $q_{1.d}$=0, we can verify $\ddot{q}_1 = 0, \dot{q}_1 = 0$,and q_1=0. Also, from (4-23), we have to examine the convergence of $[\ddot{q}_2\ \dot{q}_2\ q_2]$. By applying $\ddot{q}_1 = 0, \dot{q}_1 = 0$,and q_1=0 into (4-23), we have, $\ddot{q}_2 + M_{22}^{-1}C_{22}\dot{q}_2 = 0$,where, $\dot{q}_2 = [\dot{\phi}_1, \dot{\phi}_2]$ .Specifically, $\ddot{\phi}_i + \frac{c_b}{m_b}\dot{\phi}_i = 0 \ \ for\ i = 1,2$. We can show $\dot{q}_2 \to 0$ and $\ddot{q}_2 \to 0$ exponentially. If the initial conditions of ABD-ball are $\dot{\phi}_i(t_0) = 0$, $\phi_i(t_0) = \phi_{i.0} \ \ for\ i = 1,2$, and then the fixed equilibrium position of balls is the initial ball position(i.e, $\phi_i(T) = \phi_{i.0}$ where, T is a certain period when the control law (4-27) allows the system to reach the system origin $\ddot{q}_1 = 0, \dot{q}_1 = 0$,and q_1=0). This implies that the ball position is not changed if the control is activated when the balls stay at the fixed equilibrium(synchronous behavior) point before control activation. This result can be seen from the simulation outcomes in Figure.4.3. Also, let's consider non-synchronous limit-cycle behavior before control activation s.t, $\dot{\phi}_i(t_0) = \dot{\phi}_{i.0}$, $\phi_i(t_0) = \phi_{i.0} \ \ for\ i = 1,2$. With those initial conditions, after control activation, the trajectory of $\phi_i(t)$ is governed by $\phi_i(t) = -\frac{\dot{\phi}_{i.0}}{a}\exp[-a(t-t_0)] + \phi_{i.0} \ \ for i = 1,2$ where, $a = \frac{c_b}{m_b} > 0$. We also can see $\phi_i(\infty) = \phi_{i.0} - \frac{\dot{\phi}_{i.0}}{a}$. The proof is completed.

Thus, the equilibrium positions of q_2 are determined by the initial conditions of ABD-balls captured at the moment(defined as time t_a) of control activation and the summary of equilibrium positions of q_2 is displayed below. Additionally, the trajectory of ABD-ball is shown with three different control activation

times $t_a = 140,142,144$ sec . According to t_a, the equilibrium position of ABD ball is varied as shown in Figure.4.2.

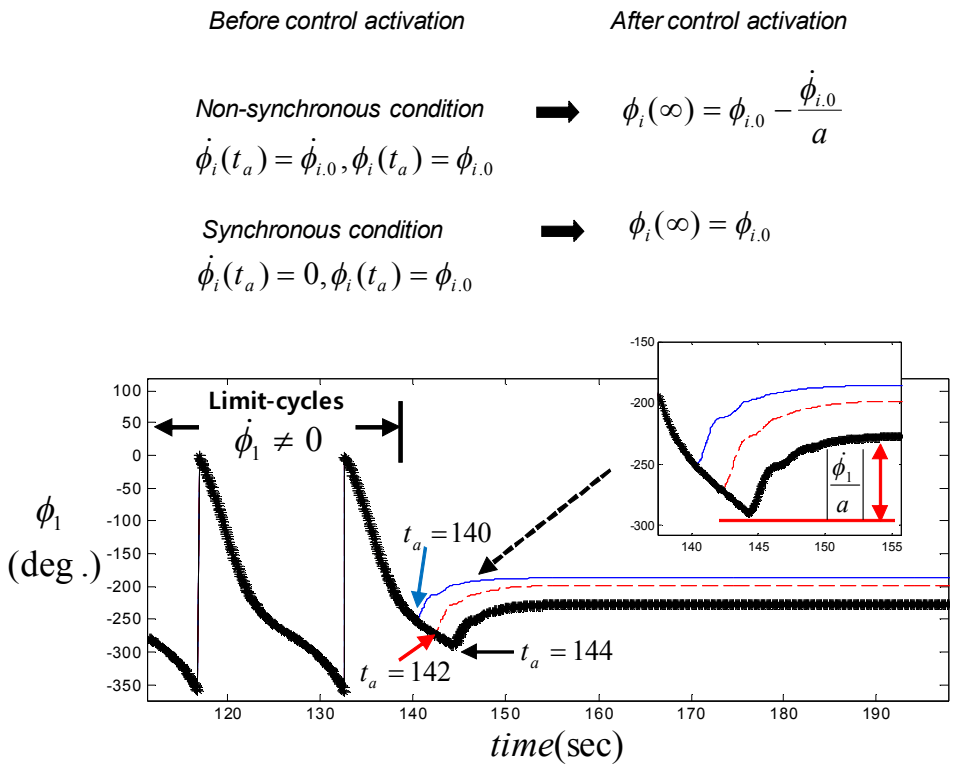


Figure.4.2 The trajectory of ABD-ball with three different control activation times

The summary and simulation result above provide us the idea that the control law suggested here possibly enhances us to achieve the desired position of ABD-balls by choosing the right activation time(t_a) with non-synchronous condition. In non-synchronous condition, the ABD balls are continuously rotating with a certain frequency in ABD-circular track. Employing the inherent nature of this unwanted condition, a particular initial condition of ABD-ball before control activation can be chosen by control law so that it is able to place the balls/balancer mass in the desired angular phase which can eliminate the imbalance effect because the fixed equilibrium point of q_2 after control activation depends on $\dot{\phi}_{i.0}$, $\phi_{i.0}$ $for\ i = 1,2$ and $a = \frac{c_b}{m_b}$. However, the control law has no capability to manipulate the fixed equilibrium position of q_2 under synchronous condition where the ABD-balls reach a stable equilibrium position, because the position of ABD-ball is not altered after the control is activated. Before control is initiated, if q_2 stay in the stable equilibrium position where can't cancel imbalance effectively, the control law must deal with three undesired imbalance effects(two-ABD masses in undesired angular phase and imbalance) to achieve the minimum vibration level. Consequently, this is the situation where we can't

take advantages of autobalancer and need to consume more control force than the case without ABD(i.e, a pure imbalance rotor) with larger imbalance vibration.

More specifically, we can compare the control force between (4-20) and (4-27). Let's suppose that the system reaches the origin of system(i.e, $q_r \to 0$ in (4-20) and $q_1 \to 0$ in (4-27)) via each control law so that all state of system go to the equilibrium condition as seen in the proof of each control strategy and then we can investigate the steady-state control force for each. The steady state force of (4-20) becomes $f_{con.ss} = -H^T \hat{\vartheta}$ while (4-27) does $U_{con.ss} = -S^T \hat{\theta} - F_{ball}(\phi_i)$. Both the estimated terms $H^T \hat{\vartheta}$ in (4-20) and $S^T \hat{\theta}$ in (4-27) are directly associated with imbalance force. For an identical imbalance condition, it should be noted that $\left\| H^T \hat{\vartheta} \right\|_2 = \left\| S^T \hat{\theta} \right\|_2 = \left\| F_{im} \right\|_2$. Beside of $S^T \hat{\theta}$, in $U_{con.ss}$, we have a force term $F_{ball}(\phi_i)$ induced by ABD-ball. In appropriate angular phase of two balls relative to imbalance effect(i.e, $S^T \hat{\theta}$), $\left\| U_{con.ss} \right\|_2$ is smaller than $\left\| f_{con.ss} \right\|_2$ for an identical imbalance mass size. However, it should be noted that $\left\| U_{con.ss} \right\|_2$ can be larger than $\left\| f_{con.ss} \right\|_2$ if the angular position of two balls $\phi_i \; for \; i = 1,2$ in $F_{ball}(\phi_i)$ are not situated at the favorable position where they cancel the imbalance effect. To have better understating for the function of ABD in synchronous condition, let's consider three cases in Figure.4.3. Case (a) indicate undesired situation where the control force must manage larger imbalance effect than pure imbalance effect in Case (b) where there is no autobalacer. However, we can take an advantage of ABD with Case (c) because the force induced by ABD partially or entirely eliminate the effect of imbalance force.

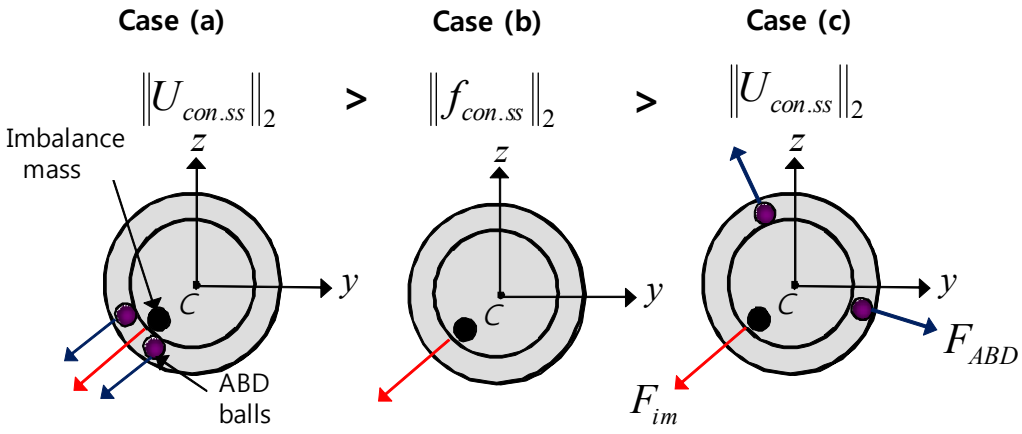


Figure.4.3 The comparison of steady-state control force due to the function of ABD

Therefore, to prevent unwanted condition and maximize the performance of ABD and achieve the better performance of system for any situations, the hybrid control strategy will be developed and discussed in next section.

4.4 HYBRID CONTROL STRATEGY

In the previous section, the performance of adaptive control law derived in (4-27) has been discussed. Although it guarantees the globally asymptotically stable of system, the balancer mass can't be place in desired position at certain operating condition. Hence, in this section, utilizing both ABD and the adaptive control (4-27) via AMB, the hybrid control strategy taking advantage of undesired non-synchronous behavior of ABD is presented not only to compensate the drawback of ABD via active control but also reduce the control power through the function of ABD for any operating condition by forcing balancer mass into favorable position relative to imbalance effect. In Figure.4.4, the detail of hybrid control logic is displayed. Each block in Figure.4.4 is explained in detail below.

1. Block (a) indicates the decision process to determine if the system is subject to non-synchronous limit cycle condition by measuring the speed of balancer mass/balls. If the absolute speed of ABD-ball $\|\phi_i\|_2$ is less than the small threshold ε_1, block (b) is the next process. Otherwise, (f) is selected.
2. (b) is the decision process to check if the static vibration level of system is allowably small(i.e, $\sqrt{y^2+z^2} \le \varepsilon_2$). It goes (a) if $\sqrt{y^2+z^2} \le \varepsilon_2$. Otherwise, (c) is chosen. Here, if the system vibration level is achieved by pure passive ABD action, and then no active control will be required(i.e, control loop (a)->(b)->(a)).
3. (c) and (f) are the decision blocks to investigate if unknown parameters(m_{im}, ϕ_{im}, c_b) are available(For an example, already estimated from a previous operation).
4. (d) is the command block to destabilize the system by turning off control or exerting destabilizing force through AMB allows system to be in non-synchronous condition forcing the ABD-balls continuously rotating in the ABD-track Once (d) is selected, it proceeds to (e).
5. (e) is the command block to initiate the active control at an appropriate control activation time t_a satisfying the domain D. $D = \left\{ \{\phi_i(t_a), \dot{\phi}_i(t_a)\} \in \Re^2 \mid \left\| \phi_i(t_a) - \frac{\dot{\phi}_i(t_a)}{a} - \phi_{i.desired} \right\|_2 \le \varepsilon \right\}$ $for\, i = 1,2$

   We can set the desired equilibrium positions (s.t, $\phi_{i.desired}(m_{im}, \phi_{im})$ $for\, i = 1,2$) of ABD balls relative to imbalance from the information of unknown parameter in block (d). Based upon $\phi_{i.desired}(m_{im}, \phi_{im})$ $for\, i = 1,2$, we can place the ABD-balls into the desired positions by initiating the active control with t_a satisfying the domain D above.
6. (g) is the command block to initiate the active control at the random time.

7. (h) is the command block to estimate unknown parameters(m_{im}, ϕ_{im}, c_b). This block is consequently executed if it goes through block (g).
8. (i) is the decision block to investigate the following condition such that, $\|f_{im} - f_{ball}(\phi_i)\|_2 = \|F_{im} - F_{ball}(\phi_i)\|_2 = \|S^T\hat{\theta} - F_{ball}(\phi_i)\|_2 \le \varepsilon_3$ ensuring that the balancing force due to ABD effectively cancels the imbalance force with appropriate angular phase of ϕ_i .

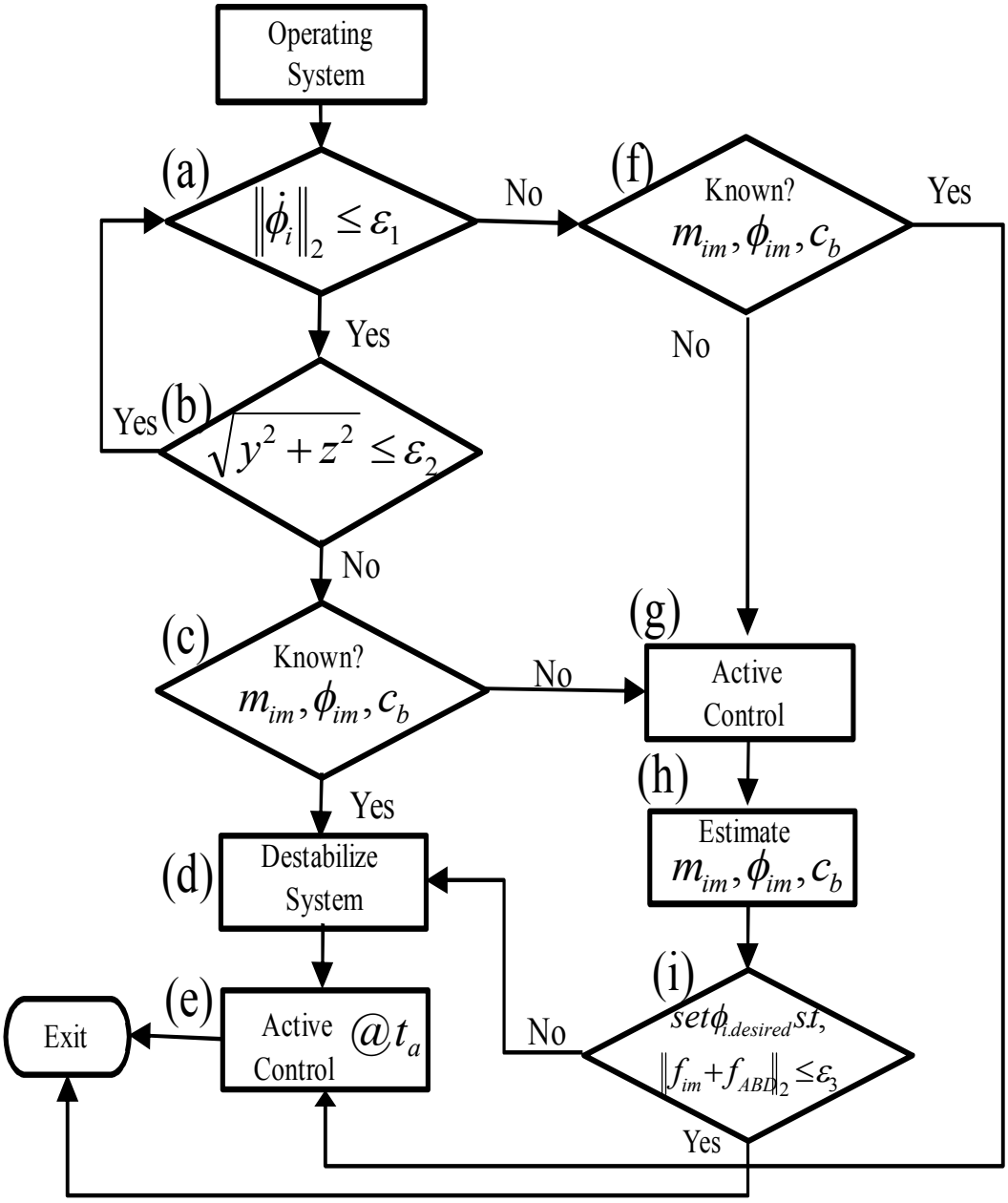
In Figure.4.4, additionally, to enhance ones to understand the function of hybrid control strategy, four possible cases are considered although the other cases are also founded (Other cases are classified as sub-cases generated by four possible case described here). In Case (A), if the speed of ABD-ball is less than the threshold ε_1 (i.e, synchronous condition) and the system vibration level is achieved by pure passive ABD action, and then no active control will be required(i.e,(a)->(b)-(a)). However, if the steady-state vibration is increased with an abrupt change of operating condition not leading to non-synchronous condition, an active control is initiated to suppress unwanted vibration after checking if unknown parameters are available from previous operation and then estimate unknowns under assumption that they are not previously estimated. Next step, the control logic investigates the condition $\|f_{im} - f_{ball}(\phi_i)\|_2 = \|F_{im} - F_{ball}(\phi_i)\|_2 = \|S^T\hat{\theta} - F_{ball}(\phi_i)\|_2 \le \varepsilon_3$ ensuring that the balancing force of ABD effectively cancels the imbalance force and then exit.

In Case (B), initially, if the balls don't reach the fixed equilibrium position (i.e, non-synchronous limit-cycle condition), then active control is initiated to destabilize the limit-cycle thus allowing the autobalancer masses to approached the balanced equilibrium condition. Here, with assumption that unknown parameters(m_{im}, ϕ_{im}, c_b) are known or already estimated from a previous operation, we can set the desired equilibrium positions (s.t, $\phi_{i.desired}(m_{im}, \phi_{im})$ $for\, i = 1,2$) of ABD balls relative to imbalance. Based upon $\phi_{i.desired}(m_{im}, \phi_{im})$ $for\, i = 1,2$, we can place the ABD-balls into the desired positions by initiating the control with an appropriate control activation time t_a satisfying the domain *D* above.

In Case (C), if the ABD-balls reach unwanted equilibrium positions in the way that an imbalance effect is increased, a control is initiated to deal with it. With assumption that unknown parameters are already estimated from a previous operation, we can set the desired equilibrium positions s.t, $\phi_{i.desired}(m_{im}, \phi_{im})$ $for\, i = 1,2$ of ABD balls relative to imbalance. Next, turning off control or exerting destabilizing force through AMB allows system to be in non-synchronous condition forcing the ABD-balls continuously rotating in the ABD-track and we can place the ABD-balls into the desired positions by initiating the control with an appropriate control activation time t_a satisfying the domain *D* above.

In Case (D), with initial non-synchronous limit cycle condition, a control is initiated and estimates the unknown parameters. Based upon estimated parameters, we can set the desired equilibrium positions s.t, $\phi_{i.desired}(m_{im}, \phi_{im})$ $for\, i = 1,2$ of ABD balls relative to imbalance. The rest of process is identical with one in Case (C).

These scenario of four particular control sequences will be discussed with the simulation results for given four different operating conditions in the next section. Through this hybrid control strategy, the system can be more reliable and robust with the reduction of control power consumption.



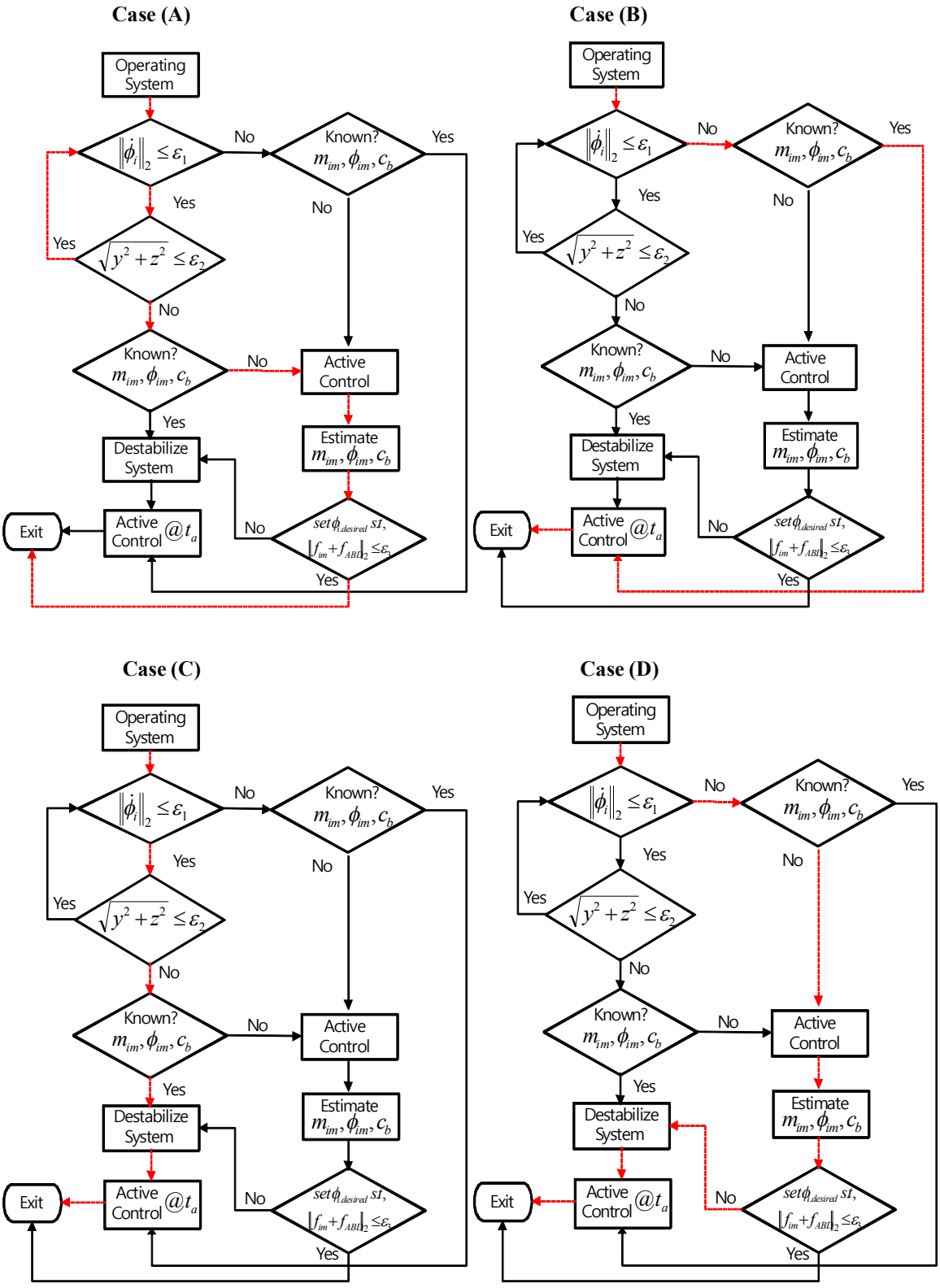
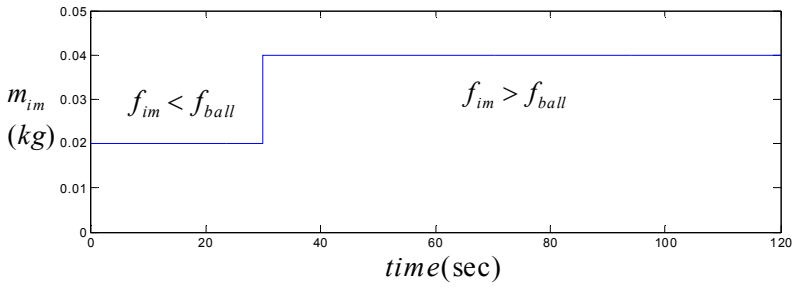


Figure.4.4 Supervisory hybrid control strategy map and four examples

4.5 Simulation Results

In this section, the simulation results are illustrated to display the effectiveness of the hybrid technique proposed in this paper.

The first plot in Figure.4.5 displays the scenario of imbalance mass change on the time domain. As the mass is changed, the static imbalance force is varied accordingly. This scenario indicates that the countermeasure force (f_{ball}) induced by ABD balls is greater than imbalance static force (f_{im}) on [0 < t < 30] sec. and the opposite condition where the imbalance force exceeds the allowable capacity of ABD is imposed after t=30 sec. On the second plot, at approximately from t=8 to t=30 sec, we observe the 1st balanced condition where the ABD effectively eliminates the imbalance vibration with an appropriate angular phase of ABD balls relative to imbalance. At 30 seconds, the system enters the 2nd balanced condition where two balancer masses are merged and situated at 180 deg. opposite phase relative to imbalance suddenly increased at 30 sec. Consequently, the steady-state vibration level in 2nd balanced condition is higher than one in 1st balanced condition because the imbalance force exceeds the maximum balancing capacity of the ABD ($f_{im} > f_{ball}$). To suppress the residual imbalance effect, the adaptive control law is initiated at t=65 seconds. This control successfully achieves the lower steady-state vibration amplitude after experiencing a transient response. Since the control is activated when the balls stay in fixed equilibrium balancing positions(synchronous condition) on the 2nd balanced period, the angular position of balls remains constant even after control stage. This is synchronous with the result of the proof in section 4.3. According to the simulation results, the angular position of ABD ball is changed with 1.5 deg. after control activation. This implies that the angular velocity of ABD ball is not exactly zero but very small prior to an active control. Due to this fact, 1.5 deg. difference of angular position between before and after control is observed but it is almost negligible. The simulation results are synchronous with the control sequence shown in Case(A) of Figure.4.4. Additionally, we can compare the effectiveness of suggested hybrid control strategy with the case actively controlled without ABD in the last simulation outcome of Figure.4.5.



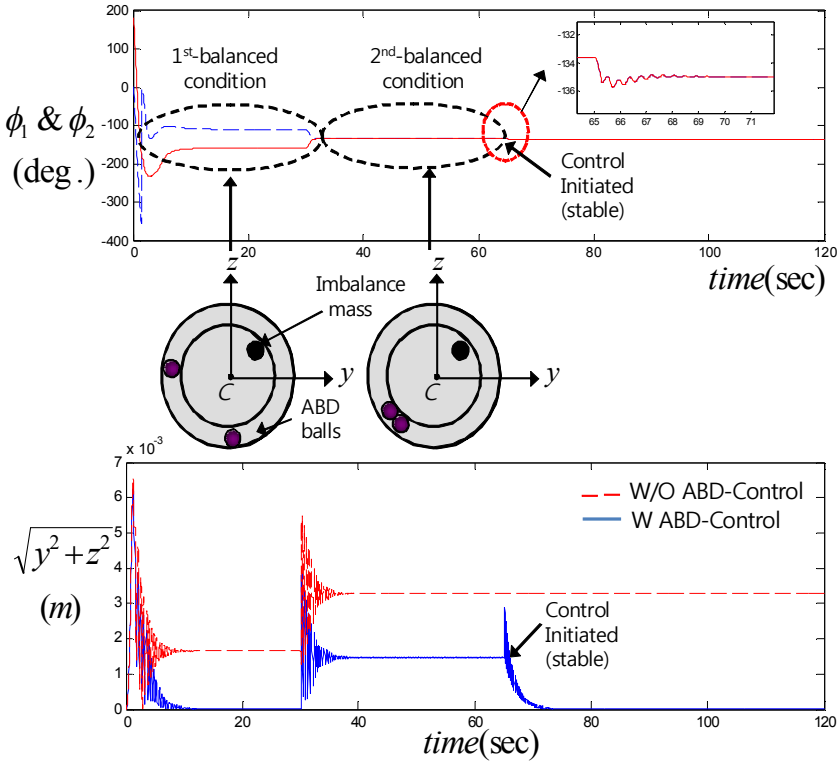


Figure. 4.5. Adaptive control for the case where the imbalance exceeds the maximum ABD balancing force ($\Omega = 3\omega_{ref}$, $\omega_{ref} = \sqrt{\frac{K_f}{m}}$) and note that the simulation results represent the Case (A) of control sequence in the previous section.

Figure.4.6 shows the adaptive estimation of unknown parameters. The dotted lines on each plot represent the estimation of three unknown system parameters $\theta = [m_{im} r_{im} \cos(\phi_{im}) \quad m_{im} r_{im} \sin(\phi_{im}) \quad c_b]^T$. The straight lines indicate the target values of unknowns. The imbalance mass information and the ball damping coefficient are estimated by the adaptive control law presented here. The guessed initial parameter values are shown before the control initiation.

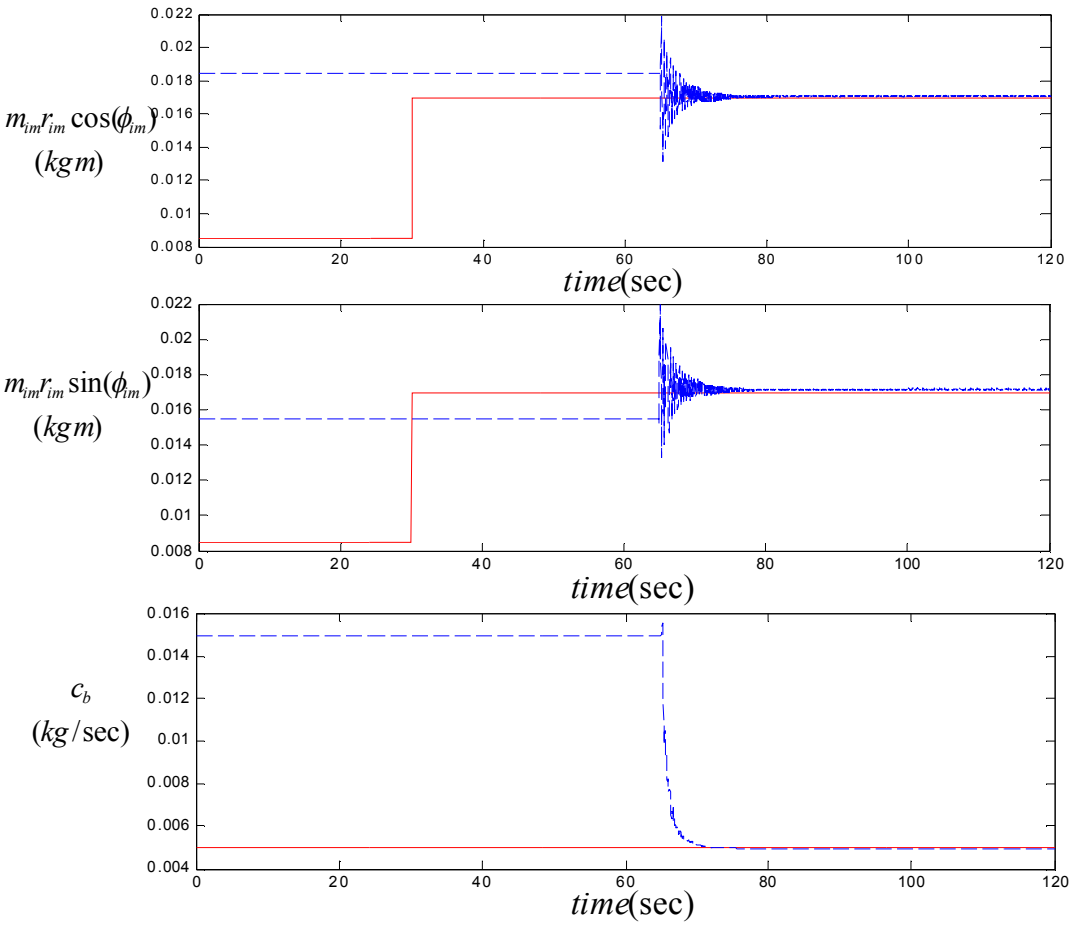


Figure.4.6 Adaptive estimation of unknown parameters.

Figure.4.7 shows the active bearing control forces between the case with the passive ABD using (4-27) and without it using (4-20). Since the ABD partially cancels the imbalance on the rotor and the bearing control force manages the residual vibration, the ABD equipped system achieves the same balancing performance with reduced AMB force. As mention earlier, despite of this advantage, the nonlinearity of the passive ABD has a significant drawback due to the potential for alternative non-balanced limit-cycle equilibrium behavior(i.e, non-synchronous condition). This situation is investigated in Figure.4.8 where a specific set of initials conditions was found which resulting in non-synchronous limit cycle behavior. As seen in Figure.4.8, with assumptions that unknown parameters are already estimated from the previous operation and the desired equilibrium position of ABD-balls is determined from the estimated unknowns, once the active control is activated at time t_a satisfying domain D discussed in the section 4.4, the limit cycle is destabilized and the ABD masses then converge to the desired balanced condition. The results in Figure.4.8 represent the control sequence of Case (B) in Figure.4.4.

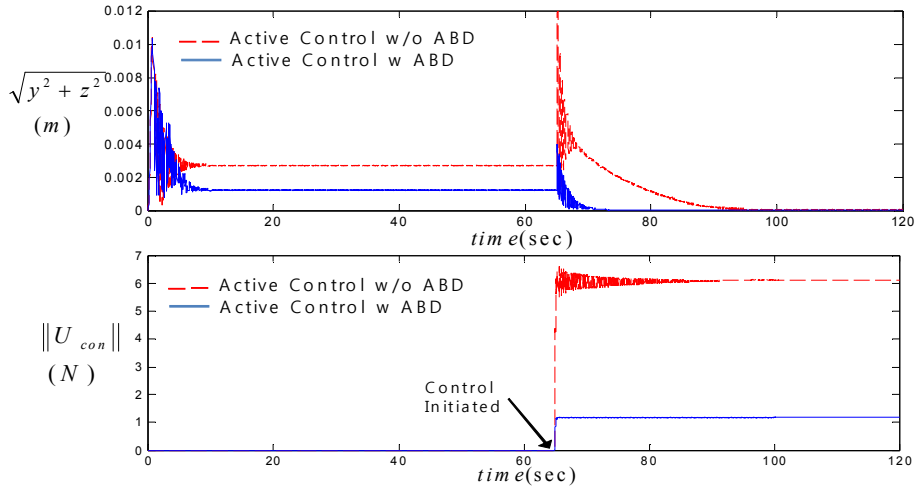


Figure. 4.7. Comparison of control force consumed between w/o ABD and w ABD to achieve the same vibration level with $m_{im} = 4.5m_b$ effect at operation speed: $\Omega = 3.5\omega_{ref}$).

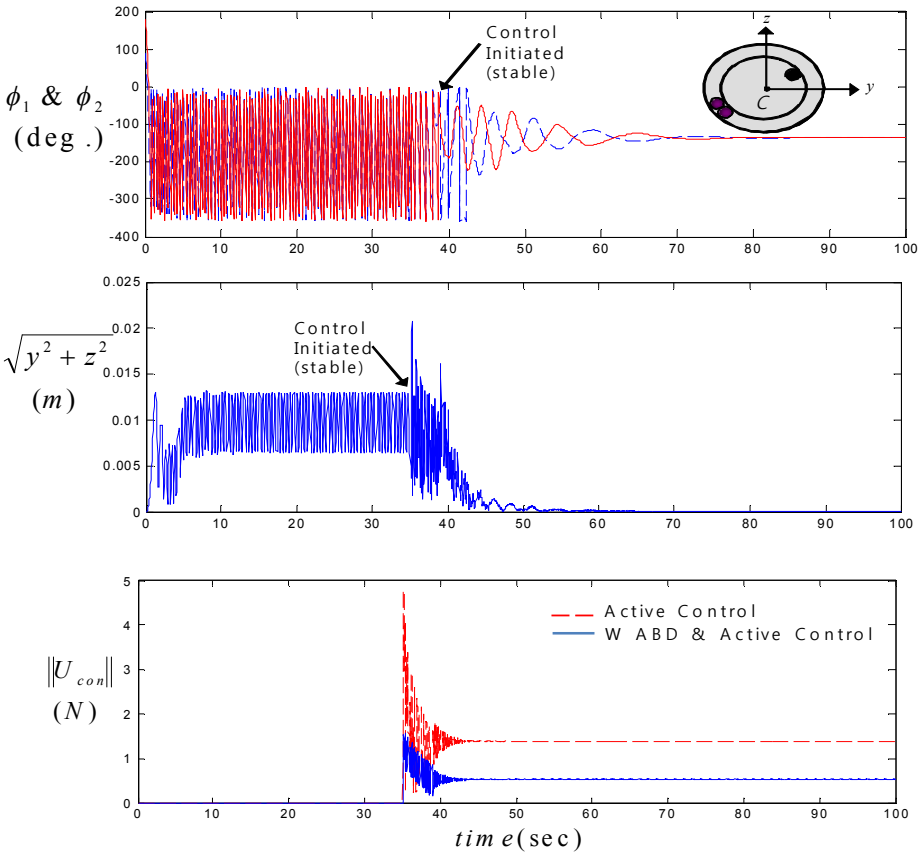


Figure.4.8 The performance of control under the limit-cycles condition (operation speed: $\Omega = 1.5\omega_{ref}$) with $m_{im} = 3m_b, r_{im} = r_b, \phi_{im} = 45^\circ$ and note that the simulation results represent the Case (B) of control sequence in the previous section.

Figure.4.9 indicates the system responses and control force consumption by the control sequence of Case (C) in the previous section. We can observe that the equilibrium position of ABD- balls is situated closely to the position of imbalance, which increases imbalance effect as shown in the simulation result on the time domain from 20 to 80 sec. Next, at 80 sec, exerting destabilizing force through AMB enables systems to be in the non-synchronous limit cycle condition. It is assumed that the desired equilibrium position of ABD-balls is determined based upon the unknown parameters estimated from previous operation. And then the balls can be placed into the desired position by activating the control at time t_a satisfying the domain *D* discussed in the previous section. Thus, the ball positions are situated in the way to cancel imbalance effect as seen in the simulation results from 140 to 200 sec. so that the control force is significantly small in this case.

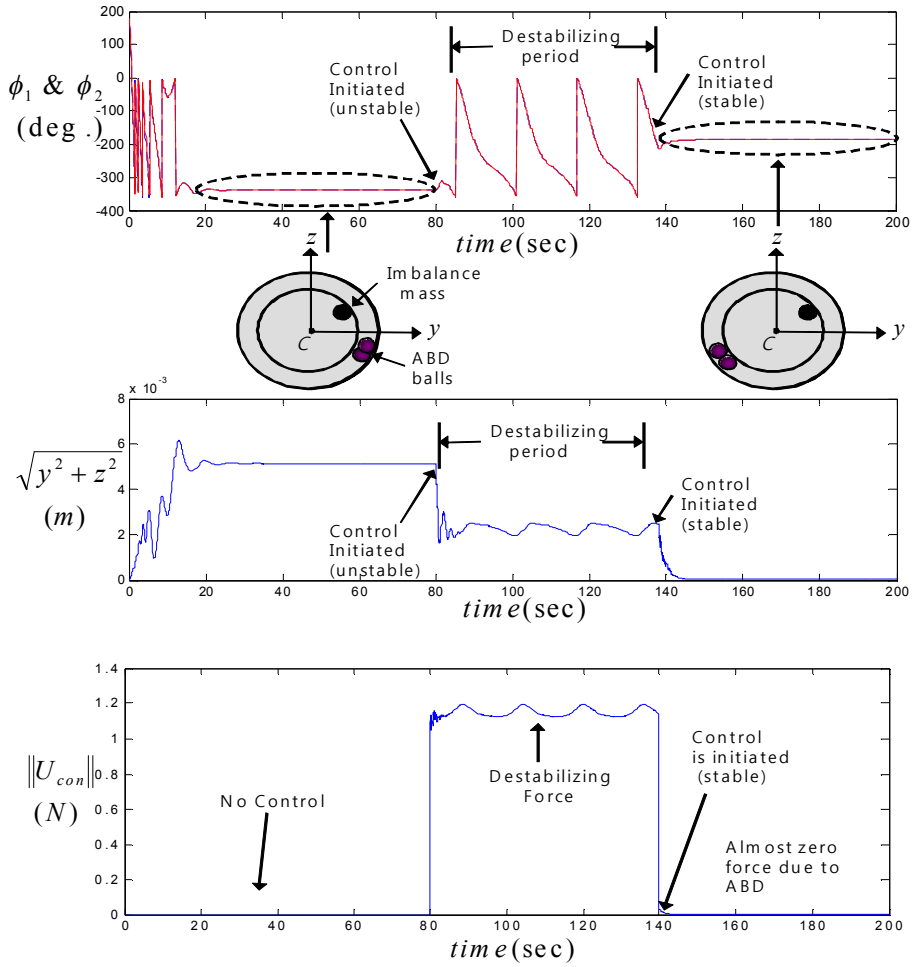
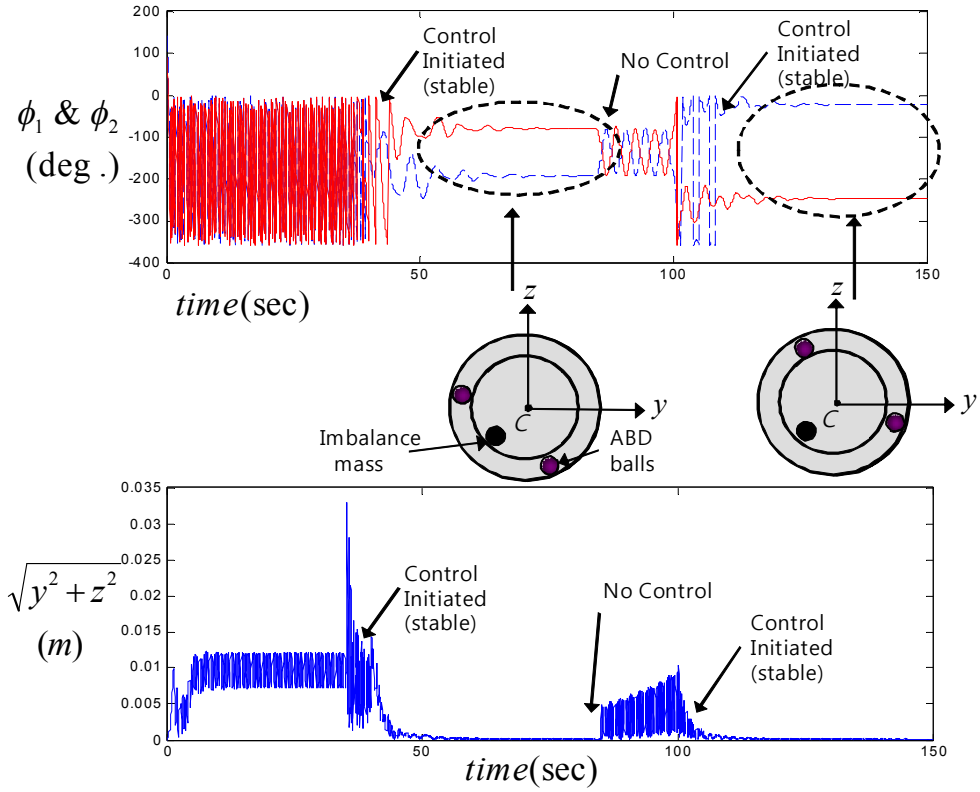


Figure.4.9 The performance of control under the undesirable synchronous condition (operation speed: $\Omega = 0.75\omega_{ref}$) with $m_{im} = 2m_b, r_{im} = r_b, \phi_{im} = 45^\circ$ note that the simulation results represent the Case (C) of control sequence in the previous section.

Figure.4.10 indicates the system responses and control force consumption by the control sequence specified in Case(D) of Figure.4.4. The limit-cycle condition is initially imposed on the time domain from 0 to 40 sec. Here, we assume that the unknown parameters are not available so that the control is activated at random time 40 sec to estimate unknowns. Since the control is actuated at the random time, the ABD-balls do not reach the favorable equilibrium position as seen the results on time domain from 50 to 83 sec, although the vibration level is minimized with a certain amount of control force. However, the desired equilibrium position of ABD-balls is determined based upon the unknowns estimated in this period(50~83 sec.). Next, at 83 sec, by switching off active force of AMB generates the non-synchronous limit cycle condition in this case. Furthermore, the balls can be placed into the desired position by activating the control at time t_a satisfying the domain *D*. Here, 101 sec is approximately chosen as t_a. Thus, the position of balls is situated in the favorable way to partially cancel imbalance effect as seen in the simulation results from 120 to 150 sec. Consequently, the control force is significantly reduced with the cooperation of ABD (i.e, appropriate phase of ABD-balls relative to imbalance phase) as seen in the control force on the time domain from 120 to 150 sec. We can compare the difference of consumed control force between the time period(50~83 sec.) and another (120~150 sec.)



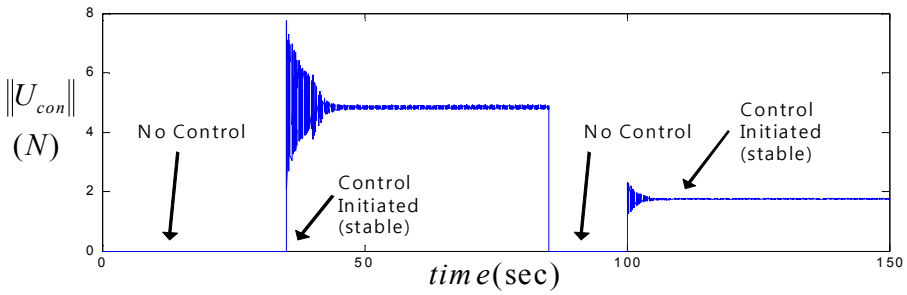


Figure.4.10 The performance of control under the limit-cycle and undesirable synchronous condition (operation speed: $\Omega = 2.5\omega_{ref}$) with $m_{im} = 2.5m_b, r_{im} = r_b, \phi_{im} = -135^\circ$ and note that the simulation results represent the Case (D) of control sequence in the previous section.

4.6 Concluding Remarks

This chapter develops a hybrid adaptive imbalance vibration control approach based on an active bearing augmented with a passive automatic balancing device (ABD) to enhance the balancing and vibration isolation capabilities. Here an adaptive active control algorithm for the rotor/bearing/ABD system is derived based on the Lyapunov approach which guarantees global asymptotic stability of the synchronous balanced condition. This approach enables the controller to cope with both the system nonlinearity introduced by the passive ABD and the rotor imbalance uncertainty. Controllability is established through an accessible distribution Lie bracket operational analysis. The simulation results demonstrate the advantages of the hybrid ABD/active bearing system for controlling and adapting to changing rotor imbalance conditions. The control law guarantees that the autobalancer reaches the balanced condition by destabilizing any non-synchronous limit-cycle behavior. Thus the system enables the autobalancer to cancel the vibrations in the rotating-frame which has the advantage of reducing the transmitted forces between the rotor and bearing.

The adaptive control of the rotor/ABD/active bearing system represents a significant step toward combining the advantages of each device. Here both devices compliment each other's function and inherent drawbacks in such a way that this hybrid control approach should be of considerable value to future rotor imbalance vibration control applications. These findings are relevant to limited power applications such as satellite reaction wheels or flywheel energy storage batteries.

CHAPTER V
LIMIT-CYCLE ANALYSIS OF THREE DIMENSIONAL RIGID ROTOR/SHAFT/AUTOBALANCER SYSTEM WITH SYMMETRIC BEARING SUPPORT

5.1 3-Dimensional Rigid shaft/Rotor/Autobalancer system

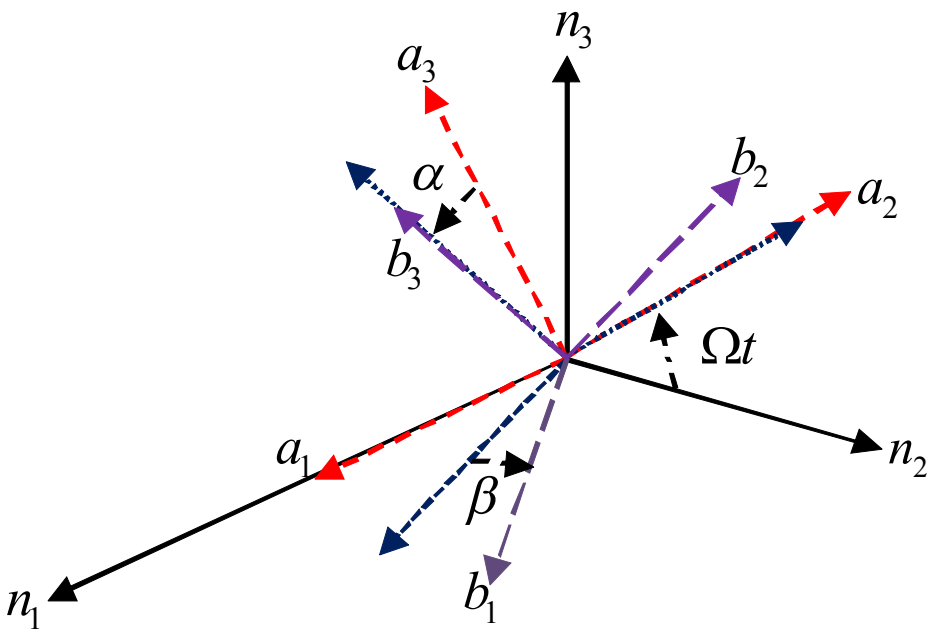
In this section, we present the mathematical model of the 3-D rigid shaft/rotor/Autobalancer system mounted on a linear symmetric bearing support. To facilitate analysis, the equations-of-motion for the dynamics of system are derived in a set of rotating coordinates, $\{a\}=\{a_1,a_2,a_3\}$, which follow the shaft rigid-body rotation, $\theta(t)$, about the $n_1$axis of the fixed frame $\{n\}=\{n_1,n_2,n_3\}$. The detail of coordinate transformation is described in Figure.5.1. The shaft is assumed to be driven with constant angular speed, Ω; hence $\theta(t)=\Omega t$.

The position vector locating point *C* on the shaft neutral axis at station *x* relative to point *O* is given by,

$$R_{OC}=v_r(x,t)a_2+w_r(x,t)a_3 \tag{5-1}$$

where $v_r(x,t)$ and $w_r(x,t)$ are the transverse deflections of the shaft neutral axis in the rotating frame.

To further describe the kinematics, a set of body-fixed coordinate, $\{b\}=\{b_1,b_2,b_3\}$, attached to the shaft cross section at station *x* is defined with transformation from $\{n\}$ to $\{a\}$ and from $\{a\}$ to $\{b\}$ given as,



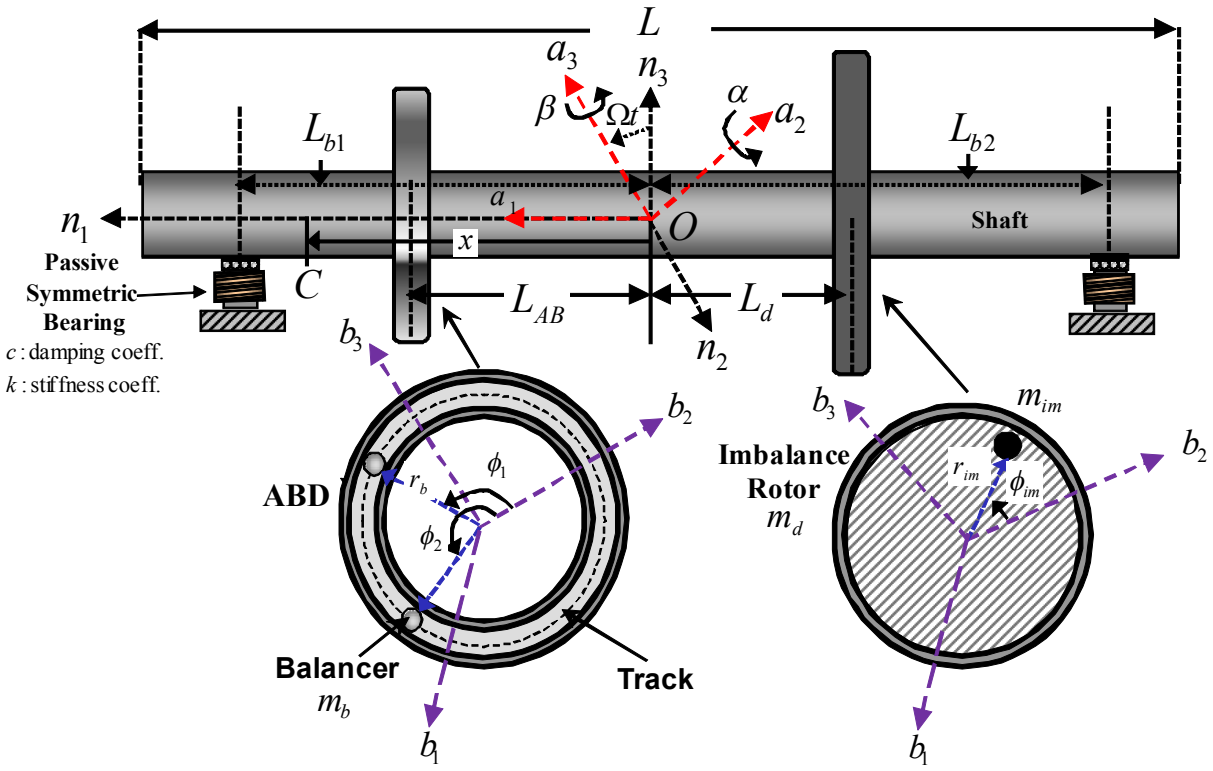


Figure.5.1 System coordinates transformation and three Dimensional Rigid shaft-rotor-ABD system supported by a passive symmetric bearing

$$\begin{bmatrix} a_1 \\ a_2 \\ a_3 \end{bmatrix} = \begin{bmatrix} 1 & 0 & 0 \\ 0 & \cos(\Omega t) & \sin(\Omega t) \\ 0 & -\sin(\Omega t) & \cos(\Omega t) \end{bmatrix} \begin{bmatrix} n_1 \\ n_2 \\ n_3 \end{bmatrix} \tag{5-2-a}$$

$$\begin{bmatrix} b_1 \\ b_2 \\ b_3 \end{bmatrix} = \begin{bmatrix} \cos(\beta) & \sin(\beta) & 0 \\ -\sin(\beta) & \cos(\beta) & 0 \\ 0 & 0 & 1 \end{bmatrix} \begin{bmatrix} \cos(\alpha) & 0 & -\sin(\alpha) \\ 0 & 1 & 0 \\ \sin(\alpha) & 0 & \cos(\alpha) \end{bmatrix} \begin{bmatrix} a_1 \\ a_2 \\ a_3 \end{bmatrix} \tag{5-2-b}$$

By assuming that both angles α and β are very small, we have $\cos(\alpha) \approx \cos(\beta) \approx 1$, $\sin(\alpha) \approx \alpha$, $\sin(\beta) \approx \beta$, and, $\alpha\beta \approx 0$. Hence, (5-2-b) have another form of transformation such that,

$$\begin{bmatrix} b_1 \\ b_2 \\ b_3 \end{bmatrix} = \begin{bmatrix} 1 & \beta & -\alpha \\ -\beta & 1 & 0 \\ \alpha & 0 & 1 \end{bmatrix} \begin{bmatrix} a_1 \\ a_2 \\ a_3 \end{bmatrix} \tag{5-2-c}$$

The position vector, R_{OB_i}, of the ith ball inside the autobalancer can be written as

$$R_{OB_i} = [R_{OC} + R_{CB_i}]\Big|_{x=L_{AB}} \quad for\ i = 1,2 \tag{5-3-a}$$

$$R_{CB_i} = r_b[\cos(\phi_i(t))b_2 + \sin(\phi_i(t))b_3]\Big|_{x=L_{AB}} \quad for\ i = 1,2 \tag{5-3-b}$$

Where r_b is the ball-track radius and $\phi_i(t)$ is the *i*-th ball angular position measured about b_1 axis.

The total system kinetic energy, *T*, in terms of shaft, disk, and autobalancer kinetic energies T_s, T_d, and T_{AB} is

$$T = T_s + T_d + T_{AB} \qquad \text{with} \tag{5-4-a}$$

$$T_s = [\frac{m_s}{2}(\dot{R}_{OC} \cdot \dot{R}_{OC}) + \frac{1}{2}(Jm_s{\omega_{B1}}^2 + Im_s{\omega_{B2}}^2 + Im_s{\omega_{B3}}^2]\Big|_{x=0} \tag{5-4-b}$$

$$T_d = [\frac{m_d}{2}(\dot{R}_{OC} \cdot \dot{R}_{OC}) + \frac{1}{2}(Jm_d{\omega_{B1}}^2 + Im_d{\omega_{B2}}^2 + Im_d{\omega_{B3}}^2]\Big|_{x=L_d} \tag{5-4-c}$$

$$T_{AB} = \sum_{i=1}^{2} \frac{m_b}{2}(\dot{R}_{OB_i} \cdot \dot{R}_{OB_i}) \tag{5-4-d}$$

Where "·" Indicates differentiation with respect to time, *t* . Also m_s, m_d and m_b are the mass of a shaft, a disk and a ball respectively, and Jm_s and Im_s are the shaft polar and transverse moment of inertia while Jm_d and Im_d are the disk polar and transverse moment of inertia. The transversal velocities in (5-4-a)-(5-4-d) are given by,

$$\dot{R}_{OC} = (\dot{v}_r - w_r\Omega)a_2 + (\dot{w}_r + v_r\Omega)a_3 \tag{5-5-a}$$

$$\dot{R}_{OB_i} = [\dot{R}_{OC} + r_b\dot{\phi}_i(t)[-\sin(\phi_i(t))b_2 + \cos(\phi_i(t))b_3] + {}^N\omega^B \times R_{CB_i}]\Big|_{x=L_{AB}} \tag{5-5-b}$$

with $\{b\}$ frame angular velocity vector ${}^N\omega^B$ given by

$${}^N\omega^B = \omega_{B1}b_1 + \omega_{B2}b_2 + \omega_{B3}b_3 \tag{5-6-a}$$

$$\omega_{B1} = \dot{\alpha}\beta + \Omega, \quad \omega_{B2} = \dot{\alpha} - \beta\Omega, \quad \omega_{B3} = \dot{\beta} + \alpha\Omega \tag{5-6-b}$$

The bearing strain energy U_b is

$$U_b = \frac{k}{2}\left[(v_r{}^2 + w_r{}^2)\Big|_{x=\frac{L_{b1}}{2}} + (v_r{}^2 + w_r{}^2)\Big|_{x=-\frac{L_{b2}}{2}}\right] \tag{5-7}$$

where *k* is the bearing stiffness. Furthermore, the total Rayleigh dissipation function, *D*, in terms of the bearing and ABD dissipation functions D_b and D_{AB} is expressed as

$$D = D_b + D_{AB} \tag{5-8-a}$$

with

$$D_b = \frac{c}{2}\left[(\dot{R}_{OC} \cdot \dot{R}_{OC})\Big|_{x=\frac{L_{b1}}{2}} + (\dot{R}_{OC} \cdot \dot{R}_{OC})\Big|_{x=-\frac{L_{b2}}{2}}\right] \tag{5-8-b}$$

$$D_{AB} = \sum_{i=1}^{2} \frac{c_b}{2} r_b{}^2\dot{\phi}_i(t)^2 \tag{5-8-c}$$

where c and c_b are the bearing damping coefficient and the viscous damping parameter due to balancer ball drag forces encountered during relative ball/track motion within ABD. Finally, the virtual work expression due to the rotor-disk mass imbalance is

$$\delta W_I = m_{im} r_{im} \Omega^2 [\cos(\phi_{im}) \delta v_r + \sin(\phi_{im}) \delta w_r]\Big|_{x=L_d} \tag{5-9}$$

where m_{im}, r_{im}, and ϕ_{im} are the imbalance mass, radial location, and phase angle, respectively.

Next, the coordinates $v_r(x,t)$ and $w_r(x,t)$ for the rigid shaft can be expressed in the following manner.

$$v_r(x,t) = v_r(0,t) + \beta(t)\, x \quad \text{and} \quad w_r(x,t) = w_r(0,t) - \alpha(t)\, x \tag{5-10}$$

Substituting (5-10) into Eqs. (5-4)-(5-9), the equation-of-motion are obtained via Lagrange's equations

$$\frac{d}{dt}\left[\frac{\partial T}{\partial \dot{q}}\right] - \frac{\partial T}{\partial q} + \frac{\partial U}{\partial q} + \frac{\partial D}{\partial \dot{q}} = Q_I \tag{5-11}$$

with the generalized coordinates $q(t) = \left[v_r(0,t) \quad w_r(0,t) \quad \alpha(t) \quad \beta(t) \quad \phi_1(t) \quad \phi_2(t)\right]$ and the generalized imbalance force vector Q_I satisfying $W_I = Q_I{}^T \delta q$.

The resulting nonlinear equation-of-motion of the shaft-disk-bearing autobalancer system are

$$M(\phi_1,\phi_2)\ddot{q} + C(\phi_1,\phi_2,\dot{\phi}_1,\dot{\phi}_2)\dot{q} + K(\phi_1,\phi_2,\dot{\phi}_1,\dot{\phi}_2,\ddot{\phi}_1,\ddot{\phi}_2)q = F(\phi_1,\phi_2,\dot{\phi}_1,\dot{\phi}_2) \tag{5-12-a}$$

with matrices and force terms decomposed in terms of the shaft, disk, and ABD subsystems as

$$\begin{aligned}
M &= N_s^T M_s N_s + N_d^T M_d N_d + N_{AB}^T M_{AB}(\phi_1,\phi_2) N_{AB} \\
C &= N_s^T C_s N_s + N_d^T C_d N_d + N_{AB}^T C_{AB}(\phi_1,\phi_2,\dot{\phi}_1,\dot{\phi}_2) N_{AB} + N_{b1}^T C_b N_{b1} + N_{b2}^T C_b N_{b2} \\
K &= N_s^T K_s N_s + N_d^T K_d N_d + N_{AB}^T K_{AB}(\phi_1,\phi_2,\dot{\phi}_1,\dot{\phi}_2,\ddot{\phi}_1,\ddot{\phi}_2) N_{AB} + N_{b1}^T K_b N_{b1} + N_{b2}^T K_b N_{b2} \\
F &= N_I^T F_I + N_{AB}^T F_{AB}(\phi_1,\phi_2,\dot{\phi}_1,\dot{\phi}_2)
\end{aligned} \tag{5-12-b}$$

with shaft subsystem matrices

$$M_s = \begin{bmatrix} m_s & 0 & 0 & 0 \\ 0 & m_s & 0 & 0 \\ 0 & 0 & Im_s & 0 \\ 0 & 0 & 0 & Im_s \end{bmatrix} \tag{5-13-a}$$

$$C_s = \Omega \begin{bmatrix} 0 & -2m_s & 0 & 0 \\ 2m_s & 0 & 0 & 0 \\ 0 & 0 & 0 & -2Im_s + Jm_s \\ 0 & 0 & 2Im_s - Jm_s & 0 \end{bmatrix} \tag{5-13-b}$$

$$K_s = \Omega^2 \begin{bmatrix} -m_s & 0 & 0 & 0 \\ 0 & -m_s & 0 & 0 \\ 0 & 0 & Jm_s - Im_s & 0 \\ 0 & 0 & 0 & Jm_s - Im_s \end{bmatrix} \tag{5-13-c}$$

Similarly, the rotor-disk subsystem matrices are

$$M_d = \begin{bmatrix} m_d & 0 & 0 & 0 \\ 0 & m_d & 0 & 0 \\ 0 & 0 & Im_d & 0 \\ 0 & 0 & 0 & Im_d \end{bmatrix} \tag{5-14-a}$$

$$C_d = \Omega \begin{bmatrix} 0 & -2m_d & 0 & 0 \\ 2m_d & 0 & 0 & 0 \\ 0 & 0 & 0 & -2Im_d + Jm_d \\ 0 & 0 & 2Im_d - Jm_d & 0 \end{bmatrix} \tag{5-14-b}$$

$$K_s = \Omega^2 \begin{bmatrix} -m_d & 0 & 0 & 0 \\ 0 & -m_d & 0 & 0 \\ 0 & 0 & Jm_d - Im_d & 0 \\ 0 & 0 & 0 & Jm_d - Im_d \end{bmatrix} \tag{5-14-c}$$

Furthermore, the bearing subsystem matrices are

$$C_b = \begin{bmatrix} c & 0 & 0 & 0 \\ 0 & c & 0 & 0 \\ 0 & 0 & 0 & 0 \\ 0 & 0 & 0 & 0 \end{bmatrix} \quad \text{and} \quad K_b = \begin{bmatrix} k & -c\Omega & 0 & 0 \\ c\Omega & k & 0 & 0 \\ 0 & 0 & 0 & 0 \\ 0 & 0 & 0 & 0 \end{bmatrix} \tag{5-15}$$

The ABD subsystem matrices and forcing terms are

$$M_{AB} = \begin{bmatrix} 2m_b & 0 & 0 & 0 & -m_b r_b \sin(\phi_1) & -m_b r_b \sin(\phi_2) \\ 0 & 2m_b & 0 & 0 & m_b r_b \cos(\phi_1) & m_b r_b \cos(\phi_2) \\ 0 & 0 & m_b r_b^2 \sum_{i=1}^{2} \cos(\phi_i)^2 & \frac{1}{2} m_b r_b^2 \sum_{i=1}^{2} \sin(2\phi_i) & 0 & 0 \\ 0 & 0 & \frac{1}{2} m_b r_b^2 \sum_{i=1}^{2} \sin(2\phi_i) & m_b r_b^2 \sum_{i=1}^{2} \sin(\phi_i)^2 & 0 & 0 \\ -m_b r_b \sin(\phi_1) & m_b r_b \cos(\phi_1) & 0 & 0 & m_b r_b^2 & 0 \\ -m_b r_b \sin(\phi_2) & m_b r_b \cos(\phi_2) & 0 & 0 & 0 & m_b r_b^2 \end{bmatrix} \tag{5-16-a}$$

$$C_{AB}=\begin{bmatrix} 0 & -4m_b\Omega & 0 & 0 & -2m_br_b\Omega\cos(\phi_1) & -2m_br_b\Omega\cos(\phi_2) \\ 4m_b\Omega & 0 & 0 & 0 & -2m_br_b\Omega\sin(\phi_1) & -2m_br_b\Omega\sin(\phi_2) \\ 0 & 0 & -m_br_b^{\,2}\sum_{i=1}^{2}\sin(\phi_i)\dot{\phi}_i & 2m_br_b^{\,2}\sum_{i=1}^{2}\cos(2\phi_i)^2\dot{\phi}_i & 0 & 0 \\ 0 & 0 & -2m_br_b^{\,2}\sum_{i=1}^{2}\cos(2\phi_i)^2\dot{\phi}_i & m_br_b^{\,2}\sum_{i=1}^{2}\sin(2\phi_i)\dot{\phi}_i & 0 & 0 \\ 2m_br_b\Omega\cos(\phi_1) & 2m_br_b\Omega\sin(\phi_1) & 0 & 0 & c_br_b^{\,2} & 0 \\ 2m_br_b\Omega\cos(\phi_2) & 2m_br_b\Omega\sin(\phi_2) & 0 & 0 & 0 & c_br_b^{\,2} \end{bmatrix} \tag{5-16-b}$$

$$K_{AB}=\begin{bmatrix} -2m_b\Omega^2 & 0 & 0 & 0 & 0 & 0 \\ 0 & -2m_b\Omega^2 & 0 & 0 & 0 & 0 \\ 0 & 0 & m_br_b^{\,2}(\Omega^2+\sum_{i=1}^{2}[2\Omega\dot{\phi}_i\cos(\phi_i)^2+\frac{1}{2}\Omega^2\cos(2\phi_i)]) & m_br_b^{\,2}(\sum_{i=1}^{2}[\sin(2\phi_i)(\frac{1}{2}\Omega^2+\Omega\dot{\phi}_i)+\frac{1}{2}\ddot{\phi}_i]) & 0 & 0 \\ 0 & 0 & m_br_b^{\,2}(\sum_{i=1}^{2}[\sin(2\phi_i)(\frac{1}{2}\Omega^2+\Omega\dot{\phi}_i)-\frac{1}{2}\ddot{\phi}_i]) & m_br_b^{\,2}(\Omega^2+\sum_{i=1}^{2}[2\Omega\dot{\phi}_i\sin(\phi_i)^2-\frac{1}{2}\Omega^2\cos(2\phi_i)]) & 0 & 0 \\ m_br_b\Omega^2\sin(\phi_1) & -m_br_b\Omega^2\cos(\phi_1) & 0 & 0 & 0 & 0 \\ m_br_b\Omega^2\sin(\phi_2) & -m_br_b\Omega^2\cos(\phi_2) & 0 & 0 & 0 & 0 \end{bmatrix} \tag{5-16-c}$$

$$F_{AB}=m_br_b\begin{bmatrix}\sum_{i=1}^{2}\cos(\phi_i)(\Omega^2+\dot{\phi}_i) & \sum_{i=1}^{2}\sin(\phi_i)(\Omega^2+\dot{\phi}_i) & 0 & 0 & 0 & 0\end{bmatrix}^T \tag{5-16-d}$$

Finally, the imbalance force due to rotor disk eccentricity is

$$F_I=m_{im}r_{im}\Omega^2\begin{bmatrix}\cos(\phi_{im}) & \sin(\phi_{im}) & 0 & 0 & 0 & 0\end{bmatrix}^T \tag{5-17}$$

The mapping matrices N_s, N_d, N_b, and N_{AB} expressed in (5-12-b) are given below.

$$\begin{aligned} N_S&=\begin{bmatrix}I_{4\times4} & 0_{4\times2}\end{bmatrix}_{x=0} \quad \text{and} \quad N_d=\begin{bmatrix}N_c(x) & 0_{4\times2}\end{bmatrix}_{x=L_d} \\ N_{b1}&=\begin{bmatrix}N_c(x) & 0_{4\times2}\end{bmatrix}_{x=L_{b1}} \quad \text{and} \quad N_{b2}=\begin{bmatrix}N_c(x) & 0_{4\times2}\end{bmatrix}_{x=L_{b2}} \\ N_{AB}&=\begin{bmatrix}N_c(x) & 0_{4\times2} \\ 0_{2\times4} & 0_{2\times2}\end{bmatrix}_{x=L_{AB}} \quad \text{and} \quad N_I=\begin{bmatrix}N_c(x) & 0_{4\times2} \\ 0_{2\times4} & 0_{2\times2}\end{bmatrix}_{x=L_d} \end{aligned} \tag{5-18}$$

$$\text{with} \quad N_c(x)=\begin{bmatrix}1 & 0 & 0 & x \\ 0 & 1 & -x & 0 \\ 0 & 0 & 1 & 0 \\ 0 & 0 & 0 & 1\end{bmatrix}$$

5.2 Limit-cycle Response

In this section, the assumed limit-cycle solution of the 3-D system derived in previous section is presented to reveal the inherent characteristic of the non synchronous limit cycle behavior. Since the dynamic system includes both in-plane transverse deflection and out-planes tilting motion with gyroscopic effect, the limit-cycle solution presented here captures these two motions. The solution is assumed as the

harmonic type one. Thus, using the harmonic balancing technique, we generate the set of nonlinear equations to solve the unknown parameters of the solution.

For further derivation, we make the following assumptions.

i) Under the limit-cycle condition, two balls are merged and rotated together so that one ball motion is absorbed into another. Consequently, the coordinate of system in (5-12) is reduced into $q(t)=[v_r(0,t) \quad w_r(0,t) \quad \alpha(t) \quad \beta(t) \quad \phi(t)]$ and the mass of merged two balls described as $\phi(t)$ is simply defined as $m_{b.m}$ equivalent to the mass of two balls (i.e, $m_{b.m}=2m_b$). Also, it should be noted that the contact mechanism of two balls is out of our research scope. Based upon [16] also characterized the balanced equilibrium attraction basin as a function of ball initial position, the non-synchronous limit cycle behavior is mostly created by setting that the initial angular position of two ABD-balls is located near for each other or identically. Reversely, if one ball is initially stayed away from another, the system is highly subject to the stable synchronous behavior due to the different angular phase between two balls according to [16]. Thus, the merging situation of two balls is highly probable under limit cycle condition. *ii)* The ball speed denoted as ω is assumed to be constant under the limit-cycle condition due to symmetric bearing support and circular track of ABD. Hence, we have, $\dot{\phi}(t)=\omega \Rightarrow \phi(t)=\omega t$ and $\ddot{\phi}=0$.

Next, the harmonic solution of the limit-cycle is assumed to be

$$\begin{aligned} v_r(0,t) &= a\cos[\omega t+\gamma]+v_{r0} \quad & w_r(0,t) &= a\sin[\omega t+\gamma]+w_{r0} \\ \alpha(t) &= b\cos[\omega t+\delta]+\alpha_0 \quad & \beta(t) &= b\cos[\omega t+\delta]+\beta_0 \end{aligned} \tag{5-19}$$

where, a and b are unknown amplitudes, ω is the whirl speed of merged ABD ball(i.e, balancer mass), γ and δ are the phase and v_{r0}, w_{r0}, α_0, and β_0 are constant offsets to be solved.

Applying the reduced coordinates assumed above into the original dynamics (5-12), substituting (5-19) into the version of (5-12) with reduced $q(t)=[v_r(0,t) \quad w_r(0,t) \quad \alpha(t) \quad \beta(t) \quad \phi(t)]$and rearranging it in terms of each harmonic yields five equations (5-20) through (5-24),

$$A_{10}+A_{11}\cos(\omega t)+A_{12}\sin(\omega t)=0 \tag{5-20}$$

where,

$$\begin{aligned} A_{10} &= [2k-m_t\Omega^2]v_{r0}+[-2c\Omega]w_{r0}+[c(L_{b1}+L_{b2})\Omega]\alpha_0+[k(L_{b1}+L_{b2})-(m_{b.m}L_{AB}+m_dL_d)\Omega^2]\beta_0-m_{im}r_{im}\Omega^2\cos(\phi_{im}) \\ A_{11} &= -m_{b.m}r_b(\Omega+\omega)^2-2ac(\Omega+\omega)\sin(\gamma)+a[2k-m_t(\Omega+\omega)^2]\cos(\gamma)+b[k(L_{b1}+L_{b2})-(m_{b.m}L_{AB}+m_dL_d)(\omega+\Omega)]\sin(\delta)+\cdots \\ &\quad \cdots+bc(L_{b1}+L_{b2})(\omega+\Omega)\cos(\delta) \\ A_{12} &= -2ac(\Omega+\omega)\sin(\gamma)+a[2k-m_t(\Omega+\omega)^2]\cos(\gamma)-bc(L_{b1}+L_{b2})(\omega+\Omega)\sin(\delta)-b[k(L_{b1}+L_{b2})-\cdots \\ &\quad \cdots-(m_{b.m}L_{AB}+m_dL_d)(\omega+\Omega)]\cos(\delta) \end{aligned}$$

$$A_{20}+A_{21}\cos(\omega t)+A_{22}\sin(\omega t)=0 \tag{5-21}$$

where, $A_{21} = -A_{12}$, $A_{22} = -A_{11}$, and,

$$A_{20} = [2c\Omega]v_{r0} + [2k - m_t\Omega^2]w_{r0} - [k(L_{b1} + L_{b2}) - (m_{b.m}L_{AB} + m_d L_d)\Omega^2]\alpha_0 + [c(L_{b1} + L_{b2})\Omega]\beta_0 - m_{im}r_{im}\Omega^2 \sin(\phi_{im})$$

$$A_{30} + A_{31}\cos(\omega t) + A_{32}\sin(\omega t) + H.O.T_3 = 0 \tag{5-22}$$

where,

$$A_{30} = [-c(L_{b1} + L_{b2})\Omega]v_{r0} - [k(L_{b1} + L_{b2}) - (m_{b.m}L_{AB} + m_d L_d)\Omega^2]w_{r0} + [k(L_{b1}^2 + L_{b2}^2) - \Omega^2(Im_d + Im_s - Jm_d + m_{b.m}L_{AB}^2 + m_r L_d^2 + \cdots$$
$$\cdots + 0.5m_{b.m}r_b^2)]\alpha_0 - [c(L_{b1}^2 + L_{b2}^2)\Omega]\beta_0 + L_d m_{im} r_{im}\Omega^2 \sin(\phi_{im})$$

$$A_{31} = -a[k(L_{b1} + L_{b2}) - (m_{b.m}L_{AB} + m_d L_d)(\omega + \Omega)^2]\sin(\gamma) - a[c(L_{b1} + L_{b2})(\Omega + \omega)]\cos(\gamma) - bc(L_{b1}^2 + L_{b2}^2)(\omega + \Omega)\sin(\delta) - \cdots$$
$$-b[-k(L_{b1}^2 + L_{b2}^2) + \Omega^2(Im_d + Im_s - Jm_d + L_{AB}^2 m_{b.m} + L_d^2 m_d - 0.5m_{b.m}r_b^2) + 2\Omega\omega(Im_d + Im_s - 0.5Jm_d + 2m_b L_{AB}^2 + m_d L_d^2) + \cdots$$
$$\cdots + \omega^2(Im_d + Im_s + L_{AB}^2 m_{b.m} + L_d^2 m_d + 0.5m_{b.m}r_b^2)]\cos(\delta)$$

$$A_{32} = m_{b.m}r_b(\Omega + \omega)^2 L_{AB} + a[c(L_{b1} + L_{b2})(\Omega + \omega)\sin(\gamma) - a(k(L_{b1} + L_{b2}) - (m_{b.m}L_{AB} + m_d L_d)(\omega + \Omega)^2]\cos(\gamma) + \cdots$$
$$\cdots + b[-k(L_{b1}^2 + L_{b2}^2) + \Omega^2(Im_d + Im_s - Jm_d + L_{AB}^2 m_{b.m} + L_d^2 m_d - m_{b.m}r_b^2) + 2\Omega\omega(Im_d + Im_s - 0.5Jm_d + m_{b.m}L_{AB}^2 + m_d L_d^2) + \cdots$$
$$\cdots + \omega^2(Im_d + Im_s + L_{AB}^2 m_{b.m} + L_d^2 m_d)]\sin(\delta) - bc(L_{b1}^2 + L_{b2}^2)(\omega + \Omega)\cos(\delta)$$

$$H.O.T_3 = \frac{1}{4}m_{b.m}r_b^2\Omega(2\omega + \Omega)(0.5\alpha_0 \sin(2\omega t) + \alpha_0 \sin(\omega t)^2 + 4\beta_0 \cos(\omega t)^2)$$

$$A_{40} + A_{41}\cos(\omega t) + A_{42}\sin(\omega t) + H.O.T_4 = 0 \tag{5-23}$$

where, $A_{41} = -A_{32}$, $A_{42} = -A_{31}$, and

$$A_{40} = [k(L_{b1} + L_{b2}) - (m_{b.m}L_{AB} + m_d L_d)\Omega^2]v_{r0} - [c(L_{b1} + L_{b2})\Omega]w_{r0} + [c(L_{b1}^2 + L_{b2}^2)\Omega]\alpha_0 + [k(L_{b1}^2 + L_{b2}^2) - \cdots$$
$$\cdots - \Omega^2(Im_d + Im_s - Jm_d + m_{b.m}L_{AB}^2 + m_r L_d^2 + 0.5m_{b.m}r_b^2)]\beta_0 - L_d m_{im} r_{im}\Omega^2 \cos(\phi_{im})$$

$$H.O.T_4 = \frac{1}{4}m_{b.m}r_b^2\Omega(2\omega + \Omega)(0.5\beta_0 \sin(2\omega t) - \beta_0 \sin(\omega t)^2 - 4\alpha_0 \cos(\omega t)^2)$$

$$\begin{aligned} &c_b r_b \omega - a m_{b.m}(\Omega + \omega)^2 \sin(\gamma) + b m_{b.m} L_{AB}(\Omega + \omega)^2 \cos(\delta) + \cdots \\ &+ m_{b.m}\Omega^2(\alpha_0 L_{AB} - w_{r0})\cos[\omega t] + m_{b.m}\Omega^2(\beta_0 L_{AB} + v_{r0})\sin[\omega t] = 0 \end{aligned} \tag{5-24}$$

where $m_t = m_s + m_d + m_{b.m}$. Again, it should be noted that $m_{b.m} = 2m_b$.

Then, from (5-20) and (5-21), we have four nonlinear equations using harmonic balancing method such that,

$$A_{11} = -A_{22} = 0 \tag{5-25}$$

$$A_{12} = -A_{21} = 0 \tag{5-26}$$

$$A_{10} = 0 \tag{5-27}$$

$$A_{20} = 0 \tag{5-28}$$

From (5-22) and (5-23), we observe the high order time-varying terms. For approximation, truncating the high order terms, we also have four nonlinear equations such that,

$$A_{31} = -A_{42} = 0 \tag{5-29}$$

$$A_{32} = -A_{41} = 0 \tag{5-30}$$

$$A_{30} = 0 \tag{5-31}$$

$$A_{40} = 0 \tag{5-32}$$

Also, the time-varying terms are appeared in (5-24). Since the whirl speed of ABD-ball is assumed to be constant, the time-varying terms are dropped out for approximation. Thus, we have,

$$c_b r_b \omega - a\, m_{b.m} (\Omega + \omega)^2 \sin(\gamma) + b\, m_{b.m} L_{AB} (\Omega + \omega)^2 \cos(\delta) = 0 \tag{5-33}$$

Now, we can solve five unknowns; amplitudes (a and b), phases(γ and δ) and whirl speed (ω) from five nonlinear equations (5-25),(5-26),(5-29), (5-30), and (5-33). In this paper, the arc-length numerical continuation method is utilized to solve for these unknowns.

Also, from (5-27), (5-28), (5-31), and (5-32), the unknown offsets v_{r0}, w_{r0}, α_0, and β_0 can be directly solved by,

$$\begin{bmatrix} v_{r0} \\ w_{r0} \\ \alpha_0 \\ \beta_0 \end{bmatrix} = S^{-1} \cdot T \tag{5-34}$$

where,

$$S = \begin{bmatrix} 2k - m_t\Omega^2 & -2c\Omega & c(L_{b1} + L_{b2})\Omega & k(L_{b1} + L_{b2}) - Q\Omega^2 \\ 2c\Omega & 2k - m_t\Omega^2 & -[k(L_{b1} + L_{b2}) - Q\Omega^2] & c(L_{b1} + L_{b2})\Omega \\ -c(L_{b1} + L_{b2})\Omega & -k(L_{b1} + L_{b2}) + Q\Omega^2 & k(L_{b1}^{\,2} + L_{b2}^{\,2}) - \Omega^2 R & -c(L_{b1}^{\,2} + L_{b2}^{\,2})\Omega \\ k(L_{b1} + L_{b2}) - Q\Omega^2 & -c(L_{b1} + L_{b2})\Omega & c(L_{b1}^{\,2} + L_{b2}^{\,2})\Omega & k(L_{b1}^{\,2} + L_{b2}^{\,2}) - \Omega^2 R \end{bmatrix}$$

$$T = m_{im} r_{im} \Omega^2 \begin{bmatrix} \cos(\phi_{im}) \\ \sin(\phi_{im}) \\ -L_d \sin(\phi_{im}) \\ L_d \cos(\phi_{im}) \end{bmatrix}$$

$R = Im_d + Im_s - Jm_d + m_{b.m} L_{AB}^{\,2} + m_r L_d^{\,2} + 0.5 m_{b.m} r_b^{\,2}$ and $Q = m_{b.m} L_{AB} + m_d L_d$.

These offsets are computed by the size of imbalance mass, inherent characteristic of bearing and rotor/shaft system as well as operating speed. As imbalance size increase, these offsets are also augmented.

Let's revisit the high order time-varying dropped out for approximation. The higher order time-varying terms(i.e, *H.O.T3* and *H.O.T4*) truncated in (5-22) and (5-23) as well as terms in (5-24) are followed.

$$\begin{aligned} &\frac{1}{4} m_{b.m} r_b^{\,2} \Omega (2\omega + \Omega)(0.5\alpha_0 \sin(2\omega t) + \alpha_0 \sin(\omega t)^2 + 4\beta_0 \cos(\omega t)^2) \\ &\frac{1}{4} m_{b.m} r_b^{\,2} \Omega (2\omega + \Omega)(0.5\beta_0 \sin(2\omega t) - \beta_0 \sin(\omega t)^2 - 4\alpha_0 \cos(\omega t)^2) \\ &m_{b.m} \Omega^2 (\alpha_0 L_{AB} - w_{r0}) \cos[\omega t] + m_{b.m} \Omega^2 (\beta_0 L_{AB} + v_{r0}) \sin[\omega t] \end{aligned} \tag{5-35}$$

The influence of these three time varying terms is determined by the size of imbalance mass. In (5-35), each term holds the offsets (v_{r0}, w_{r0}, α_0, and β_0), which is proportional to the imbalance effect as seen in (5-34).

The effect should be insignificant not to heavily deteriorate the accuracy of suggested solution. Fortunately, the effect of time-varying terms are less important in the two following reasons. *i*) v_{r0}, w_{r0}, α_0, and β_0 which are directly proportional to the size of imbalance mass. The best performance of ABD can be usually achieved under the condition $m_{im} < 2m_b = m_{b.m}$ if $r_{im} = r_b$. Under this condition $m_{im} < 2m_b$, the effect of time-varying terms can be insignificant. In other words, there exists allowable imbalance size not to heavily deteriorate the accuracy of the limit cycle solution suggested here. *ii*) The inherent nature of limit cycle related with the whirl speed of ABD-ball dominates the imbalance effect so that the time-varying terms in (5-35) directly associated with imbalance can be less important contribution to the solution. These two conditions above enhance us to achieve the well approximated solution and these aspects will be explained with and validated through the numerical simulation results.

5.3 Stability analysis

In this section, the stability analysis about non-synchronous limit cycle, synchronous balanced condition as well as synchronous merged case of ABD is presented.

First, to investigate the local stability of the system in the neighborhood of the limit-cycle solution founded in previous sections, (5-12) with $q(t) = [v_r(0,t) \quad w_r(0,t) \quad \alpha(t) \quad \beta(t) \quad \phi(t)]$ is linearized using the perturbation approach. By considering the small perturbations such that $\Delta v_L(0,t)$, $\Delta w_L(0,t)$, $\Delta \alpha_L(t)$, $\Delta \beta_L(t)$ and $\Delta \phi_L(t)$, the perturbed system configurations are $v_r(0,t) = v_L(0,t) + \Delta v_L(0,t), w_r(0,t) = w_L(0,t) + \Delta w_L(0,t)$, $\alpha(t) = \alpha_L(t) + \Delta \alpha_L(t), \beta(t) = \beta_L(t) + \Delta \beta_L(t)$ and $\phi(t) = \phi_L(t) + \Delta \phi_L(t)$, where $v_L(0,t), w_L(0,t), \alpha_L(t), \beta_L(t)$ and $\phi_L(t)$ are the limit-cycle harmonic solutions in (5-19). Substituting this perturbed configuration into the dynamics (5-12), and truncating the higher order terms results in a set of linearized equation about the set of limit-cycle solution. Denoting a set of the perturbed coordinate as $\Delta q_L = [\Delta v_L(t) \; \Delta w_L(t) \; \Delta \alpha_L(t) \; \Delta \beta_L(t) \; \Delta \phi_L(t)]^T \in \Re^5$ and a set of limit-cycle solution as $q_L = [v_L(t) \; w_L(t) \; \alpha_L(t) \; \beta_L(t) \; \phi_L(t)]^T \in \Re^5$, we have a linearized equation about Δq_L from (5-12),

$$\Delta M(q_L, t)\Delta \ddot{q}_L + \Delta C(q_L, t)\Delta \dot{q}_L + \Delta K(q_L, t)\Delta q_L = 0 \tag{5-36}$$

Defining the state vector $x(t) = [\Delta q_L{}^T \; \Delta \dot{q}_L{}^T]^T \in \Re^{10}$, we can transform (5-36) into,

$$\dot{x}(t) = A(q_L, t)x(t) \tag{5-37}$$

with a system matrix

$$A(q_L,t) = \begin{bmatrix} 0 & I \\ -\Delta M^{-1}(q_L,t)\Delta K(q_L,t) & -\Delta M^{-1}(q_L,t)\Delta C(q_L,t) \end{bmatrix} \in \Re^{10\times 10}$$

To determine the stability of (5-37) which is the linear time-varying equation, we employ the Floquet's Transition Matrix (FTM) method. By the linear theory, the solution for (5-37) is expressed as

$$x(t) = \Phi(q_L, t)x_0 \tag{5-38}$$

where, $\Phi(q_L, t) \in \Re^{10\times 10}$ and $x_0 \in \Re^{10}$ are FTM and the initial condition respectively.

Replacing the x_0 as the 10 by 10 an identical matrix, $x(t)$ becomes 10 by 10 matrix solution and then, with the period $T = \frac{2\pi}{\omega}$, we can obtain the periodic solution such that $x(T) = \Phi(q_L, T)$. Ultimately, the stability criterion is determined by

$$\begin{aligned} &\max_{1\le i\le 10} |\lambda_i(x(T))| < 1 \quad stable \\ &\max_{1\le i\le 10} |\lambda_i(x(T))| > 1 \quad unstable \end{aligned} \tag{5-39}$$

where λ_i is the eigenvalues of matrix solution $x(T) = \Phi(q_L, T)$.

To investigate the local stability of system about a fixed balanced equilibrium solution, (5-12) with full-coordinates $q(t) = [v_r(0,t)\ \ w_r(0,t)\ \ \alpha(t)\ \ \beta(t)\ \ \phi_1(t)\ \ \phi_2(t)]$ is linearized using perturbation method with perturbed system coordinates $v_r(t) = v_{eq}(t) + \Delta v_{eq}(t)$, $w_r(t) = w_{eq}(t) + \Delta w_{eq}(t)$, $\alpha(t) = \alpha_{eq}(t) + \Delta\alpha_{eq}(t)$, $\beta(t) = \beta_{eq}(t) + \Delta\beta_{eq}(t)$, and $\phi_{eq.i}(t) = \phi_{eq.i}(t) + \Delta\phi_{eq.i}(t)$ *for* $i = 1,2$ and, by substituting the perturbed coordinates into (5-12) and truncating the higher order terms, we have a linear time-invariant(LTI) equation describing the perturbed coordinate $\Delta q = [\Delta v_{eq}(t)\ \Delta w_{eq}(t)\ \Delta\alpha_{eq}(t)\ \Delta\beta_{eq}(t)\ \Delta\phi_{eq.1}(t)\ \ \Delta\phi_{eq2}(t)]^T \in \Re^6$.

Based upon this equation, the simple eigenvalue analysis can be applied to determine the local stability about the fixed equilibrium point $q_{eq} = [v_{eq}(t)\ w_{eq}(t)\ \alpha_{eq}(t)\ \beta_{eq}(t)\ \phi_{eq1}(t)\ \ \phi_{eq2}(t)]^T \in \Re^6$. The fixed balancing position $q_{eq1} = [v_{eq}(t)\ w_{eq}(t)\ \alpha_{eq}(t)\ \beta_{eq}(t)]^T \in \Re^4$ is computed as,

$$\begin{aligned} q_{eq.1} = [&K_s + N_c^T K_d N_c\,|_{x=L_d} + N_c^T K_{AB.1}(\phi_{1.eq}, \phi_{2.eq}) N_c\,|_{x=L_{AB}} + N_c^T K_b N_c\,|_{x=L_{b1}} + \cdots \\ &\cdots + N_c^T K_b N_c\,|_{x=L_{b2}}]^{-1}[N_c^T F_{I.1}\,|_{x=L_d} + N_c^T F_{AB.1}(\phi_{1.eq}, \phi_{2.eq})\,|_{x=L_{AB}}] \end{aligned} \tag{5-40}$$

where,

$$K_{AB.1}=m_b\begin{bmatrix} -2\Omega^2 & 0 & 0 & 0 \\ 0 & -2\Omega^2 & 0 & 0 \\ 0 & 0 & r_b{}^2(\Omega^2+\sum_{i=1}^{2}\frac{1}{2}\Omega^2\cos(2\phi_{i.eq})) & r_b{}^2(\sum_{i=1}^{2}[\sin(2\phi_{i.eq})\frac{1}{2}\Omega^2]) \\ 0 & 0 & r_b{}^2(\sum_{i=1}^{2}[\sin(2\phi_{i.eq})\frac{1}{2}\Omega^2]) & r_b{}^2(\Omega^2+\sum_{i=1}^{2}[-\frac{1}{2}\Omega^2\cos(2\phi_{i.eq})]) \end{bmatrix}$$

$$F_{AB.1}=m_b r_b\begin{bmatrix}\sum_{i=1}^{2}\cos(\phi_{i.eq})\Omega^2 & \sum_{i=1}^{2}\sin(\phi_{i.eq})\Omega^2 & 0 & 0\end{bmatrix}^T$$

$$F_{I.1}=m_{im}r_{im}\Omega^2\begin{bmatrix}\cos(\phi_{im}) & \sin(\phi_{im}) & 0 & 0\end{bmatrix}^T$$

$q_{eq2}=\begin{bmatrix}\phi_{eq.1}(t) & \phi_{eq2}(t)\end{bmatrix}^T=\begin{bmatrix}\phi_{bal1}{}^* & \phi_{bal2}{}^*\end{bmatrix}^T$ is used for ABD-ball position where, $\phi_{bal.i}{}^*=\phi_{im}\pm\cos^{-1}[-\delta]\ for\ i=1,2$, where, $\delta=\frac{m_{im}r_{im}}{2m_b r_b}$ and this balanced solution exists under the condition of $\delta\le 1$. The subsequent stability analysis of the balanced solution is conducted in the neighborhood of $[q_{eq.1}\quad q_{eq.2}]^T$. Additionally, the synchronous merged equilibrium solution where two balls are merged and synchronous with the operating speed of system is also considered on the subsequent stability analysis. This equilibrium solution is specified as $\phi_{megi}=\phi_{im}\pm\pi\ or\ \phi_{im}\qquad for\ i=1,2$ with the corresponding steady-state amplitude $q_{meg1}=\begin{bmatrix}v_{meg}(t) & w_{meg}(t) & \alpha_{meg}(t) & \beta_{meg}(t)\end{bmatrix}^T\in\Re^4$ assessed by

$$\begin{aligned} q_{meg.1}=&[K_s+N_c^TK_dN_c\,|_{x=L_d}+N_c^TK_{AB.1}(\phi_{meg.i})N_c\,|_{x=L_{AB}}+N_c^TK_bN_c\,|_{x=L_{b1}}+\cdots \\ &\cdots+N_c^TK_bN_c\,|_{x=L_{b2}}]^{-1}[N_c^TF_{I.1}\,|_{x=L_d}+N_c^TF_{AB.1}(\phi_{meg.i})\,|_{x=L_{AB}}] \end{aligned} \tag{5-41}$$

The simple eigenvalue analysis is also utilized to assess the local stability about the merged equilibrium position.

5.4 Numerical Simulation Results

In this section, the response of limit-cycle solution suggested here is validated by comparing it with full-nonlinear numerical simulation of (5-12) and the stability of three solutions presented in previous section is also assessed here.

The unknowns of solution in (5-19) are obtained by solving the set of nonlinear equations obtained in (5-25),(5-26),(5-29), (5-30), and (5-33) with (5-34).

Before proceeding, it should be noted that dimensionless operating speed $\overline{\Omega}$ introduced here is defined by $\frac{\Omega}{\omega_n}$ where, $\omega_n=\sqrt{\frac{k}{(m_d+m_s)}}$ and $k=500N/m$, $m_s=10kg$, $m_d=5kg$, $Im_d=\frac{1}{4}m_d r_d{}^2$, $Jm_r=\frac{1}{2}m_d r_d{}^2$, $Im_s=\frac{1}{12}m_s L^2$, $Jm_s=0$, $c_b=1e-4$, $L_{b1}=0.5L$, $L_{b2}=-0.5L$, $r_b=r_{im}=0.06\,m$, $L=0.75m$ and $\phi_{im}=45^\circ$ are commonly used for the all simulations presented here unless specified otherwise.

In Figure.5.2, we compare the limit-cycle solution in (5-19) with the numerical simulation of full nonlinear system in (5-12) which is constructed in MATLAB/Simulink environment. For the simplicity, throughout this paper, we use the short notations **LC** for the approximated analytical limit cycle solution and **FS** for the numerical results obtained through the full nonlinear simulation. In **FS**, the limit-cycle condition can be also generated by setting the initial condition leading to the outside of the provided attraction basin described in [16]. Thus, the initial position of two balls is presumed to be merged on the full nonlinear simulation such that, $\phi_1(0) = \phi_2(0)$. In *a*) and *b*) of Figure.5.2, the star-dotted lines represent the responses obtained via **FS** while the circle dotted lines do **LC**. *a*) and *b*) respectively represent the whirl orbit of in-plane transverse deflection at $\overline{\Omega} = 2.2$ and the whirl orbit of tilting out-plane angle at $\overline{\Omega} = 5.2$ commonly with $L_d = 0.25L$ and $L_{AB} = -0.1L$. In *c*) and *d*), the whirl orbits are obtained with $\overline{\Omega} = 2.5$ and $\overline{\Omega} = 7.0$ at given location $L_d = 0.025L$ and $L_{AB} = 0.2L$. Both **LC** and **FS** are synchronous for each other in *a*) through *d*). The whirl orbits displayed are perfectly circular ones due to the symmetric property of bearing support. In *e*) and *f*), the straight line on the time domain is the relative whirl speed of merged ABD's ball to the rotor from **LC** and the fluctuating lines belong to **FS**. The results in *e*) and *f*) are respectively obtained at $\overline{\Omega} = 2.5$ and $\overline{\Omega} = 5.0$ commonly using $L_d = 0.025L$ and $L_{AB} = 0.2L$. Since the effect of time-varying terms are truncated to obtain the assumed whirl speed of ABD's ball in **LC**, the fluctuating whirl speed of **FS** can't be captured by **LC.** However, the fluctuating amplitudes of whirl speed in **FS** are very small although they increase as the size of imbalance mass is augmented and the whirl speed in **LC** approximate the average of whirl speed in **FS**. The results in *e*) and *f*) support that the effect of time-varying terms truncated is proportional to the imbalance size as expected from (5-34) and (5-35) and those terms in (5-35) are insignificant under relative reasonable size of imbalance mass to balancer mass of ABD. Furthermore, in (*g*), one can see that the whirl speed (straight line) of **LC** obtained at each operating speed can capture the average of the numerically simulated ball speed (circle dots) collected for a certain sampling period at a given operating speed(i.e, $0.5\left[\max_{T-t_a<t<T}\omega_s(t) + \min_{T-t_a<t<T}\omega_s(t)\right]$ where $\omega_s(t)$ is whirl speed in **FS** and T and t_a are the end of simulation time and the sampling period). Along with the average speed at each operating speed, the minimum $\min_{T-t_a<t<T}\omega_s(t)$ and maximum $\max_{T-t_a<t<T}\omega_s(t)$ of ball speed are specified as star and triangular dots respectively. It is founded that the difference between $\min_{T-t_a<t<T}\omega_s(t)$ and $\max_{T-t_a<t<T}\omega_s(t)$ is very small. Also, *h*) in Figure.5.2 displays the difference between $\min_{T-t_a<t<T}\omega_s(t)$ and $\max_{T-t_a<t<T}\omega_s(t)$ relative to $0.5\left[\max_{T-t_a<t<T}\omega_s(t) + \min_{T-t_a<t<T}\omega_s(t)\right]$ and *d* in *h*) can be computed in the following manner such that,

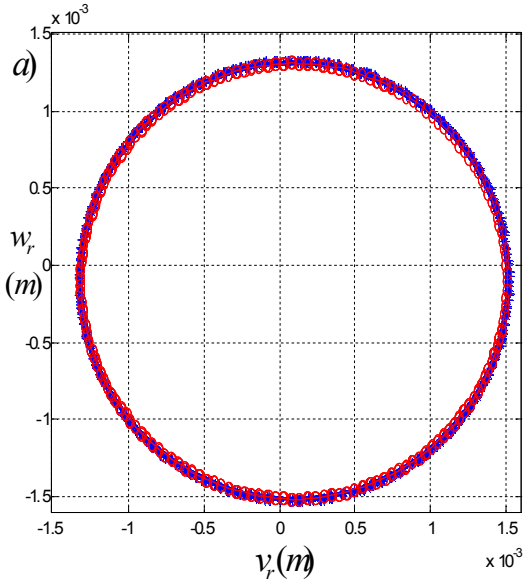
$$d = 2\frac{\max\limits_{T-t_a<t<T}\omega_s(t) - \min\limits_{T-t_a<t<T}\omega_s(t)}{\max\limits_{T-t_a<t<T}\omega_s(t) + \min\limits_{T-t_a<t<T}\omega_s(t)}$$

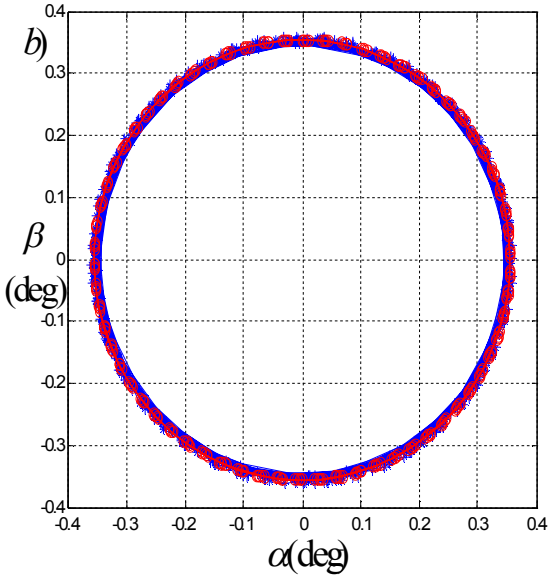
At the range of each supercritical operating speed, d is below 4% for all cases of imbalance mass in h) although d is up to more than 10% near each critical speed. However, the limit-cycle appeared in the supercritical speed is more critical issue than one below or near critical speed.

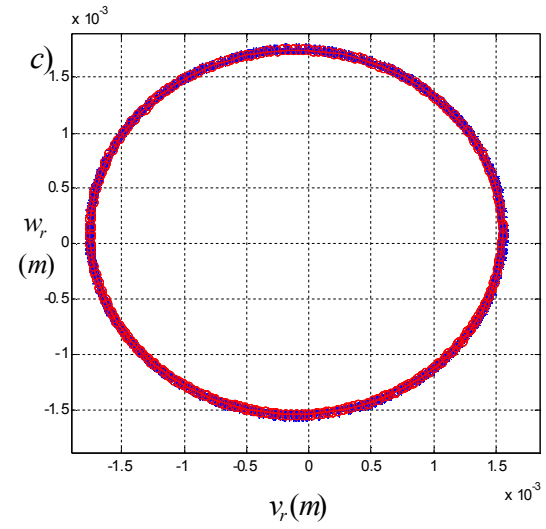
In i), the maximum amplitude of $v_r(0,t)$ is illustrated at given each operating speed. The star dotted lines represent the maximum of amplitude in **LC** computed by $a + w_{r0}$ while the circle dots describe **FS** obtained through $\max\limits_{T-t_a<t<T} v_{r.s}(0.t)$ where $v_{r.s}(0.t)$ is the vertical deflection of **FS**. In (j), the maximum pitch angle $\alpha(t)$ of system is illustrated at given each operating speed. The star dotted lines represent the maximum of angle in **LC** computed by $b + \alpha_0$ while the circle dots describe **FS** obtained through $\max\limits_{T-t_a<t<T} \alpha_s(t)$ where $\alpha_s(t)$ is system pitch angle in **FS**. $L_d = 0.025L$ and $L_{AB} = 0.2L$ are used in both i) and j).

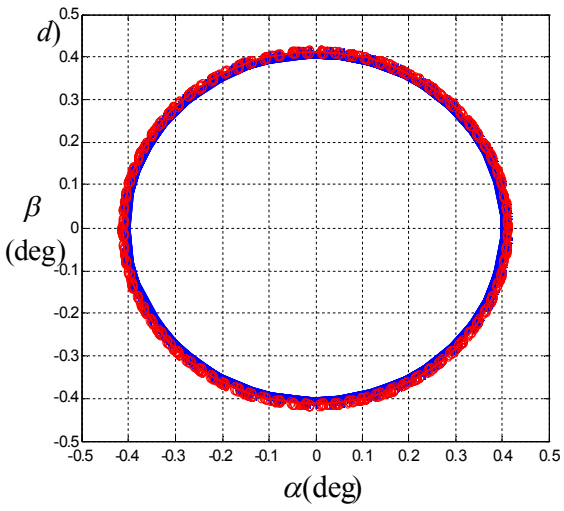
Additionally, the simulation results in both i) and j) provide us that the system is dominated by in-plane motion in the range of the first supercritical operating speed and by out-plane motion in the range of the second supercritical operating speed because $a + w_{r0}$ becomes large at $1 < \overline{\Omega} \le 3$ while $a + w_{r0}$ is very small at $\overline{\Omega} > 3$ and the opposite phenomenon is observed in $b + \alpha_0$.

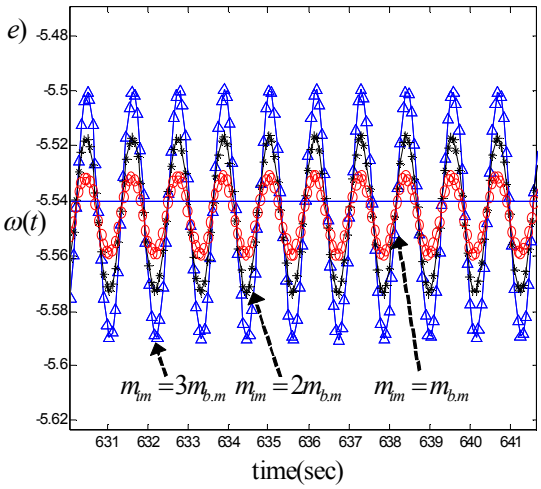
The limit cycle solution presented here is validated with numerical simulation and is accurate enough to capture the unwanted non-synchronous response with reasonable assumptions. This validated solution is used for subsequent stability simulation.

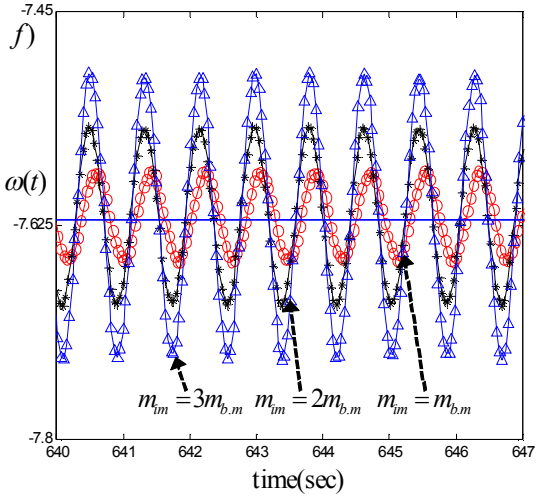


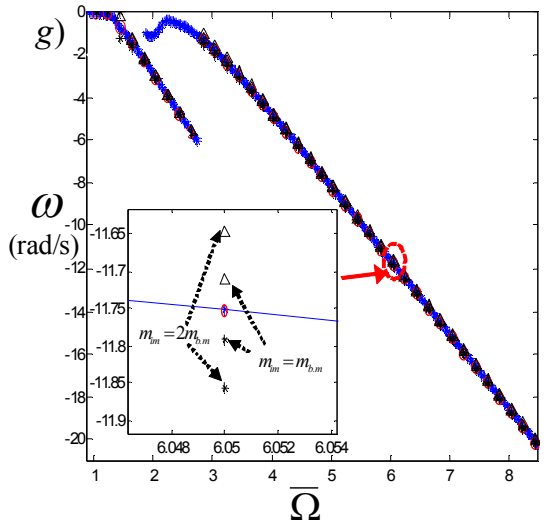


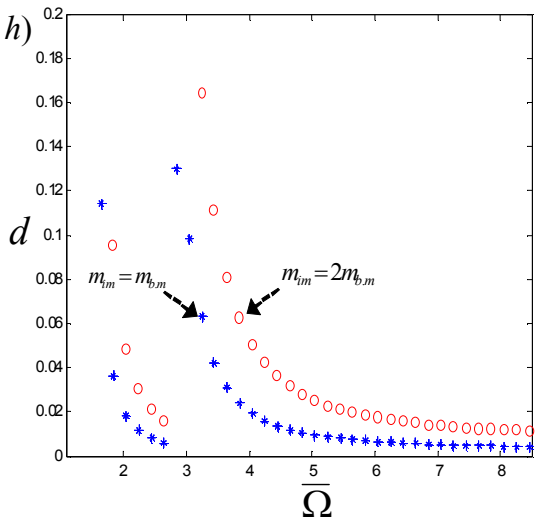

c)
x 10^-3
w_r (m)
v_r(m)
x 10^-3


d)
β (deg)
α(deg)


e)
ω(t)
m_im = 3m_b.m
m_im = 2m_b.m
m_im = m_b.m
time(sec)


f)
ω(t)
m_im = 3m_b.m
m_im = 2m_b.m
m_im = m_b.m
time(sec)


g)
ω (rad/s)
m_im = 2m_b.m
m_im = m_b.m
Ω


h)
d
m_im = m_b.m
m_im = 2m_b.m
Ω

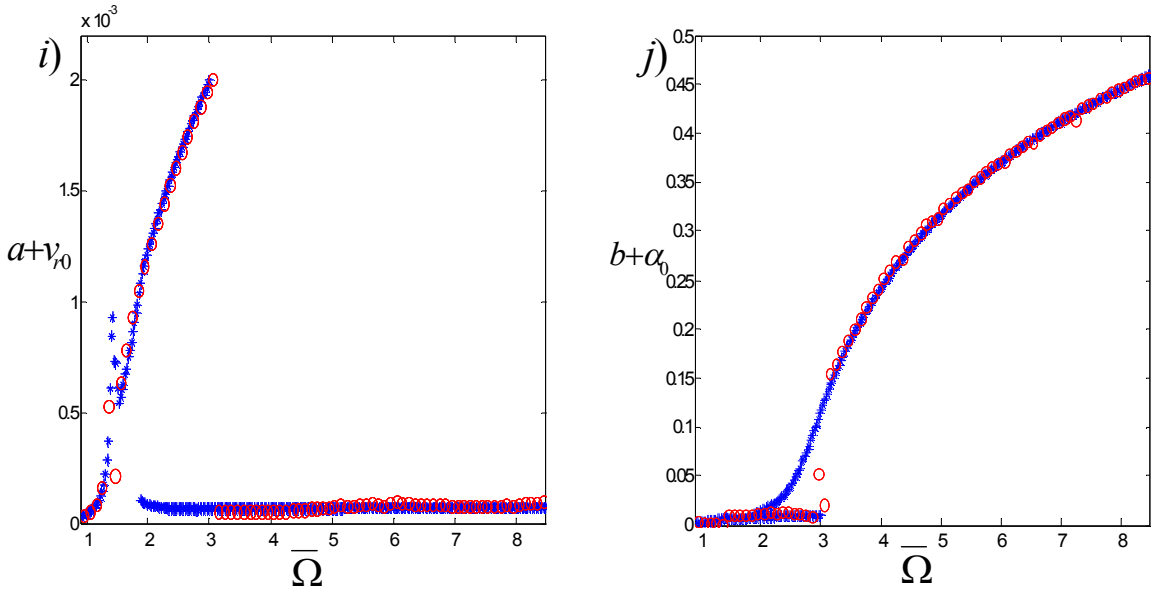


Figure.5.2. Comparison between full numerical response and analytical one

Figure.5.3 displays the whirl speed ω (displayed as star-dots) and the damped natural frequencies(displayed as dotted lines) of system without ABD which is obtained through the imaginary part of eigenvalue of A_0.

$$A_0 = \begin{bmatrix} 0 & I_{4\times4} \\ -M_0^{-1}K_0 & -M_0^{-1}C_0 \end{bmatrix} \tag{5-42}$$

where, $M_0 = M_s + N_c{}^T M_d N_c\,|_{x=L_d}$, $C_0 = C_s + N_c^T C_d N_c\,|_{x=L_d} + N_c^T C_b N_c\,|_{x=L_{b1}} + N_c^T C_b N_c\,|_{x=L_{b2}}$

$K_0 = K_s + N_c^T K_d N_c\,|_{x=L_d} + N_c^T K_b N_c\,|_{x=L_{b1}} + N_c^T K_b N_c\,|_{x=L_{b2}}$

As seen in the results in Figure.3, it is founded that the whirl speed of merged balls in ABD is synchronous with the damped natural frequency of the baseline system.

Considering $m_{b.m} << m_s + m_d$, the damped natural frequency of system with ABD can be approximated as the baseline systems'. This implies that the system is excited by the damped natural frequency of system under limit-cycle condition. We can see this point of view more clearly by investigating the force excitation term $F_{AB}(\phi_i, \dot{\phi}_i)$ in (5-12). Using the coordinate transformation (5-2-a), $F_{AB}(\phi_i, \dot{\phi}_i)$ can be expressed the force terms with respect to the fixed frame such that,

$$F_{AB} = m_b r_b \left[\sum_{i=1}^{2} \cos[(\dot{\phi}_i + \Omega)t](\Omega^2 + \dot{\phi}_i) \quad \sum_{i=1}^{2} \sin[(\dot{\phi}_i + \Omega)t](\Omega^2 + \dot{\phi}_i) \quad 0 \quad 0 \quad 0 \quad 0 \right]^T$$

Considering the merging condition of two ABD balls($\dot{\phi}_i \Rightarrow \dot{\phi}$), the driving frequency of force term above is founded as $\dot{\phi} + \Omega = \omega + \Omega$. As shown in Figure.3, at each operating speed, $\omega + \Omega$ is approximately the

damped resonance frequency of system so that the effect of this frequency property generates the large vibration amplitude of system, which implies that another force excitation term $N_I^T F_I$ in (5-12) less significantly influences to the system under the limit-cycle condition. In other words, the force excited by ABD-ball become far more dominant than one transmitted by imbalance effect deteriorating the accuracy of limit cycle solution presented here. Thus, the truncated time-varying terms in (5-35) for approximation become less significant under the limit-cycle condition because those terms are proportional to imbalance effect of system induced by $N_I^T F_I$. If $m_{im} = 0$, then there no exist time-varying terms in (5-35). Therefore, the assumptions and approximation we made for the limit-cycle solution are valid by observing the results in *e*) through *h*) in Figure.5.2 and the outcomes in Figure.5.3. The simulation results in Figure.5.3 provide us that the system is excited with the first damped natural frequency associated in-plane motion in the range of the first supercritical operating speed and with the second critical damped resonance related with out-plane motion in the range of the second supercritical operating speed. The results in Figure.5.3 support that the limit cycle condition is very critical issue in usage of ABD so that it should be avoid if possible otherwise it may cause serious destruction in system.

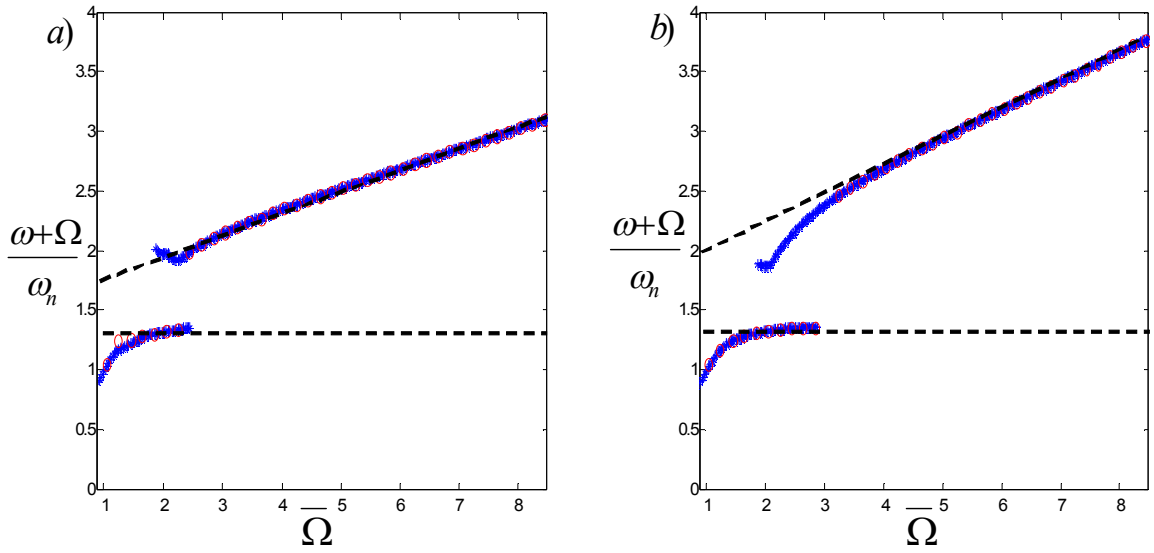


Figure.5.3 whirl speed of balancer mass in ABD and damped natural frequency of system / a) $L_d = 0.5L$ and $L_{AB} = -0.15L$ and b) $L_d = 0.2L$ and $L_{AB} = 0.45L$

At given operating speed, Figure.5.4 describes the stability region of non-synchronous limit cycle behavior and synchronous balancing condition of system with two main parameters; balancer mass $m_{b,m}$ and viscous damping coefficient c_b of ABD.

Before proceeding, the short notations used in Figure.4 are explained and will be used throughout this paper. *l*: pure limit cycle condition, *M*: merged equilibrium condition, and B_1+l: undesired coexistence zone of limit-cycle and balancing condition. Specifically, the balancing condition B_1 is defined in the following manner.

$$B_1 \equiv \{(\bar{L}_{AB}, \bar{\Omega}) \,|\, \sqrt{v_r(x,t)^2 + w_r(x,t)^2} < \sqrt{v_{r.im}(x,t)^2 + w_{r.im}(x,t)^2}\}\,|_{x=L_d}$$

where, $\bar{L}_{AB} = \frac{L_{AB}}{L}$ and $\sqrt{v_{r.im}{}^2 + w_{r.im}{}^2}$ is transverse amplitude generated by the imbalance rotor/shaft system without ABD (i.e, baseline system) to compare the vibration amplitude $\sqrt{v_r^2 + w_r^2}$ of (5-12) in balancing condition. The influence of relative $m_{b.m}$ size to entire system one is investigated in *a*) of Figure.4 while the effect of c_b of ABD is explored in *b*). As seen in *a*), both *l* and B_1+l becomes dominant as the relative $m_{b.m}$ increases. As c_b is augmented, the non-synchronous behavior is suppressed in the high operating speed. These two parameters play central role to control both synchronous and non-synchronous behavior. The outcomes in Figure.5.4 provide us that the unwanted coexistence B_1+l exists at given design parameters of ABD and operating speed. However, this behavior can be avoided with proper selection of parameters and operating environment.

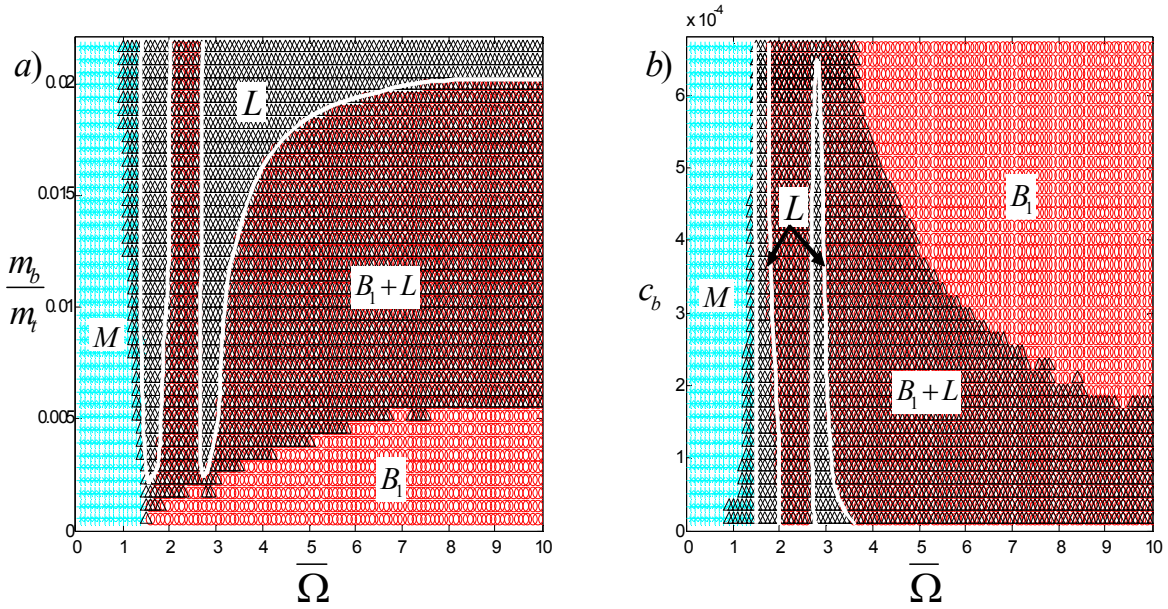


Figure.5.4. a) System stability influence of the relative mass size of ABD to entire system mass b) System stability influence of ABD ball damping coefficient

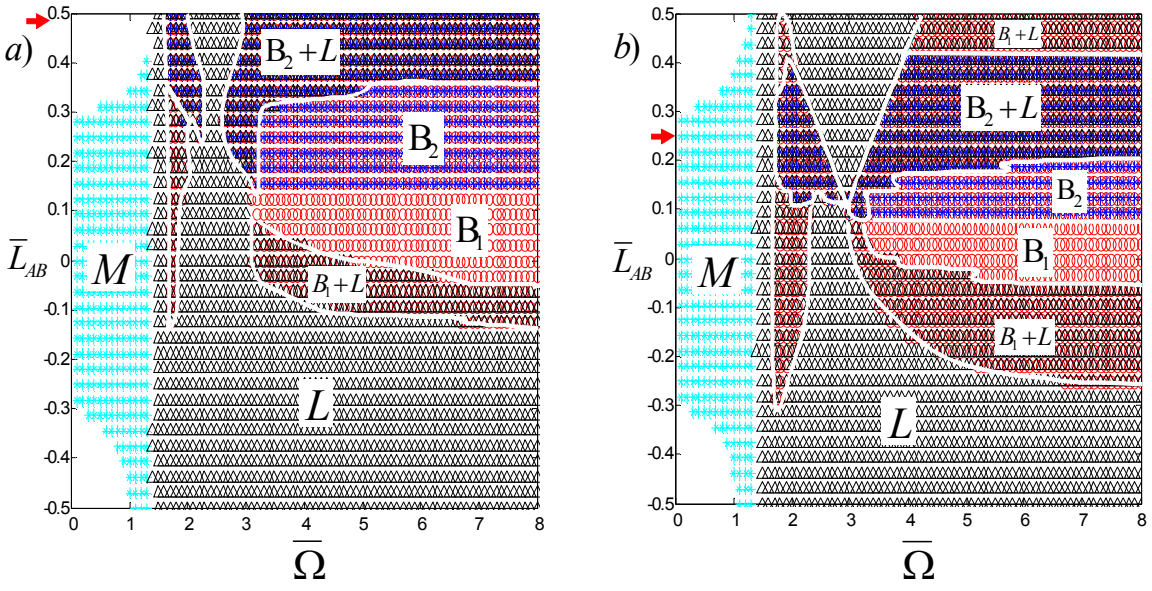
At each operating speed, Figure.5.5 shows the four stability contour plots describing the limit cycle and balancing condition generated by the relative axial location of ABD along with shaft to the four different

position of imbalance rotor(displayed as a red arrow on each plot). B_2 on each plot represents the balancing condition which is defined in the following manner.

$$B_2 \equiv B_1 \cap \{(\bar{L}_{AB}, \bar{\Omega}) \,||\, \sqrt{\alpha^2 + \beta^2} \le \sqrt{{\alpha_{im}}^2 + {\beta_{im}}^2}\}\,|_{x=L_d}$$

where, $\sqrt{{\alpha_{im}}^2 + {\beta_{im}}^2}$ indicate tilting angle amplitude generated by the baseline system to compare the tilting angle amplitude $\sqrt{\alpha^2 + \beta^2}$ of (5-12) in balancing condition. Hence, B_2 is the optimal condition where the tilting angle of system is also reduced by the action of ABD and no limit cycle condition exist. In *a*), we can find pure B_2 in the range of $0.15 < \bar{L}_{AB} < 0.35$ at high operating speed. In *b*), the pure B_2 is founded in the range of $0.1 < \bar{L}_{AB} < 0.2$ at high operating speed. In *c*), pure B_2 is situated at $\bar{L}_{AB} = 0$. When the ABD is co-located with imbalance rotor at the center of shaft (i.e, $\bar{L}_{AB} = \bar{L}_d = 0$), the optimal position B_2 of ABD along with the shaft is exactly the co-location (see plot *c*)). However, the imbalance rotor is situated away from the axial center of shaft, B_2 is not exactly the co-location as seen in a) and b). Approximately, the optimal position of ABD is a half way between the center of shaft and the axial location of imbalance rotor. Additionally, we can observe unwanted coexistence zone($B_1 + l$ and $B_2 + l$) on each plot and pure B_1 can be alternative location of ABD for pure B_2 when the ABD can't be placed at the optimal position due to the complicate structure of system or operating environment. Also, at the first supercritical speed($1.5 < \bar{\Omega} < 3$) right after the first critical operating one, undesired coexistence zone is observed on each plot.

This result provides the guideline of the relative axial location of ABD to imbalance rotor to avoid the non-synchronous condition and guarantee the synchronous one.



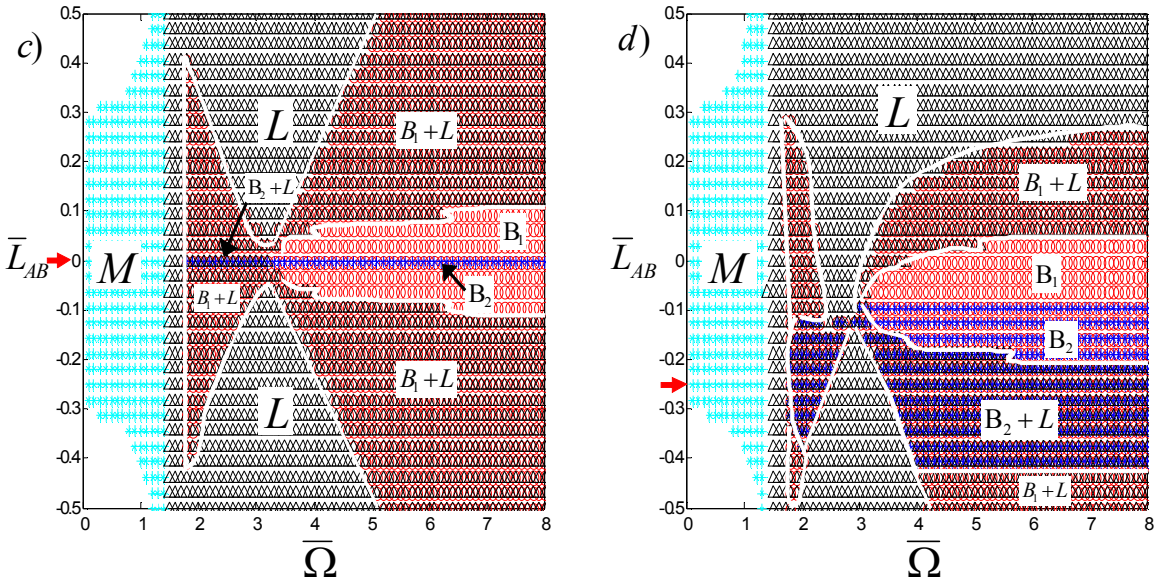


Figure.5.5 The relative suggested location of ABD along with shaft to imbalance source(displayed as a red arrow on each plot) to avoid the limit-cycles condition and unwanted coexistence zone(Note that $\overline{L}_{AB} = \frac{L_{AB}}{L}$ and the locations of imbalance rotor are $0.5L$ in a), $0.25L$ in b), 0 in c), and $-0.25L$ in d) respectively)

5.5 Concluding Remarks

With several reasonable assumptions, this paper provides the harmonic limit-cycle solutions of automatic balancing device(ABD) for three dimensional imbalanced rotor/shaft system operating with symmetric property bearing. Essentially, the solutions presented here capture both in-plane transverse deflection and out-planes tilting motion of system under the limit cycle condition. The investigation of whirl speed for ABD balancer mass provides that the system is excited with the first damped natural frequency associated in-plane motion in the range of the first supercritical operating speed and with the second critical damped resonance related with out-plane motion in the range of the second supercritical operating speed under limit-cycle condition. Also, the limit-cycle stability is assessed via a perturbation and Floquet analysis with three main parameters of ABD i) relative size of ABD balancer mass to the mass of entire system ii) viscous damping coefficient of balancer, and iii) the relative axial location of ABD along with shaft to the axial location of imbalance rotor and the coexistence of the stable balanced synchronous condition and undesired non-synchronous limit-cycle is also investigated. It is found that for certain combinations of appropriate three main parameters of ABD and operating speeds, the non-synchronous limit-cycle can be made unstable thus guaranteeing global asymptotic stability of the synchronous balanced condition. Specifically, as the balancer mass of ABD decrease and the viscous damping coefficient of balancer in ABD increases, the limit cycle condition tend to be less dominant and it is also founded that the relative

location of ABD to imbalance rotor can be effective to avoid or prevent this unwanted non-synchronous behavior.

The findings in this paper yield important insights for researchers wishing to utilize the automatic balancing devices(ABD) in three dimensional rigid rotor/shaft system considering not only transverse deflection but also tilting motion and understand inherent unwanted nature of non-synchronous condition of this system and furthermore avoid the this condition.

CHAPTER VI
LIMIT-CYCLE ANALYSIS OF THREE DIMENSIONAL FLEXIBLE SHAFT/RIGID ROTOR/AUTOBALANCER SYSTEM WITH SYMMETRIC RIGID SUPPORT

6.1 3-Dimensional flexible shaft/rigid Rotor/Autobalancer system

In this section, we present the mathematical model of the 3-D flexible shaft/rigid rotor/Autobalancer system mounted on symmetric rigid support. To facilitate analysis, the equations-of-motion for the dynamics of system are derived in a set of rotating coordinates, $\{a\}=\{a_1,a_2,a_3\}$, which follow the shaft rigid-body rotation, $\theta(t)$, about the n_1 axis of the fixed frame $\{n\}=\{n_1,n_2,n_3\}$. The detail of coordinate transformation is described in Figure.1. The shaft is assumed to be driven with constant angular speed, Ω; hence $\theta(t)=\Omega t$.

The position vector locating point ***C*** on the shaft neutral axis at station *x* relative to point ***O*** is given by,

$$R_{OC}=v_r(x,t)a_2+w_r(x,t)a_3 \tag{6-1}$$

where $v_r(x,t)$ and $w_r(x,t)$ are the transverse deflections of the shaft neutral axis in the rotating frame.

To further describe the kinematics, a set of body-fixed coordinate, $\{b\}=\{b_1,b_2,b_3\}$, attached to the shaft cross section at station *x* is defined with transformation from $\{n\}$ to $\{a\}$ and from $\{a\}$ to $\{b\}$ given as,

$$\begin{bmatrix}a_1\\a_2\\a_3\end{bmatrix}=\begin{bmatrix}1&0&0\\0&\cos(\Omega t)&\sin(\Omega t)\\0&-\sin(\Omega t)&\cos(\Omega t)\end{bmatrix}\begin{bmatrix}n_1\\n_2\\n_3\end{bmatrix} \tag{6-2-a}$$

$$\begin{bmatrix}b_1\\b_2\\b_3\end{bmatrix}=\begin{bmatrix}1-\frac{1}{2}(v_r'^2+w_r'^2)&v_r'&w_r'\\-v_r'&1-\frac{v_r'^2}{2}&-\frac{v_r'w_r'}{2}\\-w_r'&-\frac{v_r'w_r'}{2}&1-\frac{w_r'^2}{2}\end{bmatrix}\begin{bmatrix}a_1\\a_2\\a_3\end{bmatrix} \tag{6-2-b}$$

where " ' " indicates differentiation with respect to axial position, *x*.

The position vector, R_{OB_i}, of the *i*-th ball inside the autobalancer can be written as

$$R_{OB_i}=[R_{OC}+R_{CB_i}]\Big|_{x=L_{AB}}\quad for\ i=1,2 \tag{6-3-a}$$

$$R_{CB_i}=r_b[\cos(\phi_i(t))b_2+\sin(\phi_i(t))b_3]\Big|_{x=L_{AB}}\quad for\ i=1,2 \tag{6-3-b}$$

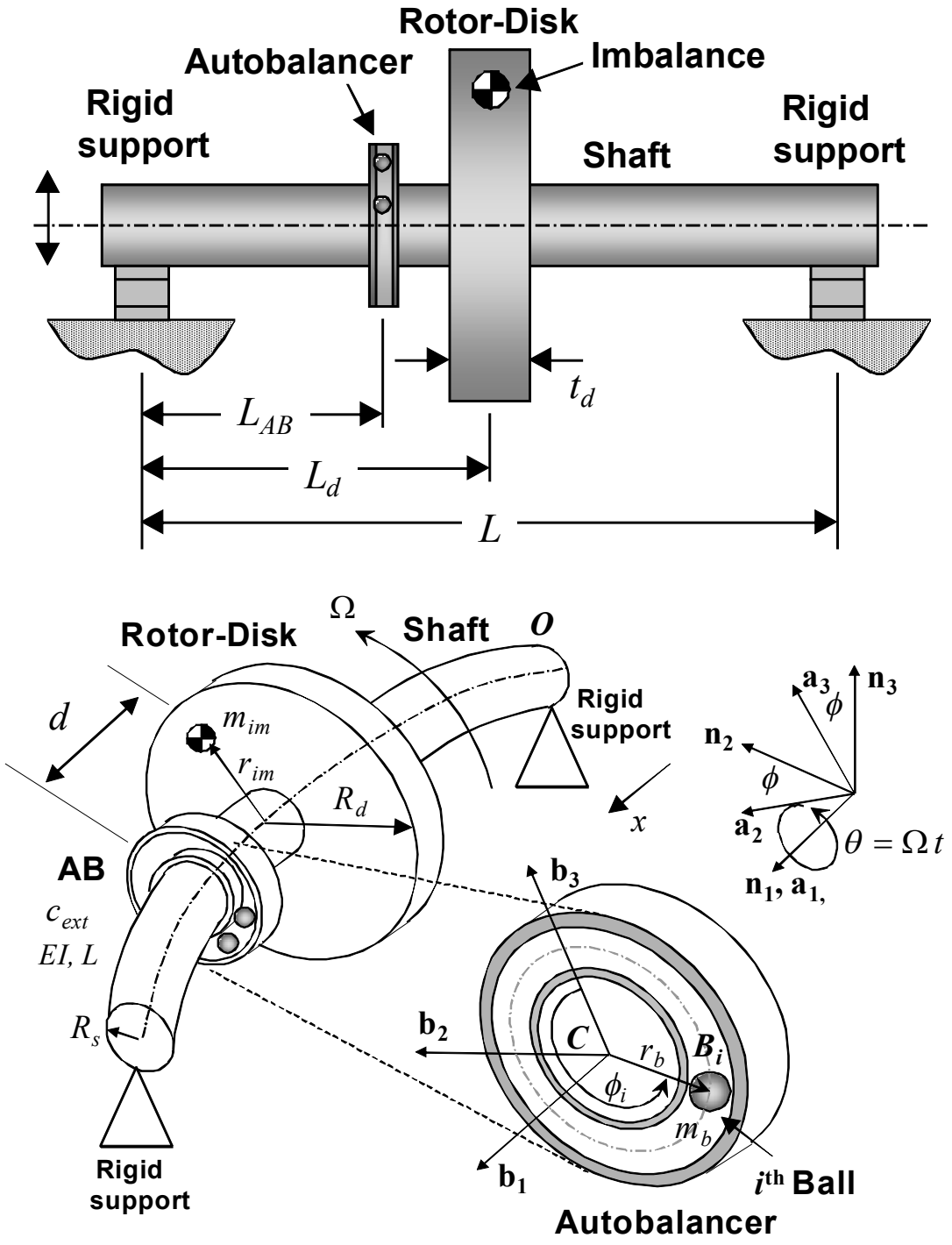


Figure.6.1 Three dimensional flexible shaft/rigid rotor/ABD system with rigid supports

where r_b is the ball-track radius and $\phi_i(t)$ is the *i*-th ball angular position measured about b_1 axis. The dual autobalancer containing two balancer masses/balls is used in this paper.

The total system kinetic energy, T, in terms of shaft, disk, and autobalancer kinetic energies T_s, T_d, and T_{AB} is

$$T = T_s + T_d + T_{AB} \qquad \text{with} \tag{6-4-a}$$

$$T_s = \int_0^L \left[\frac{m_s}{2}\left(\dot{R}_{OC} \cdot \dot{R}_{OC}\right) + \frac{1}{2}\left(Jm_s {\omega_{B1}}^2 + Im_s {\omega_{B2}}^2 + Im_s {\omega_{B3}}^2\right)\right] dx \tag{6-4-b}$$

$$T_d = \left[\frac{m_d}{2}(\dot{R}_{OC} \cdot \dot{R}_{OC}) + \frac{1}{2}(Jm_d {\omega_{B1}}^2 + Im_d {\omega_{B2}}^2 + Im_d {\omega_{B3}}^2\right]\Big|_{x=L_d} \tag{6-4-c}$$

$$T_{AB} = \sum_{i=1}^{2} \frac{m_b}{2}(\dot{R}_{OB_i} \cdot \dot{R}_{OB_i}) \tag{6-4-d}$$

where "." indicates differentiation with respect to time, t. Also m_s, m_d and m_b are the mass of a shaft per unit length, a disk and a ball respectively, and Jm_s and Im_s are the shaft polar and transverse moment of inertia while Jm_d and Im_d are the disk polar and transverse moment of inertia. The transversal velocities in (6-4-a)-(6-4-d) are given by,

$$\dot{R}_{OC} = (\dot{v}_r - w_r\Omega)a_2 + (\dot{w}_r + v_r\Omega)a_3 \tag{6-5-a}$$

$$\dot{R}_{OB_i} = \left[\dot{R}_{OC} + r_b\dot{\phi}_i(t)[-\sin(\phi_i(t))b_2 + \cos(\phi_i(t))b_3] + {}^N\omega^B \times R_{CB_i}\right]\Big|_{x=L_{AB}} \tag{6-5-b}$$

with $\{b\}$ frame angular velocity vector ${}^N\omega^B$ given by

$${}^N\omega^B = \omega_{B1}b_1 + \omega_{B2}b_2 + \omega_{B3}b_3 \tag{6-6-a}$$

$$\omega_{B1} = \Omega - \frac{1}{2}\Omega\left(v_r'^2 + w_r'^2 + \dot{w}_r'v_r' - w_r'\dot{v}_r'\right), \quad \omega_{B2} = -\dot{w}_r' - \Omega v_r', \quad \omega_{B3} = \dot{v}_r' - \Omega w_r' \tag{6-6-b}$$

The shaft strain energy U_b is

$$U_b = \frac{EI}{2}\int_0^L \left(v_r''^2 + w_r''^2\right)dx \tag{6-7}$$

Furthermore, the total Rayleigh dissipation function, D, in terms of the external damping, structural damping of shaft, and ABD dissipation functions D_e, D_{shaft} and D_{AB}, is expressed as

$$D = D_e + D_{shaft} + D_{AB} \tag{6-8-a}$$

with

$$D_e = \frac{c_{ext}}{2}\left[(\dot{R}_{OC} \cdot \dot{R}_{OC})\Big|_{x=\frac{L_{b1}}{2}}\right] \tag{6-8-b}$$

$$D_{shaft} = \xi\frac{EI}{2}\int_0^L (\dot{v}_r''^2 + \dot{w}_r''^2)dx \tag{6-8-c}$$

$$D_{AB} = \sum_{i=1}^{2} \frac{c_b}{2} r_b^{\,2} \dot{\phi}_i(t)^2 \tag{6-8-d}$$

where c_{ext}, ξ and c_b are the external damping coefficient, structural damping coefficient of shaft and the viscous damping parameter due to balancer ball drag forces encountered during relative ball/track motion within ABD.

Finally, the virtual work expression due to the rotor-disk mass imbalance is

$$\delta W_I = m_{im} r_{im} \Omega^2 [\cos(\phi_{im}) \delta v_r + \sin(\phi_{im}) \delta w_r]\Big|_{x=L_d} \tag{6-9}$$

where m_{im}, r_{im}, and ϕ_{im} are the imbalance mass, radial location, and phase angle, respectively.

Next, the system is discretized by assuming that the coordinates $v_r(x,t)$ and $w_r(x,t)$ can be approximated as following N-terms expansions,

$$v_r(x,t) = \sum_{i=1}^{n} \psi_i(x) \eta_{vi}(t) \quad \text{and} \quad w_r(x,t) = \sum_{i=1}^{n} \psi_i(x) \eta_{wi}(t) \tag{6-10}$$

with expansion coefficients $\eta_{vi}(x)$ and $\eta_{wi}(x)$ and with shape function $\psi_i(x)$ based on the eigenfunctions of an Euler-Bernoulli beam with the rigid support(fixed-fixed) boundary condition such that, $\psi_i(x) = \sin\left[\frac{i\pi x}{L}\right]$ *for* $i = 1,2,\cdots,n$.

Substituting (6-10) into Eqs. (6-4)-(6-9), the equation-of-motion are obtained via Lagrange's equations

$$\frac{d}{dt}\left[\frac{\partial T}{\partial \dot{q}}\right] - \frac{\partial T}{\partial q} + \frac{\partial U}{\partial q} + \frac{\partial D}{\partial \dot{q}} = Q_I \tag{6-11}$$

with the generalized coordinates $q(t) = [\eta_{v1} \quad \eta_{w1} \quad \eta_{v2} \quad \eta_{w2} \quad \cdots \quad \eta_{vn} \quad \eta_{wn} \quad \phi_1(t) \quad \phi_2(t)] \in \Re^{2n+2}$ and the generalized imbalance force vector Q_I satisfying $W_I = Q_I^{\,T} \delta q$.

The resulting nonlinear equation-of-motion of the shaft-disk-bearing autobalancer system are

$$M(\phi_1,\phi_2)\ddot{q} + C(\phi_1,\phi_2,\dot{\phi}_1,\dot{\phi}_2)\dot{q} + K(\phi_1,\phi_2,\dot{\phi}_1,\dot{\phi}_2,\ddot{\phi}_1,\ddot{\phi}_2)q = F(\phi_1,\phi_2,\dot{\phi}_1,\dot{\phi}_2) \tag{6-12-a}$$

with matrices and force terms decomposed in terms of the shaft, disk, and ABD subsystems as

$$\begin{aligned}
M &= M_s + N_d^T M_d N_d + N_{AB}^T M_{AB}(\phi_1,\phi_2) N_{AB} \\
C &= C_s + N_d^T C_d N_d + N_{AB}^T C_{AB}(\phi_1,\phi_2,\dot{\phi}_1,\dot{\phi}_2) N_{AB} + N_e^T C_e N_e \\
K &= K_{s.1} + K_{s.2} + N_d^T K_d N_d + N_{AB}^T K_{AB}(\phi_1,\phi_2,\dot{\phi}_1,\dot{\phi}_2,\ddot{\phi}_1,\ddot{\phi}_2) N_{AB} + N_e^T K_e N_e \\
F &= N_I^T F_I + N_{AB}^T F_{AB}(\phi_1,\phi_2,\dot{\phi}_1,\dot{\phi}_2)
\end{aligned} \tag{6-12-b}$$

with shaft subsystem matrices

$$M_s = m_s \begin{bmatrix} I_{n\times n} & 0_{n\times 2} \\ 0_{2\times n} & 0_{2\times 2} \end{bmatrix} + \pi^2 \frac{\mathrm{Im}_s}{L^2} \begin{bmatrix} 1^2 & 0 & 0 & 0 & \cdots & 0 & 0 & 0 & 0 \\ 0 & 1^2 & 0 & 0 & \cdots & 0 & 0 & 0 & 0 \\ 0 & 0 & 2^2 & 0 & \cdots & 0 & 0 & 0 & 0 \\ 0 & 0 & 0 & 2^2 & \cdots & 0 & 0 & 0 & 0 \\ \vdots & \vdots & \vdots & \vdots & \ddots & 0 & 0 & 0 & 0 \\ 0 & 0 & 0 & 0 & 0 & n^2 & 0 & 0 & 0 \\ 0 & 0 & 0 & 0 & 0 & 0 & n^2 & 0 & 0 \\ 0 & 0 & 0 & 0 & 0 & 0 & 0 & 0 & 0 \\ 0 & 0 & 0 & 0 & 0 & 0 & 0 & 0 & 0 \end{bmatrix} \tag{6-13-a}$$

$$C_s = \begin{bmatrix} \frac{\zeta\, EI\pi^4}{L^4} & -2m_s\Omega & 0 & 0 & \cdots & 0 & 0 & 0 & 0 \\ 2m_s\Omega & \frac{\zeta\, EI\pi^4}{L^4} & 0 & 0 & \cdots & 0 & 0 & 0 & 0 \\ 0 & 0 & 16\frac{\zeta\, EI\pi^4}{L^4} & -2m_s\Omega & \cdots & 0 & 0 & 0 & 0 \\ 0 & 0 & 2m_s\Omega & 16\frac{\zeta\, EI\pi^4}{L^4} & \cdots & 0 & 0 & 0 & 0 \\ \vdots & \vdots & \vdots & \vdots & \ddots & 0 & 0 & 0 & 0 \\ 0 & 0 & 0 & 0 & 0 & n^4\frac{\zeta\, EI\pi^4}{L^4} & -2m_s\Omega & 0 & 0 \\ 0 & 0 & 0 & 0 & 0 & 2m_s\Omega & n^4\frac{\zeta\, EI\pi^4}{L^4} & 0 & 0 \\ 0 & 0 & 0 & 0 & 0 & 0 & 0 & 0 & 0 \\ 0 & 0 & 0 & 0 & 0 & 0 & 0 & 0 & 0 \end{bmatrix} \tag{6-13-b}$$

$$K_{s.1} = \begin{bmatrix} \frac{EI\,\pi^4}{L^4} & 0 & 0 & 0 & \cdots & 0 & 0 & 0 & 0 \\ 0 & \frac{EI\,\pi^4}{L^4} & 0 & 0 & \cdots & 0 & 0 & 0 & 0 \\ 0 & 0 & 16\,\frac{EI\,\pi^4}{L^4} & 0 & \cdots & 0 & 0 & 0 & 0 \\ 0 & 0 & 0 & 16\,\frac{EI\,\pi^4}{L^4} & \cdots & 0 & 0 & 0 & 0 \\ \vdots & \vdots & \vdots & \vdots & \ddots & 0 & 0 & 0 & 0 \\ 0 & 0 & 0 & 0 & 0 & n^4\,\frac{EI\,\pi^4}{L^4} & 0 & 0 & 0 \\ 0 & 0 & 0 & 0 & 0 & 0 & n^4\,\frac{EI\,\pi^4}{L^4} & 0 & 0 \\ 0 & 0 & 0 & 0 & 0 & 0 & 0 & 0 & 0 \\ 0 & 0 & 0 & 0 & 0 & 0 & 0 & 0 & 0 \end{bmatrix} \tag{6-13-c}$$

$$K_{s.2}=\begin{bmatrix}
\left[\frac{\pi^2\,\mathrm{Im}_s}{L^2}-m_s\right]\Omega^2 & 0 & 0 & 0 & \cdots & 0 & 0 & 0 & 0\\
0 & \left[\frac{\pi^2\,\mathrm{Im}_s}{L^2}-m_s\right]\Omega^2 & 0 & 0 & \cdots & 0 & 0 & 0 & 0\\
0 & 0 & \left[\frac{4\pi^2\,\mathrm{Im}_s}{L^2}-m_s\right]\Omega^2 & 0 & \cdots & 0 & 0 & 0 & 0\\
0 & 0 & 0 & \left[\frac{4\pi^2\,\mathrm{Im}_s}{L^2}-m_s\right]\Omega^2 & \cdots & 0 & 0 & 0 & 0\\
\vdots & \vdots & \vdots & \vdots & \ddots & 0 & 0 & 0 & 0\\
0 & 0 & 0 & 0 & 0 & \left[\frac{n^2\pi^2\,\mathrm{Im}_s}{L^2}-m_s\right]\Omega^2 & 0 & 0 & 0\\
0 & 0 & 0 & 0 & 0 & 0 & \left[\frac{n^2\pi^2\,\mathrm{Im}_s}{L^2}-m_s\right]\Omega^2 & 0 & 0\\
0 & 0 & 0 & 0 & 0 & 0 & 0 & 0 & 0\\
0 & 0 & 0 & 0 & 0 & 0 & 0 & 0 & 0
\end{bmatrix}$$

(6-13-d)

Similarly, the rotor-disk subsystem matrices are

$$M_d=\begin{bmatrix} m_d & 0 & 0 & 0\\ 0 & m_d & 0 & 0\\ 0 & 0 & Im_d & 0\\ 0 & 0 & 0 & Im_d \end{bmatrix} \tag{6-14-a}$$

$$C_d=\Omega\begin{bmatrix} 0 & -2m_d & 0 & 0\\ 2m_d & 0 & 0 & 0\\ 0 & 0 & 0 & -2Im_d+Jm_d\\ 0 & 0 & 2Im_d-Jm_d & 0 \end{bmatrix} \tag{6-14-b}$$

$$K_d=\Omega^2\begin{bmatrix} -m_d & 0 & 0 & 0\\ 0 & -m_d & 0 & 0\\ 0 & 0 & Jm_d-Im_{d\,d} & 0\\ 0 & 0 & 0 & Jm_d-Im_{d\,d} \end{bmatrix} \tag{6-14-c}$$

Furthermore, the external damping subsystem matrices are

$$C_e=\begin{bmatrix} c_{ext} & 0 & 0 & 0\\ 0 & c_{ext} & 0 & 0\\ 0 & 0 & 0 & 0\\ 0 & 0 & 0 & 0 \end{bmatrix} \quad \text{and} \quad K_e=\begin{bmatrix} 0 & -c_{ext}\Omega & 0 & 0\\ c_{ext}\Omega & 0 & 0 & 0\\ 0 & 0 & 0 & 0\\ 0 & 0 & 0 & 0 \end{bmatrix} \tag{6-15}$$

The ABD subsystem matrices and forcing terms are

$$M_{AB}=\begin{bmatrix} 2m_b & 0 & 0 & 0 & -m_b r_b \sin(\phi_1) & -m_b r_b \sin(\phi_2) \\ 0 & 2m_b & 0 & 0 & m_b r_b \cos(\phi_1) & m_b r_b \cos(\phi_2) \\ 0 & 0 & m_b {r_b}^2 \sum_{i=1}^{2} \cos(\phi_i)^2 & \frac{1}{2} m_b {r_b}^2 \sum_{i=1}^{2} \sin(2\phi_i) & 0 & 0 \\ 0 & 0 & \frac{1}{2} m_b {r_b}^2 \sum_{i=1}^{2} \sin(2\phi_i) & m_b {r_b}^2 \sum_{i=1}^{2} \sin(\phi_i)^2 & 0 & 0 \\ -m_b r_b \sin(\phi_1) & m_b r_b \cos(\phi_1) & 0 & 0 & m_b {r_b}^2 & 0 \\ -m_b r_b \sin(\phi_2) & m_b r_b \cos(\phi_2) & 0 & 0 & 0 & m_b {r_b}^2 \end{bmatrix} \tag{6-16-a}$$

$$C_{AB}=\begin{bmatrix} 0 & -4m_b\Omega & 0 & 0 & -2m_b r_b \Omega \cos(\phi_1) & -2m_b r_b \Omega \cos(\phi_2) \\ 4m_b\Omega & 0 & 0 & 0 & -2m_b r_b \Omega \sin(\phi_1) & -2m_b r_b \Omega \sin(\phi_2) \\ 0 & 0 & -m_b {r_b}^2 \sum_{i=1}^{2} \sin(\phi_i)\dot{\phi}_i & 2m_b {r_b}^2 \sum_{i=1}^{2} \cos(2\phi_i)^2 \dot{\phi}_i & 0 & 0 \\ 0 & 0 & -2m_b {r_b}^2 \sum_{i=1}^{2} \cos(2\phi_i)^2 \dot{\phi}_i & m_b {r_b}^2 \sum_{i=1}^{2} \sin(2\phi_i)\dot{\phi}_i & 0 & 0 \\ 2m_b r_b \Omega \cos(\phi_1) & 2m_b r_b \Omega \sin(\phi_1) & 0 & 0 & c_b {r_b}^2 & 0 \\ 2m_b r_b \Omega \cos(\phi_2) & 2m_b r_b \Omega \sin(\phi_2) & 0 & 0 & 0 & c_b {r_b}^2 \end{bmatrix} \tag{6-16-b}$$

$$K_{AB}=\begin{bmatrix} -2m_b\Omega^2 & 0 & 0 & 0 & 0 & 0 \\ 0 & -2m_b\Omega^2 & 0 & 0 & 0 & 0 \\ 0 & 0 & m_b {r_b}^2 (\Omega^2 + \sum_{i=1}^{2} [2\Omega\dot{\phi}_i \cos(\phi_i)^2 + \frac{1}{2}\Omega^2 \cos(2\phi_i)]) & m_b {r_b}^2 (\sum_{i=1}^{2} [\sin(2\phi_i)(\frac{1}{2}\Omega^2 + \Omega\dot{\phi}_i) + \frac{1}{2}\ddot{\phi}_i]) & 0 & 0 \\ 0 & 0 & m_b {r_b}^2 (\sum_{i=1}^{2} [\sin(2\phi_i)(\frac{1}{2}\Omega^2 + \Omega\dot{\phi}_i) - \frac{1}{2}\ddot{\phi}_i]) & m_b {r_b}^2 (\Omega^2 + \sum_{i=1}^{2} [2\Omega\dot{\phi}_i \sin(\phi_i)^2 - \frac{1}{2}\Omega^2 \cos(2\phi_i)]) & 0 & 0 \\ m_b r_b \Omega^2 \sin(\phi_1) & -m_b r_b \Omega^2 \cos(\phi_1) & 0 & 0 & 0 & 0 \\ m_b r_b \Omega^2 \sin(\phi_2) & -m_b r_b \Omega^2 \cos(\phi_2) & 0 & 0 & 0 & 0 \end{bmatrix} \tag{6-16-c}$$

$$F_{AB} = m_b r_b \begin{bmatrix} \sum_{i=1}^{2} \cos(\phi_i)(\Omega^2 + \dot{\phi}_i) & \sum_{i=1}^{2} \sin(\phi_i)(\Omega^2 + \dot{\phi}_i) & 0 & 0 & 0 & 0 \end{bmatrix}^T \tag{6-16-d}$$

Finally, the imbalance force due to rotor disk eccentricity is

$$F_I = m_{im} r_{im} \Omega^2 \begin{bmatrix} \cos(\phi_{im}) & \sin(\phi_{im}) & 0 & 0 & 0 & 0 \end{bmatrix}^T \tag{6-17}$$

The mapping matrices N_d, N_b, and N_{AB} expressed in (6-12-b) are given below.

$$N_d = \left[N_c(x) \quad 0_{4\times 2}\right]_{x=L_d} \text{ and } N_e = \left[N_c(x) \quad 0_{4\times 2}\right]_{x=L_{b1}}$$
$$N_{AB} = \begin{bmatrix} N_c(x) & 0_{4\times 2} \\ 0_{2\times 2n} & 0_{2\times 2} \end{bmatrix}_{x=L_{AB}} \text{ and } N_I = \begin{bmatrix} N_c(x) & 0_{4\times 2} \\ 0_{2\times 2n} & 0_{2\times 2} \end{bmatrix}_{x=L_d} \tag{6-18}$$
$$\text{with } N_c(x) = \begin{bmatrix} \psi_1(x) & 0 & \psi_2(x) & 0 & \cdots & \psi_n(x) & 0 \\ 0 & \psi_1(x) & 0 & \psi_2(x) & \cdots & 0 & \psi_n(x) \\ \psi_1'(x) & 0 & \psi_2'(x) & 0 & \cdots & \psi_n'(x) & 0 \\ 0 & \psi_1'(x) & 0 & \psi_2'(x) & \cdots & 0 & \psi_n'(x) \end{bmatrix}$$

6.2 Limit-cycle Solution

In this section, the assumed limit-cycle solution of the 3-D flexible shaft/rigid rotor/ABD system with a symmetric bearing support to reveal the inherent characteristic of the non-synchronous limit cycle behavior is presented. Since the system dynamics derived here utilized *n*-expanded discretized coordinates, the limit-cycle solution presented here captures the system motion described by these *n*-numbers expansion coefficients.

The solution is assumed as the harmonic type one. Thus, using the harmonic balancing technique, we generate the set of nonlinear equations to solve the unknown parameters of the solution. For further derivation, we make the following assumptions.

i) For the limit-cycle condition, two balls are merged and rotated together so that one ball motion is absorbed into another. Consequently, the coordinate of system in (6-12) is reduced into $q(t) = \left[\eta_{v1} \quad \eta_{w1} \quad \eta_{v2} \quad \eta_{w2} \quad \cdots \quad \eta_{vn} \quad \eta_{wn} \quad \phi(t)\right] \in \Re^{2n+1}$ and the mass of merged two balls described as $\phi(t)$ (i.e, $[\phi_1(t) \;\; \phi_2(t)] \to \phi(t)$). It should be noted that the contact mechanism of two balls is out of our research scope. Based upon [16] also characterized the balanced equilibrium attraction basin as a function of ball initial position, the non-synchronous behavior is mostly created by setting that the initial angular position of two ABD-balls is located near for each other or identically. Reversely, if one ball is initially stayed away from another, the system is highly subject to the stable synchronous behavior due to the initial different angular phase between two balls according to [16]. Thus, the merging situation of two balls is highly probable under limit cycle condition. *ii)* The ball speed denoted as ω is assumed to be constant under the limit-cycle condition. Hence, we have, $\dot{\phi}(t) = \omega \Rightarrow \phi(t) = \omega t$ and $\ddot{\phi} = 0$.

Next, the harmonic solution of the limit-cycle is assumed to be

$$\eta_{vi}(t) = a_i \cos[\omega t + \gamma_i] + v_{0.i} \quad \eta_{wi}(t) = a_i \sin[\omega t + \gamma_i] + w_{0.i} \quad for \;\; i = 1,2,\cdots n \tag{6-19}$$

where, a_i are unknown amplitudes, ω is the whirl speed of merged ABD-balancer, γ_i are the phases and $v_{0.i}$ and $w_{0.i}$ are constant offsets to be solved.

In this chapter, the approximated solution with three expanded coordinates is presented.

Applying the reduced coordinates assumed above into the original dynamics (6-12), substituting (6-19) with n=3 into the version of (6-12) with reduced $q(t)=\left[\eta_{v1} \quad \eta_{w1} \quad \eta_{v2} \quad \eta_{w2} \quad \cdots \quad \eta_{vn} \quad \eta_{wn} \quad \phi(t)\right] \in \Re^{2n+1}$ and rearranging it in terms of each harmonic yields (6-20) through (6-25),

$$A_{10} + A_{11}\sin(\omega t) + A_{12}\cos(\omega t) + A_{13}\sin(\omega t)^2 + A_{14}\cos(\omega t)^2 + A_{15}\sin(\omega t)\cos(\omega t) = 0 \tag{6-20}$$

$$A_{20} + A_{21}\sin(\omega t) + A_{22}\cos(\omega t) + A_{23}\sin(\omega t)^2 + A_{24}\cos(\omega t)^2 + A_{25}\sin(\omega t)\cos(\omega t) = 0 \tag{6-21}$$

where,

$$\begin{aligned}
A_{10} = {} & \left[\Omega^2[s'_{1.d}{}^2(Jm_d - Im_d) - m_s + s'_{1.a}{}^2 m_b r_b{}^2 - m_d s_{1.d}{}^2 - 2m_b s_{1.a}{}^2] + s'_{1.a}{}^2 m_b r_b{}^2 \omega\Omega + \frac{EI\pi^4}{L^4}\right] v_{10} + \cdots \\
& \cdots + \left[\Omega^2[s'_{1.d}\, s'_{2.d}(Jm_d - Im_d) - (m_d s_{1.d} s_{2.d} + 2m_b s_{1.a} s_{2.a}) + s'_{1.a}\, s'_{2.a}\, m_b r_b{}^2] + s'_{1.a}\, s'_{2.a}\, m_b r_b{}^2 \omega\Omega\right] v_{20} + \cdots \\
& \cdots + \left[\Omega^2[s'_{1.d}\, s'_{3.d}(Jm_d - Im_d) - (m_d s_{1.d} s_{3.d} + 2m_b s_{1.a} s_{3.a}) + s'_{1.a}\, s'_{3.a}\, m_b r_b{}^2] + s'_{1.a}\, s'_{3.a}\, m_b r_b{}^2 \omega\Omega\right] v_{30} - \cdots \\
& \cdots - c_{ext}\Omega s_{1.c}{}^2 w_{10} - c_{ext}\Omega s_{1.c} s_{2.c} w_{20} - c_{ext}\Omega s_{1.c} s_{3.c} w_{30} - m_{im} r_{im} \Omega^2 s_{1.d}\cos(\phi_{im})
\end{aligned}$$

$$\begin{aligned}
A_{20} = {} & c_{ext}\Omega s_{1.c}{}^2 v_{10} + c_{ext}\Omega s_{1.c} s_{2.c} v_{20} + c_{ext}\Omega s_{1.c} s_{3.c} v_{30} - m_{im} r_{im} \Omega^2 s_{1.d}\sin(\phi_{im}) + \cdots \\
& \cdots + \left[\Omega^2[s'_{1.d}{}^2(Jm_d - Im_d) - m_s + s'_{1.a}{}^2 m_b r_b{}^2 - m_d s_{1.d}{}^2 - 2m_b s_{1.a}{}^2] + s'_{1.a}{}^2 m_b r_b{}^2 \omega\Omega + \frac{EI\pi^4}{L^4}\right] w_{10} + \cdots \\
& \cdots + \left[\Omega^2[s'_{1.d}\, s'_{2.d}(Jm_d - Im_d) - (m_d s_{1.d} s_{2.d} + 2m_b s_{1.a} s_{2.a}) + s'_{1.a}\, s'_{2.a}\, m_b r_b{}^2] + s'_{1.a}\, s'_{2.a}\, m_b r_b{}^2 \omega\Omega\right] w_{20} + \cdots \\
& \cdots + \left[\Omega^2[s'_{1.d}\, s'_{3.d}(Jm_d - Im_d) - (m_d s_{1.d} s_{3.d} + 2m_b s_{1.a} s_{3.a}) + s'_{1.a}\, s'_{3.a}\, m_b r_b{}^2] + s'_{1.a}\, s'_{3.a}\, m_b r_b{}^2 \omega\Omega\right] w_{30}
\end{aligned}$$

$$\begin{aligned}
A_{11} = -A_{22} = {} & \frac{1}{2} a_1 \sin(g_1)\left[\begin{array}{l} -2\frac{EI\pi^4}{L^4} + \Omega^2(-s'_{1.a}{}^2 m_b r_b{}^2 + 2m_d s_{1.d}{}^2 + 4m_b s_{1.a}{}^2) + 4\Omega\omega(m_d s_{1.d}{}^2 + 2m_b s_{1.a}{}^2) + \cdots \\ \cdots + 2\omega^2(m_d s_{1.d}{}^2 + 2m_b s_{1.a}{}^2) + 2m_s(\Omega+\omega)^2 + 2s'_{1.d}{}^2(\Omega+\omega)[Im_d(\Omega+\omega) - Jm_d\Omega] \end{array}\right] + \cdots \\
& \cdots + \frac{1}{2} a_2 \sin(g_2)\left[-s'_{1.a}\, s'_{2.a}\, m_b r_b{}^2\Omega^2 + 2(m_d s_{1.d} s_{2.d} + 2m_b s_{1.a} s_{2.a})(\Omega+\omega)^2 + 2s'_{1.d}\, s'_{2.d}(\Omega+\omega)[Im_d(\Omega+\omega) - Jm_d\Omega]\right] + \cdots \\
& \cdots + \frac{1}{2} a_3 \sin(g_3)\left[-s'_{1.a}\, s'_{3.a}\, m_b r_b{}^2\Omega^2 + 2(m_d s_{1.d} s_{3.d} + 2m_b s_{1.a} s_{3.a})(\Omega+\omega)^2 + 2s'_{1.d}\, s'_{3.d}(\Omega+\omega)[Im_d(\Omega+\omega) - Jm_d\Omega]\right] - \cdots \\
& \cdots - a_1\cos(g_1)\left[\xi\frac{EI\pi^4}{L^4} + c_{ext} s_{1.c}{}^2(\Omega+\omega)\right] - a_2\cos(g_2) c_{ext} s_{1.c} s_{2.c}(\Omega+\omega) - a_3\cos(g_3) c_{ext} s_{1.c} s_{3.c}(\Omega+\omega)
\end{aligned}$$

$$A_{12}=A_{21}=-m_b r_b s_{1.a}(\Omega+\omega)^2-a_1\sin(g_1)\left[\xi\frac{EI\pi^4}{L^4}+c_{ext}{s_{1.c}}^2(\Omega+\omega)\right]-a_2\sin(g_2)c_{ext}s_{1.c}s_{2.c}(\Omega+\omega)-a_3\sin(g_3)c_{ext}s_{1.c}s_{3.c}(\Omega+\omega)-\cdots$$

$$\cdots-\frac{1}{2}a_1\cos(g_1)\begin{bmatrix}-2\frac{EI\pi^4}{L^4}+\Omega^2(-3{s'_{1.a}}^2 m_b r_b^2+2m_d{s_{1.d}}^2+4m_b{s_{1.a}}^2)-4\Omega\omega(m_b r_b^2{s'_{1.a}}^2-2m_b{s_{1.a}}^2-m_d{s_{1.d}}^2)+\cdots\\ \cdots+2\omega^2(m_d{s_{1.d}}^2+2m_b{s_{1.a}}^2-m_b r_b{s'_{1.a}}^2)+2m_s(\Omega+\omega)^2+2{s'_{1.d}}^2(\Omega+\omega)[Im_d(\Omega+\omega)-Jm_d\Omega]\end{bmatrix}+\cdots$$

$$\cdots-\frac{1}{2}a_2\cos(g_2)\left[-s'_{1.a}s'_{2.a}m_b r_b^2(3\Omega^2+4\omega\Omega+2\omega^2)+2(m_d s_{1.d}s_{2.d}+2m_b s_{1.a}s_{2.a})(\Omega+\omega)^2+2s'_{1.d}s'_{2.d}(\Omega+\omega)[Im_d(\Omega+\omega)-Jm_d\Omega]\right]+\cdots$$

$$\cdots-\frac{1}{2}a_3\cos(g_3)\left[-s'_{1.a}s'_{3.a}m_b r_b^2(3\Omega^2+4\omega\Omega+2\omega^2)+2(m_d s_{1.d}s_{3.d}+2m_b s_{1.a}s_{3.a})(\Omega+\omega)^2+2s'_{1.d}s'_{3.d}(\Omega+\omega)[Im_d(\Omega+\omega)-Jm_d\Omega]\right]$$

$$A_{13}=-A_{14}=-A_{23}=A_{24}=-\frac{1}{2}s'_{1.a}m_b r_b^2\Omega(s'_{1.a}v_{10}+s'_{2.a}v_{20}+s'_{3.a}v_{30})(\Omega+2\omega)$$

$$A_{15}=A_{25}=s'_{1.a}m_b r_b^2\Omega(s'_{1.a}w_{10}+s'_{2.a}w_{20}+s'_{3.a}w_{30})(\Omega+2\omega)$$

The short notations $s_{i.d}$ $s_{i.a}$ and $s_{i.c}$ used here are $s_{i.d}=\sin\left[\frac{i\pi L_d}{L}\right]$, $s_{i.a}=\sin\left[\frac{i\pi L_{AB}}{L}\right]$,and $s_{i.c}=\sin\left[\frac{i\pi L_c}{L}\right]$. $s'_{i.d}$ $s'_{i.a}$ and $s'_{i.c}$ differentiation with respect to axial position x.

$$A_{30}+A_{31}\sin(\omega t)+A_{32}\cos(\omega t)+A_{33}\sin(\omega t)^2+A_{34}\cos(\omega t)^2+A_{35}\sin(\omega t)\cos(\omega t)=0 \qquad (6\text{-}22)$$

$$A_{40}+A_{41}\sin(\omega t)+A_{42}\cos(\omega t)+A_{43}\sin(\omega t)^2+A_{44}\cos(\omega t)^2+A_{45}\sin(\omega t)\cos(\omega t)=0 \qquad (6\text{-}23)$$

where,

$$A_{30}=\left[\Omega^2[s'_{1.d}s'_{2.d}(Jm_d-Im_d)-(m_d s_{1.d}s_{2.d}+2m_b s_{1.a}s_{2.a})+s'_{1.a}s'_{2.a}m_b r_b^2]+s'_{1.a}s'_{2.a}m_b r_b^2\omega\Omega\right]v_{10}+\cdots$$
$$\cdots+\left[\Omega^2[{s'_{2.d}}^2(Jm_d-Im_d)-m_s+{s'_{2.a}}^2 m_b r_b^2-m_d{s_{2.d}}^2-2m_b{s_{2.a}}^2]+{s'_{2.a}}^2 m_b r_b^2\omega\Omega+16\frac{EI\pi^4}{L^4}\right]v_{20}+\cdots$$
$$\cdots+\left[\Omega^2[s'_{2.d}s'_{3.d}(Jm_d-Im_d)-(m_d s_{2.d}s_{3.d}+2m_b s_{2.a}s_{3.a})+s'_{2.a}s'_{3.a}m_b r_b^2]+s'_{2.a}s'_{3.a}m_b r_b^2\omega\Omega\right]v_{30}-\cdots$$
$$\cdots-c_{ext}\Omega s_{1.c}s_{2.c}w_{10}-c_{ext}\Omega{s_{2.c}}^2 w_{20}-c_{ext}\Omega s_{2.c}s_{3.c}w_{30}-m_{im}r_{im}\Omega^2 s_{2.d}\cos(\phi_{im})$$

$$A_{40}=c_{ext}\Omega s_{1.c}s_{2.c}v_{10}+c_{ext}\Omega{s_{2.c}}^2 v_{20}+c_{ext}\Omega s_{2.c}s_{3.c}v_{30}-m_{im}r_{im}\Omega^2 s_{2.d}\sin(\phi_{im})+\cdots$$
$$\cdots+\left[\Omega^2[s'_{1.d}s'_{2.d}(Jm_d-Im_d)-(m_d s_{1.d}s_{2.d}+2m_b s_{1.a}s_{2.a})+s'_{1.a}s'_{2.a}m_b r_b^2]+s'_{1.a}s'_{2.a}m_b r_b^2\omega\Omega\right]w_{10}+\cdots$$
$$\cdots+\left[\Omega^2[{s'_{2.d}}^2(Jm_d-Im_d)-m_s+{s'_{2.a}}^2 m_b r_b^2-m_d{s_{2.d}}^2-2m_b{s_{2.a}}^2]+{s'_{2.a}}^2 m_b r_b^2\omega\Omega+16\frac{EI\pi^4}{L^4}\right]w_{20}+\cdots$$
$$\cdots+\left[\Omega^2[s'_{2.d}s'_{3.d}(Jm_d-Im_d)-(m_d s_{2.d}s_{3.d}+2m_b s_{2.a}s_{3.a})+s'_{2.a}s'_{3.a}m_b r_b^2]+s'_{2.a}s'_{3.a}m_b r_b^2\omega\Omega\right]w_{30}$$

$$A_{31} = -A_{42} = \frac{1}{2}a_1 \sin(g_1)\left[-s'_{1.a}\, s'_{2.a}\, m_b r_b{}^2\Omega^2 + 2(m_d s_{1.d} s_{2.d} + 2m_b s_{1.a} s_{2.a})(\Omega+\omega)^2 + 2s'_{1.d}\, s'_{2.d}\,(\Omega+\omega)[Im_d(\Omega+\omega) - Jm_d\Omega]\right] + \cdots$$

$$\cdots + \frac{1}{2}a_2 \sin(g_2)\begin{bmatrix} -32\frac{EI\pi^4}{L^4} + \Omega^2(-s'_{2.a}{}^2\, m_b r_b{}^2 + 2m_d s_{2.d}{}^2 + 4m_b s_{2.a}{}^2) + 4\Omega\omega(m_d s_{2.d}{}^2 + 2m_b s_{2.a}{}^2) + \cdots \\ \cdots + 2\omega^2(m_d s_{2.d}{}^2 + 2m_b s_{2.a}{}^2) + 2m_s(\Omega+\omega)^2 + 2s'_{2.d}{}^2\,(\Omega+\omega)[Im_d(\Omega+\omega) - Jm_d\Omega] \end{bmatrix} + \cdots$$

$$\cdots + \frac{1}{2}a_3 \sin(g_3)\left[-s'_{2.a}\, s'_{3.a}\, m_b r_b{}^2\Omega^2 + 2(m_d s_{2.d} s_{3.d} + 2m_b s_{2.a} s_{3.a})(\Omega+\omega)^2 + 2s'_{2.d}\, s'_{3.d}\,(\Omega+\omega)[Im_d(\Omega+\omega) - Jm_d\Omega]\right] - \cdots$$

$$\cdots - a_1 \cos(g_1) c_{ext} s_{1.c} s_{2.c}(\Omega+\omega) - a_2 \cos(g_2)\left[16\frac{\xi EI\pi^4}{L^4} + c_{ext} s_{2.c}{}^2(\Omega+\omega)\right] - a_3 \cos(g_3) c_{ext} s_{2.c} s_{3.c}(\Omega+\omega)$$

$$A_{32} = A_{41} = -m_b r_b s_{2.a}(\Omega+\omega)^2 - a_1 \sin(g_1) c_{ext} s_{1.c} s_{2.c}(\Omega+\omega) - a_2 \sin(g_2)\left[16\frac{\xi EI\pi^4}{L^4} + c_{ext} s_{2.c}{}^2(\Omega+\omega)\right] - a_3 \sin(g_3) c_{ext} s_{2.c} s_{3.c}(\Omega+\omega) - \cdots$$

$$\cdots - \frac{1}{2}a_1 \cos(g_1)\left[-s'_{1.a}\, s'_{2.a}\, m_b r_b{}^2(3\Omega^2 + 4\omega\Omega + 2\omega^2) + 2(m_d s_{1.d} s_{2.d} + 2m_b s_{1.a} s_{2.a})(\Omega+\omega)^2 + 2s'_{1.d}\, s'_{2.d}\,(\Omega+\omega)[Im_d(\Omega+\omega) - Jm_d\Omega]\right] + \cdots$$

$$\cdots - \frac{1}{2}a_2 \cos(g_2)\begin{bmatrix} -32\frac{EI\pi^4}{L^4} + \Omega^2(-3s'_{2.a}{}^2\, m_b r_b{}^2 + 2m_d s_{2.d}{}^2 + 4m_b s_{2.a}{}^2) - 4\Omega\omega(m_b r_b{}^2 s'_{2.a}{}^2 - 2m_b s_{2.a}{}^2 - m_d s_{2.d}{}^2) + \cdots \\ \cdots + 2\omega^2(m_d s_{2.d}{}^2 + 2m_b s_{2.a}{}^2 - m_b r_b s'_{2.a}{}^2) + 2m_s(\Omega+\omega)^2 + 2s'_{2.d}{}^2\,(\Omega+\omega)[Im_d(\Omega+\omega) - Jm_d\Omega] \end{bmatrix} + \cdots$$

$$\cdots - \frac{1}{2}a_3 \cos(g_3)\left[-s'_{2.a}\, s'_{3.a}\, m_b r_b{}^2(3\Omega^2 + 4\omega\Omega + 2\omega^2) + 2(m_d s_{2.d} s_{3.d} + 2m_b s_{2.a} s_{3.a})(\Omega+\omega)^2 + 2s'_{2.d}\, s'_{3.d}\,(\Omega+\omega)[Im_d(\Omega+\omega) - Jm_d\Omega]\right]$$

$$A_{33} = -A_{34} = -A_{43} = A_{44} = -\frac{1}{2}s'_{2.a}\, m_b r_b{}^2\Omega(s'_{1.a}\, v_{10} + s'_{2.a}\, v_{20} + s'_{3.a}\, v_{30})(\Omega + 2\omega)$$

$$A_{35} = A_{45} = s'_{2.a}\, m_b r_b{}^2\Omega(s'_{1.a}\, w_{10} + s'_{2.a}\, w_{20} + s'_{3.a}\, w_{30})(\Omega + 2\omega)$$

$$A_{50} + A_{51}\sin(\omega t) + A_{52}\cos(\omega t) + A_{53}\sin(\omega t)^2 + A_{54}\cos(\omega t)^2 + A_{55}\sin(\omega t)\cos(\omega t) = 0 \qquad (6\text{-}24)$$

$$A_{60} + A_{61}\sin(\omega t) + A_{62}\cos(\omega t) + A_{63}\sin(\omega t)^2 + A_{64}\cos(\omega t)^2 + A_{65}\sin(\omega t)\cos(\omega t) = 0 \qquad (6\text{-}25)$$

where,

$$A_{50} = \left[\Omega^2[s'_{1.d}\, s'_{3.d}\,(Jm_d - Im_d) - (m_d s_{1.d} s_{3.d} + 2m_b s_{1.a} s_{3.a}) + s'_{1.a}\, s'_{3.a}\, m_b r_b{}^2] + s'_{1.a}\, s'_{3.a}\, m_b r_b{}^2\omega\Omega\right] v_{10} + \cdots$$

$$\cdots + \left[\Omega^2[s'_{2.d}\, s'_{3.d}\,(Jm_d - Im_d) - (m_d s_{2.d} s_{3.d} + 2m_b s_{2.a} s_{3.a}) + s'_{2.a}\, s'_{3.a}\, m_b r_b{}^2] + s'_{2.a}\, s'_{3.a}\, m_b r_b{}^2\omega\Omega\right] v_{20} + \cdots$$

$$\cdots + \left[\Omega^2[s'_{3.d}{}^2\,(Jm_d - Im_d) - m_s + s'_{3.a}{}^2\, m_b r_b{}^2 - m_d s_{3.d}{}^2 - 2m_b s_{3.a}{}^2] + s'_{3.a}{}^2\, m_b r_b{}^2\omega\Omega + 81\frac{EI\pi^4}{L^4}\right] v_{30} - \cdots$$

$$\cdots - c_{ext}\Omega s_{1.c} s_{3.c} w_{10} - c_{ext}\Omega s_{2.c} s_{3.c} w_{20} - c_{ext}\Omega s_{3.c}{}^2 w_{30} - m_{im} r_{im}\Omega^2 s_{3.d}\cos(\phi_{im})$$

$$A_{60} = c_{ext}\Omega s_{1.c} s_{3.c} v_{10} + c_{ext}\Omega s_{2.c} s_{3.c} v_{20} + c_{ext}\Omega s_{3.c}{}^2 v_{30} - m_{im} r_{im}\Omega^2 s_{3.d}\sin(\phi_{im}) + \cdots$$

$$\cdots + \left[\Omega^2[s'_{1.d}\, s'_{3.d}\,(Jm_d - Im_d) - (m_d s_{1.d} s_{3.d} + 2m_b s_{1.a} s_{3.a}) + s'_{1.a}\, s'_{3.a}\, m_b r_b{}^2] + s'_{1.a}\, s'_{3.a}\, m_b r_b{}^2\omega\Omega\right] w_{10} + \cdots$$

$$\cdots + \left[\Omega^2[s'_{2.d}\, s'_{3.d}\,(Jm_d - Im_d) - (m_d s_{2.d} s_{3.d} + 2m_b s_{2.a} s_{3.a}) + s'_{2.a}\, s'_{3.a}\, m_b r_b{}^2] + s'_{2.a}\, s'_{3.a}\, m_b r_b{}^2\omega\Omega\right] w_{20} + \cdots$$

$$\cdots + \left[\Omega^2[s'_{3.d}{}^2\,(Jm_d - Im_d) - m_s + s'_{3.a}{}^2\, m_b r_b{}^2 - m_d s_{3.d}{}^2 - 2m_b s_{3.a}{}^2] + s'_{3.a}{}^2\, m_b r_b{}^2\omega\Omega + 81\frac{EI\pi^4}{L^4}\right] w_{30}$$

$$A_{51} = -A_{62} = \frac{1}{2}a_1 \sin(g_1)\left[-s'_{1.a}\, s'_{3.a}\, m_b r_b^{\,2}\Omega^2 + 2(m_d s_{1.d} s_{3.d} + 2m_b s_{1.a} s_{3.a})(\Omega+\omega)^2 + 2s'_{1.d}\, s'_{3.d}\,(\Omega+\omega)[Im_d(\Omega+\omega) - Jm_d\Omega]\right] + \cdots$$

$$\cdots + \frac{1}{2}a_2 \sin(g_2)\left[-s'_{2.a}\, s'_{3.a}\, m_b r_b^{\,2}\Omega^2 + 2(m_d s_{2.d} s_{3.d} + 2m_b s_{2.a} s_{3.a})(\Omega+\omega)^2 + 2s'_{2.d}\, s'_{3.d}\,(\Omega+\omega)[Im_d(\Omega+\omega) - Jm_d\Omega]\right] + \cdots$$

$$\cdots + \frac{1}{2}a_3 \sin(g_3)\begin{bmatrix} -162\dfrac{EI\pi^4}{L^4} + \Omega^2(-s'_{3.a}{}^2\, m_b r_b^{\,2} + 2m_d s_{3.d}{}^2 + 4m_b s_{3.a}{}^2) + 4\Omega\omega(m_d s_{3.d}{}^2 + 2m_b s_{3.a}{}^2) + \cdots \\ \cdots + 2\omega^2(m_d s_{3.d}{}^2 + 2m_b s_{3.a}{}^2) + 2m_s(\Omega+\omega)^2 + 2s'_{3.d}{}^2(\Omega+\omega)[Im_d(\Omega+\omega) - Jm_d\Omega] \end{bmatrix} - \cdots$$

$$\cdots - a_1 \cos(g_1) c_{ext} s_{1.c} s_{3.c}(\Omega+\omega) - a_2 \cos(g_2) c_{ext} s_{2.c} s_{3.c}(\Omega+\omega) - a_3 \cos(g_3)\left[81\frac{\xi EI\pi^4}{L^4} + c_{ext} s_{3.c}{}^2(\Omega+\omega)\right]$$

$$A_{52} = A_{61} = -m_b r_b s_{3.a}(\Omega+\omega)^2 - a_1 \cos(g_1) c_{ext} s_{1.c} s_{3.c}(\Omega+\omega) - a_2 \cos(g_2) c_{ext} s_{2.c} s_{3.c}(\Omega+\omega) - a_3 \cos(g_3)\left[81\frac{\xi EI\pi^4}{L^4} + c_{ext} s_{3.c}{}^2(\Omega+\omega)\right] - \cdots$$

$$\cdots - \frac{1}{2}a_1 \cos(g_1)\left[-s'_{1.a}\, s'_{3.a}\, m_b r_b^{\,2}(3\Omega^2 + 4\omega\Omega + 2\omega^2) + 2(m_d s_{1.d} s_{3.d} + 2m_b s_{1.a} s_{3.a})(\Omega+\omega)^2 + 2s'_{1.d}\, s'_{3.d}\,(\Omega+\omega)[Im_d(\Omega+\omega) - Jm_d\Omega]\right] + \cdots$$

$$\cdots - \frac{1}{2}a_2 \cos(g_2)\left[-s'_{2.a}\, s'_{3.a}\, m_b r_b^{\,2}(3\Omega^2 + 4\omega\Omega + 2\omega^2) + 2(m_d s_{2.d} s_{3.d} + 2m_b s_{2.a} s_{3.a})(\Omega+\omega)^2 + 2s'_{2.d}\, s'_{3.d}\,(\Omega+\omega)[Im_d(\Omega+\omega) - Jm_d\Omega]\right] + \cdots$$

$$\cdots - \frac{1}{2}a_3 \cos(g_3)\begin{bmatrix} -162\dfrac{EI\pi^4}{L^4} + \Omega^2(-3s'_{3.a}{}^2\, m_b r_b^{\,2} + 2m_d s_{3.d}{}^2 + 4m_b s_{3.a}{}^2) - 4\Omega\omega(m_b r_b^{\,2} s'_{3.a}{}^2 - 2m_b s_{3.a}{}^2 - m_d s_{3.d}{}^2) + \cdots \\ \cdots + 2\omega^2(m_d s_{3.d}{}^2 + 2m_b s_{3.a}{}^2 - m_b r_b s'_{3.a}{}^2) + 2m_s(\Omega+\omega)^2 + 2s'_{3.d}{}^2(\Omega+\omega)[Im_d(\Omega+\omega) - Jm_d\Omega] \end{bmatrix}$$

$$A_{53} = -A_{54} = -A_{63} = A_{64} = -\frac{1}{2}s'_{3.a}\, m_b r_b^{\,2}\Omega(s'_{1.a}\, v_{10} + s'_{2.a}\, v_{20} + s'_{3.a}\, v_{30})(\Omega + 2\omega)$$

$$A_{55} = A_{56} = s'_{3.a}\, m_b r_b^{\,2}\Omega(s'_{1.a}\, w_{10} + s'_{2.a}\, w_{20} + s'_{3.a}\, w_{30})(\Omega + 2\omega).$$

$$A_{70} + A_{71}\sin(\omega t) + A_{72}\cos(\omega t) = 0 \tag{6-26}$$

where, $A_{70} = r_b[c_b r_b\omega - m_b(a_1 \sin(g_1)s_{1.a} + a_2 \sin(g_2)s_{2.a} + a_3 \sin(g_3)s_{3.a})(\omega+\Omega)^2]$,

$A_{71} = m_b r_b\Omega^2\left[s_{1.a}v_{10} + s_{2.a}v_{10} + s_{3.a}v_{10}\right]$, and $A_{72} = -m_b r_b\Omega^2\left[s_{1.a}w_{10} + s_{2.a}w_{10} + s_{3.a}w_{10}\right]$.

.

From (6-20) and (6-25), we observe the high order time-varying terms associated with coefficients A_{k3} , A_{k4} ,and A_{k5} $for\ k = 1,2,\cdots,6$. For approximation, truncating these high order terms, we generate 12 nonlinear equations using harmonic balancing technique such that,

$$A_{k0} = 0 \quad for\ k = 1,2,\cdots,6 \tag{6-27}$$

$$A_{11} = 0 \quad A_{31} = 0 \quad A_{51} = 0 \tag{6-28}$$

$$A_{12} = 0 \quad A_{32} = 0 \quad A_{52} = 0 \tag{6-29}$$

Additionally, the time-varying terms are shown in (6-26). Since the whirl speed of ABD-ball is assumed to be constant, the time-varying terms are dropped out for approximation.

$$A_{70} = 0 \tag{6-30}$$

Now, we can solve three unknown amplitudes (a_1, a_2 , and a_3), three phases(g_1, g_2 , and g_3), whirl speed(ω) from seven nonlinear equations (6-28), (6-29) and (6-30). Here, the arc-length numerical continuation method is utilized to solve for these unknowns.

Also, from (6-27), the six unknown offsets $v_{k.0}$ and $w_{k.0}$ $for\ k = 1,2,3$ can be directly solved by,

$$\begin{bmatrix} v_{1.0} \\ w_{1.0} \\ v_{2.0} \\ w_{2.0} \\ v_{3.0} \\ w_{3.0} \end{bmatrix} = \begin{bmatrix} S_{11} & S_{12} & S_{13} & -c_{ext}\Omega s_{1.c}{}^2 & -c_{ext}\Omega s_{1.c}s_{2.c} & -c_{ext}\Omega s_{1.c}s_{3.c} \\ c_{ext}\Omega s_{1.c}{}^2 & c_{ext}\Omega s_{1.c}s_{2.c} & c_{ext}\Omega s_{1.c}s_{3.c} & S_{24} & S_{25} & S_{26} \\ S_{31} & S_{32} & S_{33} & -c_{ext}\Omega s_{1.c}s_{2.c} & -c_{ext}\Omega s_{2.c}{}^2 & -c_{ext}\Omega s_{2.c}s_{3.c} \\ c_{ext}\Omega s_{1.c}s_{2.c} & c_{ext}\Omega s_{2.c}{}^2 & c_{ext}\Omega s_{2.c}s_{3.c} & S_{44} & S_{45} & S_{46} \\ S_{51} & S_{52} & S_{53} & -c_{ext}\Omega s_{1.c}s_{3.c} & -c_{ext}\Omega s_{2.c}s_{3.c} & -c_{ext}\Omega s_{3.c}{}^2 \\ c_{ext}\Omega s_{1.c}s_{3.c} & c_{ext}\Omega s_{2.c}s_{3.c} & c_{ext}\Omega s_{3.c}{}^2 & S_{64} & S_{65} & S_{66} \end{bmatrix}^{-1} \begin{bmatrix} m_{im}r_{im}\Omega^2 s_{1.d}\cos(\phi_{im}) \\ m_{im}r_{im}\Omega^2 s_{1.d}\sin(\phi_{im}) \\ m_{im}r_{im}\Omega^2 s_{2.d}\cos(\phi_{im}) \\ m_{im}r_{im}\Omega^2 s_{2.d}\sin(\phi_{im}) \\ m_{im}r_{im}\Omega^2 s_{3.d}\cos(\phi_{im}) \\ m_{im}r_{im}\Omega^2 s_{3.d}\sin(\phi_{im}) \end{bmatrix} \tag{6-31}$$

where,

$$S_{11} = S_{24} = \left[\Omega^2 [s'_{1.d}{}^2 (Jm_d - Im_d) - m_s + s'_{1.a}{}^2 m_b r_b{}^2 - m_d s_{1.d}{}^2 - 2m_b s_{1.a}{}^2] + s'_{1.a}{}^2 m_b r_b{}^2 \omega\Omega + \frac{EI\pi^4}{L^4} \right]$$

$$S_{12} = S_{25} = \left[\Omega^2 [s'_{1.d}\, s'_{2.d} (Jm_d - Im_d) - (m_d s_{1.d} s_{2.d} + 2m_b s_{1.a} s_{2.a}) + s'_{1.a}\, s'_{2.a}\, m_b r_b{}^2] + s'_{1.a}\, s'_{2.a}\, m_b r_b{}^2 \omega\Omega \right]$$

$$S_{13} = S_{26} = \left[\Omega^2 [s'_{1.d}\, s'_{3.d} (Jm_d - Im_d) - (m_d s_{1.d} s_{3.d} + 2m_b s_{1.a} s_{3.a}) + s'_{1.a}\, s'_{3.a}\, m_b r_b{}^2] + s'_{1.a}\, s'_{3.a}\, m_b r_b{}^2 \omega\Omega \right]$$

$$S_{31} = S_{44} = \left[\Omega^2 [s'_{1.d}\, s'_{2.d} (Jm_d - Im_d) - (m_d s_{1.d} s_{2.d} + 2m_b s_{1.a} s_{2.a}) + s'_{1.a}\, s'_{2.a}\, m_b r_b{}^2] + s'_{1.a}\, s'_{2.a}\, m_b r_b{}^2 \omega\Omega \right]$$

$$S_{32} = S_{45} = \left[\Omega^2 [s'_{2.d}{}^2 (Jm_d - Im_d) - m_s + s'_{2.a}{}^2 m_b r_b{}^2 - m_d s_{2.d}{}^2 - 2m_b s_{2.a}{}^2] + s'_{2.a}{}^2 m_b r_b{}^2 \omega\Omega + 16\frac{EI\pi^4}{L^4} \right]$$

$$S_{33} = S_{46} = \left[\Omega^2 [s'_{2.d}\, s'_{3.d} (Jm_d - Im_d) - (m_d s_{2.d} s_{3.d} + 2m_b s_{2.a} s_{3.a}) + s'_{2.a}\, s'_{3.a}\, m_b r_b{}^2] + s'_{2.a}\, s'_{3.a}\, m_b r_b{}^2 \omega\Omega \right]$$

$$S_{51} = S_{64} = \left[\Omega^2 [s'_{1.d}\, s'_{3.d} (Jm_d - Im_d) - (m_d s_{1.d} s_{3.d} + 2m_b s_{1.a} s_{3.a}) + s'_{1.a}\, s'_{3.a}\, m_b r_b{}^2] + s'_{1.a}\, s'_{3.a}\, m_b r_b{}^2 \omega\Omega \right]$$

$$S_{52} = S_{65} = \left[\Omega^2 [s'_{2.d}\, s'_{3.d} (Jm_d - Im_d) - (m_d s_{2.d} s_{3.d} + 2m_b s_{2.a} s_{3.a}) + s'_{2.a}\, s'_{3.a}\, m_b r_b{}^2] + s'_{2.a}\, s'_{3.a}\, m_b r_b{}^2 \omega\Omega \right]$$

$$S_{53} = S_{66} = \left[\Omega^2 [s'_{3.d}{}^2 (Jm_d - Im_d) - m_s + s'_{3.a}{}^2 m_b r_b{}^2 - m_d s_{3.d}{}^2 - 2m_b s_{3.a}{}^2] + s'_{3.a}{}^2 m_b r_b{}^2 \omega\Omega + 81\frac{EI\pi^4}{L^4} \right]$$

These offsets are computed by the size of imbalance mass, inherent characteristic of bearing, rotor/shaft system as well as operating speed. As imbalance size increase, these offsets are also augmented.

Let's review the high order time-varying dropped out for approximation. The higher order time-varying terms truncated in (6-20) through (6-26) are followed.

$$A_{13} = -A_{14} = -A_{23} = A_{24} = -\frac{1}{2} s'_{1.a}\, m_b r_b{}^2 \Omega (s'_{1.a}\, v_{10} + s'_{2.a}\, v_{20} + s'_{3.a}\, v_{30})(\Omega + 2\omega)$$

$$A_{15} = A_{25} = s'_{1.a}\, m_b r_b{}^2 \Omega (s'_{1.a}\, w_{10} + s'_{2.a}\, w_{20} + s'_{3.a}\, w_{30})(\Omega + 2\omega)$$

$$A_{33} = -A_{34} = -A_{43} = A_{44} = -\frac{1}{2} s'_{2.a}\, m_b r_b{}^2 \Omega (s'_{1.a}\, v_{10} + s'_{2.a}\, v_{20} + s'_{3.a}\, v_{30})(\Omega + 2\omega)$$

$$A_{35} = A_{45} = s'_{2.a}\, m_b r_b{}^2 \Omega (s'_{1.a}\, w_{10} + s'_{2.a}\, w_{20} + s'_{3.a}\, w_{30})(\Omega + 2\omega)$$

$$A_{53} = -A_{54} = -A_{63} = A_{64} = -\frac{1}{2} s'_{3.a}\, m_b r_b{}^2 \Omega (s'_{1.a}\, v_{10} + s'_{2.a}\, v_{20} + s'_{3.a}\, v_{30})(\Omega + 2\omega)$$

$$A_{55} = A_{56} = s'_{3.a}\, m_b r_b{}^2 \Omega (s'_{1.a}\, w_{10} + s'_{2.a}\, w_{20} + s'_{3.a}\, w_{30})(\Omega + 2\omega).$$

$$A_{71} = m_b r_b \Omega^2 \left[s_{1.a} v_{10} + s_{2.a} v_{10} + s_{3.a} v_{10} \right] \quad A_{72} = -m_b r_b \Omega^2 \left[s_{1.a} w_{10} + s_{2.a} w_{10} + s_{3.a} w_{10} \right] \tag{6-32}$$

The influence of these time varying terms in (6-32) is determined by the size of imbalance mass. Each term holds the offsets($v_{k.0}$ and $w_{k.0}$ $for\ k = 1,2,3$) in (6-32), which is proportional to the imbalance effect as seen in (6-31).

The effect should be insignificant not to heavily deteriorate the accuracy of suggested solution. Fortunately, the effect of time-varying terms can be insignificant in the two following reasons. *i*) $v_{k.0}$ and $w_{k.0}$ $for\ k = 1,2,3$ which are directly proportional to the size of imbalance mass. The best performance of ABD can be usually achieved under the condition $m_{im} < 2m_b$. Under this condition $m_{im} < 2m_b$, the effect of time-varying terms can be insignificant. In other words, there exists allowable imbalance size not to heavily deteriorate the accuracy of the limit cycle solution suggested here. *ii*) The inherent nature of limit cycle related with the whirl speed of ABD-ball dominates the imbalance effect so that the time-varying terms in (6-32) directly associated with imbalance can be less important contribution to the solution. These two conditions *i*) and *ii*) above enhance us to achieve the well approximated solution and these aspects will be explained with and validated through the numerical simulation results(see the results *i*), *j*) and *k*) in Figure.6.2 and outcomes in Figure.6.3).

6.3 Stability analysis

To investigate the local stability of the system in the neighborhood of the limit-cycle solution founded in previous sections, (6-12) with reduced coordinates $q(t) = \left[\eta_{v1}(t) \quad \eta_{w1}(t) \quad \eta_{v2}(t) \quad \eta_{w2}(t) \quad \eta_{v3}(t) \quad \eta_{w3}(t) \quad \phi(t) \right]$ is linearized using the perturbation approach. By considering the small perturbations of each coordinate such that $\Delta\eta_{L.wi}(t)$, $\Delta\eta_{L.wi}(t)$ $for\ i = 1,2,3$, and $\Delta\phi_L(t)$, the perturbed system configuration is $\eta_{vi}(t) = \eta_{L.vi}(t) + \Delta\eta_{L.vi}(t)$, $\eta_{wi}(t) = \eta_{L.wi}(t) + \Delta\eta_{L.wi}(t)$, and $\phi(t) = \phi_L(t) + \Delta\phi_L(t)$, where, $\eta_{L.wi}(t)$, $\eta_{L.wi}(t)$ and $\phi_L(t)$ are the limit-cycle harmonic solutions in (6-19). Substituting this perturbed configuration into the

dynamics (6-12), and truncating the higher order terms results in a set of linearized equation about the set of limit-cycle solution $\eta_{L.wi}(t), \eta_{L.wi}(t)$ and $\phi_L(t)$.

Denoting a set of perturbed coordinate as $\Delta q_L(t) = [\Delta\eta_{L.v1}(t) \;\; \Delta\eta_{L.w1}(t) \;\; \Delta\eta_{L.v2}(t) \;\; \Delta\eta_{L.w2}(t) \;\; \Delta\eta_{L.v3}(t) \;\; \Delta\eta_{L.w3}(t) \;\; \Delta\phi_L(t)]$ and a set of limit-cycle solution as $q_L(t) = [\eta_{L.v1}(t) \;\; \eta_{L.w1}(t) \;\; \eta_{L.v2}(t) \;\; \eta_{L.w2}(t) \;\; \eta_{L.v3}(t) \;\; \eta_{L.w3}(t) \;\; \phi_L(t)]$, we have,

$$\Delta M(q_L,t)\Delta\ddot{q}_L + \Delta C(q_L,t)\Delta\dot{q}_L + \Delta K(q_L,t)\Delta q_L = 0 \tag{6-33}$$

Defining the state vector $x(t) = [\Delta {q_L}^T \; \Delta {\dot{q}_L}^T]^T \in \Re^{14}$, we can transform (6-33) into,

$$\dot{x}(t) = A(q_L,t)x(t) \tag{6-34}$$

with a system matrix $A(q_L,t) = \begin{bmatrix} 0_{7\times7} & I_{7\times7} \\ -\Delta M^{-1}(q_L,t)\Delta K(q_L,t) & -\Delta M^{-1}(q_L,t)\Delta C(q_L,t) \end{bmatrix} \in \Re^{14\times14}$.

To determine the stability of (6-34) which is the linear time-varying equation, we employ the Floquet's Transition Matrix (FTM) method. By the linear theory, the solution for (6-34) is expressed as

$$x(t) = \Phi(q_L,t)x_0 \tag{6-35}$$

where, $\Phi(q_L,t) \in \Re^{14\times14}$ and $x_0 \in \Re^{14}$ are FTM and the initial condition respectively.

Replacing the x_0 as the 14 by 14 identical matrix, $x(t)$ becomes 14 by 14 matrix solution and then, with the period $T = \frac{2\pi}{\omega}$, we can obtain the periodic solution such that $x(T) = \Phi(q_L,T)$. Ultimately, the stability criterion is determined by

$$\begin{aligned} &\max_{1\le i\le 10}\left|\lambda_i(x(T))\right| < 1 \quad \textit{stable} \\ &\max_{1\le i\le 10}\left|\lambda_i(x(T))\right| > 1 \quad \textit{unstable} \end{aligned} \tag{6-36}$$

where λ_i is the eigenvalues of matrix solution $x(T) = \Phi(q_L,T)$.

Among the limit cycle solutions q_L, we also have the solution satisfying $\dot{\phi}_L(t) = \omega \approx 0$. This is the merged equilibrium solution where two balls are merged together and synchronously rotating with rotor. This is a synchronous behavior usually exhibited before the critical speed, which is not belonging to the non-synchronous condition($\omega \neq 0$). The stability of merged equilibrium condition is also considered in the subsequent simulation results.

To investigate the local stability of system about a fixed balancing equilibrium solution, (6-12) with full-coordinate $q(t) = [\eta_{v1}(t) \;\; \eta_{w1}(t) \;\; \eta_{v2}(t) \;\; \eta_{w2}(t) \;\; \eta_{v3}(t) \;\; \eta_{w3}(t) \;\; \phi_1(t) \;\; \phi_1(t)]^T$ is linearized using perturbation method with perturbed system coordinates $\eta_{vi}(t) = \eta_{eq.vi}(t) + \Delta\eta_{eq.vi}(t)$, $\eta_{wi}(t) = \eta_{eq.wi}(t) + \Delta\eta_{eq.wi}(t)$ *for* $i = 1,2,3$ and $\phi_j(t) = \phi_{eq.j}(t) + \Delta\phi_{eq.j}(t)$ *for* $j = 1,2$ and, by substituting the perturbed coordinates into (6-12) and truncating the higher order terms, we have a linear time-invariant equation describing the perturbed

coordinate $\Delta q_{eq}(t)=\left[\Delta\eta_{eq.v1}(t)\ \ \Delta\eta_{eq.w1}(t)\ \ \Delta\eta_{eq.v2}(t)\ \ \Delta\eta_{eq.w2}(t)\ \ \Delta\eta_{eq.v3}(t)\ \ \Delta\eta_{eq.w3}(t)\ \ \Delta\phi_{eq.1}(t)\ \ \Delta\phi_{eq.2}(t)\right]^T$. Based upon this equation, the simple eigenvalue analysis can be applied to determine the local stability about the fixed equilibrium point $q_{eq}(t)=\left[\eta_{eqv1}(t)\ \ \eta_{eqw1}(t)\ \ \eta_{eqv2}(t)\ \ \eta_{eqw2}(t)\ \ \eta_{eqv3}(t)\ \ \eta_{eqw3}(t)\ \ \phi_{eq1}(t)\ \ \phi_{eq2}(t)\right]^T$. The fixed equilibrium point of balancing position $q_{eq1}=\left[\eta_{eqv1}(t)\ \ \eta_{eqw1}(t)\ \ \eta_{eqv2}(t)\ \ \eta_{eqw2}(t)\ \ \eta_{eqv3}(t)\ \ \eta_{eqw3}(t)\right]^T$ is computed as

$$q_{eq1}=[K_{s.1}+K_{s.2}+N_c^T K_d N_c|_{x=L_d}+N_c^T K_{AB1}(\phi_{1.eq},\phi_{2.eq})N_c|_{x=L_{AB}}+N_c^T K_e N_c|_{x=L_{b1}}]^{-1}[N_c^T F_{I.1}|_{x=L_d}+N_c^T F_{AB1}(\phi_{1.eq},\phi_{2.eq})|_{x=L_{AB}}] \tag{6-37}$$

where, $K_{AB.1}=\begin{bmatrix} -2m_b\Omega^2 & 0 & 0 & 0 \\ 0 & -2m_b\Omega^2 & 0 & 0 \\ 0 & 0 & m_b r_b^2(\Omega^2+\sum_{i=1}^{2}\frac{1}{2}\Omega^2\cos(2\phi_{i.eq})) & m_b r_b^2(\sum_{i=1}^{2}[\sin(2\phi_{i.eq})\frac{1}{2}\Omega^2]) \\ 0 & 0 & m_b r_b^2(\sum_{i=1}^{2}[\sin(2\phi_{i.eq})\frac{1}{2}\Omega^2]) & m_b r_b^2(\Omega^2+\sum_{i=1}^{2}[-\frac{1}{2}\Omega^2\cos(2\phi_{i.eq})]) \end{bmatrix}$

$F_{AB.1}=m_b r_b\left[\sum_{i=1}^{2}\cos(\phi_{i.eq})\Omega^2\ \ \sum_{i=1}^{2}\sin(\phi_{i.eq})\Omega^2\ \ 0\ \ 0\right]^T$, $F_{I.1}=m_{im}r_{im}\Omega^2\left[\cos(\phi_{im})\ \ \sin(\phi_{im})\ \ 0\ \ 0\right]^T$

$q_{eq2}=\left[\phi_{eq.1}(t)\ \ \phi_{eq2}(t)\right]^T$ is computed by solving for $\phi_{eq.1}(t)\ \ \phi_{eq.2}(t)$ minimizing one of nonlinear equations such that,

$$\min_{\phi_{eq.j}}\sqrt{v_r(x,t)^2+w_r(x,t)^2}\,|_{x=L_d}\ \text{or}\ \min_{\phi_{eq.j}}\sqrt{\alpha(x,t)^2+\beta(x,t)^2}\,|_{x=L_d} \tag{6-38}$$

where,

$\left[v_r(x,t)\ \ w_r(x,t)\ \ \alpha(x,t)\ \ \beta(x,t)\right]|_{x=L_d}=\cdots$

$=N_c|_{x=L_d}[K_{s.1}+K_{s.2}+N_c^T K_d N_c|_{x=L_d}+N_c^T K_{AB1}(\phi_{1.eq},\phi_{2.eq})N_c|_{x=L_{AB}}+N_c^T K_e N_c|_{x=L_{b1}}]^{-1}[N_c^T F_{I.1}|_{x=L_d}+N_c^T F_{AB1}(\phi_{1.eq},\phi_{2.eq})|_{x=L_{AB}}]$

By solving (6-38), we can obtain $\phi_{eq.1}(t)\ \ \phi_{eq.2}(t)$ to achieve minimum physical vibration amplitude of rotor at $x=L_d$. The subsequent stability analysis of the balanced solution is conducted in the neighborhood of $[q_{eq.1}\ \ q_{eq.2}]^T$.

6.4 Numerical Simulation Results

In this section, the response of limit-cycle solution suggested here is validated by comparing with full-nonlinear numerical simulation of (6-12) and the stability of solution is investigated.

The unknowns of solution in (6-19) with n=3 are obtained by solving the set of nonlinear equations obtained in (6-28) through (6-31)

Before proceeding, it should be noted that dimensionless operating speed $\overline{\Omega}$ introduced here is defined by $\frac{\Omega}{\omega_n}$ where, $\omega_n = \sqrt{\frac{EI\pi^4}{L^4 m_s}}$, $L = 2.5m$, $m_s = 4kg$, $m_d = 2kg$, $\mathrm{Im}_d = \frac{1}{4} m_d r_d^{\,2}$, $\mathrm{Im}_r = \frac{1}{2} m_d r_d^{\,2}$, $\mathrm{Im}_s = \frac{1}{12} m_s L^2, Jm_s = 0, c_b = 1e-4$, $L_{b1} = 0.45L$, $r_b = r_{im} = 0.06m$, and $\phi_{im} = 45^\circ$ are commonly used for the all simulations presented here, unless specified otherwise.

In Figure.6.2, we compare the limit-cycle solution in (6-19) with the numerical simulation of full nonlinear system in (6-12) which is constructed in MATLAB/Simulink environment. For the simplicity, we use the short notations **LC** and **FS** for limit cycle solution and the results obtained through the full nonlinear simulation throughout this paper. In **FS**, the limit-cycle condition can be also generated by setting the initial condition leading to the outside of the provided attraction basin described in [10]. Thus, the initial position of two balls is presumed to be merged on the full nonlinear simulation s.t, $\phi_1(0) = \phi_2(0)$. In *a*) and *b*) of Figure.6.2, the star-dotted lines represent the responses obtained via **FS** while the circle dotted lines do **LC**. *a*) and *b*) represent the whirl orbit of in-plane transverse deflection($v_r(t)\ vs.w_r(t)$) and the tilting out-plane whirl ($\alpha(t)\ vs.\beta(t)$) at $\overline{\Omega} = 5$ by converting the modal coordinates to the physical ones using $\left[v_r \;\; w_r \;\; \alpha \;\; \beta\right]^T = N_c(x)|_{x=L_{AB}} \left[\eta_{v1}(t) \;\; \eta_{w1}(t) \;\; \eta_{v2}(t) \;\; \eta_{w2}(t) \;\; \eta_{v3}(t) \;\; \eta_{w3}(t)\right]^T$ with an imbalance source $L_d = 0.75L$. Both **LC** and **FS** are synchronous for each other in *a*) and *b*). The whirl orbits displayed are perfectly circular ones due to the symmetric property of rigid support and external damping force. *c*), *e*) and *g*) in Figure.6.2 represent the horizontal deflection $v_r(t)$ at every axial location($\bar{x} = \frac{x}{L}$) of shaft and *d*), *f*) and *h*) indicate the pitch angle $\alpha(t)$ of shaft at given axial locations. The deflections and titling angles in *c*) through *h*) show 10 different shapes chosen at 10 different random simulation time. Here, the straight line indicates **LC** while the dots do **FS**. *c*) and *d*) are respectively $v_r(t)$ and $\alpha(t)$ at $\overline{\Omega} = 1.2$. *e*) and *f*) are respectively achieved at $\overline{\Omega} = 5$ while *g*) and *h*) are obtained at $\overline{\Omega} = 15$. As expected from shape function $\psi_i(x) = \sin(i\frac{x}{L})\ for\ i = 1,2,3$, the 1st (*c*) and *d*)), 2nd (*e*) and *f*)), and 3rd (*g*) and *h*)) mode shapes are observed for three different operating speeds.

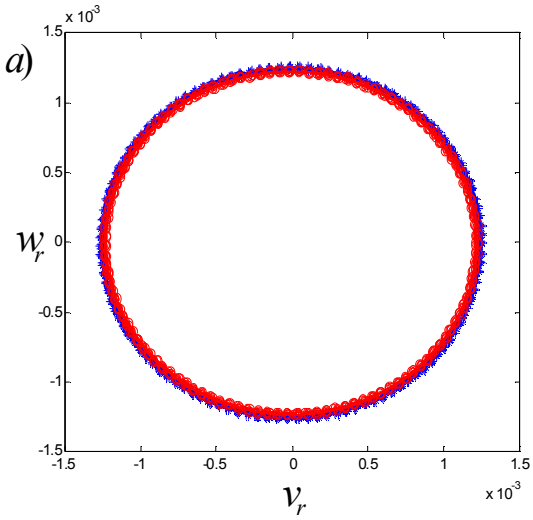
In (*i*) and (*j*), the straight line is the whirl speed of merged ABD's balancer from **LC** on the time domain and the fluctuating lines belong to **FS**. The results in (*i*) and (j) are respectively obtained at $\overline{\Omega} = 4$ and $\overline{\Omega} = 15$ commonly using $L_d = 0.75L$ and $L_{AB} = 0.6L$. Since the effect of time-varying terms are truncated to compute the assumed whirl speed of ABD's ball in **LC**, the fluctuating whirl speed of **FS** can't be

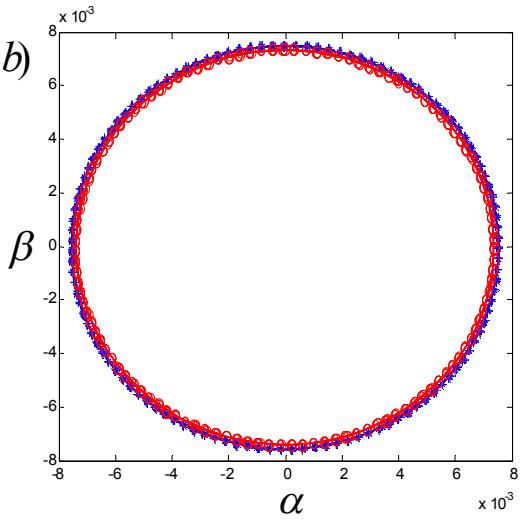
captured by analytical whirl speed of **LC.** However, the amplitudes of whirl speed in **FS** are very small although they increase as the size of imbalance mass is augmented and the whirl speed in **LC** approximate the average of whirl speed in **FS**. The results in *i*) and *j*) support that the effect of time-varying terms truncated is proportional to the imbalance size as expected from (6-31) and (6-32) and those terms in (6-32) are insignificant under relative reasonable size of imbalance mass to balancer mass in ABD. Furthermore, in (*k*), one can see that the whirl speed(straight dotted line) in **LC** obtained at each operating speed can capture the average of the numerically simulated ball speed(star dots) collected for a certain sampling period at a given operating speed(i.e, $0.5\left[\max_{T-t_a<t<T}\omega_s(t)+\min_{T-t_a<t<T}\omega_s(t)\right]$ where $\omega_s(t)$ is whirl speed in **FS** and T and t_a are the end of simulation time and the sampling period). Along with the average speed of **FS** at each operating speed, the minimum($\min_{T-t_a<t<T}\omega_s(t)$) and maximum($\max_{T-t_a<t<T}\omega_s(t)$) of ball speed are specified as triangular and circular dots respectively. It is founded that the difference between $\min_{T-t_a<t<T}\omega_s(t)$ and $\max_{T-t_a<t<T}\omega_s(t)$ is very small. (Note that *k)* displays both non-synchronous ($|\omega|\neq 0$) and synchronous merged($|\omega|=0$) conditions together). Also, (*l*) in Figure.6.2 displays the difference between $\min_{T-t_a<t<T}\omega_s(t)$ and $\max_{T-t_a<t<T}\omega_s(t)$ relative to $0.5\left[\max_{T-t_a<t<T}\omega_s(t)+\min_{T-t_a<t<T}\omega_s(t)\right]$ and d in (*l*) can be computed in the following manner such that,

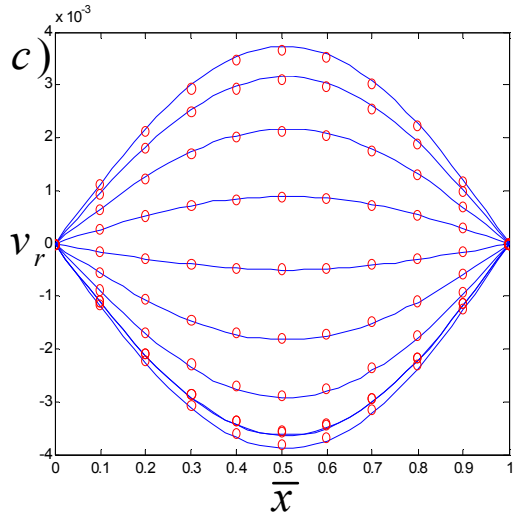
$$d=2\frac{\max_{T-t_a<t<T}\omega_s(t)-\min_{T-t_a<t<T}\omega_s(t)}{\max_{T-t_a<t<T}\omega_s(t)+\min_{T-t_a<t<T}\omega_s(t)}$$

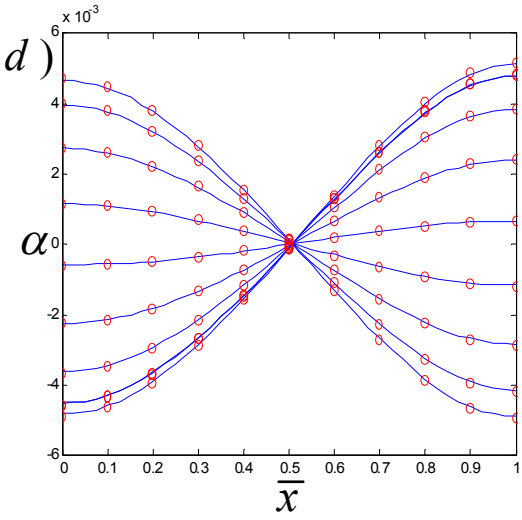
At the range of each supercritical operating speed, d is below 4% for all cases of imbalance mass in (*l*) although d is up to more than 10% near each critical speed.

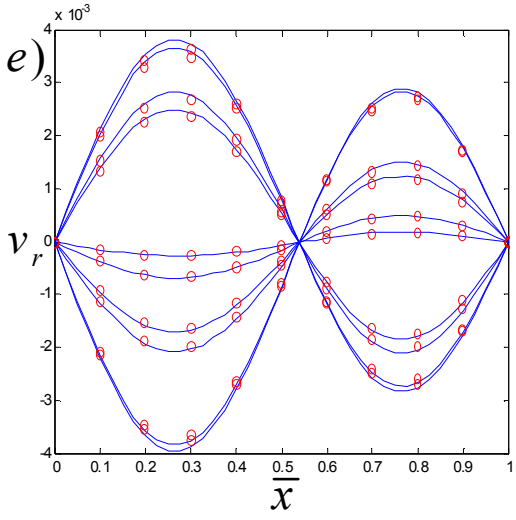
m) through *o*) in Figure.6.2 represents the maximum amplitude of $\eta_{v.i}(t)\ for\ i=1,2,3$ at given each operating speed. The thick straight lines in *m*) through *o*) represent the maximum of amplitude in **LC** computed by $a_i+v_{i.0}\ for\ i=1,2,3$ while the star dots describe **FS** results obtained through $\max_{T-t_a<t<T}\eta_{v.i.s}(t)\ for\ i=1,2,3$ where $\eta_{v.i.s}(t)$ are belong to **FS**. Here, $L_d=0.75L$ and $L_{AB}=0.5L$ are used. The limit cycle solution presented here is validated with numerical simulation and is accurate enough to capture the unwanted non-synchronous response with reasonable assumptions. This validated solution is used for subsequent stability simulation.

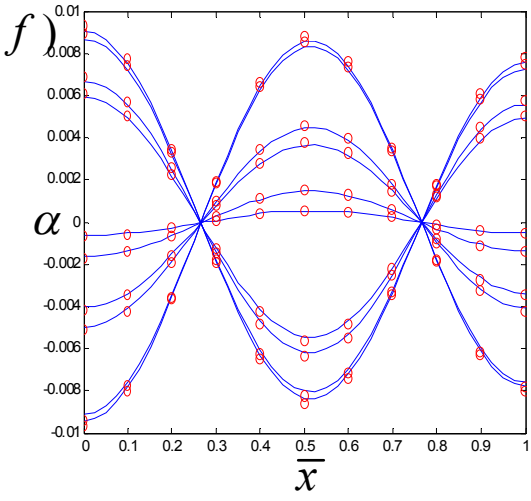

a)
x 10^3
w_r
v_r
x 10^3

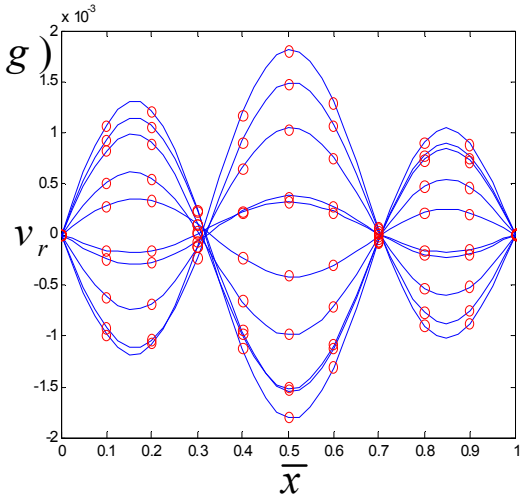

b)
x 10^3
β
α
x 10^3

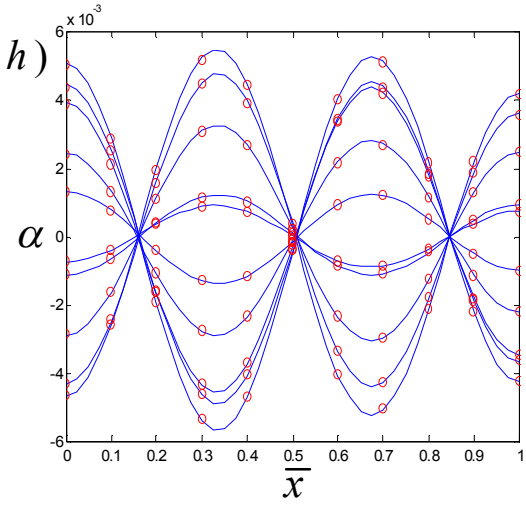

c)
x 10^3
v_r
x̄

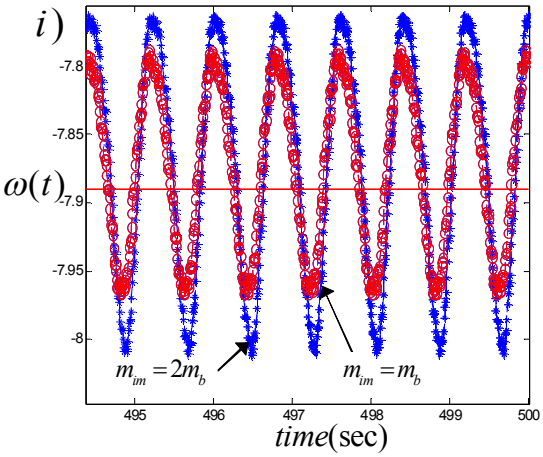

d)
x 10^3
α
x̄

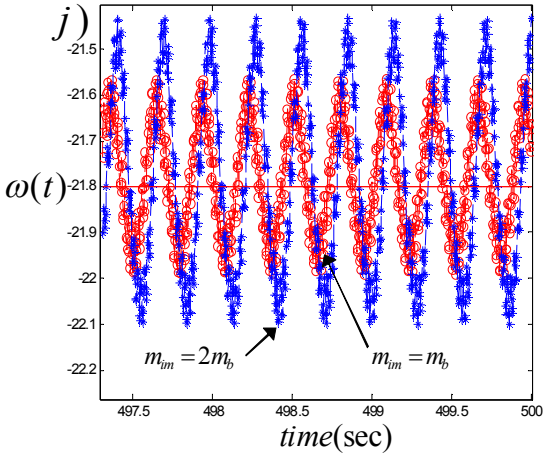

e)
x 10^3
v_r
x̄

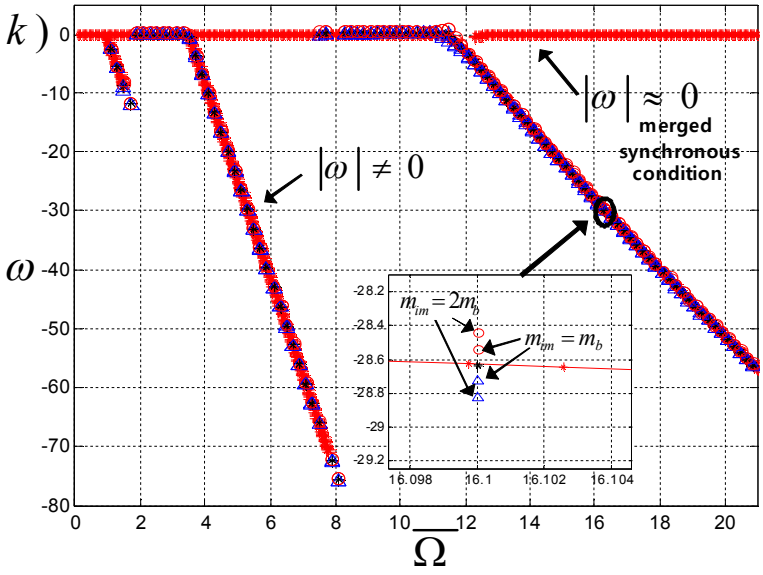

f)
α
x̄


g)
x 10^-3
v_r
x̄


h)
x 10^-3
α
x̄


i)
ω(t)
m_im = 2m_b
m_im = m_b
time(sec)


j)
ω(t)
m_im = 2m_b
m_im = m_b
time(sec)


k)
ω
|ω| ≠ 0
|ω| ≈ 0
merged
synchronous
condition
m_im = 2m_b
m_im = m_b
Ω

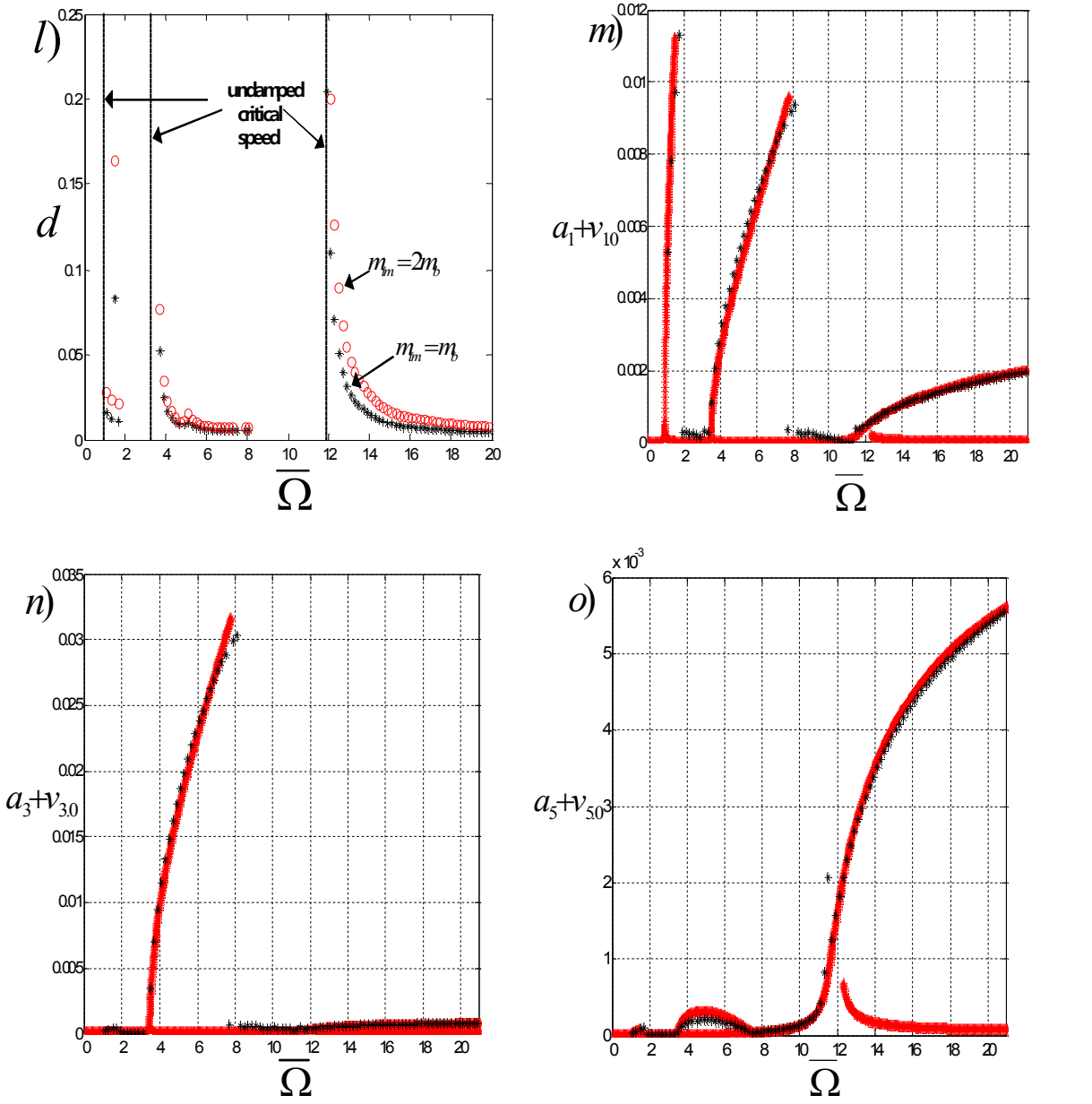


Figure.6.2. Comparison between full numerical response and analytical one

Figure.6.3 displays the whirl speed ω (displayed as star-dots) and the damped natural frequencies(displayed as dotted lines) of system without ABD which is obtained through the imaginary part of eigenvalue of A_0.

$$A_0 = \begin{bmatrix} 0_{6\times6} & I_{6\times6} \\ -M_0^{-1}K_0 & -M_0^{-1}C_0 \end{bmatrix} \tag{6-39}$$

where, $M_0 = M_s + N_c{}^T M_d N_c \mid_{x=L_d}$, $C_0 = C_s + N_c^T C_d N_c \mid_{x=L_d} + N_c^T C_e N_c \mid_{x=L_{b1}}$,

$K_0 = K_{s.1} + K_{s.2} + N_c^T K_d N_c \mid_{x=L_d} + N_c^T K_e N_c \mid_{x=L_{b1}}$

As seen in the results in Figure.6.3, it is founded that the whirl speed of system with ABD is synchronous with the damped natural frequency of baseline system(without ABD) . Considering $m_b << m_s + m_d$, the damped natural frequency of system with ABD can be approximated as the baseline systems'. This implies that the system is excited by damped natural frequency of system under limit-cycle condition. We can see this point of view more clearly by investigating the force excitation term $F_{AB}(\phi_i, \dot{\phi}_i)$ in (6-12). Using the coordinate transformation (6-2-a), $F_{AB}(\phi_i, \dot{\phi}_i)$ can be expressed the force terms with respect to the fixed frame such that,

$$F_{AB} = m_b r_b \left[\sum_{i=1}^{2} \cos[(\dot{\phi}_i + \Omega)t](\Omega^2 + \dot{\phi}_i) \quad \sum_{i=1}^{2} \sin[(\dot{\phi}_i + \Omega)t](\Omega^2 + \dot{\phi}_i) \quad 0 \quad 0 \quad 0 \quad 0 \right]^T \cdot$$

Considering the merging condition of two ABD balls($\dot{\phi}_i \Rightarrow \dot{\phi}$), the driving frequency of force term in F_{AB} above is founded as $\dot{\phi} + \Omega = \omega + \Omega$. As shown in Figure.6.3, at each operating speed, $\omega + \Omega$ is approximately the damped resonance frequency of system so that the effect of this frequency property generates the large vibration amplitude of system, which implies that another force excitation term/imbalance force $N_I^T F_I$ in (6-12) less significantly influences to the system under the limit-cycle condition. In other words, the force excited by ABD-ball become far more dominant than one transmitted by imbalance effect deteriorating the accuracy of limit cycle solution presented here. Thus, the truncated time-varying terms in (6-31) for approximation become less significant under the limit-cycle condition because those terms are proportional to imbalance effect of system induced by $N_I^T F_I$. If $m_{im} = 0$, then there no exist time-varying terms in (6-31). Therefore, the assumptions and approximation we made for the limit-cycle solution are valid by observing the results in *i*) through *l*) in Figure.6.2 and the outcomes in Figure.6.3. The simulation results in Figure.6.3 provide us that the system is excited with the three different damped natural frequencies associated with 3 expended modal coordinates. The results in Figure.6.3 support that the limit cycle condition is very critical issue in usage of ABD so that it should be avoid if possible otherwise it may cause serious destruction in system.

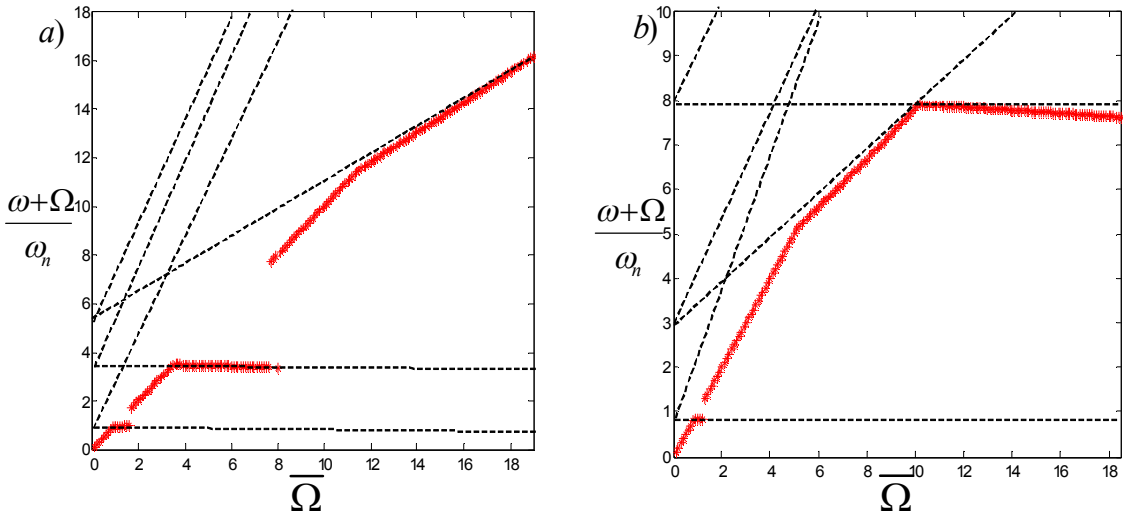


Figure.6.3. whirl speed of balancer mass in ABD and damped natural frequency of system / a) $L_d = 0.75L$ and $L_{AB} = 0.45L$ and b) $L_d = 0.5L$ and $L_{AB} = 0.3L$

Discussed in the previous section, Figure.6.4 presents typical simulation results for synchronous fixed equilibrium positions of ABD balancer mass by solving (6-38). Those positions are varied with respect to the operating speed and the relative axial position of ABD to imbalance source. The typical $\phi_{eq.1}(t)$ and $\phi_{eq.2}(t)$ are displayed below at given two different simulation conditions.

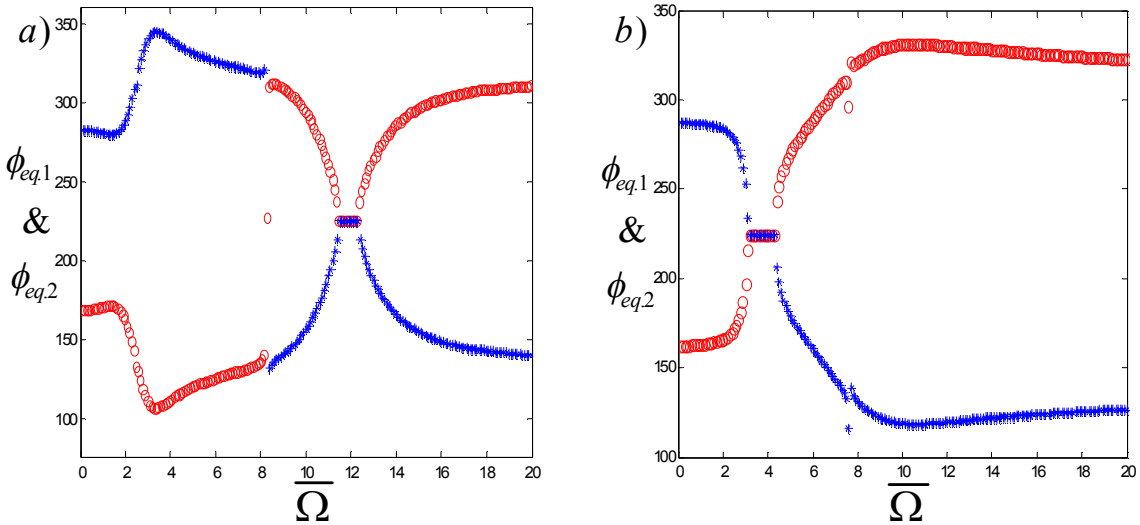


Figure.6.4 Synchronous fixed equilibrium position of ABD balls (a) $L_d = 0.75L$ and $L_{AB} = 0.3L$ b) $L_d = 0.7L$ and $L_{AB} = 0.6L$)

At given operating speed, Figure.6.5 describes the stability region of non-synchronous limit cycle behavior and synchronous balancing condition of system with two main parameters; balancer mass m_b and viscous damping coefficient c_b of ABD.

Before proceeding, the short notations used in Figure.6.5 are explained and will be used throughout this paper. *l*: pure limit cycle condition, *M*: merged equilibrium condition, and $B+l$: undesired coexistence zone of limit-cycle and balancing condition. Specifically, the balancing condition B is satisfying (6-38) and defined in the following manner.

$$B \equiv \{\sqrt{v_r(x,t)+w_r(x,t)} < \sqrt{v_{r.im}(x,t)^2+w_{r.im}(x,t)^2}\}|_{x=L_d,t=\infty} \cup \{\sqrt{\alpha^2(x,t)+\beta^2(x,t)} \le \sqrt{\alpha_{im}{}^2(x,t)+\beta_{im}{}^2(x,t)}\}|_{x=L_d,t=\infty}$$

where $\sqrt{v_{r.im}{}^2+w_{r.im}{}^2}$ is the steady-state transverse amplitude of generated by the imbalance rotor/shaft system without ABD (i.e, baseline system) to compare the vibration amplitude $\sqrt{v_r{}^2+w_r{}^2}$ at $x=L_d$ in balancing condition and $\sqrt{\alpha_{im}{}^2+\beta_{im}{}^2}$ indicate steady-state tilting angle amplitude generated by the baseline system to compare the performance index (i.e, tilting amplitude $\sqrt{\alpha^2+\beta^2}$ at $x=L_d$) in balancing condition. The influence of relative m_b size to entire system one is investigated in *a*) of Figure.5 while the effect of c_b of ABD is explored in *b*). As seen in *a*), both *l* and $B+l$ becomes dominant as the relative m_b increases. As c_b is augmented, the non-synchronous behavior is suppressed in the high operating speed($6<\bar{\Omega}<8$). These two parameters play central role to control both synchronous and non-synchronous behavior. The outcomes in Figure.6.5 provide us that the unwanted coexistence $B+l$ exists at given design parameters of ABD and operating speed. However, this behavior can be avoided through the proper selection of parameters and operating environment/speed.

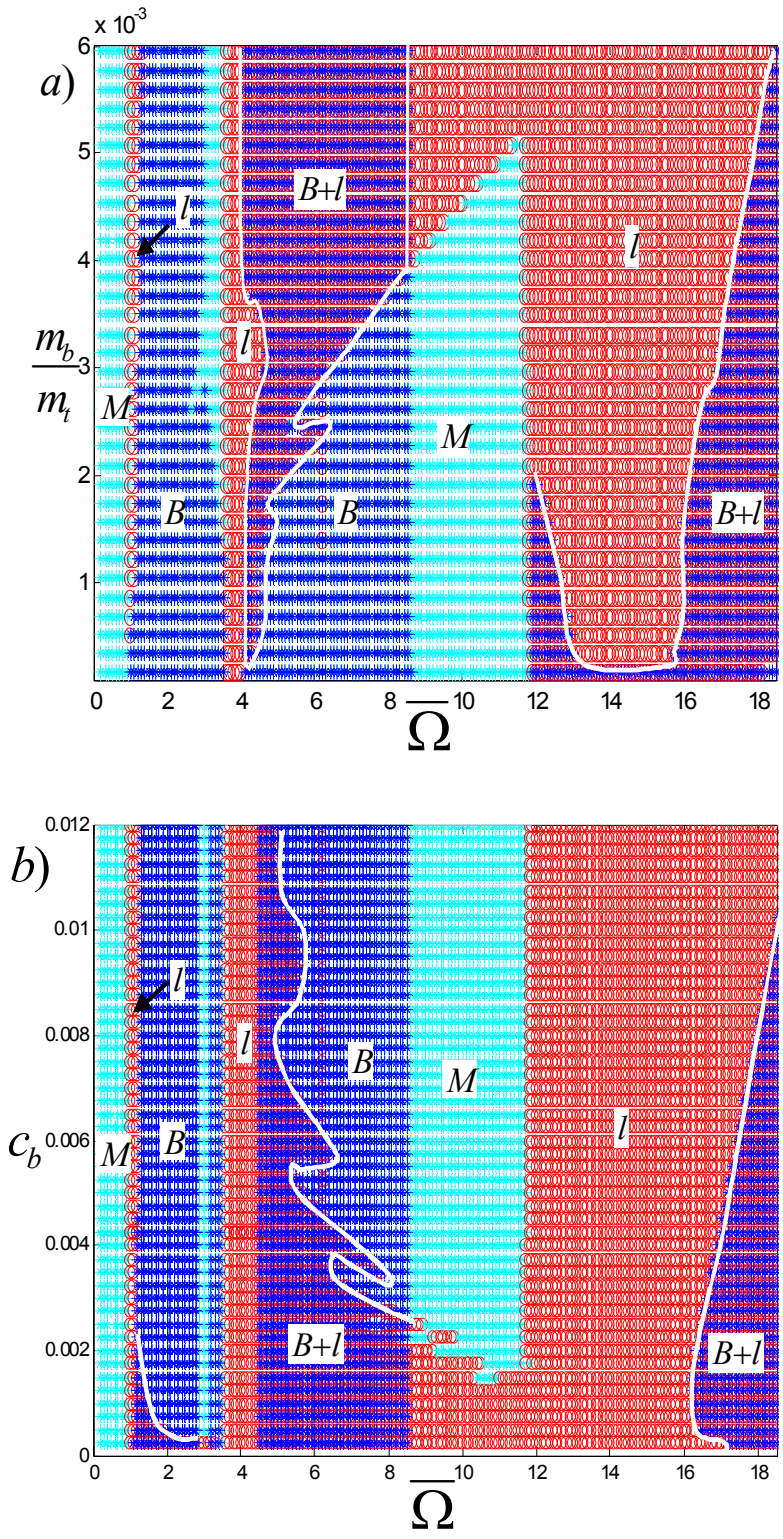
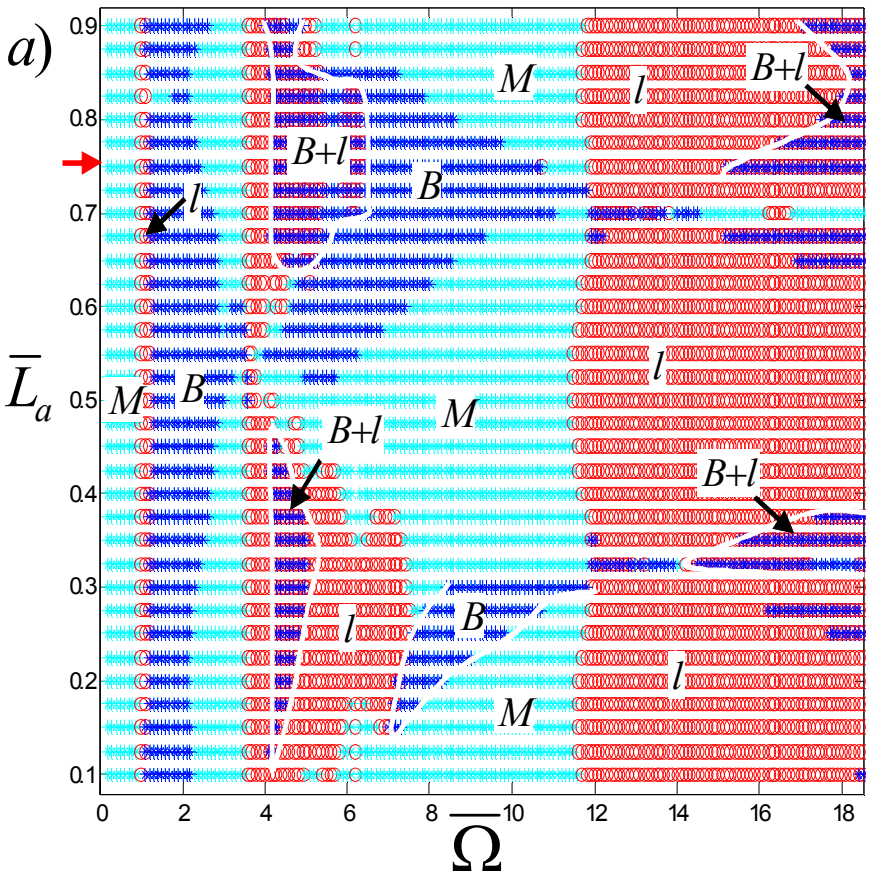


Figure.6.5 a) Stability influence of the relative mass size m_b of ABD to entire system mass b) System stability influence of ABD ball damping coefficient c_b.

At each operating speed, Figure.6.6 shows the two stability contour plots describing the limit cycle and balancing condition generated by the relative axial location of ABD along with shaft to the two different position of imbalance rotor(displayed as a red arrow on each plot). Note that $\overline{L}_a = \frac{L_{AB}}{L}$.

In *a*), we can find pure B in the range of $0.7 < \overline{L}_a < 0.8$ at operating speed $6 < \overline{\Omega} < 9$ and in the range of $0.55 < \overline{L}_a < 0.7$ at operating speed $4.5 < \overline{\Omega} < 7$. In *b*), the pure B is founded in the range of $0.1 < \overline{L}_a < 0.9$ at operating speed $1 < \overline{\Omega} < 4$ and in the range of $0.43 < \overline{L}_a < 0.57$ at operating speed $13 < \overline{\Omega} < 18$. As seen in *a*) and *b*), the non-synchronous condition(*l*) becomes suppressed when the ABD is located near the imbalance source. Specifically, B is more dominant around $\overline{L}_a = 0.75$ in a) and $\overline{L}_a = 0.5$ in *b*) respectively. However, we also observe unwanted coexistence zone($B+l$) in vicinity of B and merged synchronous condition(M) on each plot.

This result provides the guideline of the relative axial location of ABD to imbalance rotor to avoid the non-synchronous condition and guarantee the synchronous one.



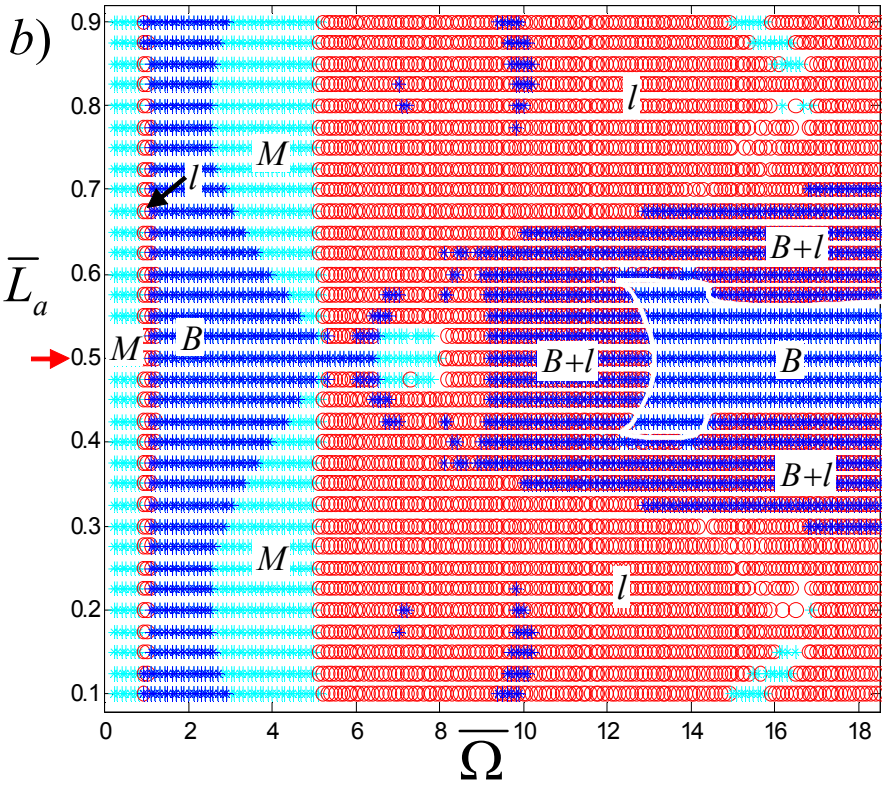


Figure.6.6 The relative suggested location of ABD along with shaft to imbalance source(displayed as a red arrow on each plot) to avoid the limit-cycles condition and unwanted coexistence zone(The locations of imbalance rotor are situated at $0.75L$ in a) and $0.5L$ in b), respectively)

6.5 Concluding Remarks

With several reasonable assumptions, this paper provides the harmonic limit-cycle solutions of automatic balancing device(ABD) for three dimensional flexible shaft/rigid imbalanced rotor system with symmetric rigid support since the rigid shaft is not valid in some situations and the flexibility of shaft can be negligible in certain applications. Essentially, this paper presents an approximate harmonic analytical solution to describe the limit-cycle behavior of system interacting with flexible shaft. The shape function of flexible shaft is determined by using well known fixed-fixed boundary condition due to symmetric rigid support. Here the whirl speed of the ABD balancer masses is determined via the solution of a non-linear characteristic equation. The characteristic of whirl speed for ABD balancer mass provides us that the system is excited with the damped natural frequencies associated expanded modal coordinates under limit-cycle condition. Also, the limit-cycle stability is assessed via a perturbation and Floquet analysis with three main parameters of ABD *i*) relative size of ABD balancer mass to the mass of entire system *ii*)

viscous damping coefficient of balancer, and *iii*) the relative axial location of ABD along with shaft to the axial location of imbalance rotor and the coexistence of the stable balanced synchronous condition and undesired non-synchronous limit-cycle is also investigated. It is found that for certain combinations of appropriate three main parameters of ABD and operating speeds, the non-synchronous limit-cycle can be made unstable thus guaranteeing global asymptotic stability of the synchronous balanced condition. Specifically, as the balancer mass of ABD decrease and the viscous damping coefficient of balancer in ABD increases, the limit cycle condition tend to be less dominant and it is also found that the relative location of ABD to imbalance rotor can be effective to avoid or prevent this unwanted non-synchronous behavior.

The findings in this paper yield important insights for researchers wishing to utilize automatic balancing devices in flexible shaft/rigid rotor systems and limit-cycle mitigation.

LIST OF REFERENCES

[1] Thearle, E.L., 1950, “Automatic dynamic balancers (Part 2-Ring, pendulum, ball balancers),” Machine Design Vol. 22, pp.103-106.

[2] Kubo, S., Jinouchi, Y., Araki, Y., and Inoue, J., 1986, “Automatic balancer (pendulum balancer),” Bulletin of JSME, Vol. 29, No. 249, pp.924-928.

[3] Bovik, P., and Hogfords, C., 1986, “Autobalancing of rotors,” Journal of Sound and Vibration, Vol.111, pp.429-440.

[4] Majewski, T., 1998, “Position error occurrence in self balancers used on rigid rotors of rotating machinery,” Mechanism and Machine Theory, Vol.23, No.1, pp71-78.

[5] Jinnouchi, Y., Araki, Y., Inoue, J., Ohtsuka, Y., and Tan, C., 1993, “Automatic balancer (static balancing and transient response of of a multi-ball balancer),” Transactions of the Japan Society of Mechanical Engineers, Part C Vol.59 (557), pp.79-84.

[6] Lindell, H., 1996, “Vibration reduction on Hand-Held Grinders by Automatic Blancers”, Central European Journal of Public Health, Vol. 4, pp.43-45.

[7] Kim, W., Lee, D. J., and Chung. J., 2005, Three-Dimensional Modeling and Dynamic Analysis of of an Automatic Ball Balancer in an Optical Disk Drive,” J. Sound Vib., 285(3), pp.547-569.

[8] Rajalingham, C., Bhat, R.B., 2006, “Complete Balancing of a disk Mounted on Vertical Cantilever Shaft Using a Two Ball Automatic Balancer”, Journal of Sound and Vibration, Vol.290, pp. 161-191.

[9] Chao., P.C.P., Haung, Y.D., and Sung, C.K., 2003, “Non-Planar Dynamic Modeling for the Optical Disk Drives Spindles Equipped with an Automatic Balancer.” Mechanism and Machine Theory, Vol. 38, pp.1289-1305.

[10] Chao., P.C.P., Sung, C.K., Wu, S.T., and Huang, J.S., 2007, “Non-Planar Modeling and Experimental Validation of a Spindle-Disk System Equipped with an Automatic Balancer sytem in Optical Disk Drives.” Microsystem Technologies, Vol. 13, pp.1227-1239.

[11] Sohn, J. S., Lee, J. W., Cho, E. H., Park, N. C., and Park Y. P., “Dynamic analysis of a pendulum dynamic automatic balancer,” Shock and Vibration, Vol.14 2007, pp.151-167.

[12] Horvath, R., Flowers, G. T., and Fausz, J., “Passive balancing of rotor systems using pendulum balancers”, ASME Journal of Vibration and Acoustic, Vol.130, No.4, 2008, Article Number 041011.

[13] Meirovitch, L., Analytical Methods in Vibrations, The Macmillan Company, New York, 1967.

[14] Bucher I., and Edwins D. J., “Modal analysis and testing of rotating structure,” Phil. Trans. Royal Soc. Lond. A, Vol. 359, 2001, pp. 61-96.

[15] Green, K., Champneys, A.R. and Lieven, N.J., 2006, “Bifurication Analysis of an Automatic Dynamics Balancing Mechanism for Eccentric Rotors”, Journal of Sound and Vibration, Vol.291, pp. 861-881.

[16] Green, K., Champneys, A.R. and Friswell, M. I., 2006, "Analysis of Transient Response of Automatic Balacer for Eccentric Rotors", Int. J. Mech. Sci., 48 pp.27-293.

[17] John M. Vance., "Rotordynamics of Turbomachinary". 1988, John Wiley and Son, Inc.

[18] Lund, J. W., *Self-Excited, Stationary whirl orbits of a Journal in a Sleeve Bearings*, Ph.D Dissertation in Engineering Mechanics, Rensselaer Polytechnic Institute (1966).

[19] Lund, J. W., and Saibel, E., "Oil whirl orbits of a Rotor in Sleeve Bearings," Journal *of Engineering for industry*, pp. 813-823 (November 1967).

[20] Lund, J. W., Arwas, E. B., Cheng, H. S., Ng, C. W., and Pan, C. H., Rotor-Bearing Dynamics Design Technology, Pt. III: Design Handbook for Fluid Film Type Bearing, Technical Report AFAPL-TR-65-45, Aero Propulsion Lab, Wright-Patterson Air Force Base, Ohio, May 1965.

[21] Chieh-LI CHEN, and Her-Terng Yau., "Chaos in the Imbalance Response of a Flexible Rotor Supported by Oil Flim Bearing with Non-Linear Suspension".

[22] Kai-Yew Lum, Vincent T. Coppola, and Dennis S. Bernstein., 1996, "Adaptive Autocentering Control for an Active Magnetic Bearing Supporting a Rotor with Unknown Mass Imbalance", *IEEE Trans.,*Vol.4, No.5, pp.587-597.

[23] L. Sun and J. M. Krodkiewski., 1998, "Self-Tuning Adaptive Control of Forced Vibration in Rotor Systems Using an Active Journal Bearing," Journal of Sound and Vibration, vol. 213, pp. 1-14.

[24] H. A. DeSmidt, 2009, "Imbalance Vibration Suppression of Supercritical Shaft via an Automatic Balancing Device," Journal of Vibration and Acoustics, vol. 131, pp. 1-13.

[25] E. Slontine and W. Li, "Applied Nonlinear Control," Prentice Hall, Englewood.

[26] Wilson J. Rugh, 1996, "Linear System Theory". Upper Saddle River, N.J Prentice Hall.

[27] Issac, FRIED, 1984, "Orthogonal Trajectory Accession to Nonlinear Equilibrium Curve", Computer Methods in Applied Mechanics and Engineering, vol.47, issue 3, pp. 283-297.

[28] G.A. Wempner, 1971, Discrete Approximations related to Nonlinear Theories of solids, Internat. J Solid Structures 7, pp. 1581-1599.

[29] Daeyi Jung and Hans. DeSmidt, "Limit-Cycle Analysis of Planar Rotor/Autobalancer System Supported on Hydrodynamic Journal Bear," *Proc. ASME Design Technical Conference & Computer and Information Engineering Conference-23rd Biennial Conference on Mechanical Vibration and Noise*, Washington, DC, Aug. 2011.

[30] Tsuyoshi Inoue, Yukiko Ishida, Hideaki Niimi, 2012, "Vibration Analysis of a Self a Self-Excited Vibration in a Rotor System Caused by a Ball Balancer", Journal of Vibration and Acoustics, Vol. 134, pp.1-11.

[31] Daeyi Jung and Hans. DeSmidt, "Limit-Cycle Analysis of Three Dimensional Rigid Rotor/Shaft/Autobalancer System with on Symmetric Bearing Support," *Proc. ASME Design*

Technical Conference & Computer and Information Engineering Conference-24th Biennial Conference on Mechanical Vibration and Noise, Chicago, IL, Aug. 2012.

[32] Daeyi Jung and Hans. DeSmidt, "Hybrid Adaptive Rotor Imbalance Vibration Control via Passive Autobalancer and Active Magnetic Bearing," Proc. *ASME Design Technical Conference & Computer and Information Engineering Conference-23rd Biennial Conference on Mechanical Vibration and Noise,* Washington, DC, Aug. 2011.

[33] Dierk Schroder, 2000, "Intelligent Observer and Control Design for Nonlinear Systems". N.Y Spinger.

[34] Jerry H. Ginsberg, 1995, " Advanced Engineering Dynamics". Cambridge University Press.

[35] K.R. Symon,1971, "Mechanic, 3rd ed.", Addison-Wesley, MA.

[36] R. Weinstock, Calculus, Dover, New York.

[37] Kemin Zhou, 1998,"Essentials of Robust Control", Prentice-Hall 1998.

[38] Kemin Zhou, J.C. Doyle, and K. Glover, 1996, "Robust and Optimal Control", Prentice Hall.

[39] Sigur Skogestad, Ian Postlethwaite, 2001, "Multivariable Feedback Control", John Wiley & Sons.

[40] J.C. Doyle, B.A. Francis and A.R. Tannenbaum, 1990, Feedback Control Theory, McMillan, N.Y..

[41] Gene F. Franklin, J. David Powell, and Abbas Emami-Naeini, 2002, " FeedBack Control of Dynamic Systems, 4th ed.", Prentice Hall.

[42] Richard C. Dorf and Robert H. Bishop, 1995, "Modern Control System 7th ed.", Addison-Wesley.

APPENDIX

The detail of system matrices in (2-10) are given below.

$$M(\phi_i,t)=\begin{bmatrix} m+2m_b & 0 & -m_b r_b \sin[\Omega t+\phi_1] & -m_b r_b \sin[\Omega t+\phi_2] \\ 0 & m+2m_b & m_b r_b \cos[\Omega t+\phi_1] & m_b r_b \cos[\Omega t+\phi_2] \\ -m_b r_b \sin[\Omega t+\phi_1] & m_b r_b \cos[\Omega t+\phi_1] & m_b {r_b}^2 & 0 \\ -m_b r_b \sin[\Omega t+\phi_2] & m_b r_b \cos[\Omega t+\phi_2] & 0 & m_b {r_b}^2 \end{bmatrix}$$

$$C(\phi_i,t)=\begin{bmatrix} C_{XX} & C_{XY} & -2m_b r_b \Omega \cos[\Omega t+\phi_1] & -2m_b r_b \Omega \cos[\Omega t+\phi_2] \\ C_{YX} & C_{YY} & -2m_b r_b \Omega \sin[\Omega t+\phi_1] & -2m_b r_b \Omega \sin[\Omega t+\phi_2] \\ 0 & 0 & c_b {r_b}^2 & 0 \\ 0 & 0 & 0 & c_b {r_b}^2 \end{bmatrix} \qquad K=\begin{bmatrix} K_{XX} & K_{XY} & 0 & 0 \\ K_{YX} & K_{YY} & 0 & 0 \\ 0 & 0 & 0 & 0 \\ 0 & 0 & 0 & 0 \end{bmatrix}$$

$$F_{ball}(\dot{\phi}_i,\phi_i,t)=\begin{bmatrix} m_b r_b \sum_{i=1}^{2}(\Omega^2+\dot{\phi}_i^{\,2})\cos[\Omega t+\phi_i] \\ m_b r_b \sum_{i=1}^{2}(\Omega^2+\dot{\phi}_i^{\,2})\sin[\Omega t+\phi_i] \\ 0 \\ 0 \end{bmatrix} \qquad F_{im}=\begin{bmatrix} m_{im} r_{im}(\Omega^2)\cos[\Omega t+\phi_{im}] \\ m_{im} r_{im}(\Omega^2)\sin[\Omega t+\phi_{im}] \\ 0 \\ 0 \end{bmatrix}$$

The detail of system matrices in (2-13) are given below.

$$M_r(\phi_i)=\begin{bmatrix} m+2m_b & 0 & -m_b r_b \sin[\phi_1] & -m_b r_b \sin[\phi_2] \\ 0 & m+2m_b & m_b r_b \cos[\phi_1] & m_b r_b \cos[\phi_2] \\ -m_b r_b \sin[\phi_1] & m_b r_b \cos[\phi_1] & m_b {r_b}^2 & 0 \\ -m_b r_b \sin[\phi_2] & m_b r_b \cos[\phi_2] & 0 & m_b {r_b}^2 \end{bmatrix}$$

$$C_r(\phi_i)=\begin{bmatrix} C_{XX} & -2(m+2m_b)\Omega & -2m_b r_b \Omega \cos[\phi_1] & -2m_b r_b \Omega \cos[\phi_2] \\ 2(m+2m_b)\Omega & C_{XX} & -2m_b r_b \Omega \sin[\phi_1] & -2m_b r_b \Omega \sin[\phi_2] \\ 2m_b r_b \Omega \cos[\phi_1] & 2m_b r_b \Omega \sin[\phi_1] & c_b {r_b}^2 & 0 \\ 2m_b r_b \Omega \cos[\phi_2] & 2m_b r_b \Omega \sin[\phi_2] & 0 & c_b {r_b}^2 \end{bmatrix}$$

$$K_r(\phi)=\begin{bmatrix} K_{XX}-(m+2m_b)\Omega^2 & -C_{XX}\Omega+K_{A.XY} & 0 & 0 \\ C_{XX}\Omega+K_{A.YX} & K_{XX}-(m+2m_b)\Omega^2 & 0 & 0 \\ m_b r_b \Omega^2 \sin[\phi_1] & -m_b r_b \Omega^2 \cos[\phi_1] & 0 & 0 \\ m_b r_b \Omega^2 \sin[\phi_2] & -m_b r_b \Omega^2 \cos[\phi_2] & 0 & 0 \end{bmatrix} \quad F_{im.r}=\begin{bmatrix} m_{im} r_{im} \Omega^2 \cos[\phi_{im}] \\ m_{im} r_{im} \Omega^2 \sin[\phi_{im}] \\ 0 \\ 0 \end{bmatrix}$$

$$F_{ball.r}(\dot{\phi},\phi)=\begin{bmatrix} m_b r_b \sum_{i=1}^{2}(\Omega^2+\dot{\phi}_i^{\,2})\cos[\phi_i] \\ m_b r_b \sum_{i=1}^{2}(\Omega^2+\dot{\phi}_i^{\,2})\sin[\phi_i] \\ 0 \\ 0 \end{bmatrix}$$

The detail of (2-14) is given by,

$$M_r(\phi)=\begin{bmatrix} m+m_{b.m} & 0 & -m_{b.m}r_b\sin[\phi] \\ 0 & m+m_{b.m} & m_{b.m}r_b\cos[\phi] \\ -m_{b.m}r_b\sin[\phi] & m_{b.m}r_b\cos[\phi] & m_{b.m}{r_b}^2 \end{bmatrix}$$

$$C_r(\phi)=\begin{bmatrix} C_{XX} & -2(m+m_{b.m})\Omega & -2m_{b.m}r_b\Omega\cos[\phi] \\ 2(m+m_{b.m})\Omega & C_{YY} & -2m_{b.m}r_b\Omega\sin[\phi] \\ 2m_{b.m}r_b\Omega\cos[\phi] & 2m_{b.m}r_b\Omega\sin[\phi] & c_b{r_b}^2 \end{bmatrix}$$

$$K_r(\phi)=\begin{bmatrix} K_{XX}-(m+m_{b.m})\Omega^2 & -C_{XX}\Omega+K_{A.XY} & 0 \\ C_{XX}\Omega+K_{A.YX} & K_{XX}-(m+m_{b.m})\Omega^2 & 0 \\ m_{b.m}r_b\Omega^2\sin[\phi] & -m_{b.m}r_b\Omega^2\cos[\phi] & 0 \end{bmatrix} \quad F_{im.r}=\begin{bmatrix} m_{im}r_{im}\Omega^2\cos[\phi_{im}] \\ m_{im}r_{im}\Omega^2\sin[\phi_{im}] \\ 0 \end{bmatrix}$$

$$F_{ball.r}(\dot{\phi},\phi)=\begin{bmatrix} m_{b.m}r_b(\Omega^2+\dot{\phi}^2)\cos[\phi] \\ m_{b.m}r_b(\Omega^2+\dot{\phi}^2)\sin[\phi] \\ 0 \end{bmatrix}$$

The detail of coefficients in (2-27) is provided by,

$$p_1=C_{XX}{m_{b.m}}^2+c_b{m_t}^2$$

$$p_2=5C_{XX}{m_{b.m}}^2\Omega+4c_b{m_t}^2\Omega-K_{A.XY}{m_{b.m}}^2$$

$$p_3=2{m_{b.m}}^2\Omega(5C_{XX}\Omega-2K_{A.XY})+c_b({C_{XX}}^2-2m_t(K_{XX}-3m_t\Omega^2))$$

$$p_4=2({m_{b.m}}^2\Omega^2(5C_{XX}\Omega-3K_{A.XY})+c_b({C_{XX}}^2\Omega+2m_t\Omega(m_t\Omega^2-K_{XX})-C_{XX}K_{A.XY})$$

$$p_5=c_b({K_{XX}}^2+{K_{A.XY}}^2-2C_{XX}K_{A.XY}\Omega+{C_{XX}}^2\Omega^2-2K_{XX}m_t\Omega^2+{m_t}^2\Omega^4)+{m_{b.m}}^2\Omega^3(5C_{XX}\Omega-4K_{A.XY})$$

$$p_6={m_{b.m}}^2\Omega^4(C_{XX}\Omega-K_{A.XY})$$

The detail of system matrices in (3-10) are given below.

$$M(\phi_i,t)=\begin{bmatrix} m+2m_b & 0 & -m_b r_b \sin[\Omega t+\phi_1] & -m_b r_b \sin[\Omega t+\phi_2] \\ 0 & m+2m_b & m_b r_b \cos[\Omega t+\phi_1] & m_b r_b \cos[\Omega t+\phi_2] \\ -m_b r_b \sin[\Omega t+\phi_1] & m_b r_b \cos[\Omega t+\phi_1] & m_b {r_b}^2 & 0 \\ -m_b r_b \sin[\Omega t+\phi_2] & m_b r_b \cos[\Omega t+\phi_2] & 0 & m_b {r_b}^2 \end{bmatrix}$$

$$C(\phi_i,t)=\begin{bmatrix} C_{XX} & C_{XY} & -2m_b r_b \Omega \cos[\Omega t+\phi_1] & -2m_b r_b \Omega \cos[\Omega t+\phi_2] \\ C_{YX} & C_{YY} & -2m_b r_b \Omega \sin[\Omega t+\phi_1] & -2m_b r_b \Omega \sin[\Omega t+\phi_2] \\ 0 & 0 & c_b {r_b}^2 & 0 \\ 0 & 0 & 0 & c_b {r_b}^2 \end{bmatrix} \qquad K=\begin{bmatrix} K_{XX} & K_{XY} & 0 & 0 \\ K_{YX} & K_{YY} & 0 & 0 \\ 0 & 0 & 0 & 0 \\ 0 & 0 & 0 & 0 \end{bmatrix}$$

$$F_{ball}(\dot{\phi}_i,\phi_i,t)=\begin{bmatrix} m_b r_b \sum_{i=1}^{2}(\Omega^2+\dot{\phi}_i^{\,2})\cos[\Omega t+\phi_i] \\ m_b r_b \sum_{i=1}^{2}(\Omega^2+\dot{\phi}_i^{\,2})\sin[\Omega t+\phi_i] \\ 0 \\ 0 \end{bmatrix} \qquad F_{im}=\begin{bmatrix} m_{im} r_{im} \Omega^2 \cos[\Omega t+\phi_{im}] \\ m_{im} r_{im} \Omega^2 \sin[\Omega t+\phi_{im}] \\ 0 \\ 0 \end{bmatrix}$$

The detail of system matrices in (3-12) are given below.

$$M(\phi,t)=\begin{bmatrix} m+m_{b.m} & 0 & -m_{b.m} r_b \sin[\Omega t+\phi] \\ 0 & m+m_{b.m} & m_{b.m} r_b \cos[\Omega t+\phi] \\ -m_{b.m} r_b \sin[\Omega t+\phi] & m_{b.m} r_b \cos[\Omega t+\phi] & m_{b.m} {r_b}^2 \end{bmatrix}$$

$$C(\phi,t)=\begin{bmatrix} C_{XX} & C_{XY} & -2m_{b.m} r_b \Omega \cos[\Omega t+\phi] \\ C_{YX} & C_{YY} & -2m_{b.m} r_b \Omega \sin[\Omega t+\phi] \\ 0 & 0 & c_b {r_b}^2 \end{bmatrix} \qquad K=\begin{bmatrix} K_{XX} & K_{XY} & 0 \\ K_{YX} & K_{YY} & 0 \\ 0 & 0 & 0 \end{bmatrix}$$

$$F_{ball}(\dot{\phi}_i,\phi_i,t)=\begin{bmatrix} m_{b.m} r_b (\Omega^2+\dot{\phi}^2)\cos[\Omega t+\phi] \\ m_{b.m} r_b (\Omega^2+\dot{\phi}^2)\sin[\Omega t+\phi] \\ 0 \end{bmatrix} \qquad F_{im}=\begin{bmatrix} m_{im} r_{im} \Omega^2 \cos[\Omega t+\phi_{im}] \\ m_{im} r_{im} \Omega^2 \sin[\Omega t+\phi_{im}] \\ 0 \end{bmatrix}$$

The detail of (4-17) is given by,

$$[f,g_{new,1}]=\begin{bmatrix} -1 \\ 0 \\ 0 \\ 0 \\ -\dfrac{C_f[-2(m+m_b)+m_b\cos(2\phi_1)+m_b\cos(2\phi_2)]}{2m^2+4mm_b+{m_b}^2-{m_b}^2\cos(2(\phi_1-\phi_2))} \\ -\dfrac{2m_b(m+2m_b)\Omega[\sin(2\phi_1)+\sin(2\phi_2)]}{2m^2+4mm_b+{m_b}^2-{m_b}^2\cos(2(\phi_1-\phi_2))} \\ \dfrac{2m_b\cos(\phi_1)\Omega[(2m+3m_b)\sin(\phi_1)-m_b\sin(\phi_1-2\phi_2)]}{2m^2+4mm_b+{m_b}^2-{m_b}^2\cos(2(\phi_1-\phi_2))} \\ \dfrac{2m_b\cos(\phi_2)\Omega[(2m+3m_b)\sin(\phi_2)+m_b\sin(2\phi_1-\phi_2)]}{2m^2+4mm_b+{m_b}^2-{m_b}^2\cos(2(\phi_1-\phi_2))} \end{bmatrix} \qquad [f,g_{new,2}]=\begin{bmatrix} 0 \\ -1 \\ 0 \\ 0 \\ \dfrac{2m_b(m+2m_b)\Omega[\sin(2\phi_1)+\sin(2\phi_2)]}{2m^2+4mm_b+{m_b}^2-{m_b}^2\cos(2(\phi_1-\phi_2))} \\ \dfrac{C_f[2(m+m_b)+m_b\cos(2\phi_1)+m_b\cos(2\phi_2)]}{2m^2+4mm_b+{m_b}^2-{m_b}^2\cos(2(\phi_1-\phi_2))} \\ -\dfrac{2m_b\sin(\phi_1)\Omega[(2m+3m_b)\cos(\phi_1)+m_b\cos(\phi_1-2\phi_2)]}{2m^2+4mm_b+{m_b}^2-{m_b}^2\cos(2(\phi_1-\phi_2))} \\ -\dfrac{2m_b\sin(\phi_2)\Omega[(2m+3m_b)\cos(\phi_2)+m_b\cos(2\phi_1-\phi_2)]}{2m^2+4mm_b+{m_b}^2-{m_b}^2\cos(2(\phi_1-\phi_2))} \end{bmatrix}$$

$$[f, g_{new3}] = \begin{bmatrix} 0 \\ 0 \\ -1 \\ 0 \\ -\dfrac{m_b[-2\dot{\phi}_1 m_b r_b \cos(\phi_1 - 2\phi_2) + 2\cos(2\phi_1)[\dot{\phi}_1(2m+m_b)r_b + (2m+3m_b)\Omega\sin(\phi_1) - m_b\Omega\sin(\phi_1 - 2\phi_2)]}{2m^2 + 4mm_b + m_b^2 - m_b^2\cos(2(\phi_1 - \phi_2))} \\ \dfrac{m_b[2(-\dot{\phi}_1(2m+m_b)r_b + m_b\Omega\cos(\phi_1 - 2\phi_2))\sin(\phi_1) + (2m+3m_b)\Omega\sin(2\phi_1) - 2\dot{\phi}_1 m_b r_b \sin(\phi_1 - 2\phi_2)]}{2m^2 + 4mm_b + m_b^2 - m_b^2\cos(2(\phi_1 - \phi_2))} \\ \dfrac{2[c_b(m^2 + 3mm_b + 2m_b^2) + \dot{\phi}_1 m_b^3 \sin(2(\phi_1 - \phi_2))]}{2m^2 + 4mm_b + m_b^2 - m_b^2\cos(2(\phi_1 - \phi_2))} \\ \dfrac{4\dot{\phi}_1 m_b(m+m_b)\sin(\phi_1 - \phi_2)}{2m^2 + 4mm_b + m_b^2 - m_b^2\cos(2(\phi_1 - \phi_2))} \end{bmatrix}$$

$$[f, g_{new4}] = \begin{bmatrix} 0 \\ 0 \\ 0 \\ -1 \\ \dfrac{m_b[2\dot{\phi}_2 m_b r_b \cos(2\phi_1 - \phi_2) - 2\cos(\phi_2)[\dot{\phi}_2(2m+m_b)r_b + (2m+3m_b)\Omega\sin(\phi_2) + m_b\Omega\sin(2\phi_1 - \phi_2)]}{2m^2 + 4mm_b + m_b^2 - m_b^2\cos(2(\phi_1 - \phi_2))} \\ \dfrac{m_b[m_b\Omega\sin(2\phi_1) - m_b\Omega\sin(2(\phi_1 - \phi_2)) + 2\dot{\phi}_2 m_b r_b \sin(2\phi_1 - \phi_2) - 4\dot{\phi}_2 m r_b \sin(\phi_2) - 2\dot{\phi}_2 m_b r_b \sin(\phi_2) + 2m\Omega\sin(2\phi_2) + 3m_b\Omega\sin(2\phi_2)]}{2m^2 + 4mm_b + m_b^2 - m_b^2\cos(2(\phi_1 - \phi_2))} \\ \dfrac{4\dot{\phi}_2 m_b(m+m_b)\sin(\phi_1 - \phi_2)}{2m^2 + 4mm_b + m_b^2 - m_b^2\cos(2(\phi_1 - \phi_2))} \\ \dfrac{2c_b(m^2 + 3mm_b + 2m_b^2) - 2\dot{\phi}_2 m_b^3 \sin(2(\phi_1 - \phi_2))}{2m^2 + 4mm_b + m_b^2 - m_b^2\cos(2(\phi_1 - \phi_2))} \end{bmatrix}$$

Vita

Daeyi Jung received the B.S degree from YeungNam University, KyoungSan, Korea in 2003 and the M.S degree from Louisiana Tech. University, LA, USA in 2005. He was a researcher of body/chassis department in KATECH(Korea Automotive Technology Institution) from 2005 to 2007.

He pursued a Doctor of Philosophy degree in Mechanical Engineering in the department of MABE at University of Tennessee, Knoxville since August 2008 under the supervision of Dr. DeSmidt, Hans August.

His research interest includes nonlinear system dynamics and control specializing in the rotor dynamics with a passive automatic balancing device, and active control.